ENERGY LABORATORY

MASSACHUSETTS INSTITUTE OF TECHNOLOGY

AN INVESTIGATION OF THE PHYSICAL AND NUMERICAL FOUNDATIONS OF TWO-FLUID REPRESENTATION OF SODIUM BOILING WITH APPLICATIONS TO LMFBR EXPERIMENTS

by

Hee Cheon No and Mujid S. Kazimi

Energy Laboratory Report No. MIT-EL 83-003
March 1983

Energy Laboratory

and

Department of Nuclear Engineering

Massachusetts Institute of Technology
Cambridge, Mass. 02139

AN INVESTIGATION OF THE PHYSICAL AND NUMERICAL FOUNDATIONS OF TWO-FLUID REPRESENTATION OF SODIUM BOILING WITH APPLICATIONS TO LMFBR EXPERIMENTS

by

Hee Cheon No and Mujid S. Kazimi

March 1983

Topical Report of the
MIT Sodium Boiling Project

sponsored by

U.S. Department of Energy

Energy Laboratory Report No. MIT-EL 83-003

AN INVESTIGATION OF THE PHYSICAL AND NUMERICAL FOUNDATIONS OF TWO-FLUID REPRESENTATION OF SODIUM BOILING WITH APPLICATIONS TO LMFBR EXPERIMENTS

by

Hee Cheon No and Mujid S. Kazimi

ABSTRACT

This work involves the development of physical models for the constitutive relations of a two-fuid, three-dimensional sodium boiling code, THERMIT-6S. The code is equipped with a fluid conduction model, a fuel pin model, and a subassembly wall model suitable for simulating LMFBR transient events.

Mathematically rigorous derivations of time-volume averaged conservation equations are used to establish the differential equations of THERMIT-6S. These equations are then discretized in a manner identical to the original THERMIT code. A virtual mass term is incorporated in THERMIT-6S to solve the ill-posed problem.

Based on a simplified flow regime, namely cocurrent annular flow, constitutive relations for two-phase flow of sodium are derived. The wall heat transfer coefficient is based on momentum-heat transfer analogy and a logarithmic law for liquid film velocity distribution. A broad literature review is given for two-phase friction factors. It is concluded that entrainment can account for some of the discrepancies in the literature. Mass and energy exchanges are modelled by generalization of the turbulent flux concept.

Interfacial drag coefficients are derived for annular flows with entrainment.

Code assessment is performed by simulating three experiments for low flow-high power accidents and one experiment for low flow/low power accidents in the LMFBR. While the numerical results for pre-dryout are in good agreement with the data, those for post-dryout reveal the need for improvement of the physical models. The benefits of two-dimensional non-equilibrium representation of sodium boiling are studied.

ACKNOWLEDGEMENTS

We are greatly indepted to our co-workers on the Sodium Boiling Project. Professor Neil E. Todreas, Robert Zielinski and Kang Y. Huh, for useful discussions on several aspects of this work. Very special thanks are given to Professor Andrei Schor, who shared tough times and provided invaluable information on the original THERMIT. Recognition is extended to Gail Jacobson for her skillful typing of this manuscript.

Funding for this project was partially provided by the United States Department of Energy. Specially acknowledged is the financial support of the Korean Government to the first author throughout the period he stayed at M.I.T.

This report is based on the thesis submitted by the first author in partial fulfillment of the requirements of the Ph.D. degree in Nuclear Engineering at M.I.T.

TABLE OF CONTENTS

LIST OF TABLES

LIST OF FIGURES

NOMENCLATURE

A : Area

C : Constant

C_d : Drag Coefficient

D : Diameter

dp : Pressure drop

e : Internal energy

E : Entrainment fraction, Effectiveness of heat transfer by eddies or Total energy

f : Friction factor

F : Force or Rate of momentum transfer per unit volume

g : Graviatational acceleration

G : Mass flux

H : Heat transfer coefficient

h : Heat transfer coefficient or Enthalpy

j : Volumetric flux

k : Thermal conductivity

L : Length

P : Pressure or Perimeter

p : Pressure

Q : Rate of heat transfer per unit volume

q" : Heat flux

Q : Volumetric heat generation rater

R : Radius

s : Slip ratio

S : Entropy

t : Time

T : Temperature

Δt : Time interval

U : Velocity

$\vec{v}$: Velocity vector

V : Volume

x : Quality

X :Lockhort-Martinelli parameter

W : Mass Flow rate

Δz : Axial mesh size

α : Void fraction

σ : Surface tension

ϕ : Two-phase multiplier

Γ : Vapor generation rate

ρ : Density

μ : Viscosity

τ : Shear force

δ : Thickness of liquid film

Subscripts

b : Bulk

d : Droplets

e : Equivalent

f : Saturated liquid or Fluid

g : Saturated vapor

i : Interfacial

i,j,k : Nodal locations

l :Liquid

ld : Liquid droplet

lf : Liquid film

r :radial

s : Saturation

t : Transverse

tt : Turbulent-turbulent flow

v : Vapor

vv : Viscous-viscous flow

w : Wall

z : Axial

1ϕ : Single-phase

2ϕ : Two-phase

Superscripts

n : Time step

s : Spatial fluctuation

t : Turbulent fluctuation

x,y,z : Spatial directions

Dimensionless Group

Nu : Nusselt number

Pe : Peclet number

pr : Prandtl number

Re : Reynolds number

We : Weber number

Chapter 1 INTRODUCTION

1.1 Background

The growing public concern about the nuclear industry places an increasingly large emphasis on the safety aspects of nuclear reactors. In order to offer sufficient safety margins to assure that the public risk will be acceptably low, the U.S. Fast Breeder Reactor Safety Program approach is to provide four levels of protection, which are mainly aimed at reducing both the probability and consequences of a Core Disrutive Accident (CDA). These levels of protection are referred to as Lines of Assurance (LOA).

Figure 1.1 illustrates possible accident paths and Lines of Assurance for a potential CDA. The main objective of LOA.1 is to reduce the probability of occurrence of a serious accident. The special emphasis is placed on quality control, inspection, and monitoring at the level of construction and operation, and on providing a multilevel redundant plant protection system. The LOA.2 is based on an assumption that low probable but mechanistically possible events involving failure of LOA.1 will occur. LOA.2 places emphasis on an assurance that accidents can be contained within a limited number of fuel assemblies. This is done by providing, through design, ways to control neutronic reactivity and reactor coolability backed up by experimental and analytical works. The failure of LOA's 1 and 2 leads to core disruption and potential release of significant amounts

of radioactivity from the containment building to the environment, which should be mitigated and terminated without harm to the public. The objective of LOA's 3 and 4 is to ensure that the consequences of a postulated CDA can be sufficiently limited by the plant containment capability.

The present work is related to LOA 2, which in general requires an understanding of the mechanisms and design conditions which enable potential accidents to be terminated with limited core damage. Specifically the objective of this work is to develop an understanding of the role multidimensional and non-equilibrium effects of sodium boiling in determining the sequence of events during various accidents. These accidents include

1) Unprotected loss of flow (LOF): loss of electrical power to the primary coolant pumps, resulting in pump rundown and loss of core flow while the reactor is operating at power; coupled with a simultaneous failure of the plant protection system to scram the reactor. This accident corresponds to the low flow/high power condition.

2) Loss of pipe integrity (LOPI): undetected defect or leak in a reactor coolant pipe resulting in rapid decrease in core flow and partial loss of coolant with scram. This accident corresponds to the low flow/low power condition.

3) Unprotected transient overpower (TOP): malfunction of plant reactivity control system or operator error resulting in a sudden increase in core reactivity and power--coupled with a failure to scram.

4) Inadequate natural circulation decay heat removal: postulated inadequate heat removal by natural circulation following shutdown and loss of forced cooling in the primary loops.

5) Local subassembly fault: inlet flow or internal subassembly blockage resulting in cooling disturbance and potential for fuel failure propagation with scram.

The key events relating to each of these accidents can be shown in Figs 1.2-1.6.

1.2 Previous Work

The first code to analyze voiding in the LMFBR was the Transfugue-1 code (2) which used a homogeneous equilibrium model and a momentum integral method (3). This code was the forerunner of SAS 1A (5). The Transfugue-II code (4), an improvement of Transfugue-I, included sectional compressibility, variable vapor densities but time steps determined by the sonic velocity of the homogeneous equilibrium two-phase flow.

SAS codes of ANL represent a long development from the single-channel SAS 1A version through SAS 2A (6), SAS 3A (7), SAS 3D (8), and SAS 4A (9) which is now under

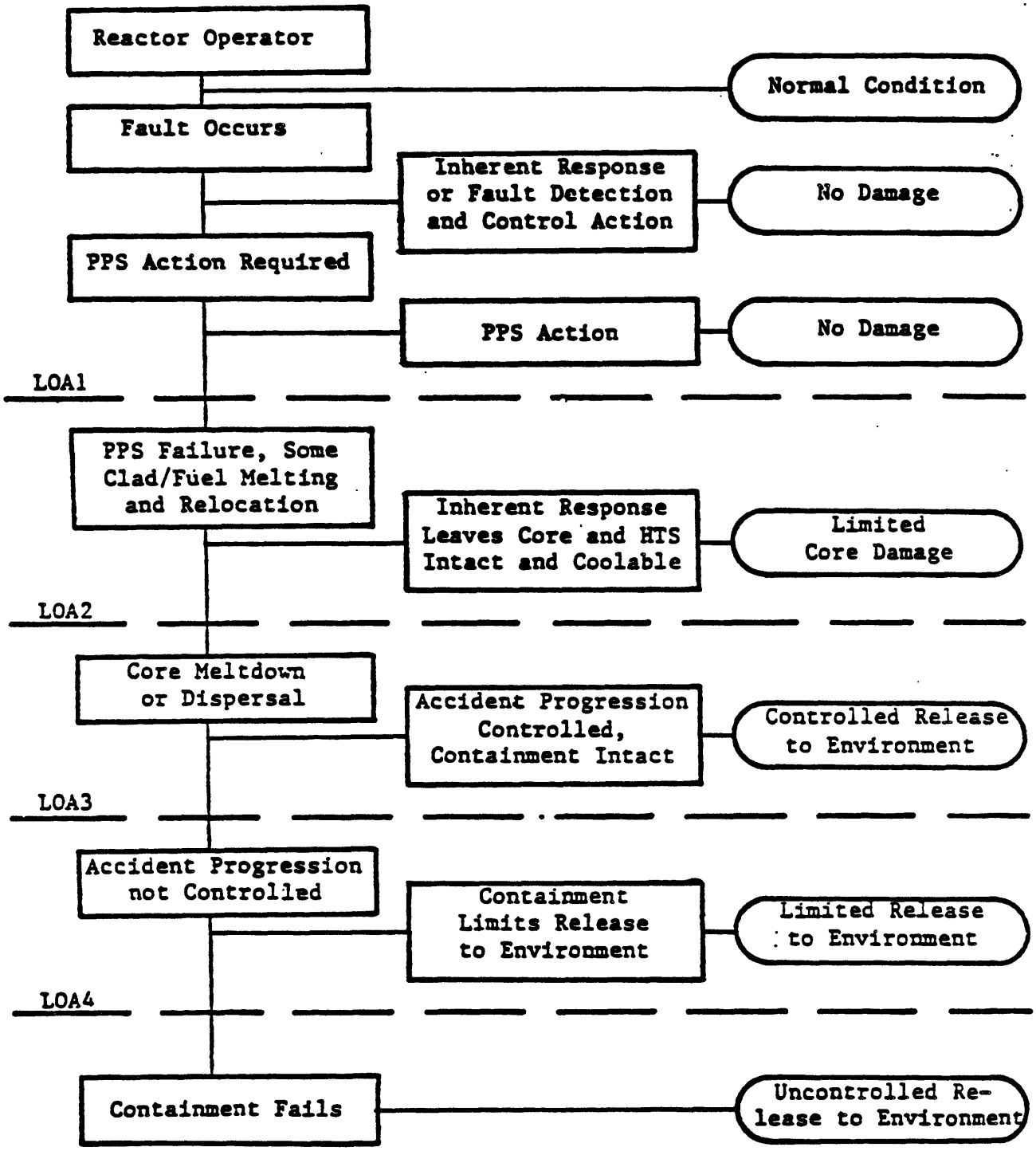

Figure 1.1

Possible Accident Paths and Lines of Assurance
For a Potential CDA
(From Reference 1)

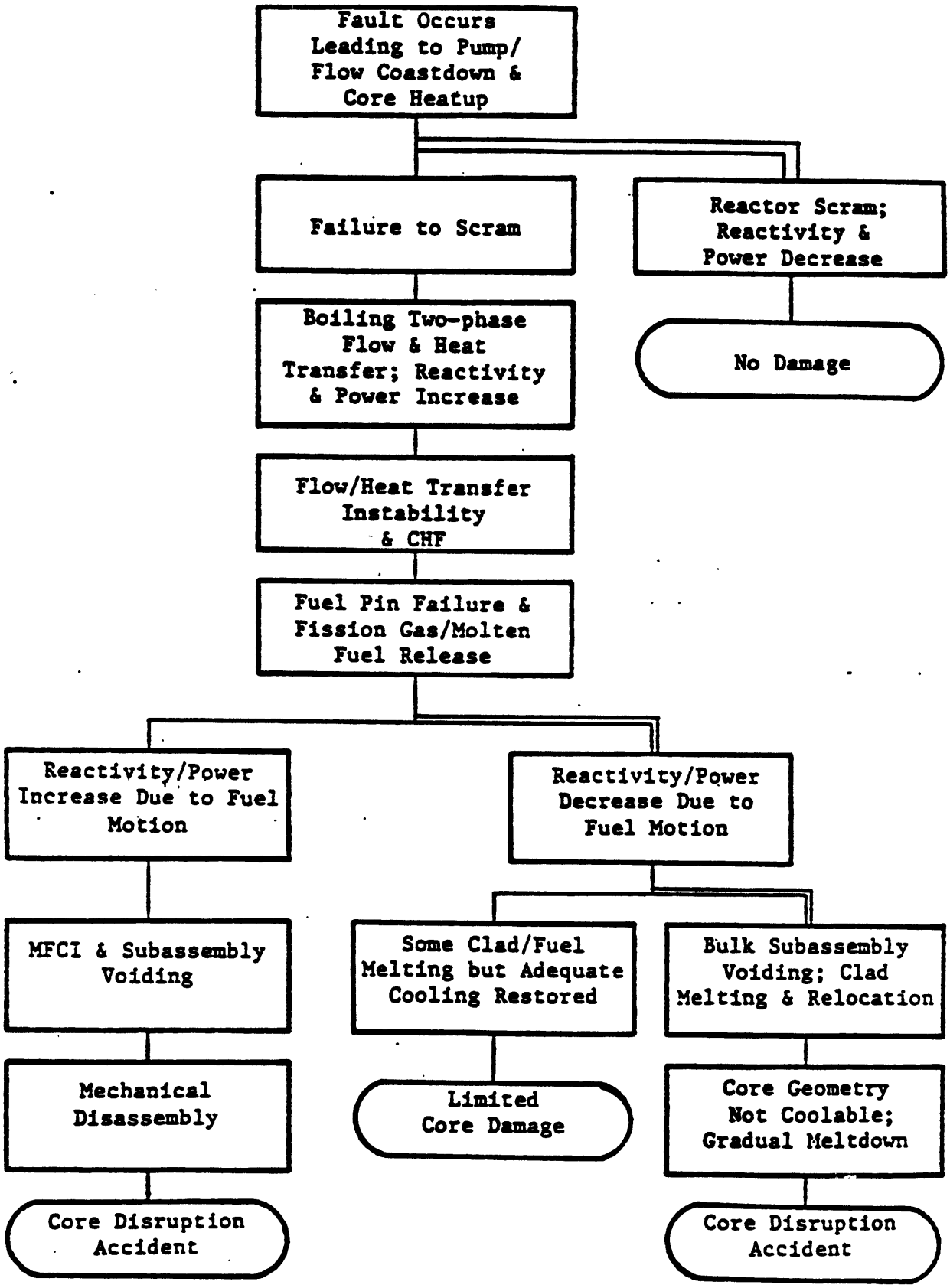

Figure 1.2

Key Events & Potential Accident Paths
For Unprotected Loss of Flow Accident

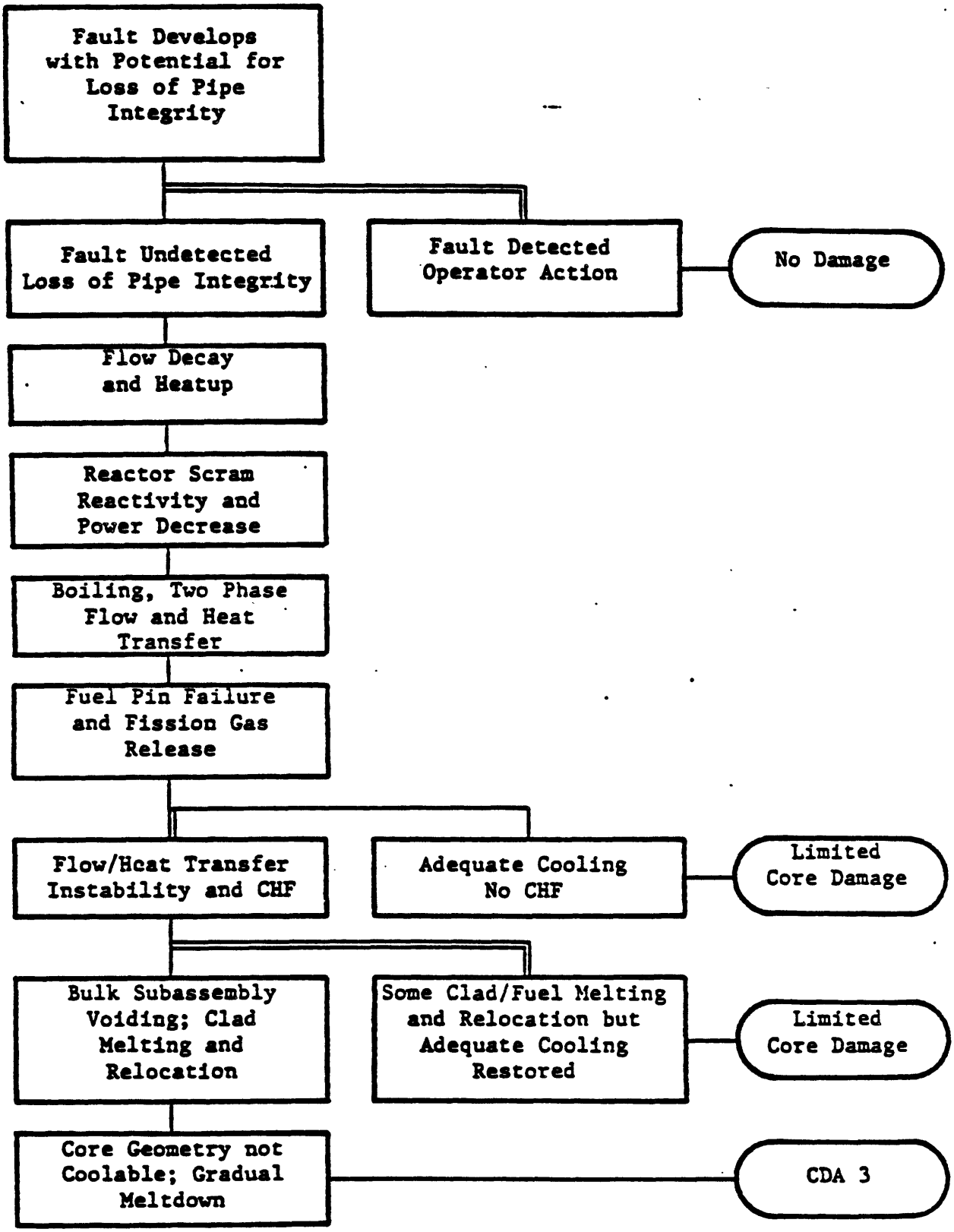

Figure 1.3

Key Events and Potential Accident Path
For Loss of Pipe Integrity Accident
(From Reference 1)

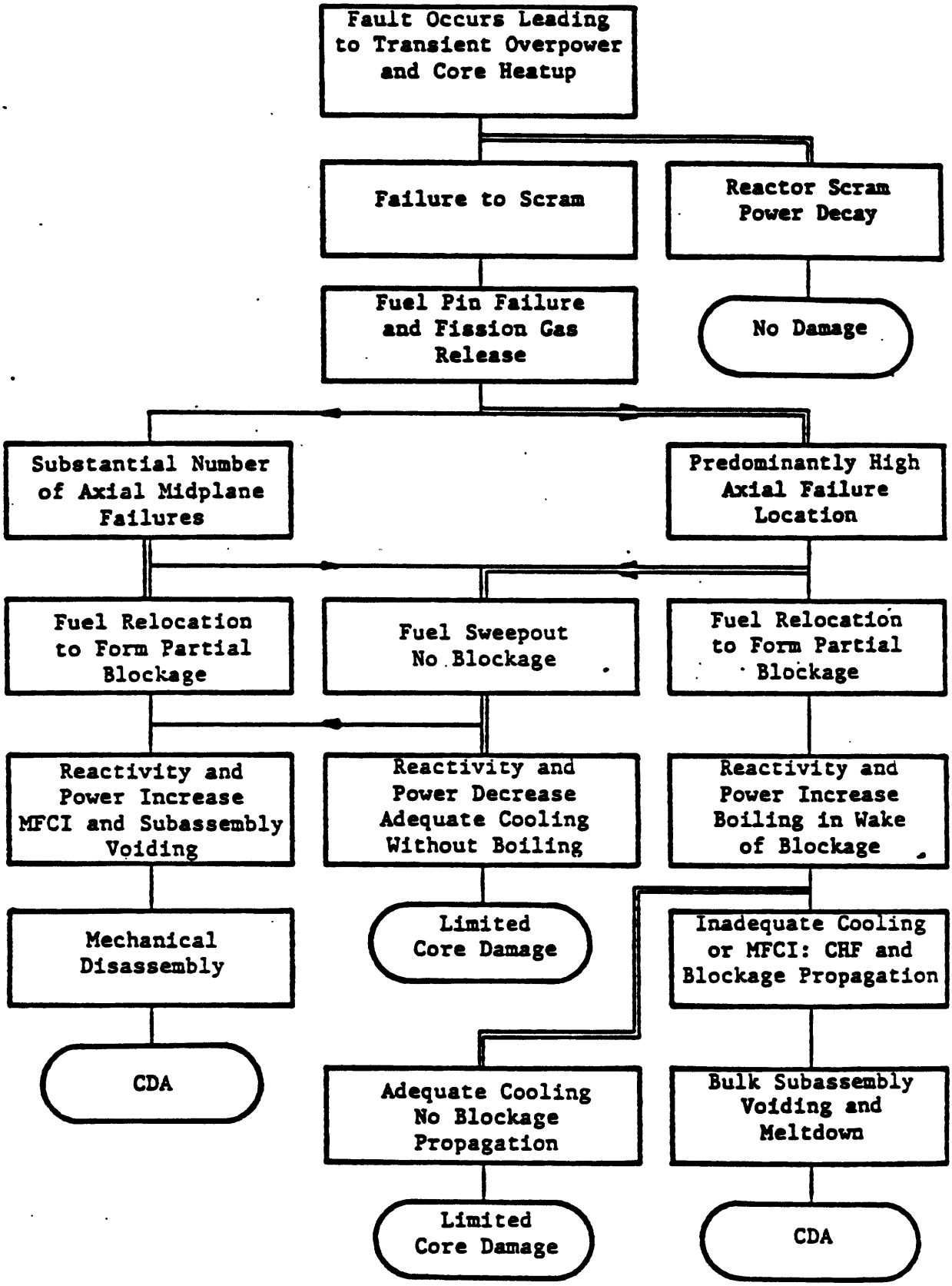

Figure 1.4

Key Events and Potential Accident Paths
For Unprotected Transient Overpower Accident

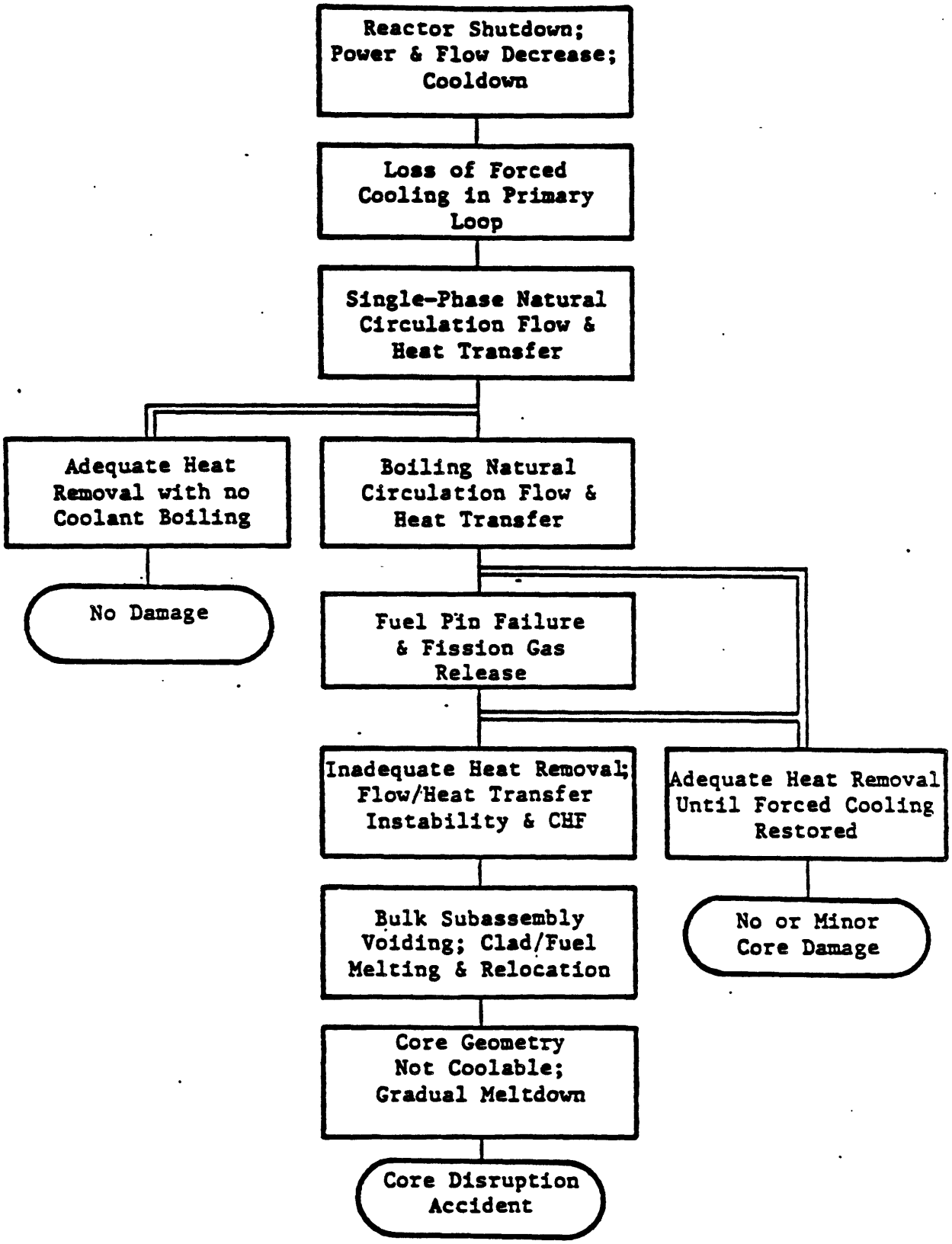

Figure 1.5

Key Events and Potential Accident Paths for Inadequate Natural Circulation Decay Heat Removal Accident

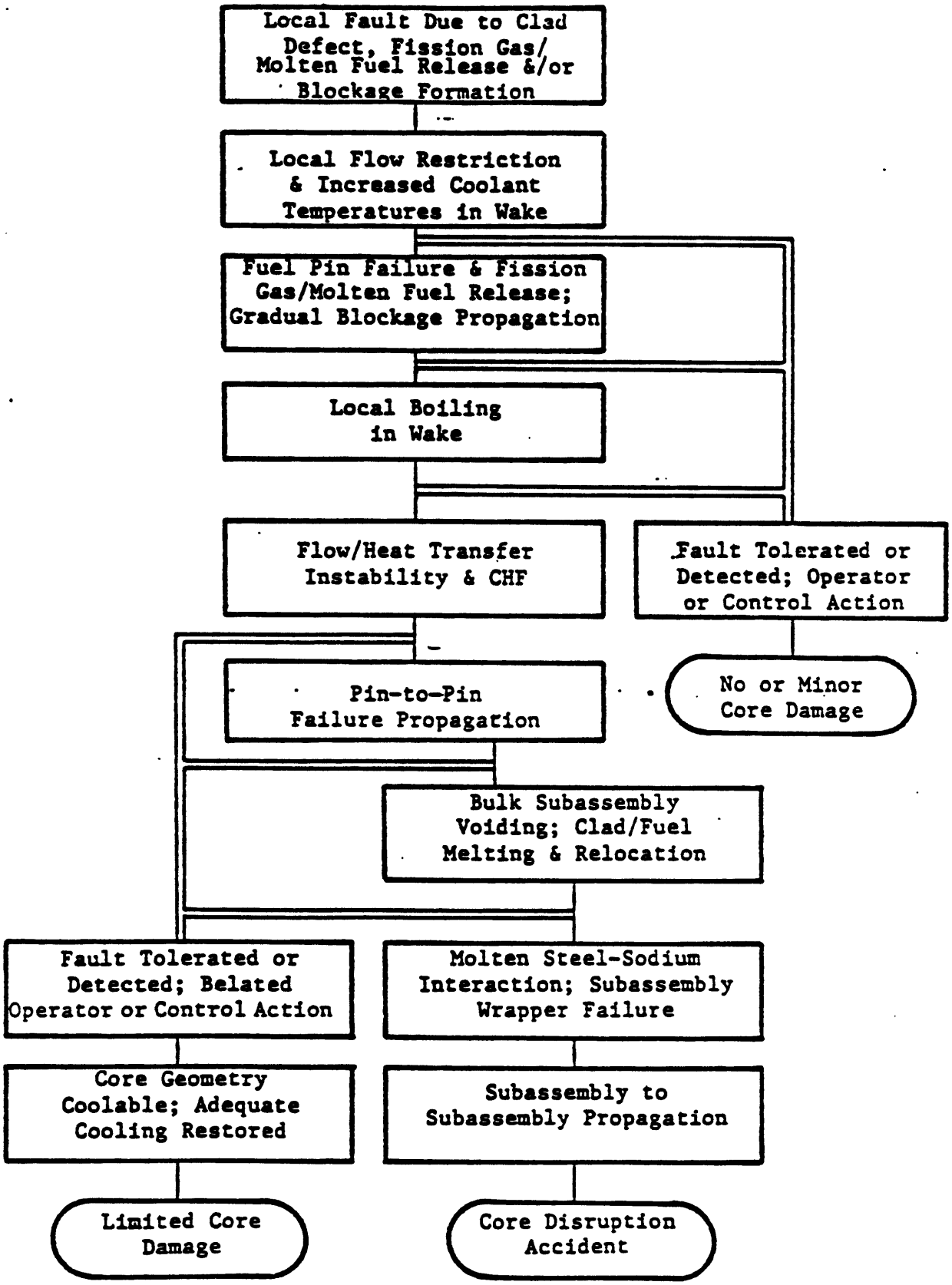

Figure 1.6

Key Events and Potential Accident Paths
For Local Subassembly Accident

development. SAS 1A was a single-channel code that included point kinetics and a combination of slip two-phase flow and single-bubble slug-boiling models. The sodium boiling model was later completely rewritten as a multibubble slug-boiling model for the multichannel SAS 2A version. SAS 3A, an expanded version of SAS 2A, contained models to allow complete calculations of cladding and fuel motions. SAS 3D used the same models as SAS 3A but restructured the code for better numerical efficiency.

The SAS coolant dynamics model calculates temporal and spatial void distribution and uses two different models for different times of boiling expulsion. A multibubble slug-boiling model is used for the initial portion of bubble formulation. Voiding is assumed to result from bubbles filling the cross section of the coolant channel, except that a liquid film is left on the clad and structure. Vapor pressure and temperature are assumed to be spatially uniform during initial bubble growth. When the bubble length exceeds a user-specified maximum value, the vapor bubble calculation is switched to a different model where axial variation in vapor pressure within the bubble is accounted for. In this model, the vapor pressure, temperatures, and mass-flow rates are calculated at fixed nodes within the bubble and also at the lower and upper interfaces. This uses a simultaneous solution of the vapor cells momentum and continuity equations with the momentum equations for the liquid slugs setting the boundary conditions at the interfaces. To

obtain numerical stability for reasonably large time steps, an implicit differencing scheme is used. SAS's main limitations are the restriction from a slug model, its lack of a mixing model, and its inability to adequately incorporate the radial heat losses and the multidimensional effect of voiding.

The BLOW code (10) developed in Germanny uses a multibubble slug-boiling model, which is similar to that in the SAS 3A, in order to describe sodium voiding phenomena. The main difference between BLOW and SAS is as follows: while the vapor velocity along a bubble can be obtained by solving the vapor momentum equation, the liquid film velocity in the BLOW is directly calculated on a basis of the assumption of an universal velocity profile across the liquid film thickness.

The MOC code (11) was developed by Siegmann in 1971 to predict the behavior of sodium during boiling and expulsion. In the two-phase region a slip flow model is assumed with the liquid and vapor in equilibrium at the saturation temperature. The conservation equations are solved using the method of characteristics. When imaginery characteristic slopes appeared in the two-phase flow with slip flow, numerical difficulties were encounted. The additional limitations of this code are its incapability to consider flow reversal and the use of small time step sizes limited by the sonic velocity.

The COBRA-3M code (12) is a homogenous equilibrium code

with models such as turbulent mixing and wire-wrap mixing on a subchannel basis. The subchannel model network allowed for radial as well as axial sodium voiding and temperature distribution. A major limitation of COBRA-3M is its lack of capability to consider flow reversal, recirculation, and a pressure-pressure boundary condition. To provide these capabilities, an ACE method scheme was developed for the COBRA-IV code (13); a temporally explicit transient pressure-velocity was selected which imposed no restriction on flow velocity and could accept either flow or pressure boundary conditions. However, this code retains a limitation of a homogeneous equilibrium model.

The main features of the BACCHUS code (14) developed at Grenoble are similar to those of COBRA-3M; the homogeneous equilibrium model, marching technique, and mixing model. Their main differences are that the BACCHUS uses the porous body analysis and the assumption that the flow is steady. A transient version is now under development.

The THERMIT-4S code (15) developed at M.I.T. is a nonhomogeneous-equilibrium 3-D code for which the numerical scheme and solution procedures are based on the THERMIT code (16). With the assumption of thermal equilibrium on the saturation line this code solves four equations; mixture mass and internal energy equations, and vapor and liquid momentum equations. This assumption eliminates the need of constitutive equations for interfacial mass and energy exchange which are required for the two-fluid model.

However, as the assumption of thermal equilibrium requires complete condensation of vapor in the subcooled region, numerical difficulties may be encountered due to large pressure fluctuation caused by complete condensation of vapor.

The NATOF code (17) developed at M.I.T. adopts a two-dimensional two-fluid model for the simulation of sodium boiling transients. The numerical scheme and solution procedure are based on THERMIT (16). The code has the structural model of heat sink through the can, the radial liquid conduction model, and the fuel conduction model. As the code solves the conservation equations for both vapor and liquid, the interfacial mass, momentum, and energy exchange must be given through the constitutive equations. The two-fluid approach has the advantage of accounting for non-equilibrium phenomena and slip flow, but heavily depends on the physical models. Although an advanced two-phase flow model and numerical scheme are used in this code, the range of validity of its physical models is limited and the ill-posedness problem of its equations remains unresolved. These are the motivation for development of the present code, THERMIT-6S.

The main features of several codes, that were designed for analysis of sodium boiling in the LMFBR, are given in Table 1.1. Limitations of the codes (see Table 1.2) are attributed to the characteristics of sodium and of the LMFBR such as the high density ratio of liquid to vapor, the

Table 1.1 : Feature of Several Sodium Boiling Codes

	1-D	2-D	3-D
H-EM	Transfugue-I,II	BACCHUS	COBRA-3M COBRA-IV
Multi-bubble slug model	SAS-3A,D BLOW		
Slip-EM (3 Eq)	MOC		
Non H-EM (4 Eq)			THERMIT-4S
Two-Fluid Model		NATOF-2D	THERMIT-6S

Table 1.2 Main Drawbacks of Various Modelling Approaches

I. Two-Phase Model

I.1 HOMOGENEOUS MODEL :	No slip - High void fraction - High pressure build-up - Early flow reversal
I.2 EQUILIBRIUM MODEL :	Temperature equilibrium - Large mass exchange - Rapid pressure transients - Numerical difficulties
I.3 SLIP MODEL :	Need correlation for slip in annular or reversed flow
I.4 TWO-FLUID MODEL :	Nonhomogeneous-Nonequilibrium - Need more correlations

II. Geometrical Representation

II.1 1-D REPRESENTATION :	No radial temperature gradient and vapor propagation
II.2 2-D REPRESENTATION :	No mixing in the θ direction
II.3 3-D REPRESENTATION :	Large CPU time

existence of the highly subcooled region, reversed flow, and sharp radial temperature gradients.

The high density ratio induces high slip between liquid and vapor and, as a result, eliminates the possibility of use of the homogeneous model which assumes no slip. The existence of a highly subcooled region in the bundle of the LMFBR, where vapor is condensed, causes numerical difficulties and large pressure fluctuations. The use of the equilibrium approach, in which vapor must be completely condensed in the subcooled region, enlarges pressure fluctuations and in turn numerical difficulties. The non-equilibrium approach instead of the equilibrium approach is better suited to represent real situations. Correlations for slip in annular or reversed flow are not readily available. Hence, the slip model is avoided in the present work. Sharp radial temperature gradients and multi-dimensional voiding behavior lead us to favor a multi-dimensional model. A 3-D model is chosen because it can be transformed into 1-D or 2-D models.

According to the above brief review, a two-fluid 3-D model is selected for the analysis of sodium boiling in the LMFBR. The THERMIT code is taken as the basic tool for the development of a two-fluid 3-D code due to its following main features:

1. Two-fluid 3-D code
2. Advanced numerical scheme
3. General Boundary conditions

Although (r, θ, z) coordinates are fitted in the geometry of the hexagonal bundle of the LMFBR, (x, y, z) coordinates are used in THERMIT-6S due to the easy adoptation of the original THERMIT code which uses (x, y, z) coordinates.

1.3 Research Objective and Summary of Study

The objective of the present work is to provide a multidimensional model for understanding and prediction of the behavior of two-phase flow before fuel melting in the LMFBR subassembly under unprotected loss of flow and loss of pipe intergrity, that is, under low flow/high power accidents and low flow/low power accidents. In order to provide information on the multidimensional and non-equilibrium behavior of sodium boiling, the THERMIT code, which is a two-fluid and three dimensional code, is taken as a basic tool for the development of the code.

The present work includes the investigation of the mathematical, numerical, and physical foundations of two-phase flow of sodium. In Chapter 2, the mathematical formulation is developed. The numerical formulation is discussed in Chapter 3. The effects of the virtual mass term on the numerical stability are discussed in Chapter 4. The physical models of the constitutive relations are developed in Chapter 5. In Chapter 6, the code predictions are compared to experimental results. A summary and recommendations are presented in Chapter 7.

Chapter 2 TWO-PHASE FLOW MODEL

General time-volume averaged conservation equations and jump conditions for two-phase flows are derived here. The time-averaged equations for a single phase region in two-phase flow are obtained from local instant balance equations by a technique often used for single phase turbulent flow equations. The results obtained by integrating the time-averaged equations over a flow volume are spatially averaged twice; first, they are averaged over a single phase region of the k-th phase and then averaged over the total volume of the k-th phase, in a flow volume. The mass, momentum, and energy conservation equations are obtained from the general time-volume averaged equations. The advantages of the present model are explained by comparing it with Ishii's model (18) and Banerjee's model (19). Finally, the assumptions and approximate terms of the equations of the THERMIT-6S are clarified.

2.1 Introduction

The most important characteristic of two phase flows is the presence of moving internal interfaces separating phases; a two-phase system consists of a number of single phase regions bounded by moving interfaces. Therefore, a formulation based on these local instant variables and moving interfaces results in a multi-boundary problem which are not known a priori. In order to overcome these difficulties, in the formulation of two-phase flow equations, we do not explicitly integrate the microscopic phenomena but preserve their effect on macroscopic phenomena.

Three approaches have been used widely to develop a two-phase flow model:

1) Mixture Model Approach
2) Control Volume Approach
3) Averaging Approach

Ishii (18,20) provides an excellent description of these three approaches. The first and second approaches are mainly based on hypothesis, physical intuition, and assumed similarity with a single phase flow system. In these two approaches, even though easy formulation and practicality in simple cases are main advantages, we encounter the difficulty of identifying the effect of the microscopic scales of phenomena on the macroscopic behavior. On the other hand, the averaging approach enables us to set up mathematically rigorous equations. The averaging approach can be classified into three main groups: Eulerian,

Lagrangian, and Boltzmann statistical averages.

In an Eulerian description, time and space coordinates are taken as independent variables and various dependent variables express their changes with respect to these coordinates. As the particle coordinate in a Lagrangian description displaces the spatial variable of the Eulerian description, the Lagrangian average is taken by following a certain particle and observing it in a time interval. The Boltzmann statistical averaging with a concept of the particle number density is widely used when the collective mechanics of large number of particles are in question. The Eulerian average has been considered as the most widely used method, due to its close relation to experimental observations and instrumentations, Therefore, here the time-volume averaged conservation equations of two phase flows are derived on a basis of the Eulerian averaging approach.

2.2 Local Instant Balance Equation

A two-phase flow is considered to be subdivided into several single phase regions separated by moving interfaces. Each separate phase can be connected through jump conditions. Jump conditions constitute a characteristic feature of moving boundaries and provide relations between the phase interaction terms. Therefore, the standard method of continuum mechanics will be first used and then jump conditions will be derived.

Let us start from a general balance equation. For a material of the k-th phase with the volume and surface, V_{mk} and A_{mk}, we can set up the general balance equation.

$$\frac{d}{dt}\int_{V_{mk}} \rho_k \Psi_k \, dV = -\oint_{A_{mk}} \vec{n}_k \cdot \vec{J}_k \, dA + \int_{V_{mk}} \rho_k S_k \, dV \qquad (2.1)$$

where ρ_k is the density of k-th phase, Ψ_k is any quantity being conserved in the k-th phase, $\vec{J}_k$ and S_k are the efflux and source of Ψ_k, and $\vec{n}_k$ is an outward unit normal vector for the k-th phase. Using the Reynolds transport theorem (20), we have

$$\frac{d}{dt}\int_{V_{mk}} \rho_k \Psi_k \, dV = \int_{V_{mk}} \frac{\partial \rho_k \Psi_k}{\partial t} \, dV + \oint_{A_{mk}} \rho_k \Psi_k \vec{v}_k \cdot \vec{n}_k \, dA \qquad (2.2)$$

where $\vec{v}_k$ denotes the velocity of a material of the k-th phase. Note that, while the Reynolds transport theorem is derived for a material volume, the Leibnitz rule (21) (given later by Eq (2.24)) is a purely geometric theorem.

The Gauss's theorem (22) gives a transformation between a volume and surface integral.

$$\oint_{A_{mk}} (\rho_k \Psi_k \vec{v}_k + \vec{J}_k) \cdot \vec{n}_k \, dA = \int_{V_{mk}} \nabla \cdot (\rho_k \Psi_k \vec{v}_k + \vec{J}_k) \, dV \qquad (2.3)$$

Substituting Eqs (2.2) and (2.3) into Eq (2.1), we have

$$\int_{V_{mk}} \left[\frac{\partial \rho_k \Psi_k}{\partial t} + \nabla \cdot (\rho_k \Psi_k \vec{v}_k + \vec{J}_k) - \rho_k S_k \right] dV = 0 \qquad (2.4)$$

By the axiom of continuum, we get the local instant differential balance equation

$$\frac{\partial \rho_k \Psi_k}{\partial t} + \nabla \cdot (\rho_k \Psi_k \vec{v}_k) + \nabla \cdot \vec{J}_k - \rho_k S_k = 0 \qquad (2.5)$$

The local instant differential balance equation, Eq (2.5) can be applied in each phase up to an interface. Let us derive an interfacial balance equation based on the control volume analysis, neglecting surface tension. As shown in Fig 2.1, control volumes, V_1 and V_2 are surrounded by the areas of each phase, A_1 and A_2 , with an interfacial area A_i. As the control volumes, V_1 and V_2, are very thin, we put $\vec{n}_1 = -\vec{n}_2$,
where $\vec{n}_1$ and $\vec{n}_2$ are outward unit normal vectors from surfaces, A_1 and A_2, respectively. Now we have the general balance equation for the control volumes, V_1 and V_2.

$$\sum_{k=1}^{2} \frac{d}{dt} \int_{V_k} \rho_k \Psi_k dV = \sum_{k=1}^{2} \left[\int_{A_k} \vec{n}_k \cdot [\rho_k \Psi_k (\vec{v}_k - \vec{v}_i) + \vec{J}_k] \, dA + \int_{V_k} \rho_k S_k \, dV \right] \qquad (2.6)$$

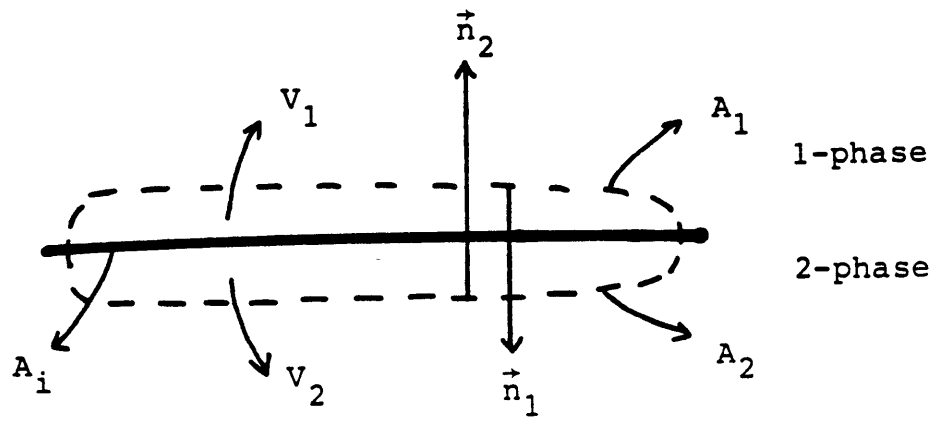

Fig. 2.1: Configuration of Interface

We let the volumes, V_1 and V_2 shrink down to the interface so that the volumes, V_1 and V_2 vanish, while the interfacial area A_i remains finite in the limit. The volume integrals vanish and A_k is equal to A_i, in the limit. Then we have the general interfacial balance equation.

$$\sum_{k=1}^{2} (\dot{m}_k \Psi_k + \vec{n}_k \cdot \vec{J}_k) = 0 \tag{2.7}$$

where $\dot{m}_k = \rho_k (\vec{v}_k - \vec{v}_i) \cdot \vec{n}_k$ (2.8)

$\dot{m}_k$ is the local instant mass flux through the interface.

2.3 General Time Averaged Balance Equation

In a single phase turbulent flow, the Eulerian time averaging is essential and a well-known technique. As a two-phase flow consists of several single phase regions, the technique used in a single phase turbulent flow is taken to obtain the general time-averaged balance equation for one of single phase regions.

Let us integrate the local instant balance equation, Eq (2.5), over a time interval Δt. The time interval Δt should be smaller than the transport time of one single phase to pass through a reference position and than the macroscopic time constant of the unsteadiness of the bulk fluid. Also Δt should be large enough to smooth out the local variations of properties. Ishii (18) and Delhaye (23) used Δt which is a time interval sufficient for several single phase regions to pass through a local position. However, as turbulence originated in a single phase region

will be confined in that phase by the interface and the effect of turbulence in a phase can be transmitted through the other phase, Δt should be smaller than a time interval for a single phase region to pass through a reference point.

As a result, we get a time-averaged equation which is identical to that made in analyzing a single phase turbulent flow.

$$\frac{\partial \overline{\rho_k \Psi_k}}{\partial t} + \nabla \cdot (\overline{\rho_k \Psi_k \vec{v}_k}) + \nabla \cdot \bar{\vec{J}}_k - \overline{\rho_k S_k} = 0, \tag{2.9}$$

where $$\bar{F} = \frac{1}{\Delta t} \int_{\Delta t} F \, dt \tag{2.10}$$

In order to obtain Eq (2.9), we used the following relationships which come from the Leibnitz rule.

$$\overline{\frac{\partial F}{\partial t}} = \frac{\partial \bar{F}}{\partial t} \quad \text{and} \quad \overline{\nabla \cdot F} = \nabla \cdot \bar{F} \tag{2.11}$$

By including a non-zero scalar weighting function w, we define the general weighted mean value of a function F as:

$$\overleftrightarrow{F} = \frac{\overline{wF}}{\bar{w}} \tag{2.12}$$

In general, the volume, momentum, energy, and entropy are considered to be extensive variables. If F is taken as a quantity per unit volume of the extensive characteristic,

it can be expressed in terms of the variable per unit mass Ψ as:

$$F = \rho\Psi \tag{2.13}$$

The appropriate mean value for Ψ should be weighted by the density as

$$\overleftrightarrow{\Psi} = \frac{\overline{\rho\Psi}}{\overline{\rho}} \tag{2.14}$$

Now let us introduce fluctuating components of variables caused by turbulence. In general, as they are defined as a difference between a local instant variable and its weighted mean value, we have

$$F'^{t} = F - \overleftrightarrow{F} \tag{2.15}$$

Since the mean values of Ψ and $\vec{v}$ are weighted by mass, the fluctuating components are given as follows:

$$\Psi_k = \overleftrightarrow{\Psi}_k + \Psi_k'^{t} \quad \text{and} \quad \vec{v}_k = \overleftrightarrow{\vec{v}}_k + \vec{v}_k'^{t} \tag{2.16}$$

Using Eqs (2.14) and (2.15), we have the additional relationships:

$$\overline{\rho_k'^{t}} = 0, \quad \overleftrightarrow{\Psi_k'^{t}} = 0, \quad \overleftrightarrow{\vec{v}_k'^{t}} = 0,$$

$$\overline{\rho_k \Psi_k'^{t}} = 0, \quad \overline{\rho_k \vec{v}_k'^{t}} = 0 \tag{2.17}$$

From Eqs (2.16) and (2.17), the convective flux term becomes

$$\overline{\rho_k \Psi_k \vec{v}_k} = \bar{\rho}_k \overleftrightarrow{\Psi}_k \overleftrightarrow{\vec{v}}_k + \overline{\rho_k \Psi_k'^t \vec{v}_k'^t} \tag{2.18}$$

Now we obtain the time-averaged balance equation

$$\frac{\partial \bar{\rho}_k \overleftrightarrow{\Psi}_k}{\partial t} + \nabla \cdot (\bar{\rho}_k \overleftrightarrow{\Psi}_k \overleftrightarrow{\vec{v}}_k) + \nabla \cdot (\bar{\vec{J}}_k + \bar{\vec{J}}_k^t) - \bar{\rho}_k \overleftrightarrow{S}_k = 0, \tag{2.19}$$

where $$\bar{\vec{J}}_k^t = \overline{\rho_k \Psi_k'^t \vec{v}_k'^t} \tag{2.20}$$

In the same manner, we can obtain the time-averaged interfacial balance equation by integrating Eq (2.7) over the time interval, Δt.

$$\sum_{k=1}^{2} \left(\bar{\dot{m}}_k \overleftrightarrow{\overline{\Psi}}_k + \vec{n}_k \cdot \bar{\vec{J}}_k \right) = 0, \tag{2.21}$$

where $$\overleftrightarrow{\overline{\Psi}} = \frac{\overline{\dot{m}_k \Psi_k}}{\overline{\dot{m}_k}} \tag{2.22}$$

$\overleftrightarrow{\overline{\Psi}}$ is weighted by the time averaged mass flux through the interface.

2.4 General Time-Volume Averaged Balance Equation

Many practical problems of two-phase flows are dealt with using time-volume averaged equations. A time-volume averaged equation can be obtained by integrating the local time averaged equation, Eq (2.19), over a flow volume V_f ,

which consists of several single phase regions.

$$\sum_{i=1}^{I} \frac{1}{V_f} \int_{V_{ki}} [\frac{\partial \overline{\rho}_k \overleftrightarrow{\Psi}_k}{\partial t} + \nabla\cdot(\overline{\rho}_k \overleftrightarrow{\Psi}_k \overleftrightarrow{\vec{v}}_k) + \nabla\cdot(\overline{\vec{J}}_k + \overline{\vec{J}}_k^t) - \overline{\rho}_k \overleftrightarrow{S}_k]\, dV = 0, \tag{2.23}$$

where I is the maximum number of the k-th phase regions in the volume V_f and V_{ki} is the volume of the i-th single phase region of the k-th phase. The theorems we will use are given below:

Leibnitz rule

$$\frac{\partial}{\partial t} \int_{V_{ki}} F dV = \int_{V_{ki}} \frac{\partial F}{\partial t}\, dV + \int_{A_{ki}} F\, \vec{v}_i \cdot \vec{n}_k\, dA, \tag{2.24}$$

Gauss' theorem

$$\int_{V_{ki}} \nabla\cdot\vec{F} dV = \nabla\cdot\int_{V_{ki}} \vec{F}\, dV + \int_{A_{ki}+A_{wi}} \vec{n}_k\cdot\vec{F}\, dA, \tag{2.25}$$

where A_{ki} is the area of the i-th single phase region of the k-th phase in the volume V_f and $\vec{v}_i\cdot\vec{n}_k$ is the surface displacement velocity of A_{ki}. For a solid interface $\vec{v}_w = 0$. Using these theorems, we obtain the equation

$$\sum_i \frac{1}{V_f} \Bigg[\frac{\partial}{\partial t} \int_{V_{ki}} \overline{\rho}_k \overleftrightarrow{\Psi}_k\, dV + \nabla\cdot\int_{V_{ki}} \overline{\rho}_k \overleftrightarrow{\Psi}_k \overleftrightarrow{\vec{v}}_k\, dV + \nabla\cdot\int_{V_{ki}} (\overline{\vec{J}}_k + \overline{\vec{J}}_k^t)\, dV - \int_{V_{ki}} \overline{\rho}_k \overleftrightarrow{S}_k\, dV$$
$$+ \int_{A_{ki}} \vec{n}_k\cdot[\overline{\rho}_k \overleftrightarrow{\Psi}_k (\overleftrightarrow{\vec{v}}_k - \vec{v}_i) + \overline{\vec{J}}_k^t]\, dA$$
$$+ \int_{A_{ki}+A_{kwj}} \vec{n}_k\cdot\overline{\vec{J}}_k\, dA \Bigg] = 0, \tag{2.26}$$

where A_{kwj} denotes the area of the j-th single phase region of the k-th phase contacting the solid surface in the volume

V_f . The fifth term in Eq (2.26) can be simplified by using the definition of the turbulent flux, Eq (2.20).

$$B = [\bar{\rho}_k \overleftrightarrow{\Psi}_k (\overleftrightarrow{\vec{v}}_k - \vec{v}_i) + \bar{\vec{J}}_k^t] \cdot \vec{n}_k$$

$$= (\bar{\rho}_k \overleftrightarrow{\Psi}_k \overleftrightarrow{\vec{v}}_k + \overline{\rho \Psi_k'^t \vec{v}_k'^t} - \overline{\rho_k} \overleftrightarrow{\Psi}_k \vec{v}_i) \cdot \vec{n}_k \tag{2.27}$$

From Eqs (2.14) and (2.18), Eq (2.27) becomes

$$B = (\overline{\rho_k \Psi_k \vec{v}_k} - \overline{\rho_k \Psi_k \vec{v}_i}) \cdot \vec{n}_k \tag{2.28}$$

Then, we have the following equation which is consistent with the jump condition, Eq (2.7).

$$B = \bar{\dot{m}}_k \overleftrightarrow{\Psi}_k \tag{2.29}$$

Let us introduce spatial averaged relationships for a single phase region.

$$\langle F \rangle = \int_{V_{ki}} F \, dV \Big/ \int_{V_{ki}} dV \tag{2.30}$$

$$\langle F \rangle_{ai} = \int_{A_{ki}} F \, dA \Big/ \int_{A_{ki}} dA \tag{2.31}$$

$$\langle F \rangle_{wj} = \int_{A_{kwj}} F \, dA \Big/ \int_{A_{kwj}} dA \tag{2.32}$$

Substituting Eqs (2.30), (2.31) and (2.32) into Eq. (2.26),

we obtain the equation averaged for a single phase region.

$$\sum_i \Big[\frac{\partial}{\partial t} \alpha_{ki} \langle \bar{\rho}_k \overleftrightarrow{\Psi}_k \rangle + \nabla \cdot \alpha_{ki} \langle \bar{\rho}_k \overleftrightarrow{\Psi}_k \overleftrightarrow{\vec{v}}_k \rangle + \nabla \cdot \alpha_{ki} \langle \bar{\vec{J}}_k + \bar{\vec{J}}_k^t \rangle$$
$$- \alpha_{ki} \langle \bar{\rho}_k \overleftrightarrow{S}_k \rangle + \frac{1}{L_{ai}} (\langle \bar{\dot{m}} \overleftrightarrow{\Psi}_k \rangle_{ai} + \langle \vec{n}_k \cdot \bar{\vec{J}}_k \rangle_{ai})$$
$$+ \frac{1}{L_{wj}} \langle \vec{n}_k \cdot \bar{\vec{J}}_k \rangle_{wj} \Big] = 0, \tag{2.33}$$

where $\alpha_{ki} = \frac{V_{fi}}{V_f}$, $\frac{1}{L_{ai}} = \frac{A_{ki}}{V_f}$, $\frac{1}{L_{wj}} = \frac{A_{kwj}}{V_f}$ (2.34)

Then Eq (2.33) is averaged over the total volume, or over the total surface, of k-th phase in the volume V_f by using the following relationships:

$$\langle\langle F \rangle\rangle = \frac{\sum_i \alpha_{ki} \langle F \rangle}{\sum_i \alpha_{ki}} = \frac{\sum_i \alpha_{ki} \langle F \rangle}{\alpha_k} \tag{2.35}$$

$$\langle\langle F \rangle\rangle_a = \frac{\sum_i \frac{1}{L_{ai}} \langle F \rangle_{ai}}{\sum_i \frac{1}{L_{ai}}} = \frac{\sum_i \frac{1}{L_{ai}} \langle F \rangle_{ai}}{\frac{1}{L_{ak}}} \tag{2.36}$$

$$\langle\langle F \rangle\rangle_w = \frac{\sum_j \frac{1}{L_{wj}} \langle F \rangle_{wj}}{\sum_j \frac{1}{L_{wj}}} = \frac{\sum_j \frac{1}{L_{wj}} \langle F \rangle_{wj}}{\frac{1}{L_{wk}}} \tag{2.37}$$

where $\alpha_k = \sum_i \alpha_{ki}$, $\frac{1}{L_{ak}} = \frac{\sum_i A_{ki}}{V_f}$, $\frac{1}{L_{wk}} = \frac{\sum_j A_{kj}}{V_f}$ (2.38)

Substituting Eqs (2.35), (2.36), and (2.37) into Eq(2.33),

we have the general time-volume averaged equation.

$$\frac{\partial}{\partial t}\alpha_k \langle\langle\bar{\rho}_k \overleftrightarrow{\Psi}_k\rangle\rangle + \nabla\cdot\alpha_k \langle\langle\bar{\rho}_k\overleftrightarrow{\Psi}_k\vec{v}_k\rangle\rangle + \nabla\cdot\alpha_k \langle\langle\bar{\vec{J}}_k+\bar{\vec{J}}_k^t\rangle\rangle$$

$$- \alpha_k \langle\langle\bar{\rho}_k\overleftrightarrow{S}_k\rangle\rangle + \frac{1}{L_{ak}} \langle\langle\bar{\dot{m}}_k \overleftrightarrow{\Psi}_k\rangle\rangle_a$$

$$+ \frac{1}{L_{ak}} \langle\langle n_k\cdot\bar{\vec{J}}_k\rangle\rangle_a + \frac{1}{L_{wk}} \langle\langle n_k\cdot\bar{\vec{J}}_k\rangle\rangle_w = 0 \qquad (2.39)$$

Let us obtain the time-volume averaged interfacial jump condition from Eq (2.21). Integrating Eq (2.21) over the interfacial surface area A_{ki}, we get the jump condition.

$$\sum_{k=1}^{2}\sum_i \int_{A_{ki}} (\bar{\dot{m}}_k \overleftrightarrow{\Psi}_k + \vec{n}_k\cdot\bar{\vec{J}}_k)\,dA$$

$$= \sum_{k=1}^{2} \frac{1}{L_{ak}} \langle\langle\bar{\dot{m}}_k \overleftrightarrow{\Psi}_k + \vec{n}_k\cdot\bar{\vec{J}}_k\rangle\rangle_a = 0 \qquad (2.40)$$

2.5 Time-Volume Averaged Conservation Equations

The forms of the time-volume averaged conservation equations for mass, momentum, and energy of the k-th phase can be written by specifying Eq (2.39) as follows:

<u>Mass</u>

In this case,

$$\Psi_k = 1, \quad \vec{J}_k = 0, \quad S_k = 0 \qquad (2.41)$$

We have

$$\frac{\partial}{\partial t}\alpha_k \langle\langle\bar{\rho}_k\rangle\rangle + \nabla\cdot\alpha_k \langle\langle\bar{\rho}_k \overleftrightarrow{\vec{v}_k}\rangle\rangle = \Gamma_k, \tag{2.42}$$

where $\bar{\vec{J}}_k^t = \overline{\rho_k \vec{v}_k'^t} = 0$

and $$\Gamma_k = -\frac{1}{L_{ak}}\langle\langle\bar{\dot{m}}_k\rangle\rangle_a \tag{2.43}$$

Γ_k is the time-volume averaged interfacial mass flow rate per unit volume of k-th phase.

<u>Momentum</u>

In this case,

$$\Psi_k = \vec{v}_k, \quad \bar{\bar{J}}_k = p_k\,\bar{\bar{I}} - \bar{\bar{\tau}}_k, \quad S_k = \vec{F}_k \tag{2.44}$$

We have

$$\begin{aligned}
&\frac{\partial}{\partial t}\alpha_k \langle\langle\bar{\rho}_k\overleftrightarrow{\vec{v}_k}\rangle\rangle + \nabla\cdot\alpha_k\langle\langle\bar{\rho}_k\overleftrightarrow{\vec{v}_k}\overleftrightarrow{\vec{v}_k}\rangle\rangle + \nabla\alpha_k\langle\langle\bar{p}_k\rangle\rangle \\
&- \nabla\cdot\alpha_k\langle\langle\bar{\bar{\tau}}_k\cdot\vec{n}_k\rangle\rangle - \alpha_k\langle\langle\bar{\rho}_k\overleftrightarrow{\vec{F}_k}\rangle\rangle - \nabla\cdot\alpha_k\langle\langle\bar{\bar{\tau}}_k^t\cdot\vec{n}_k\rangle\rangle \\
&+ \frac{1}{L_{ak}}\langle\langle\bar{\dot{m}}_k\overleftrightarrow{\vec{v}_k}\rangle\rangle_a + \frac{1}{L_{ak}}\langle\langle\overline{p_{ki}}\rangle\rangle_a - \frac{1}{L_{ak}}\langle\langle\bar{\bar{\tau}}_k\cdot\vec{n}_k\rangle\rangle_a \\
&- \frac{1}{L_{wk}}\langle\langle\bar{\bar{\tau}}_k\cdot\vec{n}_k\rangle\rangle_w = 0
\end{aligned} \tag{2.45}$$

where $$\bar{\bar{\tau}}_k^t = \overline{\rho_k \vec{v}_k'^t\,\vec{v}_k'^t} \tag{2.46}$$

and p_{ki} is the local interfacial pressure.

The time-averaged local interfacial pressure $\bar{p}_{ki}$ can be

divided into three terms as follows:

$$\bar{p}_{ki} = \langle\langle\bar{p}_k\rangle\rangle + \Delta p_{ki} + \Delta p'_{ki} \ , \tag{2.47}$$

where $\Delta p_{ki} = \langle\langle\bar{p}_{ki}\rangle\rangle_a - \langle\langle\bar{p}_k\rangle\rangle,$ (2.48)

$$\Delta p'_{ki} = \bar{p}_{ki} - \langle\langle\bar{p}_{ki}\rangle\rangle_a, \tag{2.49}$$

and Δp_{ki} is the difference between the average interfacial and average phase pressures and $\Delta p'_{ki}$ is the difference between the local and average interfacial pressures.

Using Eq (2.25) , we obtain the following relationship:

$$\frac{1}{L_{ak}} \langle\langle\bar{p}_k\rangle\rangle_a = - (\langle\langle\bar{p}_k\rangle\rangle + \Delta p_{ki}) \nabla\cdot\alpha_k + \frac{1}{L_{ak}} \langle\langle\Delta p'_{ki}\rangle\rangle_a \tag{2.50}$$

The second term on the right-hand side in Eq (2.50) is the term which leads to the virtual mass for inviscid flows. Substituting Eq (2.50) into Eq (2.45), we obtain the momentum conservation equation.

$$\frac{\partial}{\partial t} \alpha_k \langle\langle\bar{\rho}_k \overleftrightarrow{\vec{v}}_k\rangle\rangle + \nabla\cdot\alpha_k \langle\langle\bar{\rho}_k \overleftrightarrow{\vec{v}}_k \overleftrightarrow{\vec{v}}_k\rangle\rangle + \alpha_k \nabla\langle\langle\bar{p}_k\rangle\rangle$$

$$- \alpha_k \langle\langle\bar{\rho}_k \overleftrightarrow{\vec{F}}_k\rangle\rangle - \nabla\cdot\alpha_k \langle\langle\bar{\bar{\tau}}_k\cdot\vec{n}_k\rangle\rangle$$

$$- \nabla\cdot\alpha_k \langle\langle\bar{\bar{\tau}}_k^t\cdot\vec{n}_k\rangle\rangle - \Delta p_{ki} \nabla\cdot\alpha_k$$

$$= - \frac{1}{L_{ak}} \langle\langle\bar{\dot{m}}_k \overleftrightarrow{\vec{v}}_k + \Delta p'_{ki} - \bar{\bar{\tau}}_k\cdot\vec{n}_k\rangle\rangle_a + \frac{1}{L_{wk}} \langle\langle\bar{\bar{\tau}}_k\cdot\vec{n}_k\rangle\rangle_w \tag{2.51}$$

<u>Energy</u>

In this case,

$$\psi_k = E_k = e_k + \frac{v_k^2}{2},$$

$$\vec{J}_k = \vec{q}_k - (p_k\bar{\bar{I}} - \bar{\bar{\tau}})\cdot\vec{v}_k, \tag{2.52}$$

$$S_k = \vec{F}_k\cdot\vec{v}_k + Q_k$$

where e_k and Q_k are the specific internal energy and volumetric internal energy generation rate.

In solving two-phase problems, it is often useful to separate the mechanical and thermal effects in the total energy equation. From dotting the local instant momentum equation derived by combining Eqs (2.5) and (2.44) by the velocity of k-th phase $\vec{v}_k$, we have the mechanical energy balance equation.

$$\frac{\partial}{\partial t}\left(\frac{1}{2}\rho_k v_k^2\right) + \nabla\cdot\left(\frac{1}{2}\rho_k v_k^2\vec{v}_k\right) + \nabla\cdot p_k\vec{v}_k - p_k\nabla\cdot\vec{v}_k$$

$$+ \nabla\cdot(\bar{\bar{\tau}}_k\cdot\vec{v}_k) - \bar{\bar{\tau}}_k:\nabla\vec{v}_k - \rho_k\vec{F}_k\cdot\vec{v}_k = 0 \tag{2.53}$$

Using Eqs (2.5) and (2.52), we have the local instant energy balance equation.

$$\frac{\partial}{\partial t}\rho_k\left(e_k + \frac{1}{2}v_k^2\right) + \nabla\cdot\rho_k\vec{v}_k\left(e_k + \frac{1}{2}v_k^2\right) + \nabla\cdot\vec{q}_k$$

$$+ \nabla\cdot(p_k\vec{v}_k) + \nabla\cdot(\bar{\bar{\tau}}_k\cdot\vec{v}_k) - \rho_k(\vec{F}_k\cdot\vec{v}_k + Q_k) = 0 \tag{2.54}$$

Subtracting Eq (2.53) from Eq (2.54), we can obtain the internal energy equation.

$$\frac{\partial}{\partial t}\rho_k e_k + \nabla\cdot\rho_k e_k \vec{v}_k + \nabla\cdot\vec{q}_k + p_k \nabla\cdot\vec{v}_k + \bar{\bar{\tau}}_k : \nabla\vec{v}_k - \rho_k Q_k = 0 \tag{2.55}$$

If we compare the equations of mechanical and thermal energy, Eqs (2.53) and (2.55), we find out that $(p_k \nabla\cdot\vec{v}_k)$ and $(\bar{\bar{\tau}}_k : \nabla\vec{v}_k)$ are common to both equations and that they appear with opposite signs in the two equations. Therefore, these terms describe the interconversion of mechanical and thermal energy. The term can be either positive or negative, depending on whether the fluid is expanding or contracting. As a result, it represents a reversible mode of interchange. Using the continuity equation, we have

$$p_k \nabla\cdot\vec{v}_k = -p_k \frac{1}{\rho_k}\left[\frac{\partial\rho_k}{\partial t} + \vec{v}_k\cdot\nabla\rho_k\right] = -p_k \frac{1}{\rho_k}\frac{D\rho_k}{Dt} \tag{2.56}$$

For a fluid of constant density, the term $(p_k \nabla\cdot\vec{v}_k)$ becomes zero. On the othere hand, the term $(-\bar{\bar{\tau}}_k : \nabla\vec{v}_k)$ is always positive and therefore represents an irreversible degradation of mechanical to thermal energy.

Let us get the time averaged internal energy from Eq (2.55).

$$\frac{\partial}{\partial t}\overline{\rho_k e_k} + \nabla\cdot\overline{\rho_k e_k \vec{v}_k} + \nabla\cdot\bar{\vec{q}}_k + \overline{p_k \nabla\cdot\vec{v}_k} + \overline{\bar{\bar{\tau}}_k : \nabla\vec{v}_k}$$

$$- \overline{\rho_k Q_k} = 0 \tag{2.57}$$

Using Eqs (2.16), (2.17), and (2.18), we can obtain the time averaged internal energy equation.

$$\frac{\partial}{\partial t}\bar{\rho}_k \overleftrightarrow{e}_k + \nabla\cdot(\bar{\rho}_k \overleftrightarrow{e}_k \overleftrightarrow{\vec{v}}_k) + \nabla\cdot(\bar{\vec{q}}_k + \bar{\vec{q}}_k^{\,t})$$

$$+ \overline{p_k \nabla\cdot\vec{v}_k} + \overline{\bar{\bar{\tau}}_k : \nabla\vec{v}_k} = 0, \tag{2.58}$$

where $\bar{\vec{q}}_k^{\,t} = \overline{\rho_k e_k'^{\,t} \vec{v}_k'^{\,t}}$

The time-volume averaged internal energy equation can be obtained by integrating Eq (2.58) over the flow volume V_f . In order to perform that , the term $\overline{(p_k \nabla\cdot\vec{v}_k)}$ requires a special manipulation as follows. The local instant pressure can be divided into two components: time-averaged local pressure and local time fluctuation of pressure.

$$p_k = \bar{p}_k + p_k'^{\,t} \tag{2.59}$$

Then $\overline{(p_k \nabla\cdot\vec{v}_k)}$ becomes

$$\overline{p_k \nabla\cdot\vec{v}_k} = \overline{p_k}\nabla\cdot\bar{\vec{v}}_k + \overline{p_k'^{\,t}\nabla\cdot\vec{v}_k} \tag{2.60}$$

Let us integrate Eq (2.60) over the flow volume V_f . Then,

we have

$$\sum_{i=1}^{I} \frac{1}{V_f} \int_{V_{ki}} \overline{p_k \nabla \cdot \vec{v}_k}\, dV = \sum_i \frac{1}{V_f} \int_{V_{ki}} (\bar{p}_k \nabla \cdot \bar{\vec{v}}_k + \overline{p_k'^t \nabla \cdot \vec{v}_k})\, dV \quad (2.61)$$

Also the time averaged local pressure can be divided into two components: time-space averaged pressure and time averaged space fluctuation of pressure.

$$\bar{p}_k = \langle\langle \bar{p}_k \rangle\rangle + p_k'^s \quad (2.62)$$

Substituting Eq (2.62) into Eq (2.61), Eq (2.61) becomes

$$\sum_i \frac{1}{V_f} \left[\langle\langle \bar{p}_k \rangle\rangle \int_{V_{ki}} \nabla \cdot \bar{\vec{v}}_k \, dV + \int_{V_{ki}} (p_k'^s \nabla \cdot \bar{\vec{v}}_k + \overline{p_k'^t \nabla \cdot \vec{v}_k})\, dV \right] \quad (2.63)$$

Using Eq (2.25), the first term in Eq (2.63) is expressed as follows:

$$\frac{1}{V_f} \langle\langle \bar{p}_k \rangle\rangle \int_{V_{ki}} \nabla \cdot \bar{\vec{v}}_k \, dV$$

$$= \langle\langle \bar{p}_k \rangle\rangle \nabla \cdot \frac{1}{V_f} \int_{V_{ki}} \bar{\vec{v}}_k \, dV + \langle\langle \bar{p}_k \rangle\rangle \frac{1}{V_f} \int_{A_{ki}} \vec{n}_k \cdot \bar{\vec{v}}_k \, dA \quad (2.64)$$

Then, taking the procedure described in Section 2.4 and

assuming that $\bar{\vec{v}}_k$ is equal to $\overleftrightarrow{\vec{v}}_k$, we have

$$\sum_i \frac{1}{V_f} \int_{V_{ki}} \overline{p_k \nabla \cdot \vec{v}_k} dV = \langle\langle \bar{p}_k \rangle\rangle \nabla \cdot \alpha_k \langle\langle \overleftrightarrow{\vec{v}}_k \rangle\rangle$$

$$+ \langle\langle \bar{p}_k \rangle\rangle \frac{1}{L_{ak}} \langle\langle \vec{n}_k \cdot \overleftrightarrow{\vec{v}}_k \rangle\rangle_a + \alpha_k \langle\langle p_k^{'s} \nabla \cdot \overleftrightarrow{\vec{v}}_k + \overline{p_k^{'t} \nabla \cdot \vec{v}_k} \rangle\rangle \quad (2.65)$$

Applying the same procedures for other terms in Eq (2.58), we have the time-volume averaged internal energy equation.

$$\frac{\partial}{\partial t} \alpha_k \langle\langle \bar{\rho}_k \overleftrightarrow{e}_k \rangle\rangle + \nabla \cdot \alpha_k \langle\langle \bar{\rho}_k \overleftrightarrow{e}_k \overleftrightarrow{\vec{v}}_k \rangle\rangle + \nabla \cdot \alpha_k \langle\langle \bar{\vec{q}}_k + \bar{\vec{q}}_k^t \rangle\rangle$$

$$+ \langle\langle \bar{p}_k \rangle\rangle \nabla \cdot \alpha_k \langle\langle \overleftrightarrow{\vec{v}}_k \rangle\rangle + \langle\langle \bar{p}_k \rangle\rangle \frac{1}{L_{ak}} \langle\langle \vec{n}_k \cdot \overleftrightarrow{\vec{v}}_k \rangle\rangle$$

$$+ \alpha_k \langle\langle \overline{\bar{\bar{\tau}}_k : \nabla \vec{v}_k} \rangle\rangle + \alpha_k \langle\langle p_k^{'s} \nabla \cdot \overleftrightarrow{\vec{v}}_k + \overline{p_k^{'t} \nabla \cdot \vec{v}_k} \rangle\rangle$$

$$= - \frac{1}{L_{ak}} \langle\langle \overline{\dot{m}_k \overleftrightarrow{\vec{e}}_k + \vec{n}_k \cdot \bar{\vec{q}}_k} \rangle\rangle_a - \frac{1}{L_{wk}} \langle\langle \vec{n}_k \cdot \bar{\vec{q}}_k \rangle\rangle_w \quad (2.66)$$

The term $(\dot{m}_k e_k)$ can be expressed in terms of enthalpy, h. The enthalpy is defined as follows:

$$h = e + \frac{p}{\rho} \quad (2.67)$$

Using the definition $\dot{m}_k = \rho_k (\vec{v}_k - \vec{v}_i) \cdot \vec{n}_k$, we have

$$\dot{m}_k \frac{p_k}{\rho_k} = p_k (\vec{v}_k - \vec{v}_i) \cdot \vec{n}_k \quad (2.68)$$

By Eq (2.68), we have

$$\langle\langle \bar{\dot{m}}_k \overleftrightarrow{\vec{e}}_k \rangle\rangle = \langle\langle \bar{\dot{m}}_k \overleftrightarrow{\vec{h}}_k \rangle\rangle - \langle\langle \overline{\bar{p}_k (\vec{v}_k - \vec{v}_i) \cdot \vec{n}_k} \rangle\rangle$$

$$\cong \langle\langle \bar{\dot{m}}_k \overleftrightarrow{\vec{h}}_k \rangle\rangle - \langle\langle \bar{p}_k (\overleftrightarrow{\vec{v}}_k - \vec{v}_i) \cdot \vec{n}_k \rangle\rangle \quad (2.69)$$

Using the definition Eq (2.62), we have

$$<<\bar{p}_k(\overleftrightarrow{\vec{v}}_k - \vec{v}_i)\cdot\vec{n}_k>>$$

$$= <<\bar{p}_k>><<\overleftrightarrow{\vec{v}}_k - \vec{v}_i)\cdot\vec{n}_k>> + <<p_k^{'s}(\overleftrightarrow{\vec{v}}_k - \vec{v}_i)\cdot\vec{n}_k>> \qquad (2.70)$$

Combining the second term in Eq (2.65) and the first term in Eq (2.70), then we obtain

$$\frac{1}{L_{ak}}\ [<<\bar{p}_k>><<\vec{n}_k\cdot\overleftrightarrow{\vec{v}}_k>> - <<\bar{p}_k>><<\vec{n}_k\cdot(\overleftrightarrow{\vec{v}}_k - \vec{v}_i)>>]$$

$$= \frac{1}{L_{ak}}\ <<\bar{p}_k>><<\vec{v}_i\cdot\vec{n}_k>> \qquad (2.71)$$

Applying Leibnitz rule to Eq (2.71), Eq (2.71) becomes

$$\frac{1}{L_{ak}}\ <<\bar{p}_k>><<\vec{v}_i\cdot\vec{n}_k>> = <<\bar{p}_k>>\ \frac{\partial\alpha_k}{\partial t} \qquad (2.72)$$

Then we obtain the final internal energy equation:

$$\frac{\partial}{\partial t}\ \alpha_k<<\bar{\rho}_k\overleftrightarrow{e}_k>> + \nabla\cdot\alpha_k<<\bar{\rho}_k\overleftrightarrow{e}_k\overleftrightarrow{\vec{v}}_k>> + \nabla\cdot\alpha_k<<\bar{\vec{q}}_k + \bar{\vec{q}}_k^{\,t}>>$$

$$+ <<\bar{p}_k>>\nabla\cdot\alpha_k<<\bar{\vec{v}}_k>> + <<\bar{p}_k>>\ \frac{\partial\alpha_k}{\partial t}$$

$$+ \alpha_k\ <<\overline{\vec{\tau}_k:\nabla\vec{v}_k}>> + \alpha_k\ <<p_k^{'s}\nabla\cdot\bar{\vec{v}}_k + \overline{p_k^{'t}\nabla\cdot\vec{v}_k}>>$$

$$= -\ \frac{1}{L_{ak}}\ <<\bar{\dot{m}}_k\overleftrightarrow{h}_k + \vec{n}_k\cdot\bar{\vec{q}}_k>>_a$$

$$-\ \frac{1}{L_{wk}}\ <<\vec{n}_k\cdot\bar{\vec{q}}_k>>_w \qquad (2.73)$$

Using the definition of enthalpy, we can obtain the enthalpy energy equation from Eq (2.73). The first and

second terms on the left-hand side in Eq (2.73) become

$$\frac{\partial}{\partial t}\,\alpha_k\langle\langle\bar{\rho}_k\overleftrightarrow{e}_k\rangle\rangle = \frac{\partial}{\partial t}\,\alpha_k\,\langle\langle\bar{\rho}_k\overleftrightarrow{h}_k\rangle\rangle - \frac{\partial}{\partial t}\,\alpha_k\langle\langle\bar{p}_k\rangle\rangle \tag{2.74}$$

and $\nabla\cdot\alpha_k\langle\langle\bar{\rho}_k\overleftrightarrow{e}_k\overleftrightarrow{\vec{v}}_k\rangle\rangle$

$$= \nabla\cdot\alpha_k\langle\langle\bar{\rho}_k\overleftrightarrow{h}_k\overleftrightarrow{\vec{v}}_k\rangle\rangle - \nabla\cdot\alpha_k\langle\langle\bar{p}_k\overleftrightarrow{\vec{v}}_k\rangle\rangle$$

$$= \nabla\cdot\alpha_k\langle\langle\bar{\rho}_k\overleftrightarrow{h}_k\overleftrightarrow{\vec{v}}_k\rangle\rangle - \langle\langle\bar{p}_k\rangle\rangle\nabla\cdot\alpha_k\langle\langle\overleftrightarrow{\vec{v}}_k\rangle\rangle$$

$$- \langle\langle\overleftrightarrow{\vec{v}}_k\rangle\rangle\cdot\nabla\alpha_k\langle\langle\bar{p}_k\rangle\rangle - \nabla\cdot\alpha_k\langle\langle p_k'^{s}\,\overleftrightarrow{\vec{v}}_k\rangle\rangle \tag{2.75}$$

Then, we have the final enthalpy energy equation

$$\frac{\partial}{\partial t}\,\alpha_k\langle\langle\bar{\rho}_k\overleftrightarrow{h}_k\rangle\rangle + \nabla\cdot\alpha_k\langle\langle\bar{\rho}_k\overleftrightarrow{h}_k\overleftrightarrow{\vec{v}}_k\rangle\rangle + \nabla\cdot\alpha_k\langle\langle\bar{\vec{q}}_k + \bar{\vec{q}}_k^{\,t}\rangle\rangle$$

$$- \langle\langle\overleftrightarrow{\vec{v}}_k\rangle\rangle\cdot\nabla\alpha_k\langle\langle\bar{p}_k\rangle\rangle - \alpha_k\,\frac{\partial}{\partial t}\,\langle\langle\bar{p}_k\rangle\rangle$$

$$+ \alpha_k\langle\langle\overline{\bar{\bar{\tau}}_k:\nabla\vec{v}_k}\rangle\rangle - \nabla\cdot\alpha_k\langle\langle p_k'^{s}\,\overleftrightarrow{\vec{v}}_k\rangle\rangle + \alpha_k\langle\langle p_k'^{s}\nabla\cdot\overleftrightarrow{\vec{v}}_k + \overline{p_k'^{t}\nabla\cdot\vec{v}_k}\rangle\rangle$$

$$= -\frac{1}{L_{ak}}\,\langle\langle\overline{\dot{m}_k\overleftrightarrow{h}_k} + \vec{n}_k\cdot\bar{\vec{q}}_k\rangle\rangle_a - \frac{1}{L_{wk}}\,\langle\langle n_k\cdot\bar{\vec{q}}_k\rangle\rangle_w \tag{2.76}$$

2.6 Interfacial Jump Condition

From Eq (2.40) we can obtain the interfacial jump conditions.

Mass

In this case,

$$\Psi_k = 1,\ J_k = 0$$

we have

$$\sum_k \Gamma_k = 0 \tag{2.77}$$

<u>Momentum</u>

In this case,

$$\Psi_k = \vec{v}_k, \quad \bar{\bar{J}}_k = p_k \bar{\bar{I}} - \bar{\bar{\tau}}_k$$

we have

$$\sum_{k=1}^{2} \frac{1}{L_{ak}} \langle\langle \overline{\dot{m}_k \overleftrightarrow{\vec{v}}_k} + \vec{n}_k \, (\bar{p}_k \bar{\bar{I}} - \bar{\bar{\tau}}_k) \rangle\rangle_a = 0 \tag{2.78}$$

<u>Energy</u>

In this case,

$$\Psi_K = E_k = e_k + \frac{v_k^2}{2}, \quad \vec{J}_k = \vec{q}_k - (p_k \bar{\bar{I}} - \bar{\bar{\tau}}_k) \cdot \vec{v}_k$$

We have

$$\sum_{k=1}^{2} \frac{1}{L_{ak}} \langle\langle \overline{\dot{m}_k \overleftrightarrow{E}_k} + \vec{n}_k \cdot [\bar{\vec{q}}_k - \overline{(p_k \bar{\bar{I}} - \bar{\bar{\tau}}_k) \cdot \vec{v}_k}] \rangle\rangle_a = 0 \tag{2.79}$$

The equation can be written in enthalpy form

$$\sum_{k=1}^{2} \frac{1}{L_{ak}} \langle\langle \overline{\dot{m}_k \overleftrightarrow{h}_k} + \vec{n}_k \cdot (\bar{\vec{q}}_k - \bar{p}_k \cdot \vec{v}_i + \overline{\bar{\bar{\tau}}_k \cdot \vec{v}_k}) \rangle\rangle_a = 0 \tag{2.80}$$

2.7 Comparison

Ishii (20) derived time averaged equations by averaging the local equations over a time interval Δt in which several single phase regions with singular interfaces pass through a reference point. Therefore, he was forced to use limiting forms of the Leibniz rule derived by Delhaye and

Achard (23), which lead to a question about the validity about their derivation and an ambiguous physical interpretation of terms describing interfacial transfer phenomena. Ishii's time-averaged conservation equations are as follows:

<u>Mass</u>

$$\frac{\partial}{\partial t}\alpha_k\bar{\rho}_k + \nabla\cdot\alpha_k\bar{\rho}_k\overleftrightarrow{\vec{v}}_k = \Gamma_{ki} \tag{2.81}$$

<u>Momentum</u>

$$\frac{\partial}{\partial t}\alpha_k\bar{\rho}_k\overleftrightarrow{\vec{v}}_k + \nabla\cdot\alpha_k\bar{\rho}_k\overleftrightarrow{\vec{v}}_k\overleftrightarrow{\vec{v}}_k + \nabla\alpha_k\bar{p}_k$$

$$- \nabla\cdot\alpha_k(\bar{\bar{\tau}}_k + \bar{\bar{\tau}}_k^t) - \alpha_k\bar{\rho}_k\overleftrightarrow{\vec{F}}_k = M_{ki} \tag{2.82}$$

<u>Energy</u>

$$\frac{\partial}{\partial t}\alpha_k\bar{\rho}_k\overleftrightarrow{E}_k + \nabla\cdot\alpha_k\bar{\rho}_k\overleftrightarrow{E}_k\overleftrightarrow{\vec{v}}_k + \nabla\cdot\alpha_k(\bar{\vec{J}}_k + \bar{\vec{J}}_k^t)$$

$$- \alpha_k\bar{\rho}_k(\overleftrightarrow{\vec{F}}_k\cdot\overleftrightarrow{\vec{v}}_k + \overleftrightarrow{Q}_k) = E_{ki} \tag{2.83}$$

where Q_k is the body source of energy, and Γ_{ki}, M_{ki}, and E_{ki} are the rate of interfacial mass,

momentum, and energy transfer, respectively:

$$\Gamma_{ki} = -\frac{1}{\Delta t}\sum_j \{\frac{1}{v_{ni}} n_k \cdot \rho_k(\vec{v}_k - \vec{v}_i)\} \tag{2.84}$$

$$M_{ki} = -\frac{1}{\Delta t}\sum_j \{\frac{1}{v_{ni}} n_k \cdot [\rho_k(\vec{v}_k - \vec{v}_i)\vec{v}_k - (p_k\bar{\bar{I}} - \bar{\bar{\tau}}_k)\} \tag{2.85}$$

$$E_{ki} = -\frac{1}{\Delta t}\sum_j \{\frac{1}{v_{ni}} \vec{n}_k \cdot [\rho_k(\vec{v}_k - \vec{v}_i)(e_k + \frac{v_k^2}{2})$$

$$-(p_k\bar{\bar{I}} - \bar{\bar{\tau}}_k)\cdot\vec{v}_k + \vec{q}_k]\} \tag{2.86}$$

where $v_{ni} = \vec{v}_i \cdot \vec{n}_k$: displacement velocity of the interface

We may notice that Ishii's time averaged equations are basically in the same forms as the time-volume averaged equations derived here. However, it is noticed that Ishii's equations leave difficulties in obtaining time-volume averaged equations which give clear physical meaning for two reasons. First, he introduced the concept of time-averaged void fraction when he derived local time-averaged equations and the natural question is how this concept can be transformed to the concept of volume-averaged void fraction. Secondly, Eqs (2.84)-(2.86) which describe interfacial transfer phenomena are not well-defined forms such as $\int_A \vec{F}_k \cdot \vec{n}_k \, dA$. As a result, Delhaye and Archard assumed the commutativity of averaging operators to express Eqs (2.84)-(2.86) into the well-defined forms as follows:

$$\int_V \sum_j \frac{1}{\Delta t \; v_{ni}} (\vec{F}_k \cdot \vec{n}_k)_j \; dV = \int_{A_i} \vec{F}_k \cdot \vec{n}_k \; dA \tag{2.87}$$

These difficulties mainly come from their averaging the local equations over a time interval in which several single phase with singular interface are allowed to pass through a reference point.

Banerjee and Chan (19) derived one dimensional volume averaged equations by averaging the local equations over a fluid volume V_f which consists of several single phase regions. As their equations are not averaged over a time interval, turbulent contribution terms do not appear in the conservation equations. Except for these turbulent terms and the use of instantaneous properties, their equations are the same as the equations derived here.

Let us compare the time-averaged conservation equations, Eqs (2.42), (2.51), and (2.73) with the conservation equations of the THERMIT-6S. The following equations are used in the THERMIT-6S.

Mass

$$\frac{\partial}{\partial t}(\alpha_k \rho_k) + \nabla \cdot (\alpha_k \rho_k \vec{v}_k) = \Gamma_k \tag{2.88}$$

Momentum

$$\frac{\partial}{\partial t}\alpha_k \rho_k \vec{v}_k + \nabla \cdot (\alpha_k \rho_k \vec{v}_k \vec{v}_k) + \alpha_k \nabla p_k$$

$$= \Gamma_k \vec{v}_i - \vec{F}_{sk} - \vec{F}_{vk} - \vec{F}_{wk} + \alpha_k \rho_k \vec{g} \tag{2.89}$$

Energy

$$\frac{\partial}{\partial t}\alpha_k\rho_k e_k + \nabla\cdot(\alpha_k\rho_k e_k\vec{v}_k) + p\nabla\cdot(\alpha_k\vec{v}_k)$$

$$+ p\frac{\partial\alpha_k}{\partial t} = Q_{ik} + Q_{wk} + Q_{kk} \qquad (2.90)$$

where

$\vec{F}_{sk}$, $\vec{F}_{vk}$, and Q_{ik} : interfacial standard drag force and virtual mass force, energy exchange rate, per unit volume, respectively,

$\vec{F}_{wk}$ and Q_{wk} : wall friction force and wall heat transfer rate, per unit volume, respectively,

$Q_{\ell\ell}$: liquid energy conduction rate per unit volume,

$\vec{g}$: gravitational force

Note that Q_{vv} is put to be zero for the vapor energy equation of the THERMIT-6S. The relationships between Eq (2.89) and Eq (2.51), and between Eq (2.90) and Eq (2.73)

are as follows:

$$v_i = \langle\langle \overleftrightarrow{v} \rangle\rangle_a, \quad \vec{F}_k = \rho_k \vec{g}_k$$

$$\vec{F}_{sk} = -\frac{1}{L_{ak}} \langle\langle \vec{n}_k \cdot \overline{\overline{\tau}}_k \rangle\rangle_a$$

$$\vec{F}_{vk} = \frac{1}{L_{ak}} \langle\langle \Delta p'_{ki} \rangle\rangle_a$$

$$\vec{F}_{wk} = -\frac{1}{L_{wk}} \langle\langle \vec{n}_k \cdot \overline{\overline{\tau}}_k \rangle\rangle_w$$

$$Q_{ik} = -\frac{1}{L_{ak}} \langle\langle \overline{\dot{m}}_k \overleftrightarrow{h}_k + \vec{n}_k \cdot \overline{\vec{q}}_k \rangle\rangle_a$$

$$Q_{wk} = -\frac{1}{L_{wk}} \langle\langle n_k \cdot \overline{\vec{q}}_k \rangle\rangle_w$$

$$Q_{\ell\ell} = -\nabla \cdot \alpha_\ell (\vec{q}_\ell + \vec{q}^{\,t}_\ell)$$

Implicitly each property in the equations of the THERMIT-6S can be considered to be averaged in time and volume. Therefore, the THERMIT-6S neglects the fluctuating terms from the nonuniform spatial distribution of properties. Properties can be expressed as the sum of a

spatial average and spatial fluctuating component:

$$\bar{\rho}_k = \langle\langle\bar{\rho}_k\rangle\rangle + \rho_k^{'s} \quad \text{and} \quad \overleftrightarrow{\Psi}_k = \langle\langle\overleftrightarrow{\Psi}_k\rangle\rangle + \Psi_k^{'s}$$

Then, $\langle\langle\bar{\rho}_k\overleftrightarrow{\Psi}_k\rangle\rangle$ and $\langle\langle\bar{\rho}_k\overleftrightarrow{\Psi}_k\overleftrightarrow{v}_k\rangle\rangle$ become

$$\langle\langle\bar{\rho}_k\overleftrightarrow{\Psi}_k\rangle\rangle = \langle\langle\rho_k\rangle\rangle\langle\langle\overleftrightarrow{\Psi}_k\rangle\rangle + \langle\langle\rho_k^{'s}\ \Psi_k^{'s}\rangle\rangle$$

$$\begin{aligned}\langle\langle\bar{\rho}_k\overleftrightarrow{\Psi}_k\overleftrightarrow{v}_k\rangle\rangle = {} & \langle\langle\bar{\rho}_k\rangle\rangle\langle\langle\overleftrightarrow{\Psi}_k\rangle\rangle\langle\langle\overleftrightarrow{v}_k\rangle\rangle + \langle\langle\bar{\rho}_k\rangle\rangle\langle\langle\Psi_k^{'s}\ v_k^{'s}\rangle\rangle \\ & + \langle\langle\overleftrightarrow{\Psi}_k\rangle\rangle\langle\langle\rho_k^{'s}\ v_k^{'s}\rangle\rangle + \langle\langle\overleftrightarrow{v}_k\rangle\rangle\langle\langle\rho_k^{'s}\ \Psi_k^{'s}\rangle\rangle \\ & + \langle\langle\rho_k^{'s}\ \Psi_k^{'s}\ v_k^{'s}\rangle\rangle\end{aligned}$$

An adequate assessment should be given for all terms in the equations by assessing their comparative magnitudes and thereby justify the neglect of these spatial fluctuating terms.

In addition to neglecting the distribution terms, in the momentum equation of the THERMIT-6S, several assumptions are made:

1) Negligible turbulent contribution term, $\nabla\cdot\alpha_k\langle\langle\bar{\bar{\tau}}_k^t\cdot\vec{n}_k\rangle\rangle$
2) Negligible phase shear force, $\nabla\cdot\alpha_k\langle\langle\bar{\bar{\tau}}_k\cdot\vec{n}_k\rangle\rangle$
3) The average interfacial pressure $\langle\langle\bar{p}_{ki}\rangle\rangle_a$ equals the phase pressure $\langle\langle\bar{p}_k\rangle\rangle$. As a result, we have

$$\Delta p_{ki} = 0$$

Similarily, beside the omission of the distribution terms the following assumptions are made in the internal energy equation of the THERMIT-6S:

1) Negligible irreversible conversion to internal energy, $\langle\langle\overline{\bar{\bar{\tau}}_k : \nabla\vec{v}_k}\rangle\rangle$

2) Negligible vapor energy conduction rate,

$\nabla\cdot\alpha \ \langle\langle\bar{\vec{q}}_v + \bar{\vec{q}}_v^{\,t}\rangle\rangle$

Chapter 3 DESCRIPTION OF THERMIT-6S Equations

3.1 Differential Equations of THERMIT-6S

The mathematically rigorous differential equations of two-phase flow derived in Chapter 2 are simplified with several assumptions in order to derive the differential equations of the THERMIT-6S. Eqs (2.42), (2.51), and (2.73) for conservation equations, and Eqs (2.77), (2.78), and (2.80) for jump conditions are used to obtain the equations of the THERMIT-6S.

Conservation Equations

1. Vapor Mass

$$\frac{\partial}{\partial t}(\alpha_v \rho_v) + \nabla\cdot(\alpha_v \rho_v \vec{v}_v) = \Gamma_v \tag{3.1}$$

2. Liquid Mass

$$\frac{\partial}{\partial t}(\alpha_\ell \rho_\ell) + \nabla\cdot(\alpha_\ell \rho_\ell \vec{v}_\ell) = \Gamma_\ell \tag{3.2}$$

3. Vapor Energy

$$\frac{\partial}{\partial t}(\alpha_v \rho_v e_v) + \nabla\cdot(\alpha_v \rho_v e_v \vec{v}_v) + p\nabla\cdot(\alpha_v \vec{v}_v) + p\frac{\partial \alpha_v}{\partial t} = Q_{iv} + Q_{wv} \tag{3.3}$$

4. Liquid Energy

$$\frac{\partial}{\partial t}(\alpha_\ell \rho_\ell e_\ell) + \nabla\cdot(\alpha_\ell \rho_\ell e_\ell \vec{v}_\ell) + \nabla\cdot\alpha_\ell(\vec{q}_\ell + \vec{q}_\ell^{\,t}) + p\nabla\cdot(\alpha_\ell \vec{v}_\ell) + p\frac{\partial \alpha_\ell}{\partial t} = Q_{i\ell} + Q_{w\ell} \tag{3.4}$$

5. Vapor Momentum

$$\frac{\partial}{\partial t}(\alpha_v \rho_v \vec{v}_v) + \nabla\cdot(\alpha_v \rho_v \vec{v}_v \vec{v}_v) + \alpha_v \nabla p$$

$$= \Gamma_v \vec{v}_i - \vec{F}_{iv} - \vec{F}_{wv} + \alpha_v \rho_v \vec{g} \tag{3.5}$$

6. Liquid Momentum

$$\frac{\partial}{\partial t}(\alpha_\ell \rho_\ell \vec{v}_\ell) + \nabla\cdot(\alpha_\ell \rho_\ell \vec{v}_\ell \vec{v}_\ell) + \alpha_\ell \nabla p$$

$$= \Gamma_\ell \vec{v}_i - \vec{F}_{i\ell} - \vec{F}_{w\ell} + \alpha_\ell \rho_\ell \vec{g} \tag{3.6}$$

Jump Condition

1. Mass

$$\Gamma_v + \Gamma_\ell = 0 \;:\; \Gamma = \Gamma_v = -\Gamma_\ell \tag{3.7}$$

2. Energy

$$Q_{iv} + Q_{i\ell} = 0 \;:\; Q_i = Q_{iv} = -Q_{i\ell} \tag{3.8}$$

3. Momentum

$$\vec{F}_{iv} + \vec{F}_{i\ell} = 0 \;:\; \vec{F}_i = \vec{F}_{iv} = -\vec{F}_{i\ell} \tag{3.9}$$

Here Q_i and $\vec{F}_i$ denote interfacial energy and momentum exchange rate, per unit volume, and Q_{wv}, $Q_{w\ell}$, $\vec{F}_{wv}$, and $\vec{F}_{w\ell}$ are the wall heat transfer rates and wall friction force of vapor and liquid, per unit volume, respectively. Note that $\vec{v}_i$ in the above equations is different from $\vec{v}_i\cdot\vec{n}_k$ in Eq (2.24); $\vec{v}_i$ and $\vec{v}_i\cdot\vec{n}_k$ are the interfacial material velocity and displacement velocity of

the interfacial surface, respectively.

For reasons involved with the selection of a difference strategy for solving these equations, momentum equations are rewritten in a non-conservative form by using mass equations. Then Eqs (3.5) and (3.6) become

$$\alpha_v \rho_v \frac{\partial \vec{v}_v}{\partial t} + \alpha_v \rho_v \vec{v}_v \cdot \nabla \vec{v}_v + \alpha_v \nabla p$$

$$= \Gamma(\vec{v}_i - \vec{v}_v) - \vec{F}_i - \vec{F}_{wv} + \alpha_v \rho_v \vec{g} \tag{3.10}$$

$$\alpha_\ell \rho_\ell \frac{\partial \vec{v}_\ell}{\partial t} + \alpha_\ell \rho_\ell \vec{v}_\ell \cdot \nabla \vec{v}_\ell + \alpha_\ell \nabla p$$

$$= - \Gamma(\vec{v}_i - \vec{v}_\ell) + \vec{F}_i - \vec{F}_{w\ell} + \alpha_\ell \rho_\ell \vec{g} \tag{3.11}$$

If we assume that $\vec{v}_i$ is equal to $\vec{v}_\ell$, then

$$\Gamma(\vec{v}_i - \vec{v}_v) = \Gamma(\vec{v}_\ell - \vec{v}_v)$$

$$\Gamma(\vec{v}_i - \vec{v}_\ell) = 0$$

In THERMIT-6S $\vec{F}_i$ consists of two components: the standard drag force ($\vec{F}_s$) and virtual mass force ($\vec{F}_v$), per unit volume. Both terms are defined as follows

$$\vec{F}_s \equiv K(\vec{v}_v - \vec{v}_\ell) \tag{3.12}$$

$$\vec{F}_v \equiv \alpha_v \rho_\ell C_v \left\{ \frac{\partial \vec{v}_v}{\partial t} - \frac{\partial \vec{v}_\ell}{\partial t} + \vec{v}_v \cdot \nabla(\vec{v}_v - \vec{v}_\ell) \right.$$

$$\left. + (\vec{v}_v - \vec{v}_\ell) \cdot [(\lambda - 2)\nabla \vec{v}_v + (1 - \lambda)\nabla \vec{v}_\ell] \right\} \tag{3.13}$$

For details of the virtual mass force, refer to Chapter 4. Introducing Eqs (3.12) and (3.13) into Eqs (3.10) and (3.11), we get the final momentum equation used in the THERMIT-6S.

$$(\alpha_v\rho_v + \alpha_v\rho_\ell C_v)\frac{\partial\vec{v}_v}{\partial t} - \alpha_v\rho_\ell C_v\frac{\partial\vec{v}_\ell}{\partial t} + E_v + E_{vm} + \alpha_v\nabla p$$

$$= -(\Gamma + K)(\vec{v}_v - \vec{v}_\ell) - \vec{F}_{wv} + \alpha_v\rho_v\vec{g} \tag{3.14}$$

$$(\alpha_\ell\rho_\ell + \alpha_v\rho_\ell C_v)\frac{\partial\vec{v}_\ell}{\partial t} - \alpha_v\rho_\ell C_v\frac{\partial\vec{v}_v}{\partial t} + E_\ell - E_{vm} + \alpha_\ell\nabla p$$

$$= K(\vec{v}_v - \vec{v}_\ell) - \vec{F}_{w\ell} + \alpha_\ell\rho_\ell\vec{g} \tag{3.15}$$

where

$$E_v = \alpha_v\rho_v\vec{v}_v\cdot\nabla\vec{v}_v \tag{3.16}$$

$$E_\ell = \alpha_\ell\rho_\ell\vec{v}_\ell\cdot\nabla\vec{v}_\ell \tag{3.17}$$

$$E_{vm} = \alpha_v\rho_\ell C_v[(\lambda - 1)\vec{v}_v\cdot\nabla\vec{v}_v - (\lambda - 2)\vec{v}_\ell\cdot\nabla\vec{v}_v$$

$$- \lambda\vec{v}_v\cdot\nabla\vec{v}_\ell - (1 - \lambda)\vec{v}_\ell\cdot\nabla\vec{v}_\ell] \tag{3.18}$$

As shown in Eq (2.59), Q_{iv} and $Q_{i\ell}$ can be divided into two components contributed by mass exchange and interfacial heat flux. These are defined as follows:

$$Q_{iv} = \frac{1}{L_a}(g_m h_{iv} + q''_{iv}) \tag{3.19}$$

$$Q_{i\ell} = -\frac{1}{L_a}(g_m h_{i\ell} + q''_{i\ell}), \tag{3.20}$$

where $h_{i\ell}$ and h_{iv} are the enthalpy on the liquid and vapor side of the interface, respectively.

$q''_{i\ell}$ and q''_{iv} are the heat flux on the liquid and vapor side of the interface,

g_m and $\frac{1}{L_a}$ are the interfacial mass flux and the ratio of interfacial area to fluid volume in the control volume.

$$q''_{ik} = \langle\langle n_k \cdot \bar{\vec{q}}_k \rangle\rangle_a$$

$$g_m = -\langle\langle \bar{\dot{m}}_k \rangle\rangle_a$$

The mass exchange rate Γ can be expressed in terms of g_m and $\frac{1}{L_a}$

$$\Gamma = \frac{g_m}{L_a} \tag{3.21}$$

According to the jump condition, Eq (2.67) with the neglected term $\langle\langle \bar{p}_k \cdot \vec{v}_i + \overline{\bar{\bar{\tau}}_k \cdot \vec{v}_k} \rangle\rangle_a$, the following relation can be obtained

$$g_m h_{i\ell} + q''_{i\ell} = g_m h_{iv} + q''_{iv} \tag{3.22}$$

Assuming the saturation state at the interface, we obtain the relationship between the interfacial mass flux and heat flux.

$$g_m = \frac{q''_{i\ell} - q''_{iv}}{h_{fg}} \tag{3.23}$$

As the interfacial heat flux in the gas phase, q''_{iv} is usually much smaller than $q''_{i\ell}$, a simplified relationship can be obtained by neglecting q''_{iv}:

$$g_m = q''_{i\ell}/h_{fg} \tag{3.24}$$

If we set up a physical model of $q''_{i\ell}$, then mass exchange rate can be obtained by using Eqs (3.21) and (3.24). Substituting Eq (3.24) into Eq (3.19), we have the interfacial energy transfer rate per unit volume,

$$Q_i = \frac{1}{L_a} \frac{q''_{i\ell}\, h_g}{h_{fg}} \tag{3.25}$$

In addition to these conservative equations there are four equations of state:

$$\rho_v = \rho_v(p,T_v), \quad \rho_\ell = \rho_\ell(p,T_\ell)$$
$$e_v = e_v(p,T_v), \quad e_\ell = e_\ell(p,T_\ell) \tag{3.26}$$

These equations of state can be used to eliminate the densities and internal energies in terms of temperature and pressure. For the closure of the conservation equations terms, which represent the transfer of mass, energy, or momentum at the interface between the solid and fluid, and between liquid and vapor, must be explicitly expressed in terms of primary variables and properties. These terms are as follows:

$$\Gamma,\ \vec{F}_i,\ Q_i,\ \vec{F}_{wv},\ \vec{F}_{w\ell},\ Q_{wv},\ \text{and}\ Q_{w\ell}$$

The physical models of the above terms, so called constitutive equations, are described in Chapter 5.

3.2 Difference Equations of THERMIT-6S

The difference equations of THERMIT-6S are basically those of THERMIT (17) and can be obtained by discretizing the proceeding set of differential equations. The spatial discretization is characterized by a first-order spatial scheme, donor cell method, and staggered mesh layout. For time discretization a first-order semi-implicit scheme treats implicitly sonic terms and terms relating to local phenomena such as the exchange processes, and explicitly convective terms. A fully explicit method represents the fastest method on a per time step basis, but requires extremely small time steps due to Courant conditions. A implicit method, on the other hand, allows large time steps but leads to greatly increased code structure. The semi-implicit method is a compromise between these two extremes; reasonable time step size but less computation time per time step and simpler code structure than the implicit method.

We begin with the mass and energy equations, which are differenced about the centers of the mesh cells. (See Fig 3.1) The subscripts i, j, and k are used to indicate positions along the x, y, and z axes, respectively. The superscripts n or n+1 refers to the time level at which the variables are evaluated. A superscript n+½ is used only for the exchange terms which are functions of both new and old time values of variables. A and V represents the flow areas of the cell faces and the flow volumes of the cell, respectively. With these definition, the mass and energy

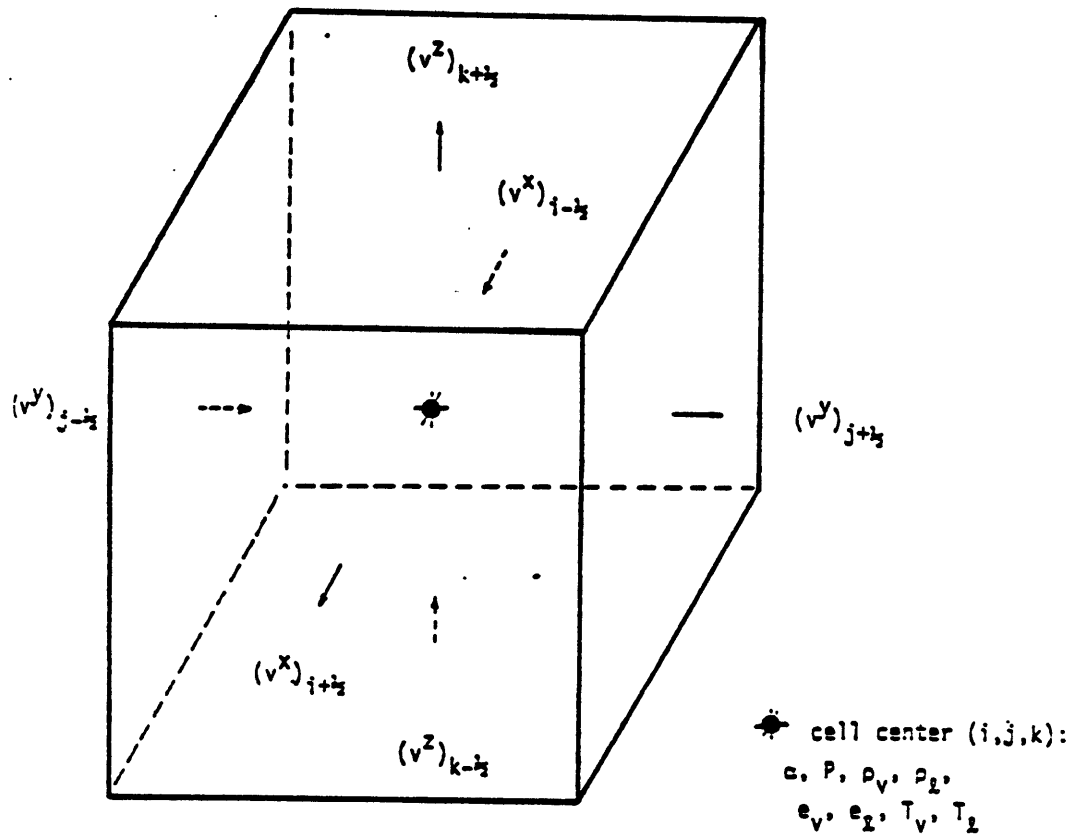

Fig. 3.1: A Typical Fluid Mesh Cell Showing Location of Variables and Subscripting Conventions

difference equations are as follows:

Vapor Mass:

$$\frac{(\alpha_v\rho_v)^{n+1} - (\alpha_v\rho_v)^n}{\Delta t} + \frac{1}{V}\{[A(\alpha_v\rho_v)^n(v_v^x)^{n+1}]_{i+\frac{1}{2}}$$

$$-[A(\alpha_v\rho_v)^n(v_v^x)^{n+1}]_{i-\frac{1}{2}} + [A(\alpha_v\rho_v)^n(v_v^y)^{n+1}]_{j+\frac{1}{2}}$$

$$-[A(\alpha_v\rho_v)^n(v_v^y)^{n+1}]_{j-\frac{1}{2}} + [A(\alpha_v\rho_v)^n(v_v^z)^{n+1}]_{k+\frac{1}{2}}$$

$$-[A(\alpha_v\rho_v)^n(v_v^z)^{n+1}]_{k-\frac{1}{2}}\} = \Gamma^{n+\frac{1}{2}} \tag{3.27}$$

Liquid Mass:

Same as Eq. (3.27) with α_v replaced by α_ℓ, subscript v by ℓ and Γ by $-\Gamma$ (3.28)

Vapor Energy:

$$\frac{(\alpha_v\rho_v e_v)^{n+1} - (\alpha_v\rho_v e_v)^n}{\Delta t} + \frac{1}{V}\,[A(\alpha_v\rho_v e_v + p)^n(v_v^x)^{n+1}]_{i+\frac{1}{2}}$$

$$-[A(\alpha_v\rho_v e_v + p)^n(v_v^x)^{n+1}]_{i-\frac{1}{2}}$$

$$+[A(\alpha_v\rho_v\rho_v + p)^n(v_v^y)^{n+1}]_{j+\frac{1}{2}} - [A(\alpha_v\rho_v e_v + p)^n(v_v^y)^{n+1}]_{j-\frac{1}{2}}$$

$$+[A(\alpha_v\rho_v e_v + p)^n(v_v^z)^{n+1}]_{k+\frac{1}{2}}$$

$$-[A(\alpha_v\rho_v e_v + p)^n(v_v^z)^{n+1}]_{k-\frac{1}{2}}\} + p^n\,\frac{\alpha_v^{n+1} - \alpha_v^n}{\Delta t}$$

$$= Q_i^{n+\frac{1}{2}} + Q_{w\ell}^{n+\frac{1}{2}} \tag{3.29}$$

Liquid Energy:

Same as Eq. (3.29) with α_v replaced by α_ℓ, subscript v by ℓ and Q_i by $-Q_i$, and added $Q_{\ell\ell}$ (3.30)

The liquid conduction term $\nabla\cdot\alpha_\ell(\vec{q}_\ell + \vec{q}_\ell^{\,t})$ is expressed as $Q_{\ell\ell}$ in Eq (3.30) and models for it will be presented in Appendix A. The properties transferred through the cell faces must be explicitly expressed in terms of cell centered quantities such as α, ρ_v, ρ_ℓ, e_v and e_ℓ . The THERMIT-6S uses a particular relationship often referred to as donor-cell differencing; the properties will be transferred through the cell faces with all centered quantities upstream of that cell. If C stands for any cell-centered quantity, the value of $C_{i+\frac{1}{2}}$ is determined as

$$C_{i+\frac{1}{2}} = \begin{cases} C_{i+1} & \text{if} \quad v_{i+\frac{1}{2}}^{n+1} < 0 \\ C_i & \text{if} \quad v_{i+\frac{1}{2}}^{n+1} \geq 0 \end{cases} \tag{3.31}$$

For the donor cell decisions updated velocities are used. The primary reason to use updated velocities is to solve the packing problem which occurred if old velocities for donor-cell criteria were used.

Now let us consider only a single component of the vapor momentum. The additional equations are obtained by permutation of the axes and indices. According to the staggered mesh scheme, each momentum equation is differenced about the center of a face of a mesh cell. Based on Eq (3.14), the one-dimensional vapor momentum equation in the x direction is differenced at the point (i+½,j,k) as follows:

$$(\alpha_v\rho_v + \alpha_v\rho_\ell C_v)^n_{i+\frac{1}{2}} \frac{(v_v^{x\,n+1} - v_v^{x\,n})_{i+\frac{1}{2}}}{\Delta t}$$

$$- (\alpha_v\rho_\ell C_v)^n_{i+\frac{1}{2}} \frac{(v_\ell^{x\,n+1} - v_\ell^{x\,n})_{i+\frac{1}{2}}}{\Delta t} + E^n_{v\,i+\frac{1}{2}} + E^n_{vm\,i+\frac{1}{2}}$$

$$+ \alpha^n_{vi+\frac{1}{2}} \frac{(p_{i+1} - p_i)^{n+1}}{\Delta x_{i+\frac{1}{2}}} = K^n(v_v - v_\ell)^{n+1}_{i+\frac{1}{2}} - F^{n+\frac{1}{2}}_{w\ell}, \quad (3.32)$$

where $E^n_{v\,i+\frac{1}{2}} = (\alpha_v\rho_v)^n_{i+\frac{1}{2}}\ \Delta v^n_{vv}$

$$E^n_{vm\,i+\frac{1}{2}} = (\alpha_v\rho_v C_v)^n_{i+\frac{1}{2}}\ [(\lambda - 1)\Delta v^n_{vv} - (\lambda - 2)\Delta v^n_{\ell v}$$

$$- \lambda\Delta v^n_{v\ell} - (1 - \lambda)\Delta v^n_{\ell\ell}]$$

$$\Delta v^n_{vv} = v^{x\,n}_{v\,i+\frac{1}{2}} \left(\frac{\Delta_x v^x_v}{\Delta x}\right)_{i+\frac{1}{2}} v^{y\,n}_{v\,i+\frac{1}{2}} \left(\frac{\Delta_y v^x_v}{\Delta y}\right)^n_{i+\frac{1}{2}}$$

$$+ v^z_{v\,i+\frac{1}{2}} \left(\frac{\Delta_z v^x_v}{\Delta z}\right)^n_{i+\frac{1}{2}}$$

$$\Delta v^n_{\ell v} = v^{x\,n}_{\ell i+\frac{1}{2}} \left(\frac{\Delta_x v^x_v}{\Delta x}\right)^n_{i+\frac{1}{2}} + v^{y\,n}_{\ell i+\frac{1}{2}} \left(\frac{\Delta_y v^x_v}{\Delta y}\right)^n_{i+\frac{1}{2}}$$

$$+ v^z_{\ell i+\frac{1}{2}} \left(\frac{\Delta_z v^x_v}{\Delta z}\right)^n_{i+\frac{1}{2}}$$

$\Delta v^n_{v\ell}$: same as $\Delta v^n_{\ell v}$ with subscripts ℓ replaced by v and v by ℓ.

$\Delta v^n_{\ell\ell}$: same as Δv^n_{vv} with subscript v replaced by ℓ.

In the above equation we have used an expression of the form $\frac{\Delta_x v_v^x}{\Delta x}$ to designate the difference approximation of $\frac{\partial v_v^x}{\partial x}$ associated with the point $(i+\frac{1}{2}, j, k)$. Similar expressions have been written for the y and z directions. In Eq (3.32) we are again faced with the problem of variables appearing at locations other than those already defined. We first consider the quantity α:

$$\alpha_{i+\frac{1}{2}} = \frac{\alpha_{i+1}\,\Delta x_{i+1} + \alpha_i \Delta x_i}{\Delta x_{i+1} + \Delta x_i} \tag{3.33}$$

The quantity $\rho_{vi+\frac{1}{2}}$ can be expressed in the same way as Eq (3.33). Every velocity except $v^x_{vi+\frac{1}{2}}$ is at the wrong position, so an averaging must be performed. We define

$$v^y_{vi+\frac{1}{2}} = \frac{1}{4}\,[v^y_{vi,j-\frac{1}{2}} + v^y_{vi,j+\frac{1}{2}} + v^y_{vi+1,j-\frac{1}{2}} + v^y_{vi+1,j+\frac{1}{2}}] \tag{3.34}$$

$$v^z_{vi+\frac{1}{2}} = \frac{1}{4}[v^z_{vi,k-\frac{1}{2}} + v^z_{vi,k+\frac{1}{2}} + v^z_{vi+1,k-\frac{1}{2}} + v^z_{vi+1,k+\frac{1}{2}}] \tag{3.35}$$

Finally, according to the donor cell scheme, the difference

approximations of the convective derivatives are given by;

$$\left(\frac{\Delta_x v_v^x}{\Delta x}\right)_{i+\frac{1}{2}} = \begin{cases} \left(v^x_{vi+3/2} - v^x_{vi+\frac{1}{2}}\right) \Big/ \Delta x_{i+1} & \text{if } v^x_{vi+\frac{1}{2}} < 0 \\ \left(v^x_{vi+\frac{1}{2}} - v^x_{vi-\frac{1}{2}}\right) \Big/ \Delta x_i & \text{if } v^x_{vi+\frac{1}{2}} \geq 0 \end{cases} \tag{3.36}$$

$$\left(\frac{\Delta_y v_v^x}{\Delta y}\right)_{i+\frac{1}{2}} = \begin{cases} \left(v^x_{vi+\frac{1}{2},j+1} - v^x_{vi+\frac{1}{2},j}\right) \Big/ \Delta y_{j+\frac{1}{2}} & \text{if } v^y_{vi+\frac{1}{2}} < 0 \\ \left(v^x_{vi+\frac{1}{2},j} - v^x_{vi+\frac{1}{2},j-1}\right) \Big/ \Delta y_{j-\frac{1}{2}} & \text{if } v^y_{vi+\frac{1}{2}} \geq 0 \end{cases} \tag{3.37}$$

$$\left(\frac{\Delta_z v_v^x}{\Delta z}\right)_{i+\frac{1}{2}} = \begin{cases} \left(v^x_{vi+\frac{1}{2},k+1} - v^x_{vi+\frac{1}{2},k}\right) \Big/ \Delta z_{k+\frac{1}{2}} & \text{if } v^z_{vi+\frac{1}{2}} < 0 \\ \left(v^x_{vi+\frac{1}{2},k} - v^x_{vi+\frac{1}{2},k-1}\right) \Big/ \Delta z_{k-\frac{1}{2}} & \text{if } v^z_{vi+\frac{1}{2}} \geq 0 \end{cases} \tag{3.38}$$

The mesh spacings $\Delta y_{j+\frac{1}{2}}$ and $\Delta z_{k+\frac{1}{2}}$ appearing in the above expressions are evaluated as;

$$\Delta y_{j+\frac{1}{2}} = (\Delta y_j + \Delta y_{j+1})/2 \tag{3.39}$$

$$\Delta z_{k+\frac{1}{2}} = (\Delta z_k + \Delta z_{k+1})/2 \tag{3.40}$$

We have now completed our specification of the difference equations, with the exception of the exchange terms. These terms are discussed in Chapter 5.

3.3 Solution Procedure of THERMIT-6S

The most important characteristic of our difference equations lies in the treatment of coupling terms. An examination of the mass and energy equations reveals that

cell-centered variables appearing in these equations such as α^{n+1}, p^{n+1}, and $e^{n+1}$are coupled only to the new-time velocities v^{n+1} on the faces of the mesh cell. The momentum equation relates these velocities only to the pressure in the mesh cell in question and in the six surrounding cells. Thus we see that coupling between mesh cells at time level n+1 is through the pressure variable. Hence, we need to solve only the reduced pressure equation.

Let us describe how this solution is accomplished. Denote the system of two-fluid finite difference equations by $F(x) = 0$. Here, x is a vector containing the ten principal unknown variables. We shall use a Newton iteration to solve the non-linear system,

$$F(x) = 0 \tag{3.41}$$

We first linearize the old iterate x^m as

$$F(x) \cong F(x^{m+1}) = F(x^m) + J(x^m)(x^{m+1} - x^m) = 0 \tag{3.42}$$

where the Jacobian matrix $J(x^m)$ is defined as $(\frac{\partial F}{\partial x})_{x^m}$
We then solve the following linear system for

$$J(x^m)\Delta x^{m+1} = -F(x^m) \tag{3.43}$$

where Δx^{m+1} is the iteration error $(x^{m+1}-x^m)$ and $F(x^m)$ is called a residual error.

This linear system is solved either by the direct method or iteration method. (For detail refer to Ref 15) This process is called as the inner iteration. This Newton iteration,

called as the outer iteration, continues until the iteration error Δx^{m+1} or the residual error $F(x^m)$ is sufficiently small.

The first procedure is to express velocities in the momentum equations in terms of pressure. Because the interfacial momentum exchange term has been treated implicitly, the liquid and vapor velocities are coupled with each other. At the face of each mesh cell, the momentum equations can be put in the form

$$\begin{bmatrix} x & x \\ x & x \end{bmatrix} \begin{bmatrix} v_v^{m+1} \\ v_\ell^{m+1} \end{bmatrix} = \begin{bmatrix} a\Delta p^{m+1} + f \\ b\Delta p^{m+1} + g \end{bmatrix} \tag{3.44}$$

By solving the above 2x2 matrix, we determine each velocity in terms of the pressure difference as

$$v_v^{m+1} = c\ \Delta p^{m+1} + f'$$

$$v_\ell^{m+1} = d\ \Delta p^{m+1} + g' \tag{3.45}$$

The above equations can now be used to eliminate all velocities appearing in the mass and energy. Then we finally obtain a set of four equations for each mesh cell involving the four unknowns, p, α, T_v, and T_ℓ, at the center of the mesh cells and pressures, at the centers of

the six adjacent cells.

$$\begin{bmatrix} x & x & x & x \\ x & x & x & x \\ x & x & x & x \\ x & x & x & x \end{bmatrix} \begin{bmatrix} p \\ \alpha \\ T_v \\ T_\ell \end{bmatrix} + \begin{bmatrix} x & x & x & x & x & x \\ x & x & x & x & x & x \\ x & x & x & x & x & x \\ x & x & x & x & x & x \end{bmatrix} \begin{bmatrix} p_1 \\ \vdots \\ p_6 \end{bmatrix} = \begin{bmatrix} x \\ x \\ x \\ x \end{bmatrix} \tag{3.46}$$

By inverting the 4x4 matrix that appears above, we can put this system in the reduced form;

$$\begin{bmatrix} 1 & & & 0 \\ & 1 & & \\ & & 1 & \\ & & & 1 \\ 0 & & & \end{bmatrix} \begin{bmatrix} p \\ \alpha \\ T_v \\ T_\ell \end{bmatrix} + \begin{bmatrix} x & x & x & x & x & x \\ x & x & x & x & x & x \\ x & x & x & x & x & x \\ x & x & x & x & x & x \end{bmatrix} \begin{bmatrix} p_1 \\ \vdots \\ p_6 \end{bmatrix} = \begin{bmatrix} x \\ x \\ x \\ x \end{bmatrix} \tag{3.47}$$

The first equation in the above set is an equation involving only the pressure in a cell and its six neighbors. The remaining three equations relate the void fraction and temperature to the pressure. The pressure equation can be solved iteratively with each complete sweep referred to as an inner iteration. Once the pressure field is found, the other unknowns α, T_v , and T_ℓ can be found by back substitution. The above procedure is repeated until the pressure iteration error, Δp^{m+1} is sufficiently small. If convergence is not attained in a specified number of iterations, the time step size is reduced and the same procedure is repeated. The method will always converge, if

the time step size is small enough.

A crucial property of the reduced pressure problem is its diagonal dominance. In the one-dimensional flow the pressure equations can be expressed as follows:

$$p_{i+1}^{m+1} - \left[2 + \left(\frac{a^{-1}\ \Delta x}{\Delta t}\right)^2\right] p_i^{m+1} + p_{i-1}^{m+1} = \ldots$$

where a is the sound speed

$$a^{-2} = \left(\frac{\partial \rho}{\partial p}\right)_p$$

The amount by which the sum of any row of coefficients exceeds zero can always be expressed in the form $\left(\frac{a^{-1}\ \Delta x}{\Delta t}\right)^2$.

Chapter 4 STUDIES OF VIRTUAL MASS

It is known that the typical six equation two-fluid model of the two-phase flow possesses complex characteristics, exhibits unbounded instabilities in the short-wavelength limit and constitutes an ill-posed initial value problem. Among the suggestions to overcome these difficulties, one model for the virtual mass force terms is studied here. The virtual mass represents real physical effects which provide dissipation for numerical stability. Also, it was found that the virtual mass has a profound effect upon the mathematical characteristic and numerical stability. Here, quantitative bounds on coefficients of the virtual mass terms are suggested for mathematical hyperbolicity, numerical stability, and satisfaction of the Second Law of Thermodynamics. It is concluded that the finite difference scheme with the suggested virtual mass model is restricted only by the convective stability conditions with the above suggested values.

4.1 Introduction

Among the several models of two-phase flow the two-fluid model offers the most detailed and general description of two-phase flow. But it was reported in early work that the model has inherent instability problems. In 1965 Jarvis (24) tried to solve the two-phase equations using the two-fluid model for modeling the cooldown process in cryogenics and faced instability problems. He attributed the instabilities to the fact that the system was found to be nonhyperbolic. In 1967 Richtmyer and Morton (25) showed that, if the initial value problem (IVP) is ill-posed, then no difference scheme that is consistent with the problem can be stable. In 1971 Siegmann (11) encountered numerical instabilities in his transient sodium boiling code called MOC. In 1973 Boure (26) appears to have encountered severe stability difficulties in the GEVATRAN code. In a round table discussion during the Fifth International Heat Transfer Conference (27), the instability problems in the two-fluid model were shown to be caused by its ill-posed equations. In 1976 Bryce (28) experienced large-scale pressure oscillations with the RELAP-UK code. He demonstrated that any simple two-fluid model with complex characteristics does not give solutions which converge as the mesh size and time step size are refined. He concluded that, though solutions may be obtained by using numerical technique, the significance of these solutions is not clear. In 1976 Lyczkowski (29) did a sample calculation

illustrating error growth caused by complex characteristics. In the 1977 ANS topical meeting on thermal reactor safety, Anderson (30) reported his attempt to achieve stability by using virtual mass terms in the RISQUE code. It was found that the virtual mass has a profound effect on the dynamics of two-phase flow. His code was used to perform numerical calculations on the behavior of interfacial waves. It was observed that for no virtual mass, the wave amplitude grows rapidly, but the computed result with virtual mass shows a stable oscillatory behavior for the wave amplitude. In 1979 Rivard and Travis (31) successfully dealt with critical flow with the two-fluid code, K-FIX. But for the results presented, the value of the interfacial drag coefficient was chosen sufficiently large that there was no relative motion between the phases. In 1980 investigators at R.P.I. (32) showed that without virtual mass it was more costly to run the problem, and even could not run the complete problem using their code, GEAR. Computer running time without virtual mass was forty times longer than that with virtual mass.

It may well be argued that equation sets with complex characteristics may still be adequate for a range of phenomena if the numerical method introduces sufficient dissipation to damp the high frequency instabilities. Obviously there are real physical effects to accomplish the dissipation needed for numerical stability. Among several candidates suggested for numerical stability, Drew's model

(33,38) with the virtual mass terms will be studied here.

4.2 Physical Significance of Virtual Mass

Let us consider a solid sphere motion in an infinite, inviscid, and incompressible fluid. In this perfect fluid there is no dissipation of energy. For inviscid flow about a sphere with the radius r, the pressure distribution along the surface is given by Lamb (34) as

$$\frac{P}{\rho_\ell} = \frac{1}{2} r \frac{dU}{dt} \cos\theta + \frac{9}{16} U^2 \cos 2\theta - \frac{1}{16} U^2 \tag{4.1}$$

where U is the instantaneous relative velocity between the sphere and fluid, θ is the polar angle measured with respect to the direction of U, and the time derivative is made following the particle, that is,

$$\frac{dU}{dt} = \frac{\partial U}{\partial t} + U \cdot \nabla U \tag{4.2}$$

The last two terms on the right-hand side of Eq (4.1) are the same for surface elements in the positions θ and $\pi-\theta$; so that, when U is constant, the pressures on the various elements of the anterior half of the sphere are balanced by equal pressures on the corresponding elements of the posterior half. But when the sphere is being accelerated, there is an excess of pressure on the anterior, and a defect on the posterior half. The reverse holds when the motion is being retarded.

Integrating the local pressure, Eq (4.1) over the

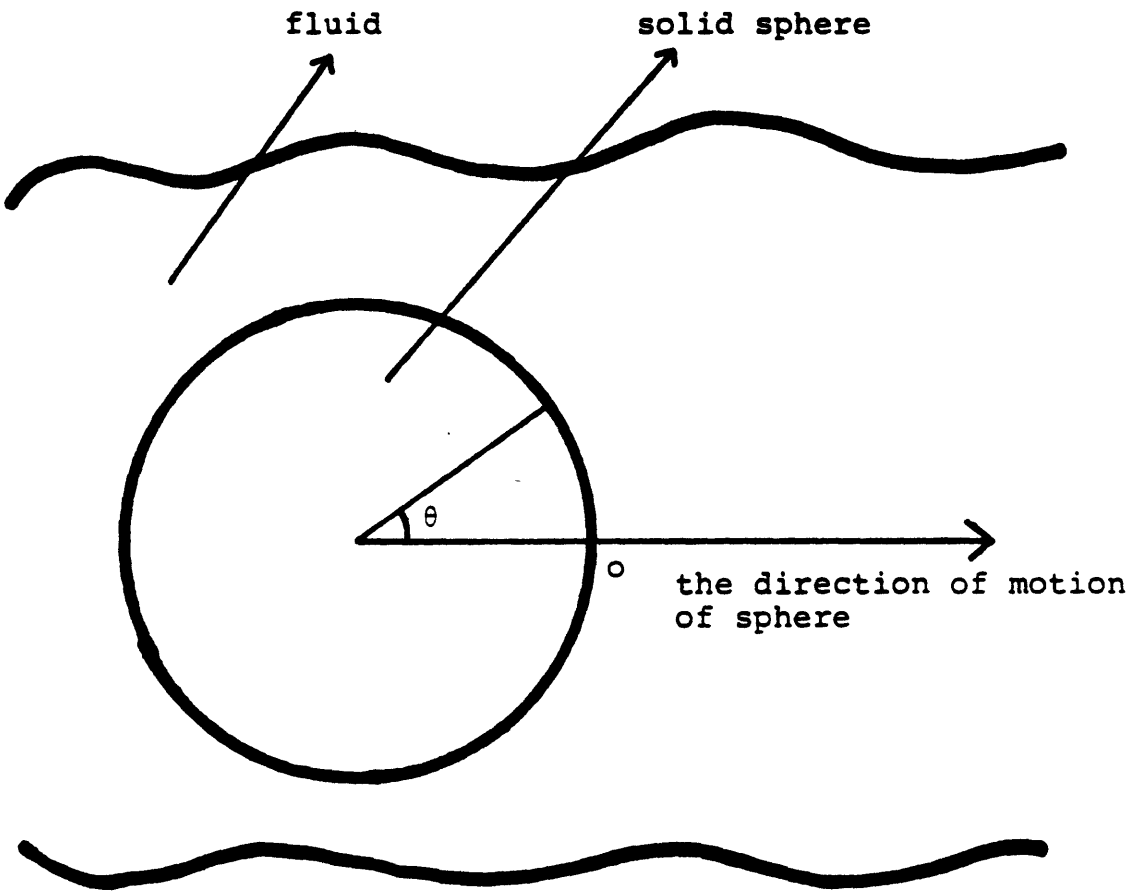

Fig. 4.1: Configuration of the Solid Sphere Accelerating in Fluid

surface area of the sphere, we obtain the resultant force in the direction of the motion of the sphere due to acceleration of the body.

$$-\int_A PdA = -\int_0^{2\pi}\int_0^{\pi} 2\pi r^2 \sin\theta \cos\theta \, Pd\theta d\phi$$

$$= -\frac{2}{3}\pi r^3 \rho_\ell \frac{dU}{dt}$$

$$= -M' \frac{dU}{dt} = -\frac{1}{2} M \frac{dU}{dt}, \tag{4.2}$$

where $M' = \frac{2}{3}\pi r^3 \rho_\ell$, $M = \frac{4}{3}\pi r^3 \rho_\ell$

M: mass of the fluid displaced by the sphere

Then, it appears that the effect of the fluid pressure is equivalent simply to an addition to the inertia of the solid, the increment being half the mass of the fluid displaced. Also, note that Eq (4.2) specifies the equivalent momentum transmitted to the fluid in unit time, F. The external force f must be equal to the sum of the time derivative of the total momentum of the sphere and F:

$$M_s \frac{dU}{dt} + F = f \tag{4.3}$$

where M_s is the mass of the sphere.

Using Eq (4.2), we then obtain

$$(M_s + M') \frac{dU}{dt} = f \tag{4.4}$$

This is the equation for a body immersed in a perfect fluid. The presence of the liquid effectively increases the mass of a moving sphere from M to M+M'. M' is the virtual mass to be considered for accelerating objects in the fluid.

If we use the notation described in Section 2.5, Eq (4.2) can be expressed as

$$\frac{1}{L_a} \langle\langle \bar{p} \rangle\rangle_a = M' \frac{dU}{dt} \Big/ V_f = \frac{1}{2} \alpha_b \rho_\ell \frac{dU}{dt} \tag{4.5}$$

where $\alpha_b = \frac{4}{3} \pi r^3 / V_f$

Referring to Eq (3.13), the coefficient of the virtual mass for a sphere, C_v is 0.5.

4.3 Ill-posed Problems and Mathematical Stability

Quantitative physical laws are idealizations of reality. As knowledge grows, a given physical situation can be idealized mathematically in a number of different ways. It is therefore important to characterize those reasonable idealized formulations. Hadamard (35) examined this problem, asserting that a physical formulation is well-posed if its solution exists, is unique, and depends continuously on the external (boundary) conditions. Existence and uniqueness are an affirmation of the principle of determination without which experiments could not be repeated with the expectation of consistent data. The continuous dependence criterion is an expression of the stability of the solution; a small change in any of the

problem's data should produce only a correspondingly small change in the solution.

The general one-dimensional problem can be represented in matrix form, as follows:

$$A(x)\frac{\partial x}{\partial t} + B(x)\frac{\partial x}{\partial z} + C(x) = 0, \tag{4.6}$$

where x is a column vector of independent variables, A(x) and B(x) are the coefficient matrices, and C(x) is a source or sink vector.

The Initial Value Problem consideration is to find a solution of Eq (4.6) in some region

$$a \leq z \leq b$$

subject to the initial condition

$$x(0,z) = u_o(z) \tag{4.7}$$

and the value of x or its derivatives prescribed on the boundaries,

$$z = a \text{ and } z = b \tag{4.8}$$

When the definition of a well-posed problem by Hadamard (35) is applied to the above system, it is said to be well-posed if the solution of Eq (4.6) exists, is unique, and depends continuously on both of the initial condition, Eq (4.7) and the boundary conditions Eq (4.8). Also Eq (4.6) is defined as hyperbolic if all values of the characteristics of Eq (4.6) are distinct and real.

According to Lax (36) the requirement of a well-posedness in linear partial differential equations of a form like Eq (4.6) is the same as that of hyperbolicity.

Along characteristic curves, the highest-order derivatives in a partial differential equation are indeterminate; characteristics may separate discontinuities in the solution. Therefore, the characteristics are trajectories of discontinuities in the solution. Physically they represent the speed of travel of information in a physical system. The typical two-fluid models have four real and two imaginary characteristics. The real characteristics are two convective velocities of liquid and vapor, and two relative sound velocities to both convective velocities of liquid and vapor through the system. The two imaginary characteristics may represent two relative velocities of interfacial wave propagation to both liquid and vapor. The complex values of the characteristics indicate an instability of interfacial waves.

Characteristics and stability can be shown to be related only in the limit of large frequency, as discussed in the following. The characteristics, μ, of Eq (4.6) are defined by the equation

$$\mathrm{Det}\ (\mu A - B) = 0 \tag{4.9}$$

To examine the local linear stability behavior of Eq (4.6), x is replaced by $(x_o+\delta x)$ and the result is linearized with

respect to δx , so that

$$A(x_o)\ \frac{\partial(\delta x)}{\partial t} + B(x_o)\ \frac{\partial(\delta x)}{\partial z} + \left(\delta x\left(\frac{\partial A}{\partial x}\right)_{x_o}\right)\frac{\partial x_o}{\partial t} + \left(\delta x\left(\frac{\partial B}{\partial x}\right)_{x_o}\right)\frac{\partial x_o}{\partial z} + \delta x\ \left(\frac{\partial C}{\partial x}\right)_{x_o} = 0 \tag{4.10}$$

As Eq (4.10) describes small perturbations, δx , about an unperturbed solution, a uniform steady-state unperturbed solution is assumed, which means that x_o is independent of z and t. We take a wave form for the perturbed amount, δx

$$\delta x = \delta x_o \exp[i(kz - wt)] \tag{4.11}$$

Then Eq (4.10) becomes

$$-iw\ A(x_o)\ \delta x_o + ik\ B(x_o)\delta x_o + \delta x_o \left(\frac{\partial C}{\partial x}\right)_{x_o} = 0 \tag{4.12}$$

Eq (4.12) is a homogeneous linear equation in the components of δx_o. For a nontrivial solution the determinant of the coefficient matrix must vanish:

$$\mathrm{Det}(-iwA + ikB + D) = 0, \tag{4.13}$$

where

$$D = \left(\frac{\partial C}{\partial x}\right)^T_{x_o},$$

and the superscipt T denoting the matrix transpose.
For nonzero k Eq (4.13) can be rewritten as

$$\mathrm{Det}\ \left(\frac{w}{k}\ A - B + \frac{i}{k}\ D\right) = 0 \tag{4.14}$$

Inspection of Eq (4.11) shows that the condition for stability is that the imaginary part, (Im(w)), of w must be less than or equal to zero for all roots of w. Comparison of Eq (4.9) and Eq (4.14) shows that, if $D = 0$ or $k \to \infty$, the dispersion relations can be obtained from the characteristics simply by equating w/k to μ. Physically the instability at long wavelenths is the well-known Helmholtz instability (37). But the system which possesses complex characteristics exhibits unphysical and unbounded instabilities in the short-wavelength limit. One of the reasons for this behavior lies in the choice that the interfacial pressure is spatially constant and equal to the bulk pressure. This choice leads to an equation set with all real characteristics when the two fluid velocities are equal. The spatial interfacial pressure distribution may be accounted for by the implementation of the virtual mass term and that motivated the present study.

4.4 Characteristic and Stability Analysis of the Two-Fluid Model

The effect of virtual mass on the characteristics can be illustrated by adding the virtual mass terms to the one-dimensional momentum equations of both liquid and vapor. Here Drew's model (33,38) for the virtual mass terms is considered.

The conservation equations for one dimensional flow are as follows:

Conservation of vapor mass:

$$\frac{\partial}{\partial t}(\alpha_v \rho_v) + \frac{\partial}{\partial z}(\alpha_v \rho_v V_v) = \Gamma \tag{4.15}$$

Conservation of liquid mass:

$$\frac{\partial}{\partial t}(\alpha_\ell \rho_\ell) + \frac{\partial}{\partial z}(\alpha_\ell \rho_\ell V_\ell) = -\Gamma \tag{4.16}$$

Conservation of vapor momentum:

$$\alpha_v \rho_v \frac{\partial V_v}{\partial t} + \alpha_v \rho_v V_v \frac{\partial V_v}{\partial z}$$

$$= \Gamma(V_i - V_v) - \alpha_v \frac{\partial P}{\partial z} - [F_s + F_v] - \alpha_v \rho_v g - F_{wv}, \tag{4.17}$$

where V_i, F_s, F_v and F_{wv} are the interfacial velocity, the standard drag force, the virtual mass force, and the vapor wall friction force, per unit volume, respectively, and F_s and, F_v are defined as follows:

$$F_s = K(V_v - V_\ell) \tag{4.18}$$

$$F_v = \alpha_v \rho_\ell C_v \left\{ \frac{\partial V_v}{\partial t} - \frac{\partial V_\ell}{\partial t} + V_v \frac{\partial}{\partial z}(V_v - V_\ell) + (V_v - V_\ell)\left[(\lambda - 2)\frac{\partial V_v}{\partial z} + (1 - \lambda)\frac{\partial V_\ell}{\partial z}\right] \right\} \tag{4.19}$$

Conservation of liquid momentum

$$\alpha_\ell \rho_\ell \frac{\partial V_\ell}{\partial t} + \alpha_\ell \rho_\ell V_\ell \frac{\partial V_\ell}{\partial z} = \Gamma(V_\ell - V_i) - \alpha_\ell \frac{\partial P}{\partial z} + [F_s + F_v] - \alpha_\ell \rho_\ell g - F_{w\ell}, \tag{4.20}$$

where $F_{w\ell}$ is the liquid wall friction force per unit volume.

For convenience by summing up Eq (4.17) and Eq (4.20), we get the momentum equation:

$$\alpha_v\rho_v \frac{\partial V_v}{\partial t} + \alpha_\ell\rho_\ell \frac{\partial V_\ell}{\partial t} + \alpha_v\rho_v V_v \frac{\partial V_v}{\partial z} + \alpha_\ell\rho_\ell V_\ell \frac{\partial V_\ell}{\partial z}$$

$$= \Gamma(V_\ell - V_v) - \frac{\partial P}{\partial z} - (\alpha_v\rho_v + \alpha_\ell\rho_\ell)\, g - (F_{wv} + F_{w\ell}) \qquad (4.21)$$

By multiplying Eq (4.17) by α_ℓ and Eq (4.20) by α_v and then subtracting the first term from the second term, we obtain:

$$\alpha_v(\alpha_\ell\rho_v + \rho_\ell C_v) \frac{\partial V_v}{\partial t} - \alpha_v(\alpha_\ell\rho_\ell + \rho_\ell C_v) \frac{\partial V_\ell}{\partial t}$$

$$+ \{[\alpha_\ell\alpha_v\rho_v + \alpha_v\rho_\ell C_v(\lambda - 1)]\, V_v - \alpha_v\rho_\ell\, C_v(\lambda - 2)V_\ell\} \frac{\partial V_v}{\partial z} \qquad (4.22)$$

$$- \{[\alpha_\ell\alpha_v\rho_\ell + \alpha_v\rho_\ell C_v(1 - \lambda)]\, V_\ell + \alpha_v\rho_\ell\, C_v\, \lambda V_v\} \frac{\partial V_\ell}{\partial z}$$

$$= \Gamma(V_i - \alpha_v V_\ell - \alpha_\ell V_v) - F_s + \alpha_\ell\alpha_v(\rho_\ell - \rho_v)g - \alpha_\ell F_{wv} + \alpha_v F_{w\ell}$$

Conservation of vapor energy:

$$\frac{\partial}{\partial t}(\alpha_v\rho_v e_v) + \frac{\partial}{\partial z}(\alpha_v\rho_v e_v V_v) + P\frac{\partial}{\partial z}(\alpha_v V_v) + P\frac{\partial \alpha_v}{\partial t} = Q_{wv} + Q_i\,, \qquad (4.23)$$

where Q_{wv} and Q_i are the heat transfer per unit volume from wall to vapor and from the interface, respectively.

Conservation of liquid energy:

$$\frac{\partial}{\partial t}(\alpha_\ell\rho_\ell e_\ell) + \frac{\partial}{\partial z}(\alpha_\ell\rho_\ell e_\ell V_\ell) + P\frac{\partial}{\partial z}(\alpha_\ell V_\ell) - P\frac{\partial \alpha_v}{\partial t} = Q_{w\ell} - Q_i, \qquad (4.24)$$

where $Q_{w\ell}$ is the heat transfer per unit volume from wall to liquid.

The above conservation equations can be put together in the following matrix form:

$$A(x)\,\frac{\partial x}{\partial t} + B(x)\,\frac{\partial x}{\partial z} + C(x) = 0, \tag{4.25}$$

where x is a column vector of independent variables:

$$x = (\alpha, P, V_v, V_\ell, e_v, e_\ell)^T$$

It is assumed that the density of both liquid and vapor is a function of pressure. Vapor and liquid densities with spatial and time derivatives can be expressed in terms of pressure by using the following definitions of the sound velocities of vapor and liquid:

$$a_v^{-2} = \left(\frac{\partial \rho_v}{\partial P}\right)_P \quad , \quad a_\ell^{-2} = \left(\frac{\partial \rho_\ell}{\partial P}\right)_P$$

Then, the matrices of A(x) and B(x) in Eq (4.25) can be constructed as follows:

$$A = \begin{bmatrix} \rho_v & \alpha_v a_v^{-2} & & & & \\ -\rho_\ell & \alpha_\ell a_\ell^{-2} & & & & \\ & & \alpha_v \rho_v & \alpha_\ell \rho_\ell & & \\ & & \alpha_\ell \rho_v + \rho_\ell C_v & -\alpha_\ell \rho_\ell - \rho_\ell C_v & & \\ \rho_v e_v + P & \alpha_v e_v a_v^{-2} & & & \alpha_v \rho_v & \\ -\rho_\ell e_\ell - P & \alpha_\ell \rho_\ell a_\ell^{-2} & & & & \alpha_\ell \rho_\ell \end{bmatrix} \tag{4.26}$$

$$B = \begin{bmatrix} \rho_v V_v & \alpha_v V_v a_v^{-2} & \alpha_v \rho_v & & \\ -\rho_\ell V_\ell & \alpha_\ell V_\ell a_\ell^{-2} & & \alpha_\ell \rho_\ell & \\ & 1 & \alpha_v \rho_v V_v & \alpha_\ell \rho_\ell V_\ell & \\ & & \begin{matrix}[\alpha_\ell \rho_v + \rho_\ell C_v \\ (\lambda-1)] V_v \\ -\rho_\ell C_v (\lambda-2) V_\ell\end{matrix} & \begin{matrix}-[(1-\alpha)\rho_\ell + \rho_\ell \\ C_v (1-\lambda)] V_\ell \\ -\rho_\ell C_v V_v \lambda\end{matrix} & \\ \begin{matrix}\rho_v e_v V_v \\ + P V_v\end{matrix} & \alpha_v e_v V_v a_v^{-2} & \alpha_v \rho_v e_v + P \alpha_v & & \alpha_v \rho_v \quad V_v \\ \begin{matrix}-\rho_\ell e_\ell V_\ell \\ - P V_\ell\end{matrix} & (\alpha_\ell) e_\ell V_\ell a_\ell^{-2} & & \alpha_\ell \rho_\ell e_\ell - \alpha_v P & \alpha_\ell \rho_\ell V_\ell \end{bmatrix} \tag{4.27}$$

In the same way as Eq (4.9) the characteristics μ of Eq (4.25) is defined by the following equation;

$$\text{Det}\ (\mu A - B) = 0 \tag{4.28}$$

Reducing the terms related to the energy equations from Eq (4.28), we get

$$\alpha_v\rho_v(\mu - V_v) \times \alpha_\ell\rho_\ell(\mu - V_\ell) \times$$

$$\text{Det}\begin{bmatrix} \rho_v(\mu - V_v) & \alpha_v a_v^{-2}(\mu - V_v) & -\alpha_v\rho_v & 0 \\ -\rho_\ell(\mu - V_\ell) & \alpha_\ell a_\ell^{-2}(\mu - V_\ell) & 0 & -\alpha_\ell\rho_\ell \\ 0 & -1 & \alpha_v\rho_v(\mu - V_v) & \alpha_\ell\rho_\ell(\mu - V_\ell) \\ 0 & 0 & (\alpha_\ell\rho_v + \rho_\ell C_v)(\mu - V_v) & -(\alpha_\ell\rho_\ell + \rho_\ell C_v)(\mu - V_\ell) \\ & & -\rho_\ell C_v(\lambda - 2)(V_v - V_\ell) & +\rho_\ell C_v\lambda(V_v - V_\ell) \end{bmatrix} = 0 \tag{4.29}$$

From the terms related to the energy equations we obtained $\mu = V_v, V_\ell$. Physically this means that energy is transferred only by convection.

For simplicity we assume that $a_v >> V_v$ and $a_\ell >> V_\ell$. Then, we can neglect

$$\alpha_\ell a_\ell^{-2}(\mu - V_\ell) \text{ and } \alpha_v a_v^{-2}(\mu - V_v)$$

These terms are related to the sonic velocities transferred through liquid and vapor. Now we get the simplified

determinant form

$$\mathrm{Det}\begin{bmatrix} \rho_v(\mu-V_v) & -\alpha_v\rho_v & 0 \\ -\rho_\ell(\mu-V_\ell) & 0 & -\alpha_\ell\rho_\ell \\ 0 & \begin{matrix}(\alpha_\ell\rho_v+\rho_\ell C_v)(\mu-V_v) \\ -\rho_\ell C_v(\lambda-2)(V_v-V_\ell)\end{matrix} & \begin{matrix}-(\alpha_\ell\rho_\ell+\rho_\ell C_v)(\mu-V_\ell) \\ +\rho_\ell C_v\lambda\ (V_v-V_\ell)\end{matrix} \end{bmatrix} = 0 \tag{4.30}$$

From Eq (4.30) we obtain an algebraic equation of the form

$$aq^2 + bq + c = 0, \tag{4.31}$$

where $a = \alpha_\ell^{\ 2}\ \rho_v + \alpha_v\alpha_\ell\rho_\ell + \gamma$

$b = [\gamma(2-\lambda) + 2\alpha_v\alpha_\ell\rho_\ell]V_r$

$c = [\alpha_v\alpha_\ell\rho_\ell + \alpha_v\ \gamma(1-\lambda)]V_r^{\ 2}$

$\gamma = \rho_\ell C_v$

$q = \mu - V_v$

$V_r = V_v - V_\ell$

In order for Eq (4.31) to have real and distinct

characteristics, the following must be satisfied;

$$b^2 - 4ac = [\gamma^2(\lambda^2 + 4(1-\lambda)\alpha_\ell) + 4\gamma(1-\lambda)\alpha_v\alpha_\ell^2(\rho_\ell - \rho_v)$$

$$-4\alpha_v\alpha_\ell^3\ \rho_v\rho_\ell]\ V_r^2 > 0 \qquad (4.32)$$

Now, let us consider special cases;

i) There is no virtual mass; $C_v = 0$ and hence $\gamma = 0$

Then,

$$b^2 - 4ac = -4\alpha_v\alpha_\ell^3\ \rho_v\rho_\ell$$

Therefore, the system with no virtual mass always has two complex characteristics except in the single phase region ($\alpha_v = 0$ or $\alpha_\ell = 0$)

ii) If $\alpha_v \to 0$, then $b^2 - 4ac = \gamma^2(\lambda-2)^2$.

Therefore, if $C_v \neq 0$ and $\lambda \neq 2$, then

$$\lim_{\alpha_v \to 0} (b^2 - 4ac) > 0$$

iii) If $\alpha_\ell \to 0$, then $b^2 - 4ac = \gamma^2\lambda^2$

Therefore, if $C_v \neq 0$ and $\lambda \neq 0$, then

$$\lim_{\alpha_\ell \to 0} (b^2 - 4ac) > 0$$

iv) If $\lambda = 1$, then $b^2 - 4ac = \gamma^2 - 4\ \alpha_v\alpha_\ell^3\rho_v\rho_\ell$.

Therefore,

$$\text{if } C_v > \sqrt{\frac{4\alpha_v\alpha_\ell^3\ \rho_v}{\rho_\ell}}\ , \text{ then } b^2 - 4ac > 0$$

v) If $0 \leq \lambda < 1$, then

$$C_v^2 \; [\lambda^2 + 4(1-\lambda)\alpha_\ell] + 4\alpha_v\alpha_\ell^2\gamma(1-\lambda)(1-\frac{\rho_v}{\rho_\ell})$$

$$> 4 \; \alpha_v\alpha_\ell^3 \frac{\rho_v}{\rho_\ell} \; . \qquad (4.33)$$

Therefore, if $(C_v\lambda) > \sqrt{4\alpha_v\alpha_\ell^3 \frac{\rho_v}{\rho_\ell}}$, then $b^2 - 4ac > 0$. This relationship is drawn in Fig. 4.2.

vi) If $1 < \lambda < 2$, then

$$C_v^2(\lambda-2)^2 - 4\alpha_v\alpha_\ell^2 C_v > 4\alpha_v\alpha_\ell^3 \frac{\rho_v}{\rho_\ell} \; .$$

Therefore, if $[C_v(\lambda-2)]^2 > 4\alpha_v\alpha_\ell^2 \; [C_v + \alpha_\ell \frac{\rho_v}{\rho_\ell}]$

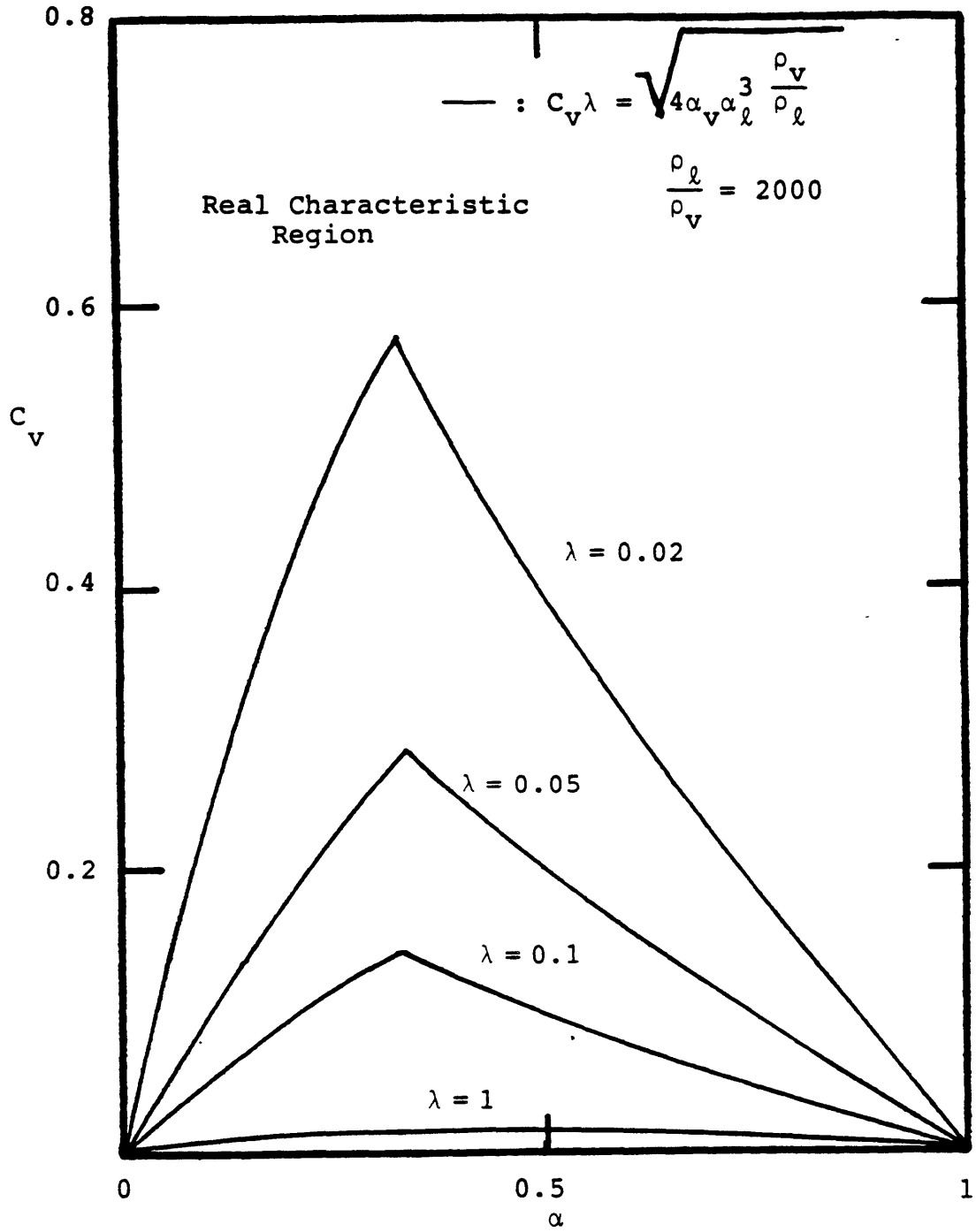

Fig. 4.2: Characteristics Map with Real Characteristics for Given Values of λ

The effect of virtual mass on stability can be simply illustrated by using the characteristics analysis. If the mass exchange rate, standard drag force, wall friction, and the energy equations are neglected in order to clearly know the effect of virtual mass on stability, D in Eq (4.14) reduced to zero.

As shown μ in Section 4.3, if D = 0, the characteristics μ in Eq (4.9) become equal to w/k in Eq (4.14)

$$w = k\,\mu \tag{4.34}$$

Then, when the conditions for all real characteristics are satisfied, we have all real values, w. As all real values, w satisfy the stability condition, $Im(w) \leq 0$ for all values w, the stability condition is equivalent to the condition for real and distinctive characteristics, Eq (4.32).

4.5 Numerical Stability

Here we examine the numerical stability of the equation system including virtual mass. We form the difference scheme in a similar way to the THERMIT (17). For the same reason as in the stability analysis, the mass exchange rate, standard drag force, and wall friction are neglected. Also the energy equations are dropped because they only represent convective properties as we found in the preceeding characteristic analysis

vapor mass

$$\frac{(\alpha_v\rho_v)_j^{n+1} - (\alpha_v\rho_v)_j^n}{\Delta t} + \frac{1}{\Delta z}\left[(\alpha_v^n\rho_v^n\, V_v^{n+1})_{j+1/2} - (\alpha_v^n\rho_v^n\, V_v^{n+1})_{j-1/2}\right] = 0 \tag{4.35}$$

liquid mass

$$\frac{(\alpha_\ell\rho_\ell)_j^{n+1} - (\alpha_\ell\rho_\ell)_j^n}{\Delta t} + \frac{1}{\Delta z}\left[(\alpha_\ell^n\rho_\ell^n\, V_\ell^{n+1})_{j+1/2} - (\alpha_\ell^n\rho_\ell^n\, V_\ell^{n+1})_{j-1/2}\right] = 0 \tag{4.36}$$

momentum equations

$$(\alpha_v\rho_v)^n \frac{(V_v^{n+1} - V_v^n)_{j+1/2}}{\Delta t} + (\alpha_\ell\rho_\ell)^n \frac{(V_\ell^{n+1} - V_\ell^n)_{j+1/2}}{\Delta t} + (\alpha_v\rho_v V_v \frac{\Delta V_v}{\Delta z})_{j+1/2}^n$$

$$+ (\alpha_\ell\rho_\ell V_\ell \frac{\Delta V_\ell}{\Delta z})_{j+1/2}^n + \frac{(P_{j+1} - P_j)^{n+1}}{\Delta z} = 0 \tag{4.37}$$

$$\alpha_v^n\,[\alpha_\ell\rho_v + \rho_\ell C_v]^n \frac{(V_v^{n+1} - V_v^n)_{j+1/2}}{\Delta t} - \alpha_v^n\,[\alpha_\ell\rho_\ell + \rho_\ell C_v]^n \frac{(V_\ell^{n+1} - V_\ell^n)_{j+1/2}}{\Delta t}$$

$$+ \{<\alpha_\ell\alpha_v\rho_v + \alpha_v\rho_\ell C_v(\lambda-1)]V_v - \alpha_v\rho_\ell C_v(\lambda-2)V_\ell> \frac{\Delta V_v}{\Delta z}$$

$$- <[\alpha_\ell\alpha_v\rho_\ell + \alpha_v\rho_\ell C_v(1-\lambda)]V_\ell + \alpha_v\rho_\ell C_v\lambda V_v> \frac{\Delta V_\ell}{\Delta z}\}_{j+1/2}^n = 0 \tag{4.38}$$

The above numerical scheme can be modified as follows:

vapor mass

$$\rho_{vj}^{n+1}\,(\alpha_v^{n+1}-\alpha_v^n)_j+\alpha_{vj}^n\,(\rho_v^{n+1}-\rho_v^n)_j+\frac{\Delta t}{\Delta z}\,[\rho_{vj}^n\,V_{vj+1/2}^{n+1}$$

$$(\alpha_{vj}^n-\alpha_{vj-1}^n)+\alpha_{vj-1}^n\,V_{vj+1/2}^{n+1}\,(\rho_{vj}^n-\rho_{vj-1}^n)$$

$$+\,\alpha_{vj-1}^n\,\rho_{vj-1}^n\,(V_{vj+1/2}^{n+1}-V_{vj-1/2}^{n+1})]=0 \qquad (4.39)$$

liquid mass

Same as Eq. (4.39) with α_v replaced by α_ℓ, subscript v by ℓ.

(4.40)

momentum equations

$$(\alpha_v\rho_v)^n\,(V_v^{n+1}-V_v^n)_j+(\alpha_\ell\rho_\ell)^n\,(V_\ell^{n+1}-V_\ell^n)_j$$

$$+\frac{\Delta t}{\Delta z}\,[(\alpha_v\rho_v V_v)^n\,(V_{v_j}-V_{v_{j-1}})^n+(\alpha_\ell\rho_\ell V_\ell)^n\,(V_{\ell_j}-V_{\ell_{j-1}})^n$$

$$+\,(P_{j+1/2}-P_{j-1/2})^{n+1}]=0 \qquad (4.41)$$

$$[\alpha_\ell\rho_v+\rho_\ell C_v]^n\,(V_v^{n+1}-V_v^n)_j-[\alpha_\ell\rho_\ell+\rho_\ell C_v]^n\,(V_\ell^{n+1}-V_\ell^n)_j$$

$$+\,\{<[\alpha_\ell\rho_v+\rho_\ell C_v(\lambda-1)]V_v-\rho_\ell C_v(\lambda-2)V_\ell>\frac{\Delta t}{\Delta z}\,(V_{vj}-V_{vj-1})$$

$$-\,<[\alpha_\ell\rho_\ell+\rho_\ell C_v(1-\lambda)]V_\ell+\rho_\ell C_v\lambda V_v>\frac{\Delta t}{\Delta z}\,(V_{\ell j}-V_{\ell j-1})>\}^n$$

$$=0 \qquad (4.42)$$

Treating the coefficients as constants and using Von Neumann local stability analysis, $U_j^n = \zeta^n \exp(ikj\Delta z)$, we obtain the determinant form for a nontrivial solution.

$$\mathrm{Det}\begin{bmatrix} \rho_v(\zeta-1+\tilde{V}_v) & a_v^{-2}\alpha_v(\zeta-1+\tilde{V}_v) & \alpha_v\rho_v\zeta q & 0 \\ -\rho_\ell(\zeta-1+\tilde{V}_\ell) & a_\ell^{-2}\alpha_\ell(\zeta-1+\tilde{V}_\ell) & 0 & \alpha_\ell\rho_\ell\,\zeta q \\ 0 & \zeta q & \alpha_v\rho_v(\zeta-1+\tilde{V}_v) & \alpha_\ell\rho_\ell(\zeta-1+\tilde{V}_\ell) \\ 0 & 0 & \begin{array}{l}(\alpha_\ell\rho_v+\rho_\ell C_v)(\zeta-1) \\ +\{[\alpha_\ell\rho_v+\rho_\ell C_v(\zeta-1)]\tilde{V}_v \\ -\rho_\ell C_v(\lambda-2)\,\tilde{V}_\ell\}\end{array} & \begin{array}{l}-(\alpha_\ell\rho_\ell+\rho_\ell C_v)(\zeta-1) \\ -\{(\alpha_\ell\rho_\ell+\rho_\ell C_v(1-\lambda)]\tilde{V}_\ell \\ +\rho_\ell C_v\lambda\tilde{V}_v\}\end{array} \end{bmatrix} = 0 \tag{4.43}$$

where $\tilde{V}_v = \frac{\Delta t}{\Delta z} V_v(1-\exp(-ik\Delta z))$

$\tilde{V}_\ell = \frac{\Delta t}{\Delta z} V_\ell(1-\exp(-ik\Delta z))$

$q = 2i\,\frac{\Delta t}{\Delta z}\sin\left(\frac{k\Delta z}{2}\right)$

$k = \frac{\pi}{n\Delta z}$: $n=1\sim J$:J: the number of axial mesh

For simplicity we assume in the same way as in the previous analysis that $a_v \gg V_v$, $a_\ell \gg V_\ell$

Then the determinant reduces to the 3 x 3 determinant

$$\mathrm{Det}\begin{bmatrix} \rho_v(\zeta-1+\tilde{V}_v) & \alpha_v\rho_v\,\zeta q & 0 \\ -\rho_\ell(\zeta-1+\tilde{V}_v) & 0 & \alpha_\ell\rho_\ell\zeta q \\ 0 & \begin{array}{l}(\alpha_\ell\rho_v+\rho_\ell C_v)(\zeta-1+\tilde{V}_v) \\ +\rho_\ell C_v(\lambda-2)(\tilde{V}_v-\tilde{V}_\ell)\end{array} & \begin{array}{l}-(\alpha_\ell\rho_\ell+\rho_\ell C_v)(\zeta-1+\tilde{V}_\ell) \\ -\rho_\ell C_v\lambda(\tilde{V}_v-\tilde{V}_\ell)\end{array} \end{bmatrix} = 0 \tag{4.44}$$

As we notice that ζq appears as a common coefficient, resolving the determinant we obtain the modified determinant

$$\mathrm{Det}\begin{bmatrix} \rho_v(\mu-\tilde{V}_v) & -\alpha_v\rho_v & 0 \\ -\rho_\ell(\mu-\tilde{V}_\ell) & 0 & -\alpha_\ell\rho_\ell \\ 0 & \begin{matrix}(\alpha_\ell\rho_v+\rho_\ell C_v)(\mu-\tilde{V}_v) \\ -\rho_\ell C_v(\lambda-2)(\tilde{V}_v-\tilde{V}_\ell)\end{matrix} & \begin{matrix}-(\alpha_\ell\rho_\ell+\rho_\ell C_v)(\mu-\tilde{V}_\ell) \\ +\rho_\ell C_v\lambda(\tilde{V}_v-\tilde{V}_\ell)\end{matrix} \end{bmatrix} = 0 \qquad (4.45)$$

where $\mu = -(\zeta-1)$

The above determinant, Eq (4.45) is in the exact same form as Eq (4.30). Therefore we can use Eq (4.31) as follows:

$$aq^2 + b\tilde{V}_r q + c\tilde{V}_r^2 = 0 \quad , \qquad (4.46)$$

where $a = \alpha_\ell^2\,\rho_v + \alpha_v\alpha_\ell\rho_\ell + \rho_\ell C_v$

$b = \rho_\ell C_v(2-\lambda) + 2\alpha_v\alpha_\ell\rho_\ell$

$c = \alpha_v\alpha_\ell\rho_\ell + \alpha_v\rho_\ell C_v(1-\lambda)$

$q = \mu - \tilde{V}_v$

$\tilde{V}_r = \tilde{V}_v - \tilde{V}_\ell$

For the numerical stability the absolute value of the growth factor, $|\zeta|$,must be less than 1. From Eq (4.46)

$$q = \frac{-b \pm \sqrt{b^2-4ac}}{2a} \tilde{V}_r \tag{4.47}$$

From Eq(4.47) and the relationship $\mu = -(\zeta-1)$, we have

$$\zeta-1 = -\left[1 + \frac{(-b \pm \sqrt{b^2-4ac})(\tilde{V}_v - \tilde{V}_\ell)}{2a}\right], \tag{4.48}$$

where $\zeta-1 = -\mu = -(V_v + q)$ (4.49)

Assuming that $\lambda = 1$ and $C_v^2 >> 4\alpha_v\alpha_\ell^3 \rho_v/\rho_\ell$, each root in Eq (4.48) can be simplified separatively as follows:

i) For the root with $+\sqrt{b^2-4ac}$ in Eq (4.48), we have

$$\begin{aligned} 0 &< (\alpha_\ell^2\rho_v + \rho_\ell C_v)\frac{\Delta t}{\Delta z} V_v + (\alpha_v\alpha_\ell\rho_\ell)\frac{\Delta t}{\Delta z} V_\ell \\ &< (\alpha_\ell^2\rho_v + \rho_\ell C_v + \alpha_v\alpha_\ell\rho_\ell) \\ &= -p + p\exp(-ik\Delta z) , \end{aligned} \tag{4.50}$$

where $$p = \frac{(\alpha_\ell^2\rho_v + \rho_\ell C_v)\frac{\Delta t}{\Delta z} V_v + (\alpha_v\alpha_\ell\rho_\ell)\frac{\Delta t}{\Delta z} V_\ell}{\alpha_\ell^2\rho_v + \alpha_v\alpha_\ell\rho_\ell + \rho_\ell C_v}$$

Fig (4.3) shows the stability region derived from Eq (4.50). For the numerical stability p in Eq (4.50) must satisfy the condition, $0 < p < 1$. From the above stability condition we have

$$\zeta-1 = -\frac{(\alpha_\ell^2\rho_v + \rho_\ell C_v)\tilde{V}_v + (\alpha_v\alpha_\ell\rho_\ell)\tilde{V}_\ell}{\alpha_\ell^2\rho_v + \alpha_v\alpha_\ell\rho_\ell + \rho_\ell C_v} \tag{4.51}$$

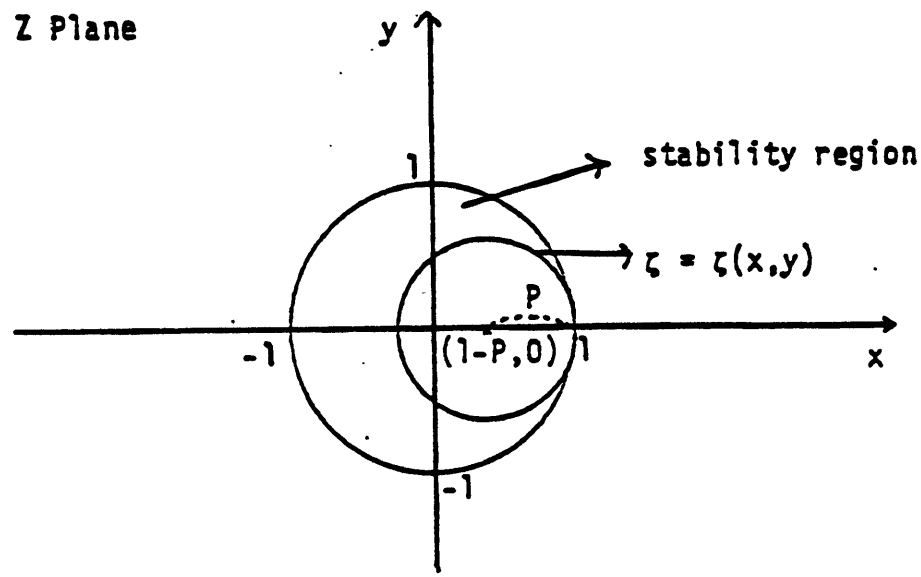

Fig. 4.3: Stability Diagram of Eq. (4.50)

If $\frac{\Delta t}{\Delta z} V_v < 1$ and $\frac{\Delta t}{\Delta z} V_\ell < 1$, the above condition is always met. ii) For the root with $-\sqrt{b^2-4ac}$ in Eq (4.48), we have

$$\zeta - 1 = -\left[\frac{(\alpha_\ell^2 \rho_v) \frac{\Delta t}{\Delta z} \tilde{V}_v + (\rho_\ell C_v + \alpha_v \alpha_\ell \rho_\ell) \frac{\Delta t}{\Delta z} \tilde{V}_\ell}{\alpha_\ell^2 \rho_v + \rho_\ell C_v + \alpha_v \alpha_\ell \rho_\ell}\right] \tag{4.52}$$

$$= -r + r \exp(-ik\Delta z) ,$$

where $r = \dfrac{(\alpha_\ell^2 \rho_v) \frac{\Delta t}{\Delta z} V_v + (\rho_\ell C_v + \alpha_v \alpha_\ell \rho_\ell) \frac{\Delta t}{\Delta z} V_\ell}{\alpha_\ell^2 \rho_v + \rho_\ell C_v + \alpha_v \alpha_\ell \rho_\ell}$.

For the numerical stability, r in Eq (4.52) must satisfy the condition, $0 < r < 1$. The above condition is equivalent to the following inequality;

$$0 < (\alpha_\ell^2 \rho_v) \frac{\Delta t}{\Delta z} V_v + (\rho_\ell C_v + \alpha_v \alpha_\ell \rho_\ell) \frac{\Delta t}{\Delta z} V_\ell$$

$$< (\alpha_\ell^2 \rho_v + \rho_\ell C_v + \alpha_v \alpha_\ell \rho_\ell) \tag{4.53}$$

Also, if $\frac{\Delta t}{\Delta z} V_v < 1$ and $\frac{\Delta t}{\Delta z} V_\ell < 1$, the above inequality is always met.

Therefore, it can be concluded that, if $\lambda = 1$ and $C_v > \sqrt{4\alpha_v \alpha_\ell^3 \rho_v/\rho_\ell}$, the finite difference scheme is restricted only by the convective stability conditions.

4.6 Application of the Second Law of Thermodynamics to Drew's Virtual Mass

Drew et al. (38) derived a constitutive equation for virtual mass by applying the general principles such as coordinate invariance and objectivity to the two-phase flow situation. It was found that their virtual mass model is consistent with any combination of material acceleration first order derivative terms. However, it was found that their neglect of the Second Law of Thermodynamics may lead to violation of this important and universal law. Although Drew and Lahey (39) tried a general approach to give a meaningful quantitative result for the second law implications, complexities involved in the problem made it impossible. Here, a simple procedure is suggested to obtain a quantitative range of the viable form of the virtual mass term.

Ishii (18) has shown that the average rate of production of entropy at the interface is given by,

$$\begin{aligned}\Delta S = \Gamma \Bigg\{ & T_v \left[h_{vi} \left(\frac{1}{T_v} - \frac{1}{T_i} \right) - \left(\frac{g_v}{T_v} - \frac{g_{vi}}{T_i} \right) \right. \\ & \left. - T_\ell \left[h_{\ell i} \left(\frac{1}{T_\ell} - \frac{1}{T_i} \right) - \left(\frac{g_\ell}{T_\ell} - \frac{g_{\ell i}}{T_i} \right) \right] \right] \Bigg\} \\ & + \sum_{k=1}^{2} \frac{q''_{ki}}{L_a} \left(1 - \frac{T_k}{T_i} \right) \\ & + F_i \cdot [V_v - V_\ell + (V_{vi} - V_{\ell i})] \end{aligned} \tag{4.54}$$

where ΔS is the volumetric rate of production of entropy at the interface, Γ is the volumetric vapor generation rate, T_k is the average temperature, h_{ki} is the

interfacial enthalpy of phase-k, g_k is the Gibbs free energy of phase-k, q''_{ki} is the interfacial heat flux to phase-k, $\frac{1}{L_a}$ is the interfacial area density, V_k is the average velocity of phase-k, and F_i is the volumetric interfacial drag force on the liquid phase. For the purpose of this thesis isothermal flow without phase change and a no slip condition at the interface are assumed. Then, we obtain the result that the volumetric interfacial mechanical dissipation rate is non-negative;

$$\Delta S = F_i \cdot (V_v - V_\ell) \geq 0 \tag{4.55}$$

The physical meaning of Eq(4.54) is that, if $V_v > V_\ell$,the interfacial drag force should be transfered from vapor to liquid in order to satisfy the condition of non-negative entropy production. Taking the standard drag force and Drew's virtual mass force for volumetric interfacial drag force, we obtain

$$F_i = F_s + F_v \tag{4.56}$$

Refer to Eqs (4.18) and (4.19) for F_s and F_v . Here C_v is the coefficient of virtual mass, and λ is the arbitrary coefficient but must be given in order to satisfy Eq (4.55). F_i is always positive, that is, a dissipation term.

For simplicity we assume steady state, one-dimensional and incompressible two-phase flow.

Continuity equation

$$\frac{\partial V_v}{\partial z} = -\frac{V_v}{\alpha_v}\frac{\partial \alpha_v}{\partial z} \tag{4.57}$$

$$\frac{\partial V_\ell}{\partial z} = -\frac{V_\ell}{\alpha_\ell}\frac{\partial \alpha_\ell}{\partial z} \tag{4.58}$$

Momentum equation

$$\alpha_v \rho_v V_v \frac{\partial V_v}{\partial z} = -\alpha_v \frac{\partial P}{\partial z} - F_i - \alpha_v \rho_v g \tag{4.59}$$

$$\alpha_\ell \rho_\ell V_\ell \frac{\partial V_\ell}{\partial z} = -\alpha_\ell \frac{\partial P}{\partial z} + F_i - \alpha_\ell \rho_\ell g - F_{w\ell} \tag{4.60}$$

Multiplying Eq (4.59) by α_ℓ and Eq (4.60) by α_v , and then subtracting each other, we get the equation

$$F_i = \alpha_\ell(\rho_\ell V_\ell \frac{\partial V_\ell}{\partial z} - \rho_v V_v \frac{\partial V_v}{\partial z}) + \alpha_v \alpha_\ell (\rho_\ell - \rho_v) g + \alpha_v F_{w\ell} \tag{4.61}$$

Using the continuity equations we obtain

$$F_i = \alpha_\ell\left(\frac{\rho_\ell V_\ell^2}{\alpha_\ell} + \frac{\rho_v V_v^2}{\alpha_v}\right)\frac{\partial \alpha_v}{\partial z} + \alpha_v \alpha_\ell (\rho_\ell - \rho_v) g + \alpha_v F_{w\ell} \tag{4.62}$$

First we take the case, $V_v \geq V_\ell \geq 0$

i) If $\frac{\partial \alpha_v}{\partial z} > 0$,

F_i always satisfies the Second Law because $\left(\frac{\rho_\ell V_\ell^2}{\alpha_\ell} + \frac{\rho_v V_v^2}{\alpha_v}\right) > 0$

ii) If $\frac{\partial \alpha_v}{\partial z} < 0$, it is not clear whether F_i is non-negative or negative. Therefore, we have to assure that $F_i > 0$ in the case of $V_v > V_\ell > 0$ and $\frac{\partial \alpha_v}{\partial z} > 0$. Being used Eq (4.59) and (4.60), Eq (4.56) becomes the equation

$$F_i = K(V_v - V_\ell) - \frac{\rho_\ell C_v}{\alpha_\ell}\left[V_v V_\ell(\alpha_v + \alpha_\ell) + (\lambda - 1)(V_v - V_\ell) + (\alpha_\ell V_v + \alpha_v V_\ell)\right]\frac{\partial \alpha_v}{\partial z} \geq 0 \tag{4.63}$$

In order to satisfy the inequality, Eq (4.63) in case of $V_v > V_\ell > 0$, $C_v > 0$ and $\frac{\partial \alpha_v}{\partial z} < 0$, we simply obtain the inequality,

$$V_v V_\ell (\alpha_v + \alpha_\ell) + (\lambda - 1)(V_v - V_\ell)(\alpha_\ell V_v + \alpha_v V_\ell) \geq 0 \qquad (4.64)$$

Notice that we obtain the same result as Eq (4.63) in case of $V_\ell > V_v > 0$ and $C_v \geq 0$.

If $V_v = V_\ell$, then $V_v^2 (\alpha_v + \alpha_\ell) \geq 0$

If $\alpha_v \to 0$, $\lambda \geq 1 - \frac{V_\ell}{V_v}$

If $\alpha_v \to 1$, $\lambda \geq \frac{V_\ell}{V_v}$

In a general case

$$\lambda \geq 1 - \frac{s}{(s-1)(\alpha_\ell s + \alpha_v)} \quad , \qquad (4.65)$$

where s is a slip ratio, $\frac{V_v}{V_\ell}$

Fig 4.4 shows that the range of λ based on Eq (4.65) to satisfy $\Delta S \geq 0$. Conservatively, λ is set as 1 in the THERMIT-6S. In conclusion, in order to satisfy the Second Law, λ must be specified within the range of the inequality, Eq (4.65).

4.7 Numerical Results and Discussion

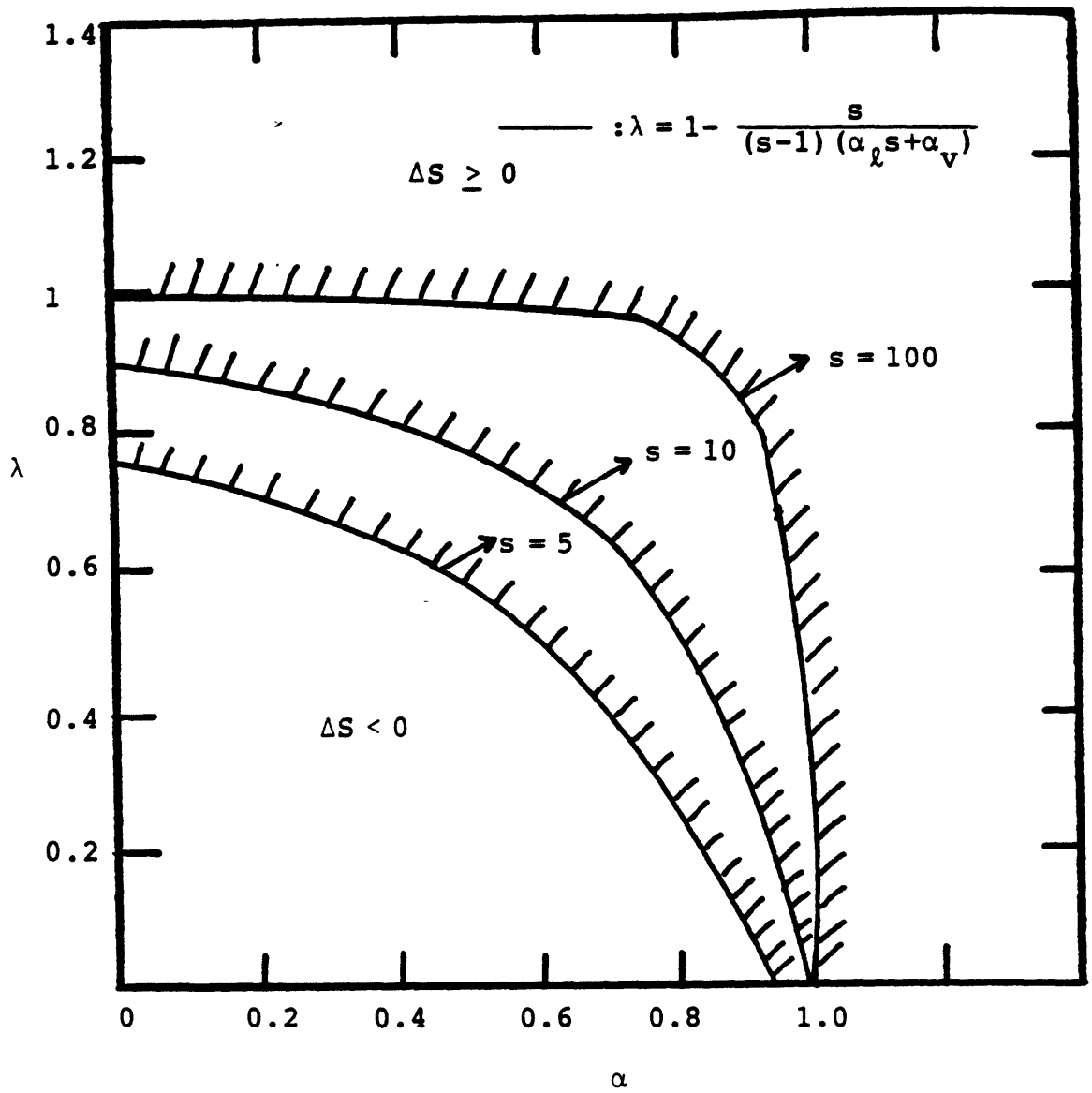

Fig. 4.4: Restriction on λ to Insure that $\Delta S \geq 0$ for Interfacial Momentum Exchange

An one-dimensional numerical simulation is performed by the THERMIT-6S code containing the stated virtual mass model. For the numerical simulation the geometry of the THORS test (40) and the same axial mesh size, 4" are used in order to see the effects of virtual mass on the numerical stability in the real geometry. No mass exchange and no heat transfer, but wall friction and interfacial friction are included in the computation.

Initially, a constant pressure difference between the inlet and outlet is applied to the stagnant two-phase mixture of sodium with constant void fraction along the channel. Physically, it may be expected that vapor velocities are nearly linealy accelerated with time as Hancox et al.'s results (41) showed.

Their studies involved the acceleration from rest of a stratified steam-water mixture with a constant pressure difference between the inlet and outlet. Their simulation was done with wall heat and momentum transfer, and interfacial mass, heat, and momentum transfer set to zero. The steam velocities were obtained with 8, 16, 32, 64, and 128 equal mesh sizes. The steam velocity transients showed no indication of solution instability but linearly accelerated vapor velocities with time. However, when 128 space increments were used, the oscillation of rapidly increasing amplitude developed.

The present analysis illustrates that in some cases vapor velocities are initially in growing modes but they are

damped soon as shown in Figs 4.5 and 4.6. The reason for this behavior of vapor velocities can be explained as follows: while the initial small interfacial friction force can not stabilize a growing instability, later the interfacial friction force, which increases with time, becomes enough to damp growing oscillations. These results are consistent with Stewart's conclusion (42) that for a given mesh size, a minimum interfacial force is required to stabilize growing modes.

Bryce (28) noticed the same type of damping oscillations when the LOCA code RELAP-UK was used for the numerical simulation of Edward's simple blowdown experiment. Note that, as interfacial momentum transfer in Hancox et al.'s studies was set to zero, steam velocities did not damp but grew with time unlike the present results, in which interfacial momentum is allowed to be transferred between vapor and liquid.

Even though the present stability criterion was derived for negligible compressibility, it is noted in Figs 4.5 and 4.6 that the derived criterion predicts well the cut-off stability limits. Ardon (43) revealed the same result, that the boundary of the unstable region is virtually unaltered by compressibility.

With the much lower coefficient of interfacial force, the same simulation is performed. In this simulation oscillations do not occur but higher acceleration of both vapor and liquid with lower slip ratios is noticed. Considering that vapor reaches sonic velocities, this

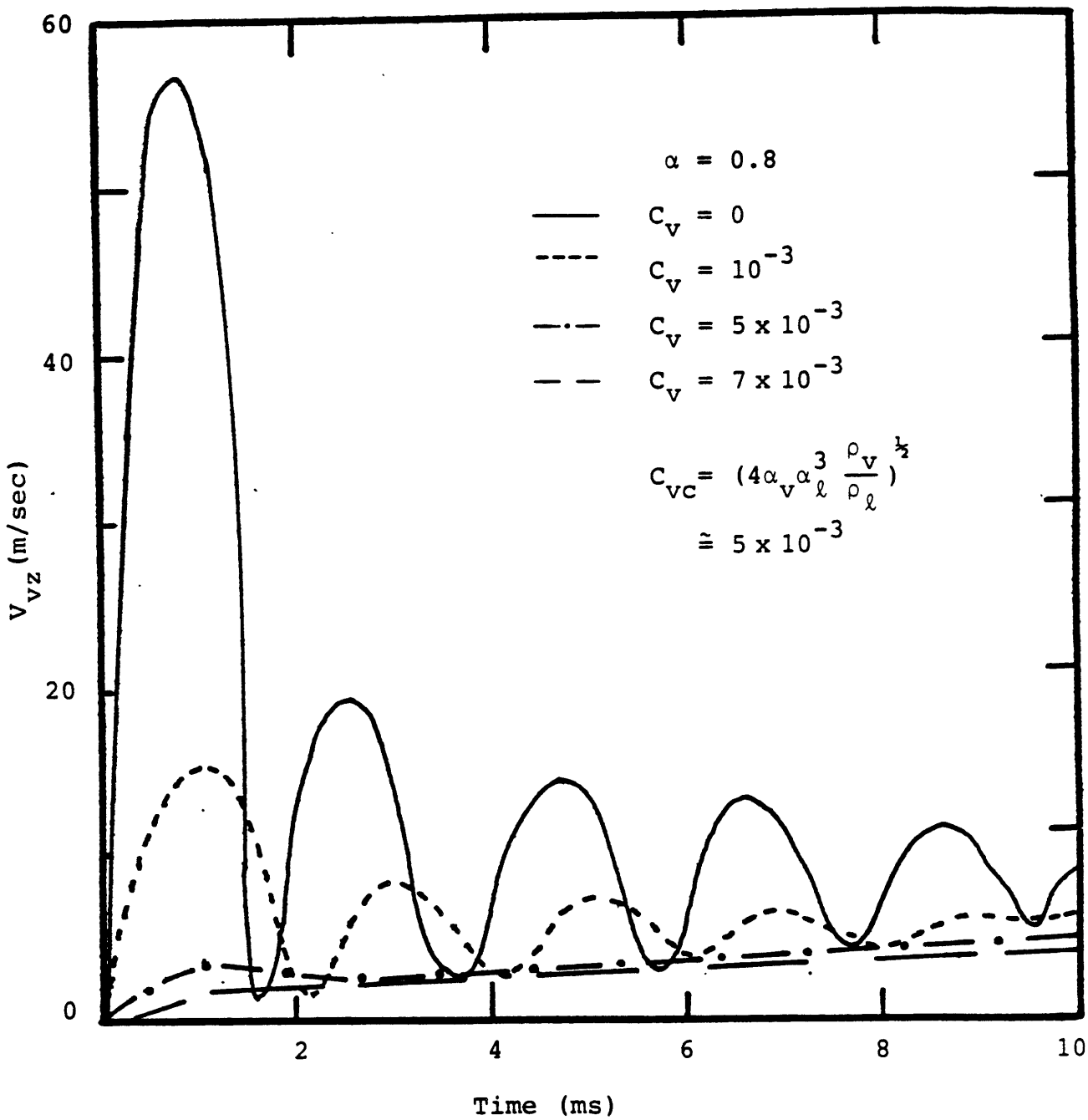

Fig. 4.5: Vapor Velocity Transients with $\alpha = 0.8$

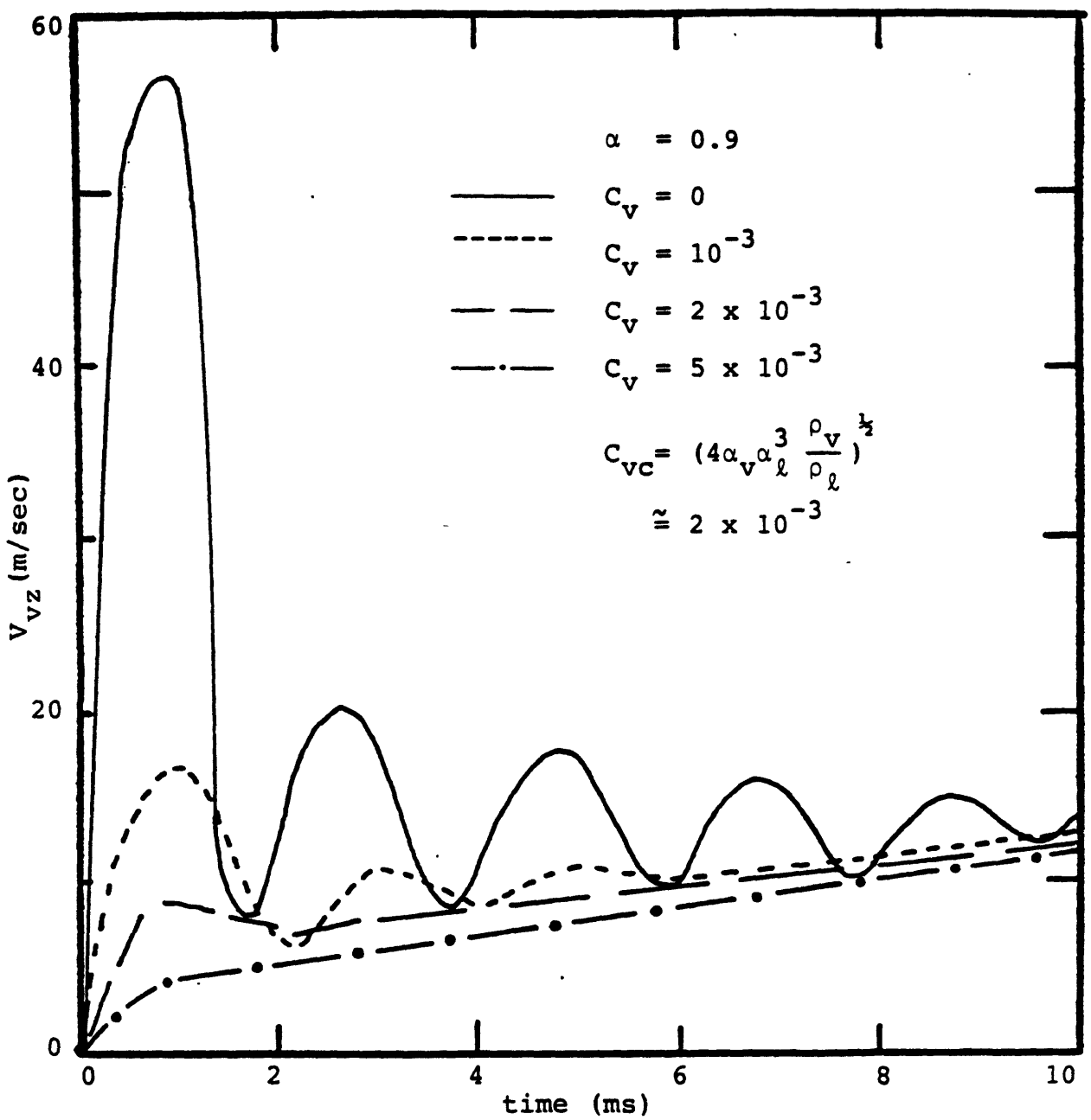

Fig. 4.6: Vapor Velocity Transients with $\alpha = 0.9$

phenomena may be explained by the following argument. At subsonic flows the instability is a long wavelength Kelvin-Helmholtz instability, which is driven by pressure reduction at a wave crest caused by the constriction of the vapor flow. However, at supersonic velocities, area reduction causes a recovery in vapor pressure which opposes wave growth. Therefore, with the zero virtual mass coefficient, the flow can be stabilized.

Fig 4.5 and Fig 4.6 show that vapor velocities depend on virtual mass coefficient ; higher C_v produces lower vapor velocities, as expected. That indicates that virtual mass has a considerable physical effect in the sodium flow due to the high acceleration of the flow resulting from the high density ratio of liquid to vapor. Including virtual mass in the prediction of critical flow for the annular flow with wavy interfaces or with droplets, Henry (44) found a considerable physical effect for virtual mass on the critical flow. His models generally described the data well for the high void fraction flow regime.

4.8 Conclusions

The results from this Chapter can be summarized as follows;

1. If $C_v > \sqrt{4\alpha_v \alpha_\ell^3 \rho_v/\rho_\ell}$, the semi-implicit finite difference scheme is only restricted by the convective stability conditions.

2. Numerical simulation showed that the above stated

inequality for numerical stability predicts well the onset of instability. A growing instability may be possible, if interfacial friction is not enough to stabilize growing modes. This growing instability was always damped with time due to an increase in interfacial friction. At supersonic velocities of vapor, all of wave modes can be stabilized by a recovery in vapor pressure from the constriction of the vapor flow.

3. It is noticed that virtual mass has a considerable physical effect in the sodium flow due to high acceleration resulting from high density ratio.

4. It is recommended that virtual mass be included in the two-fluid model because it functions as a stabilizer with real physical effects, and we can not assure that sufficient interfacial force for stability always exists. Moreover, including virtual mass in THERMIT-6S neither changes the numerical scheme nor requires large coding and computational effort. Future effort must be focussed on the evaluation of C_v and to recommend specific values in terms of flow parameters.

5. For the second law of thermodynamics to be satisfied, λ must be specified within the range of the inequality, $\lambda \geq 1 - \frac{s}{(s-1)(\alpha_\ell s + \alpha_v)}$

Chapter 5 CONSTITUTIVE RELATIONS

While the two fluid model provides more applicability and flexibility in the analysis of two-phase flow than other models do, its accuracy strongly depends on its constitutive equations. As shown in Table 5.1, the constitutive equations of THERMIT-6S can be subdivided into seven categories: mass exchange, energy exchange, momentum exchange, and wall friction and wall heat transfer, for each phase.

5.1 Constitutive Relations in Single Phase Region

The THERMIT-6S code requires two kinds of constitutive equations in the single phase region: wall friction factor and wall heat transfer coefficient. (Refer to Table 5.1) The wall friction factor can be subdivided into the axial wall friction factor and transverse wall friction factor. The models adopted here are those of Wilson and Kazimi (45). The transverse friction factor holds for bare rod geometry only while that of the axial wall friction is for wire-wrapped rod bundles.

5.1.1 Wall Friction in Single Phase Region

5.1.1.1 Axial Wall Friction in Liquid Region

In order to solve the momentum equation for the axial direction of fluid flow it is necessary to calculate the pressure drop due to friction. This change in pressure is defined in terms of the friction factor, f as:

$$\Delta p_z = f \frac{\Delta z}{D_e} \frac{\rho_\ell V_z |V_z|}{2} \qquad (5.1.1\text{-}1)$$

TABLE 5.1

Constitutive Relations of THERMIT-6S

	Single Phase Liquid Region	Pre-Dryout Region ($0<\alpha<0.957$)	Post-Dryout Region ($0.957<\alpha<1$)	Single Phase Vapor Region
Wall Friction Force F_w	X	◎	0	X
Wall Heat Transfer Q_w	X	◎	0	X
Interfacial Mass Exchange Γ		◎	0	
Interfacial Energy Exchange Q_i		◎	0	
Interfacial Momentum Exchange F_i		◎	0	

X: previous work
0: simple extension of present work

◎: present work

where Δp_z = pressure drop in the axial direction

Δz = node length in the axial direction

D_e = equivalent diameter for the flow

V_z = velocity in the axial direction

Then, the rate of wall momentum transfer per unit volume, F_w is expressed as

$$F_w = \Delta p_z / \Delta z \qquad (5.1.1\text{-}2)$$

For the axial wall friction factor, f in the single phase liquid region, THERMIT-6S uses a combination of the laminar correlation of Markely and Engel (46) and simplified Novendstern's turbulent correlation (47). In laminar flow, Markley et al. suggested the following correlation.

$$f_L = \frac{32}{\sqrt{H}} \left(\frac{P}{D}\right)^{1.5} \frac{1}{Re}, \text{ for } Re \leq 400 \qquad (5.1.1\text{-}3)$$

where H=wire wrap lead length

P/D= pitch to diameter ratio

In turbulent flow, Novendstern's correlation simplified by Wilson (45) is used in THERMIT-6S:

$$f_T = \frac{0.316\ M}{Re^{0.25}}, \text{ for } 2600 \leq Re \leq 200{,}000 \qquad (5.1.1\text{-}4)$$

where

$$M = \left[\frac{1.034}{(P/D)^{0.124}} + \frac{29.7 (P/D)^{6.94}\ Re^{0.086}}{(H/D)^{2.239}} \right]^{0.885} \qquad (5.1.1\text{-}5)$$

In the transition region, the following relationship is

employed without any verification:

$$f_{Tt} = f_T \sqrt{\Psi} + f_L \sqrt{1-\Psi} \text{ , for } 400 < Re < 2600 \quad (5.1.1\text{-}6)$$

where $\Psi = \dfrac{Re - 400}{2200}$

5.1.1.2 Axial Wall Friction in Vapor Region

The Markley-Novendstern correlation described above is implemented with vapor properties being substituted for the liquid properties.

5.1.1.3 Transverse Wall Friction in Liquid Region

The momentum equations in the x and y directions also require a friction pressure drop term. In this case, the geometry is different from the axial direction: instead of flow along rods, we have flow across rods. The single phase friction factor in the transverse direction is defined by:

$$\Delta p_t = f \frac{\Delta t}{D_v} \frac{\rho v_{max} |v_{max}|}{2} \quad (5.1.1\text{-}7)$$

where

Δp_t = frictional pressure drop in the transverse direction

Δt = length in the transverse direction

v_{max} = transverse velocity at the point of maximum flow constriction between rods

D_v = volumetrically defined transverse hydraulic diameter

$$= \frac{4 \text{ x volume of fluid in tube bank}}{\text{Exposed surface area of tubes}}$$

The correlation employed in THERMIT-6S was developed by Gunter and Shaw (48), for the transverse wall friction factor in the single phase liquid region. Gunter and Shaw define both a laminar and a turbulent correlation for the friction factor, f with the transition occurring at a Reynolds number of 202.5. Thus,

$$f = \begin{cases} 180/Re & , \text{ for } Re \leq 202.5 \\ 1.92/Re^{0.145}, & \text{ for } Re > 202.5 \end{cases} \qquad (5.1.1\text{-}8)$$

where $Re = \dfrac{\rho |v_{max}| D_v}{\mu}$

Note that this correlation was obtained, based on bare-rod data.

5.1.1.4 Transverse Wall Friction in Vapor Region

The Gunter and Shaw correlation described above is used with vapor properties being substituted for the liquid properties.

5.1.2 Wall Heat Transfer in Single Phase Region

In order to solve the energy equation, we need to specify the heat flux from the wall to the fluid. The wall heat flux is defined as:

$$q''_w = h(T_w - T_s) \qquad (5.1.2\text{-}1)$$

Then, the rate of wall heat transfer per unit volume, Q_w is expressed as

$$Q_w = q''_w/L_w \tag{5.1.2-2}$$

where $\frac{1}{L_w}$ is the wall area density defined as the ratio of the wall surface area to the fluid volume.

The wall heat transfer coefficient, h can be obtained by an empirical formulation.

5.1.2.1 Wall Heat Transfer in Liquid Region

The wall heat transfer coefficient in the single phase liquid region is based on Kazimi and Carelli's recommendation (49). These correlations are selected as reasonably conservative in the range specified. Recommended correlations for bare-rod bundle heat transfer are:

i) For $1.15 \leq \frac{P}{D} \leq 1.3$; $10 \leq Pe \leq 5000$,

$$Nu = 4.0 + 0.33 \left(\frac{P}{D}\right)^{3.8} \left(\frac{Pe}{100}\right)^{0.86} + 0.16 \left(\frac{P}{D}\right)^{5.0}, \tag{5.1.2-3}$$

ii) For $1.05 \leq \frac{P}{D}$ 1.15; $150 \leq Pe \leq 1000$,

$$Nu = Pe^{0.3}[-16.15 + 24.96 \left(\frac{P}{D}\right) - 8.55\left(\frac{P}{D}\right)^2]; \tag{5.1.2-4}$$

iii) For $Pe \leq 150$,

$$Nu = 4.50[-16.15 + 24.96 \left(\frac{P}{D}\right) - 8.55 \left(\frac{P}{D}\right)^2] \tag{5.1.2-5}$$

5.1.2.2 Wall Heat Transfer in Vapor Region

As the liquid metal in the single phase region loses its high thermal conductivity and low Nusselt number, the single phase liquid correlation can not be used. The Dittus-Boelter correlation is recommmended:

$$Nu = 0.023\ Re_v^{0.8}\ Pr_v^{0.4} \qquad (5.1.2\text{-}6)$$

Note that this correlation was obtained, based on circular-tube data.

5.2 Constitutive Relations in Two-Phase Pre-Dryout Region

The fundamental nature of the internal structures of two-phase flow , i.e. ,flow regimes, makes the analysis of two-phase flow more complicated from numerical and physical points of view.

Here we shall use a simplified flow regime based on the following assumptions:

1. The exchange mechanism is dominantly controlled by local phenomena.
2. While vapor appears in the form of a large bubble within a subassembly, liquid films remain on the cladding and hence an annular flow is dominant on the scale of a subchannel.

Numerically, use of a simple flow regime is very important. If several flow regimes are implemented in the code, abrupt change of flow properties due to different constitutive equations often makes it difficult to obtain convergence with reasonable time step sizes.

The greatest obstacle to obtaining constitutive equations lies in the limited experimental data available for two-phase flow of sodium. Moreover, there exist discrepancies between data of different authors. Here the main reasons of these discrepancies will be clarified and constitutive relations for two-phase flow of sodium will be derived within our present capabilities, based on the above assumptions.

5.2.1 Axial Pressure Drop Coefficient in Two-Phase Flow

By reviewing several publications on frictional pressure drop in the two-phase flow of liquid metals, discrepancies between data of different authors become evident. It is also found that acceleration loss by droplets has a considerable effect on the hydraulic models, due to the high density ratio of the two fluids and the high-slip ratio. The objective of the following investigation of the friction pressure drop multiplier is to identify the primary reasons of these discrepancies.

5.2.1.1 Literature Review

The important questions in the area of two-phase pressure drop characteristics of liquid metals have often been stated as

1. Can the two-phase pressure drop of liquid metals be satisfactorily predicted by the correlations now in use for ordinary fluids?
2. If not, what modified or new correlations are required?
3. How well can friction pressure drop correlations for adiabatic two-phase flow be used to predict the two-phase pressure drop for heated channels?

To answer the above question, the Lockhart-Martinelli

correlation (50) is chosen to represent non-metalic fluids. Several experiments on liquid-metal, two-phase pressure drop are cited in Table 5.2.

The low-quality pressure drop of sodium was investigated by Lurie (51). A comparison between these sodium data and the potassium data obtained at the University of Michigan showed excellent agreement. Over the range of flow rates and pressure covered in the experiment, no additional parametric dependencies could be discerned when the pressure drop ratio was plotted as a function of the Lockhart-Martinelli parameter, X_{tt} . It was also concluded that the high scatter in the low-quality and high X_{tt} region, as seen in Fig 5.1, is due to experimental variations and errors. However, most of the data fall between the Lockhart-Martinelli predictions for viscous-viscous and turbulent-turbulent flow.

The pressure drop data of Fauske and Grolmes (52) were obtained for forced convection flashing sodium flow in a tube under both the subsonic and sonic flow conditions. Friction factor data reduced from experiments under subsonic conditions are displayed in Fig 5.1. The data fall slightly below the Lockhart-Martinelli correlation for turbulent-turbulent flow.

Russian data (53) with low-mass flux of potassium under adiabatic conditions are shown in Fig 5.1. Results are in good agreement with the Lockhart-Martinelli correlation in the high-quality region.

TABLE 5.2

Main Parameters of Sodium Boiling Experiments

Classification				Range of Parameters		
Author	Fluid	Geometry*	Condition**	Pressure Bar	Mass Flux $kg/m^2 \cdot sec$	Quality %
Lurie, 1965 [51]	Na	S	A	0.1∿0.7	160∿950	∿14
Fauske, 1970 [52]	Na	S	F	0.35∿0.55	640∿1815	0.92∿2.5
Alad'yev, 1969 [53]	K	S	A	1∿1.5	105∿277	1.5∿88
Smith, 1966 [54]	K	S	A	0.037∿1.075	110∿763	∿37.84
Baroczy, 1968 [55]	K	S	A	0.95∿1.16	165∿608	1∿9.4
Zeigarnick, 1980 [57]	Na	S	D	1∿2	150∿400	∿45
Chen, 1970 [58]	K	S	A	0.6∿2.9	200∿1330	1∿31
Kaiser, 1974 [59]	Na	S	A	0.5∿1.7	74∿3345	∿86
Kaiser, 1977 [60]	Na	7B	A	1∿2.04	788∿1523	∿35
				0.96∿1.73	23∿233	0.2∿87

*S = Single tube
7B = 7 pin bundle

**A - Adiabatic condition
D - Diabatic condition
F - Flashing condition

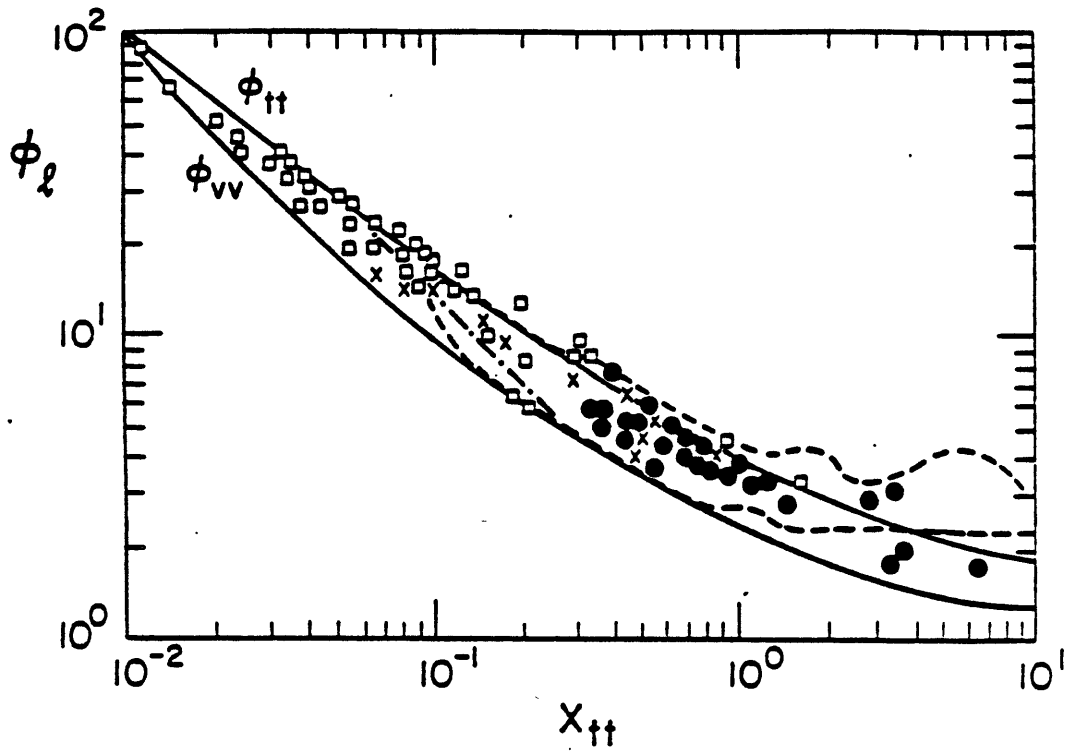

□ : Potassium data from Ref. 53
● : Sodium data from Ref. 52
× : Data of Baroczy [55]
- - - - : Data range of Lurie [51]
——— : Lockhart-Martinelli correlation
—·— : Smith correlation [54]

Fig. 5.1: Experimental Two-Phase Friction Pressure Drop with Low Mass Flux or Low Quality Flow

Smith et al. (54) measured the pressure drop in the horizontal two-phase flow of potassium. They estimated that acceleration losses never exceed 3%. This evaluation demonstrated that the experimental potassium pressure drops in a horizontal duct were essentially frictional. The Lockhart-Martinelli correlation predicts substantially greater potassium pressure gradients than shown by the data. If their results are evaluated in terms of the Lockhart-Martinelli multiplier, $\phi^2_{\ell,L}$, and parameter X_{tt} , we obtain an approximate relationship for Smith's multiplier, $\phi^2_{\ell,S}$:

$$\phi^2_{\ell,S} = \phi^2_{\ell,L} \times 1.58 \left(\frac{1}{1+43.5\ X_{tt}^{1.1}}\right)^{0.444}$$

In Fig 5.1 this relationship shows that the deviation between the Smith correlation and the Lockhart-Martinelli correlation in the high-quality region is small. But, as quality decreases, the deviation becomes larger and larger. As expected, the decreasing influence of heat loss calibration accuracy with increasing quality results in closed correspondence between the data and the Lockhart-Martinelli correlation at high quality.

Pressure drop data for two-phase potassium flowing through a straight horizontal tube were presented by Baroczy (55). Ref. 55 demonstrated that his data were better predicted by the Lockhart-Martinelli correlation than that by the Baroczy correlation (56). As Fig 5.1 shows, the data are typically lower than the Lockhart-Martinelli correlation.

As the two-phase multiplier, $\phi^2_{\ell o}$ in Ref 55, was evaluated for total flow, the two-phase multiplier, $\phi^2_{\ell o}$ for liquid flow was obtained by dividing $\phi^2_{\ell o}$ by $(1-x)^{1.8}$, implying a Blausius-type single-phase friction factor ($f=c/Re^{0.2}$) was assumed. We next discuss diabatic data in the literature.

Most recently Zeigarnick and Litvinov (57) presented data on the pressure drop in sodium with heat addition. They showed that the pressure drop associated with the acceleration of entrained droplets can be neglected in the range investigated. In Fig 5.2 a comparison of their experimental data with the Lockhart-Martinelli correlation for adiabatic and non-metallic flow showed that the experimental data lie significantly below the correlation. The average discrepancy is about -35%. They explained that this is associated with a "push aside" effect of the vapor flow from the interface and the change of liquid film characteristics.

Chen and Kalish (58) reported quite different results from an experimental investigation of two-phase pressure drop for potassium without vaporization. Their data lie fairly above the Lockhart-Martinelli correlation (Fig 5.3). Although they reported that all data from their study corresponded to the annular-dispersed flow regime, they neglected the momentum-acceleration effect of the droplets in the vapor core.

Kaiser et al. (59) investigated the pressure drop in tube flow under adiabatic conditions, as well as the type of

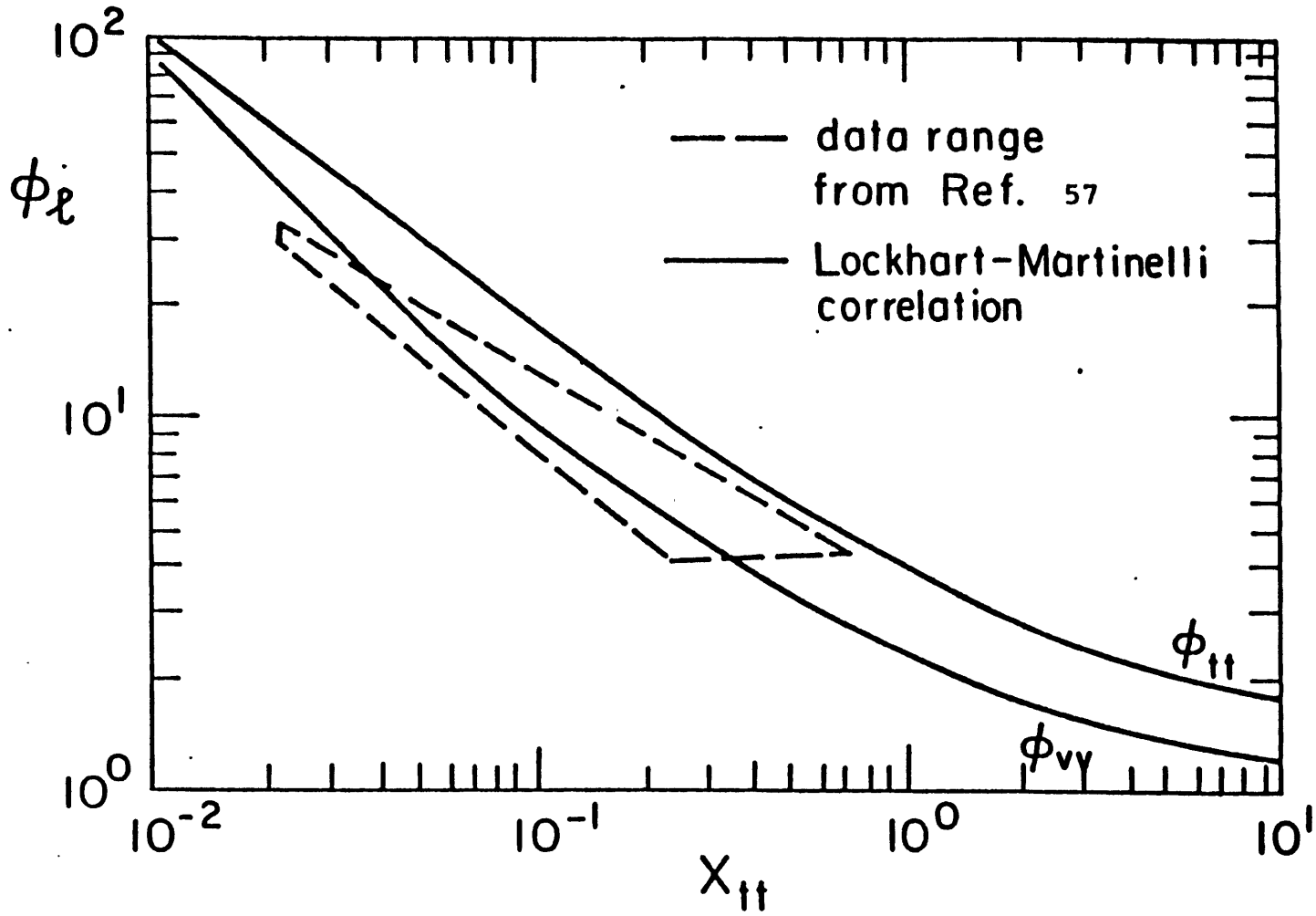

Fig. 5.2: Experimental Two-Phase Friction Pressure Drop under the Diabatic Condition

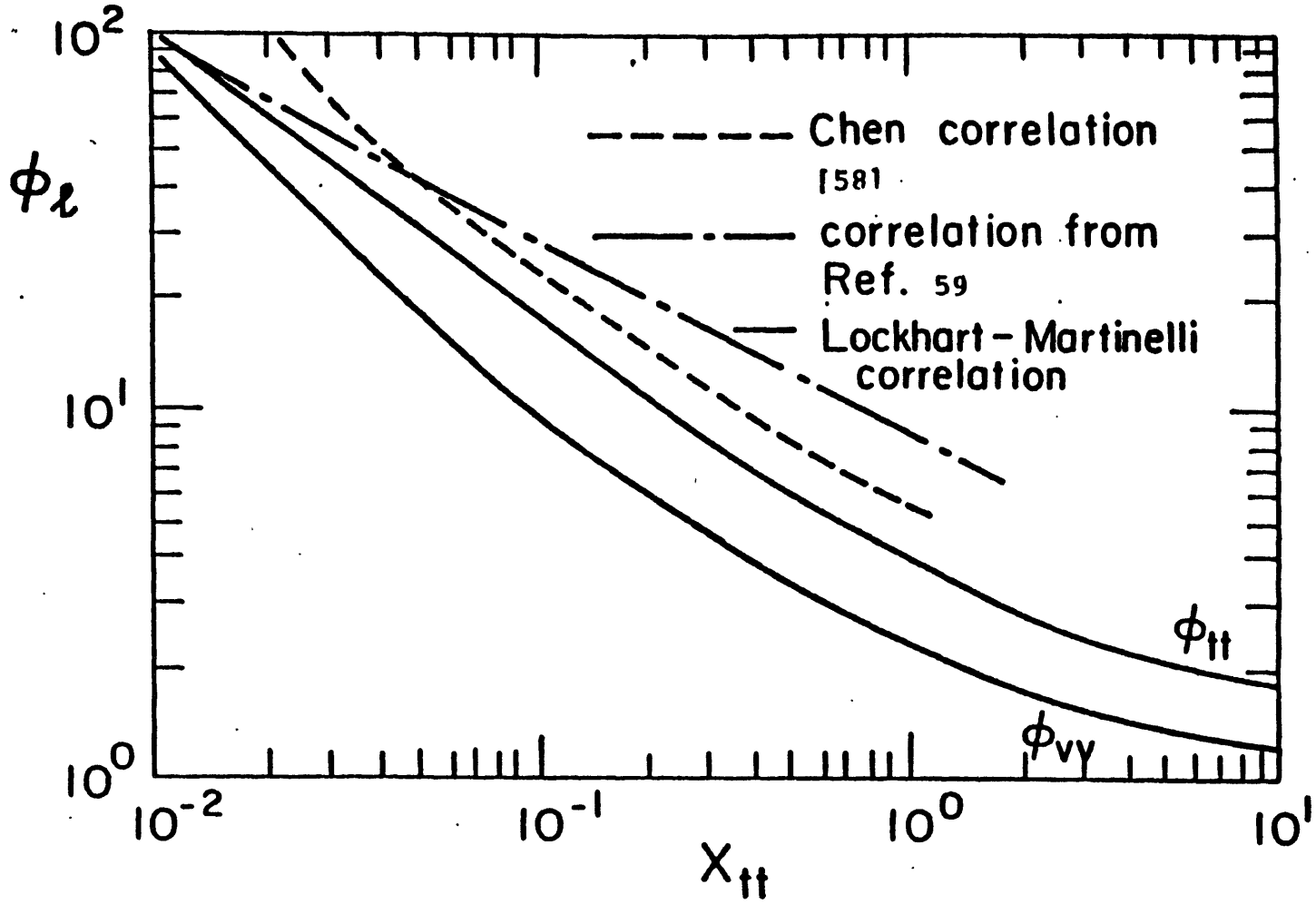

Fig. 5.3: Experimental Two-Phase Friction Pressure Drop with High Mass Flux and High Quality Flow

flow and critical heat flux of boiling sodium. They reported that the flow patterns of pure annular flow and annular-dispersed flow were dominating. Most of the data in Fig 5.3 lie fairly above even Chen's results.

Kaiser and Peppler (60) evaluated the two-phase pressure drop of sodium in seven-pin bundle geometries under adiabatic conditions. Experiments were done over two ranges of conditions, as given in Table 5.2. In Fig 5.4 data of the pin bundle experiment is seen to fall slightly below the Lockhart-Martinelli correlation. However, comparison with the results from the single tube experiments shows a displacement by a factor of 0.6 toward lower values. Although an attempt was made to explain these differences by investigating the influence of void fractions and of resistance coefficients for the single-phase flow, no explanation was found for deviations in the experiments. A systematic failure seems unlikely as the same measurement principles were employed in both sets.

5.2.1.2 Effect of Entrainment on Pressure Drop

The above review indicates that data are divided into two groups. Each group may be characterized by the flow pattern: "pure annular" flow or "annular-dispersed" flow. While the data which fall below the Lockhart-Martinelli correlation, were taken in annular flow without or with a small number of droplets, the data which fall fairly above the Lockhart-Martinelli correlation, were taken in

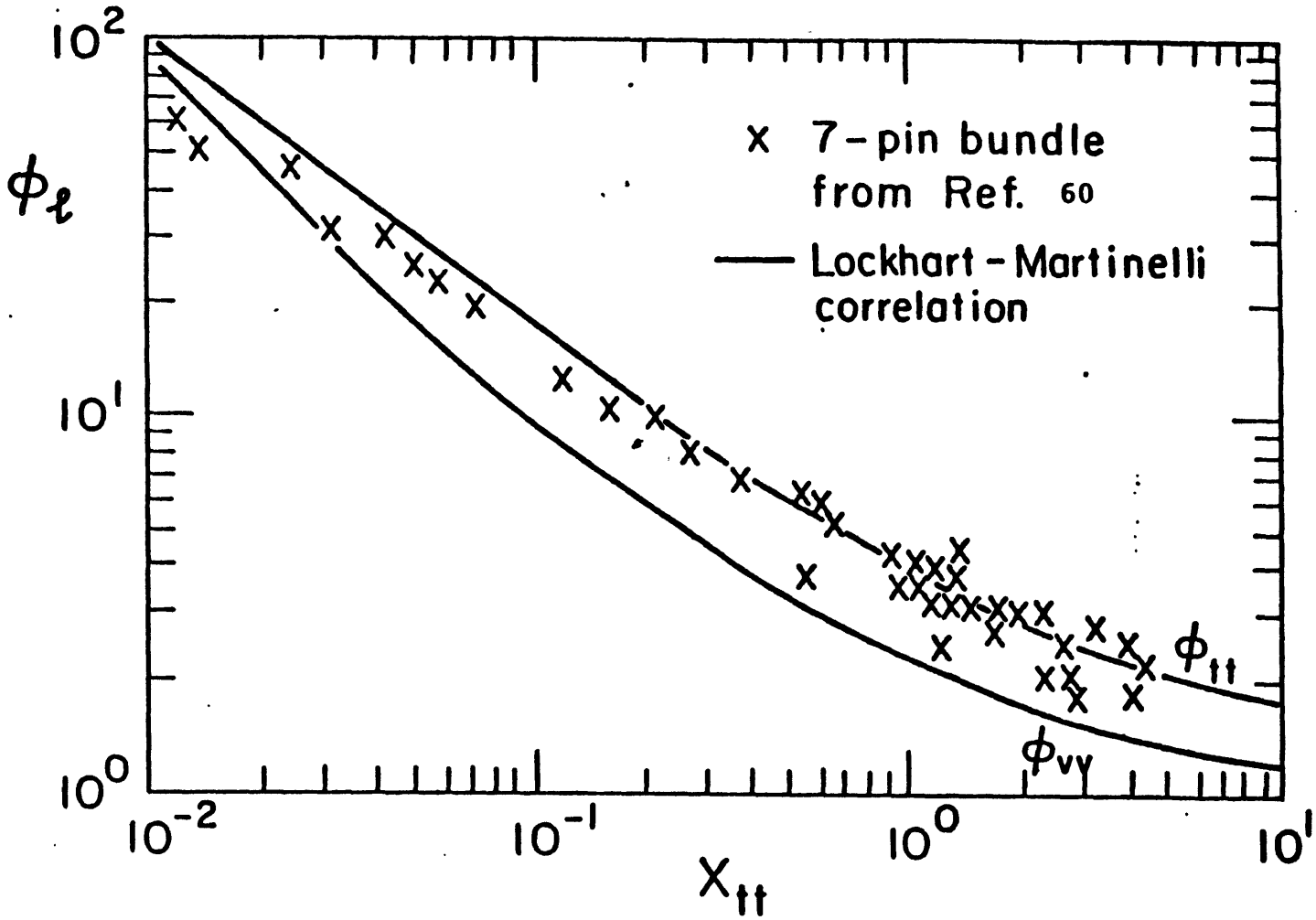

Fig.5.4: Experimental Two-Phase Friction Pressure Drop in Seven-Pin Bundle

annular-dispersed flow. Therefore, it can be argued that the difference between the two groups is caused by the acceleration pressure drop of droplets in the gas core, which was neglected in the evaluation of the pressure drop in annular-dispersed flow.

Entrainment effects on pressure drop can be included in the following equation:

$$dP_{2\phi} = dP_{2\phi f} + d(\alpha_{\ell f}\rho_\ell U_{\ell f}^2 + \alpha_{\ell d}\rho_\ell U_{\ell d}^2 + \alpha_g\rho_g U_g^2) + (\alpha_\ell\rho_\ell + \alpha_g\rho_g)g\,dz \qquad (5.2.1\text{-}1)$$

where

$dP_{2\phi}$	=total pressure drop
$dP_{2\phi f}$	=frictional pressure drop
$\alpha_{\ell f}, \alpha_{\ell d}, \alpha_g$	=volumetric fraction of liquid film, liquid droplets, and gas in the flow channel, respectively
$U_{\ell f}$	=liquid film velocity
$U_{\ell d}$	=liquid droplet velocity
U_ℓ	=total liquid average velocity
U_g	=gas average velocity

Obviously, $\alpha_\ell + \alpha_g = 1$

and $\alpha_{\ell d} + \alpha_{\ell f} = \alpha_\ell$

Given values for G, x, and $\alpha_{\ell f}$, the velocities U_ℓ, $U_{\ell f}$

, and U_g can be evaluated by the following equations:

$$U_\ell = G(1-x)/(\rho_\ell \alpha_\ell) \tag{5.2.1-2}$$

$$U_{\ell f} = (1-E)\ G(1-x)/(\rho_\ell \alpha_{\ell f}) \tag{5.2.1-3}$$

$$U_g = G\ x/(\alpha_g \rho_g), \tag{5.2.1-4}$$

where $$E = (\alpha_{\ell d}\ \rho_\ell\ U_{\ell d})/(\alpha_\ell \rho_\ell U_\ell) \tag{5.2.1-5}$$

From the definition of entrainment fraction, E, we obtain a core liquid fraction, $\alpha_{\ell d}$, in terms of $\alpha_{\ell f}$ and E as

$$\alpha_{\ell d} = \alpha_{\ell f} \frac{EU_\ell}{U_{\ell d} - EU_\ell} \tag{5.2.1-6}$$

We assume flow conditions within the gas such that the velocities of the gas and of the droplets are equal, i.e., $U_{\ell d} = U_g$. As both U_g and U_ℓ are functions of $\alpha_{\ell d}$, G, and x, then $\alpha_{\ell d}$ can be expressed in terms of $\alpha_{\ell d}$, G, and x and solved by iteration if we know the entrainment fraction, E. Also the two-phase multiplier, ϕ_ℓ , can be expressed in terms of $\alpha_{\ell f}$ and E.

By definition

$$\phi_\ell^2 = \frac{\tau_w}{\tau_\ell} \tag{5.2.1-7}$$

where $$\tau_w = f_{\ell f}\ \frac{\rho_\ell U_{\ell f}^2}{2} \tag{5.2.1-8}$$

$$\tau_\ell = f_\ell\ \frac{\rho_\ell j_\ell^2}{2} \tag{5.2.1-9}$$

$$j_\ell = U_\ell \alpha_\ell \tag{5.2.1-10}$$

and where τ_ℓ is the wall shear stress when the total liquid flows along the channel.

Substituting Eqs (5.2.1-8) and (5.2.1-9) into Eq (5.2.1-7),we obtain

$$\phi_\ell^2 = \left(\frac{f_{\ell f}}{f_\ell}\right)\left(\frac{U_{\ell f}}{U_\ell \alpha_\ell}\right)^2 \qquad (5.2.1\text{-}11)$$

Using the definition of the Reynolds number and assuming the same Blausius-type relation for $f_{\ell f}$ and f_ℓ, we obtain

$$\frac{f_{\ell f}}{f_\ell} = \left(\frac{\alpha_\ell \cdot U_\ell}{\alpha_{\ell f} U_{\ell f}}\right)^{0.2} \qquad (5.2.1\text{-}12)$$

Substituting Eq (5.2.1-12)into Eq (5.2.1-11) and using the definition of the entrainment fraction, E, we obtain the final form of ϕ_ℓ^2 :

$$\phi_\ell^2 = \frac{1}{\alpha_{\ell f}^2} (1 - E)^{1.8} \qquad (5.2.1\text{-}13)$$

A detailed derivation of Eq (5.2.3-33) is described in Appendix C . Equation (5.2.1-13) shows that the two-phase multiplier, ϕ_ℓ^2 , in annular flow with droplets is lower than in annular flow with no droplets for the same void fraction. If the single-phase pressure drop for the total liquid flow, τ_ℓ in Eq (5.2.1-7), is replaced by that for the liquid film flow, $f_{\ell f}$ is equal to f_ℓ from Eq (5.2.1-12). Therefore, we obtain the relationship suggested by Turner and Wallis (61):

$$\phi_\ell^2 = \frac{1}{\alpha_{\ell f}^2} \qquad (5.2.1\text{-}14)$$

Note that for no entrainment, ϕ_ℓ^2 in Eq (5.2.1-13) is equal to $\phi_{\ell f}^2$ in Eq (5.2.1-14).

So far the only unknown variable is the entraiment

fraction, E. For Reynolds numbers between 200 and 3000, the amount of entrainment is a function of both vapor and liquid flow rate. Steen and Wallis (62) showed that in fully turbulent flow above a film Reynolds number of 3000, the amount of entrainment and the conditions for the onset of entrainment are largely independent of the liquid film flow rate and depend primarily on the vapor velocity. Unfortunately, this approach fails to take into account a general increase in the fraction of liquid entrained as the channel diameter increases. As there are no data available for liquid metals, the Steen-Wallis relationship can be taken to represent the entrainment fraction, E, here and to provide a rough estimation of acceleration loss by droplets. If we apply this approach to the data of Ref 63, the entrainment fraction from Steen and Wallis leads to a negative friction pressure drop for most of the experiments. This implies that the relationship from Steen and Wallis overpredicts the entrainment fraction, and the acceleration pressure drop by the droplets. Conversely, the entrainment fraction can be calculated when the friction pressure drop is known. If the Lockhart-Martinelli correlation is used to predict the friction pressure drop, the results imply, for most of the experiments, a smaller entrainment fraction than predicted by Steen and Wallis.

The large acceleration effect of droplets in liquid metals is primarily due to the high ratio of liquid-to-vapor densities and the high-slip ratio. Assuming complete

homogenization, a gas void fraction of 0.9, a core liquid fraction of 0.001, and a density ratio of 3000 the acceleration loss by droplets is about three times that by vapor. In conclusion, acceleration loss by droplets should not be neglected in the evaluation of frictional pressure drop in the annular-dispersed flow.

5.2.2 Transverse Pressure Drop Coefficient in Two-Phase Flow

As there are few data for transverse pressure drop coefficients in two-phase flows, the following correlations recommended by Wilson and Kazimi (45) are adopted in the present version.

For transverse two-phase flow with both liquid and vapor Reynolds number in the laminar regime, the Gunter and Shaw correlation (48) for single phase flow is transformed as follows:

$$\Delta p_L = f \frac{\Delta t}{D_v} \frac{\rho_\ell v_{\ell max}^2}{2} \quad \text{for } Re_\ell < 202.5 \qquad (5.2.2\text{-}1)$$

where $f = 180/Re_\ell$

$$Re_\ell = \frac{\alpha_\ell \rho_\ell D_v}{\mu_\ell} |v_{\ell max}|$$

If either liquid or vapor is in the turbulent regime, the Ishihara correlation (64) is applied to the friction

pressure drop to yield the following equation:

$$\Delta p_T = f \frac{\Delta t}{D_v} \frac{G^2}{2\rho_\ell} \phi^2_{\ell o}, \qquad (5.2.2\text{-}2)$$

where $G = G_\ell + G_v$

$$= \alpha_\ell \rho_\ell v_{\ell max} + \alpha_v \rho_v v_{vmax}$$

$$f = \frac{1.92}{Re^{0.145}}$$

$$Re = G\, D_v/\mu_\ell$$

$$\phi^2_{\ell o} = 1 + \frac{8}{X_{tt}} + \frac{1}{X^2_{tt}}$$

$$\frac{1}{X^2_{tt}} = \left(\frac{x}{1-x}\right)^{1.855} \left(\frac{\rho_\ell}{\rho_v}\right) \left(\frac{\mu_v}{\mu_\ell}\right)^{0.145}$$

5.2.3 Wall Heat Transfer Coefficient in Two-Phase Flow

5.2.3.1 Literature Review

Analogies between heat and momentum transport processes have been used successfully for single-phase flow analysis since Reynolds (65) remarked on the similarity between the two processes. While Reynolds assumed the entire flow field to be highly turbulent, Prandtl (66) and Taylor (67) developed analogies based on two zones-a laminar zone near the wall and a highly turbulent core. Von Karman (68) extended the universal velocity profile to three zones-a laminar sublayer, a buffer zone, and a turbulent core. Martinelli (69) successfully applied this approach for predicting single-phase heat transfer in liquid metals. More recent adaptations of the analogy concept have concentrated on incorporating improved expressions for momentum and energy eddy diffusivities in the well-known equations for momentum flux and heat flux:

$$\tau = - (\nu + \varepsilon_m)\rho \frac{dV}{dy} \qquad (5.2.3\text{-}1)$$

$$q'' = - (\alpha + \varepsilon_h)\rho\, C_p \frac{dT}{dy} \qquad (5.2.3\text{-}2)$$

In his falling film analysis, Dukler (70) used the velocity form of Deissler for both laminar and buffer zones and the form of von Karman for a turbulent core. Assuming that the ratio of the eddy thermal diffusivity to the eddy viscosity is unity and the molecular conductivity is

negligible, a temperature profile was constructed. The above assumption results in an overestimated heat transfer coefficient at low values of the Prandtl number. Traviss et al. (71) modified the Dukler film analsis to include the effect of total pressure drop. Their prediction method for condensation heat transfer has been verified for data with Freon-12 and -22. As their derivation is quite general, it can be extended to liquid metals. Applying the Traviss et al.'s analytical method to annular flow evaporation without nucleation, Bjorge (72) obtained a correlation that appeared to be in better agreement with water data than the Chen correlation (73).

There are few correlations for flow boiling heat transfer for liquid metals. A first attempt was made by Chen (74) following the same approach as his method for non-metalic flows. He postulated that two mechanisms contribute to total wall heat transfer-the macro-and micro-convection mechanisms. He used the suppression function, S, and the measure of the effectiveness of two-phase momentum transfer, F, which were obtained from data with water and organic fluids. He proposed the following modified form of the Lyon-Martinelli equation for the evaluation of the macro-convective contribution to total wall heat transfer:

$$h_{mac} = [\delta + 0.024\ (F\ Re_{\ell}^{0.8})(\beta\ Pr_{\ell})^{\alpha}]\ \frac{\gamma k_{\ell}}{D_h} \qquad (5.2.3\text{-}3)$$

For the two-phase flow, he recommended the values 7, 1, 1, and 0.8 for δ, β, γ, and α, respectively. The NATOF code (16) used a modified Chen correlation:

$$h_{mac} = F^{0.375}\, h_{\ell} \,, \qquad (5.2.3\text{-}4)$$

where h_{ℓ} is the single-phase liquid heat transfer coefficient at the same inlet mass flow.

During the last two decades, several experimental investigations of heat transfer and pressure drop for sodium boiling and condensation have been made. As experimental data were accumulated, discrepancies emerged among the results obtained by different authors. Recently Zeigarnick and Litvinov (57) provided data that give better insight into the mechanisms determining the heat transfer and friction pressure loss characteristics. The accuracy and reliability of the two-phase alkali-metal heat transfer data depend on the accuracy of the determination of the saturation temperature and the flow stability. Previously, investigators measured the saturation temperature with thermocouples. Zeigarnick and Litvinov observed that saturation temperature measurements in alkali-metal, two-phase flow with thermocouples are inherently associated with uncertainties caused by significant local pressure drops around the thermocouple location. To overcome this problem they measured the saturation pressure directly, thus determining more accurately the saturation temperature. For alkali-metal flow, the occurrence of a significant wall

superheat is known to be probable. In their experiments, flow boiling stabilization over a sufficiently long period was achieved either by drilling artificial double-reentrant, angle-type cavities in the heating surface or by injection of a small amount of inert gas at the test tube entrance. It was also found that the phase change in sodium occurs by evaporation from the vapor-liquid interface without bubble generation at the wall. This suggested that the macroscopic contribution to the wall heat transfer in forced two-phase convection in sodium is highly dominant over nucleate boiling. In the present work, a macroscopic heat transfer correlation will be developed on the basis of the above-stated observation.

5.2.3.2 Model Development

With the aid of Fig 5.5, an approximate distribution of shear stress in the liquid film can be obtained from the steady-state differential momentum equation in the liquid film, assuming negligible radial velocity and incompressible liquid flow:

$$\frac{1}{r}\frac{\partial}{\partial r}(r\,\tau_{rz}) = \frac{\partial P}{\partial z} + \rho_\ell g \qquad (5.2.3\text{-}5)$$

As the right-hand side is a function of z alone, it is taken to be constant in the r direction. Integrating Eq (5.2.3-5) from the wall, R, to r in the liquid film and using the boundary conditions, $\tau_w = \tau_{rz}|_R$ and $\tau_i = \tau_{rz}|_{R-\delta}$ we

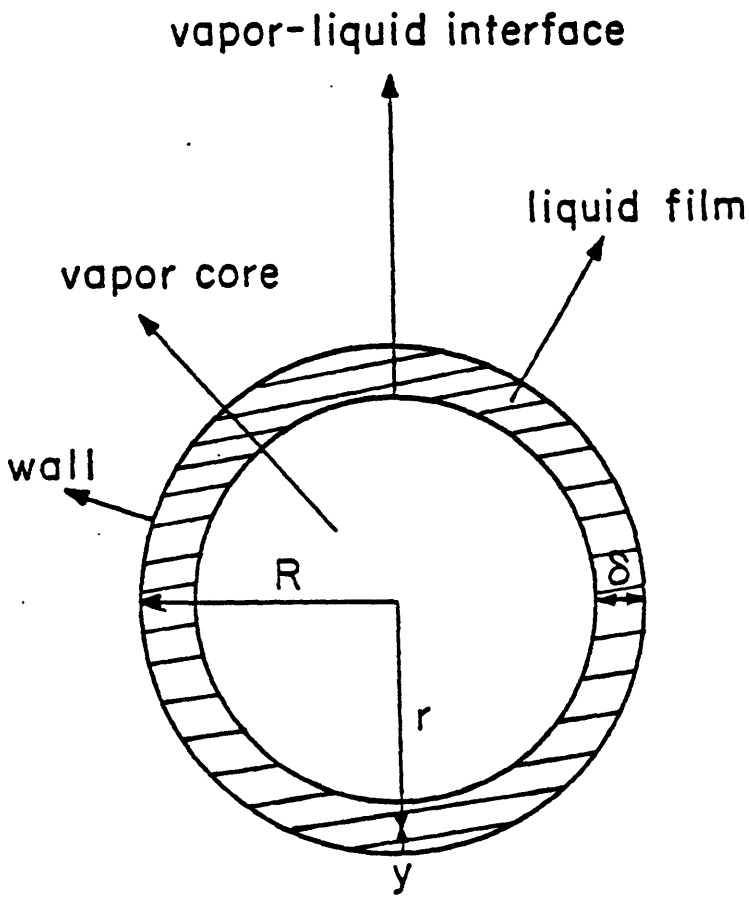

Fig. 5.5: Ideal Liquid Film in the Tube

obtain the equation

$$\tau_{rz} = \frac{R}{r}\,\tau_w + \left(\frac{R^2-r^2}{2r}\right)\left[\frac{R^2-(R-\delta)^2}{2(R-\delta)}\right]^{-1}\left(\tau_i - \frac{R}{R-\delta}\,\tau_w\right) \quad (5.2.3\text{-}6)$$

Assuming a thin film, $R \gg \delta$, we get the distribution of shear stress in the thin liquid film:

$$\tau_{rz} = \tau_w\,\left(1 - \frac{y^+}{\delta^+}\,M\right), \quad (5.2.3\text{-}7)$$

where $M = 1 - \tau_i/\tau_w$

$$y^+ = y\,U_\tau/\nu_\ell$$

$$\delta^+ = \delta U_\tau/\nu_\ell$$

$$U_\tau = (g_o\,\tau_w/\rho_\ell)^{1/2}$$

Traviss et al. (71) assumed a linear shear stress distribution in the thin liquid film and then obtained the same expression as Eq (5.2.3-7).

Assuming that the von Karman momentum-heat transfer analogy is applicable to the liquid layer, the shear stress and heat flux are written as

$$\tau = -\frac{\rho_\ell}{g_o}\,(\nu_\ell + \varepsilon_m)\,\frac{dV_z}{dy} \quad (5.2.3\text{-}8)$$

$$q'' = -\rho_\ell\,C_{p\ell}\,(\alpha_\ell + \varepsilon_h)\,\frac{dT}{dy} \quad (5.2.3\text{-}9)$$

Rearranging Eq (5.2.3-8) and solving for ε_m, we obtain

$$\varepsilon_m = \left[\frac{\tau g_o}{\rho_\ell} \frac{1}{U_\tau^2} \frac{1}{\left(\frac{dV_z^+}{dy^+}\right)} - 1 \right] \nu_\ell, \qquad (5.2.3\text{-}10)$$

where $V_z^+ = V_z/U_\tau$

The von Karman universal velocity distributions for the laminar and the buffer zones are assumed to be

$$0 < y^+ < 5; \quad V_z^+ = y^+ \qquad (5.2.3\text{-}11)$$

$$5 < y^+ < 30; \quad V_z^+ = -3.05 + 5 \ln y^+ \qquad (5.2.3\text{-}12)$$

For the turbulent zone, the von Karman universal distribution, which was obtained from single-phase flow data, is not directly applicable to the liquid film in the two-phase flow. Therefore, the applicability of a logarithmic law is assumed as

$$y^+ > 30; \quad V_z^+ = a + b \ln y^+ \qquad (5.2.3\text{-}13)$$

The value of a is determined by the requirement of continuity between the buffer and the turbulent zones, which yields

$$a = -3.05 + (5 - b) \ln 30 \qquad (5.2.3\text{-}14)$$

The only empirically determined coefficient, b, is obtained by applying the suggested correlation to a subset of the Zeigarnick and Litvinov data, namely the data at q"=1.0

MW/m^2. The results are b=6 and a=-6.45.

Now let us obtain an expression of ε_m for each zone. For the laminar zone, we obtain

$$0 < y^+ < 5; \ \varepsilon_m = 0 \qquad (5.2.3\text{-}15a)$$

For the buffer zone, the eddy viscosity is of the same order of magnitude as the kinematic viscosity and $\tau_{rz}/\tau_w \approx 1$. Therefore,

$$5 < y^+ < 30; \ \varepsilon_m = \nu_\ell \left(\frac{y^+}{5} - 1 \right) \qquad (5.2.3\text{-}15b)$$

For the turbulent zone, assuming $\varepsilon_m / \nu_\ell >> 1$ and using Eq (5.2.3-7).

$$y^+ > 30; \ \varepsilon_m = \frac{\nu_\ell}{6} y^+ \left[1 - M \left(\frac{y^+}{\delta^+} \right) \right] \qquad (5.2.3\text{-}15c)$$

Since $(q/A) \approx (q/A)_w$, Eq (5.2.3-9) can be integrated from the wall to the interface in the liquid layer to yield

$$\frac{1}{h} = \frac{T_w - T_\delta}{q''}$$

$$= \int_0^{\delta^+} \frac{\nu_\ell}{\rho_\ell \ C_{p\ell} \left(\alpha_\ell + E\varepsilon_m \right) U_\tau} \ dy^+, \qquad (5.2.3\text{-}16)$$

where T_w and T_δ are the wall temperature and the interfacial liquid temperature, respectively, and $E == \varepsilon_h / \varepsilon_m$.

Substituting Eq (5.2.3-15) into Eq (5.2.3-16) and completing

the integration we obtain

$$Nu = \frac{hD_h}{k_\ell} = \frac{\rho_\ell \; C_{p\ell} \; U_\tau \; D_h}{k_\ell F_2} \qquad (5.2.3\text{-}17)$$

where $\delta^+ > 30$; $F_2 = 5\,Pr_\ell + \frac{5}{E} \ln\,(1 + 5\,EPr_\ell) +$

$$\frac{6}{E\gamma} \ln \left[\frac{2M + \gamma - 1}{1 + \gamma - 2M} \times \frac{\gamma + 1 - 60M/\delta^+}{\gamma - 1 + 60M/\delta^+} \right]$$

$0 < \delta^+ < 5$; $F_2 = \delta^+ \; Pr_\ell$

$5 < \delta^+ < 30$; $F_2 = 5\;Pr_\ell + \frac{5}{E} \ln\left[1 + E\,Pr_\ell\left(\frac{\delta^+}{5} - 1\right)\right]$

where $\gamma = \sqrt{1 + \frac{10M}{E\delta^+ \; Pr_\ell}}$

Using the continuity of mass in the film and approximating, with an error of <4%, we can obtain δ^+ as an explicit function of Re_ℓ :

$$0 < Re_\ell < 50; \; \delta^+ = 0.7071 \; Re_\ell^{\,0.5} \qquad (5.2.3\text{-}18a)$$

$$50 < Re_\ell < 1125; \; \delta^+ = 0.4818 \; Re_\ell^{\,0.585} \qquad (5.2.3\text{-}18b)$$

$$Re_\ell > 1125; \; \delta^+ = 0.133 \; Re_\ell^{\,0.7614} \qquad (5.2.3\text{-}18c)$$

For the value of E in Eq (5.2.3-17) the following simplified

Rohsenow and Cohen correlation (75) is used

$$E = 27.73\ Pr_{\ell} \qquad (5.2.3\text{-}19)$$

(More recent correlations, while available, do not alter the results significantly.)

To approximate τ_i / τ_w in Eq (5.2.3-7), the approach of Wallis (62) can be applied in the following manner.

The momentum of both phases is governed by

$$\frac{dP}{dz} + \frac{4}{D}\tau_w = 0 \quad ; \qquad (5.2.3\text{-}20)$$

the momentum of the vapor phase is governed by

$$\alpha \frac{dP}{dz} + \frac{4\sqrt{\alpha}}{D}\tau_i = 0 \quad ; \qquad (5.2.3\text{-}21)$$

from Eqs (5.2.3-20) and (5.2.3-21) we obtain

$$\frac{\tau_i}{\tau_w} = \sqrt{\alpha} \quad ; \qquad (5.2.3\text{-}22)$$

For computational purposes, it is necessary to derive the relationship between the bulk liquid temperature, T_m, and the interfacial liquid temperature, T_δ. From the definition of the bulk liquid temperature, we have

$$T_w - T_m = \frac{\int_{A_\ell} (T - T_w)\ V_z\ dA_\ell}{\int_{A_\ell} V_z\ dA_\ell} , \qquad (5.2.3\text{-}23)$$

where A_ℓ and dA_ℓ are the area and the differential area to be occupied by liquid, respectively.

For simplicity a linear temperature distribution is assumed along the radial direction in the liquid layer. This is an excellent approximation for liquid metals because of their

high thermal conductivity. Therefore,

$$T_w - T_m = \frac{T_w - T_\delta}{\delta^+} \frac{\int_0^{\delta^+} V_z^+ \, y^+ \, dy^+}{\int_0^{\delta^+} V_z^+ \, dy^+} \qquad (5.2.3\text{-}24)$$

Thus, in the laminar zone we obtain

$$0 < \delta^+ < 5; \; V_z^+ = y^+$$

$$T_w - T_m = \frac{2}{3} (T_w - T_\delta) \qquad (5.2.3\text{-}25a)$$

In the buffer zone we obtain

$$5 < \delta^+ < 30; \; V_z^+ = -3.05 + 5 \ln y^+$$

$$T_w - T_m = \frac{T_w - T_\delta}{\delta^+} \frac{10.45 - 2.775 \, \delta^{+2} + 2.5\delta^{+2} \ln\delta^+}{12.31 - 8.05\,\delta^+ + 5\delta^+ \ln \delta^+}$$

In the case of $\delta^+ = 30$, $T_w - T_m = 0.613(T_w - T_\delta)$; in the case of $\delta^+ = 5$, $T_w - T_m = 0.66(T_w - T_\delta)$. From the above result, $(T_w - T_m)$ is approximated in this zone as

$$T_w - T_m \approx 0.64 (T_w - T_\delta) \qquad (5.2.3\text{-}25b)$$

In the turbulent zone, we obtain

$$\delta^+ > 30; \; V_z^+ = -6.45 + 6 \ln y^+$$

$$T_w - T_m = \frac{T_w - T_\delta}{\delta^+} \frac{234.9 - 4.725 \, \delta^{+2} + 3\delta^{+2} \ln \delta^+}{42.27 - 12.45\delta^+ + 6\delta^+ \ln \delta^+}$$

In the case of $\delta^+ \to \infty$, $T_w - T_m = 0.5(T_w - T_\delta)$; in the case of $\delta^+ \to 30$, $T_w - T_m = 0.613(T_w - T_\delta)$. From the above

result, $(T_w - T_m)$ is approximated in this zone as

$$T_w - T_m \approx 0.55(T_w - T_\delta) \tag{5.2.3-25c}$$

From Eq (5.2.3-17), and relating τ_w to the two-phase friction pressure drop, we obtain

$$h = \frac{1}{F_2}\rho_\ell C_{p\ell}\left(\frac{g_o}{\rho_\ell}\right)^{1/2}\left[\frac{D_h}{4}\,\phi_v^2\left(-\frac{dP}{dz}\right)_f^v\right]^{1/2} \tag{5.2.3-26}$$

Using the Blausius-type correlation for $[-(dP/dz)]_f^v$, it can be easily recognized that for turbulent flow

$$\left(-\frac{dP}{dz}\right)_f^v = 0.092\,\frac{\mu_v^{0.2}\,G^{1.8}\,x^{1.8}}{g_o\,\rho_v\,D_h^{1.2}} \tag{5.2.3-27}$$

Substituting Eq (5.2.3-27) into Eq (5.2.3-26) and rearranging the result, we derive the final form of the Nusselt number correlation as

$$Nu = \frac{0.152}{F_2}\,Pr_\ell\,Re_\ell^{0.9}\,\frac{\phi_v}{x_{tt}}$$

$$= \frac{0.152}{F_2}\,Pr_\ell\,Re_\ell^{0.9}\,\phi_\ell \tag{5.2.3-28}$$

where

$$Pr_\ell = C_{p\ell}\mu_\ell/k_\ell$$

$$Re_\ell = G(1-x)D_h/\mu_\ell$$

$$x_{tt} = \frac{\phi_v}{\phi_\ell} = \left(\frac{1-x}{x}\right)^{0.9}\left(\frac{\rho_v}{\rho_\ell}\right)^{0.5}\left(\frac{\mu_\ell}{\mu_v}\right)^{0.1}$$

by the Lockhart and Martinelli definition.

Considering the definition of the Nusselt number in terms of the bulk liquid temperature, we obtain

$$Nu_b = \frac{q''_w}{T_w - T_m} \frac{D_h}{k_\ell}$$

$$= Nu \cdot \frac{T_w - T_\delta}{T_w - T_m}$$

$$= Nu \cdot F_1 \quad , \qquad (5.2.3\text{-}29)$$

Therefore, we get the final form of the new correlation:

$$Nu_b = 0.152 \frac{F_1}{F_2} Pr_\ell \, Re_\ell^{0.9} \, \phi_\ell \qquad (5.2.3\text{-}30)$$

where

i) $Re_\ell < 50$; $F_1 = 1.5$

$$F_2 = 0.7071 \, Re_\ell^{0.5} \, Pr_\ell$$

ii) $50 < Re_\ell < 1125$;

$$F_1 = 1.563$$

$$F_2 = 5Pr_\ell + \frac{5}{E} \ln \left[1 + EPr_\ell \left(\frac{\delta^+}{5} - 1 \right)\right],$$

where $E = 0.00375 \, Pe_\ell \, [1 - \exp(-0.00375 \, Pe_\ell)]$

$$\delta^+ = 0.4818 \, Re_\ell^{0.585}$$

iii) $Re_\ell > 1125$;

$$F_1 = 1.818$$

$$F_2 = 5Pr_\ell + \frac{5}{E}(1 + 5EPr_\ell) + \frac{6}{E\gamma} \ln\left[\frac{2M+\gamma-1}{1+\gamma-2M} \times \frac{1+\gamma-\beta}{\beta+\gamma-1}\right],$$

where $\beta = 60 \dfrac{M}{\delta^+}$

$$\gamma = \sqrt{1 + \frac{10M}{E\delta^+ Pr_\ell}}$$

$$\delta^+ = 0.133\ Re_\ell^{0.7614}$$

$$M = 1 - \sqrt{\alpha}$$

The parameter ϕ_ℓ in Eqs (5.2.3-28) is taken from the empirical relation between the Zeigarnick and Litvinov work and the Lockhart and Martinelli correlation. Ziegarnick and Litvinov found that frictional pressure losses in an alkali-metal, two-phase flow with heat input are less than in an adiabatic flow. They explained this by a "push-aside" effect of the vapor flow from the interface on the main stream and the change of liquid film characteristics. The empirical relationship between their results and the Lockhart and Martinelli correlation is

$$\phi_\ell = \phi_{\ell tt}^{0.88} , \qquad (5.2.3\text{-}31)$$

where

$$\phi_{\ell tt} = \sqrt{1 + \frac{20}{x_{tt}} + \frac{1}{x_{tt}^2}} .$$

5.2.3.3 Comparison to Experiments

Several correlations are now to be compared with the Zeigarnick and Litvinov data and the data from Ref 76. The former experiments were made in the following range of parameters: heat flux at the wall up to 1.1 MW/m·s, mass flow rate 150 to 400 kg/m·s, flow quality up to 0.45, and operating pressure 0.1 to 0.2 MPa. They reported a much higher forced convection boiling sodium heat transfer coefficient than the previous results as shown in Fig 5.6. According to several experiments (e.g., Ref 77), the heat transfer correlations for alkali metals in forced convection

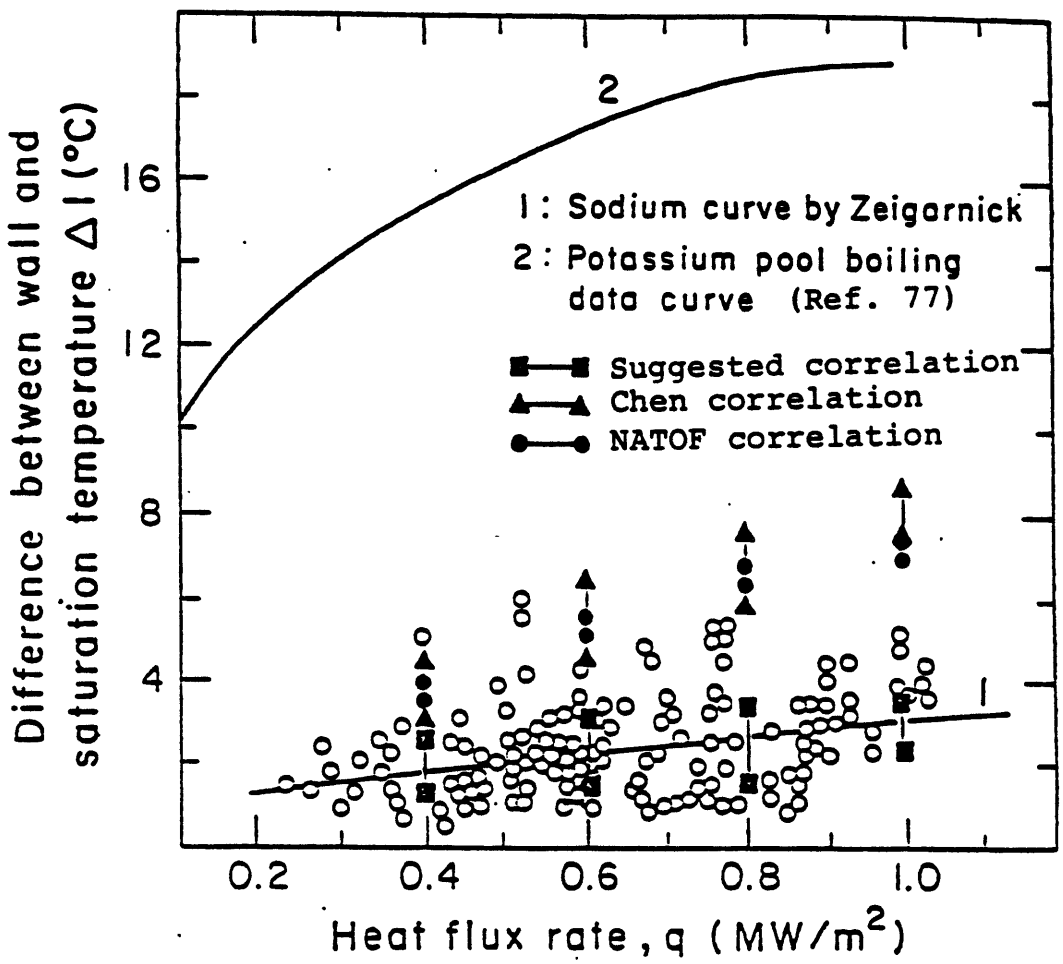

Fig. 5.6: Comparison between Data and Correlations

boiling and in pool boiling coincide. It seems that the previous results were subject to unstable boiling and uncertainties in saturation-temperature measurement. Also the results from several correlations over the whole range in the Zeigarnick and Litvinov experiments are shown in Fig 5.6. While the suggested correlation is in excellent agreement with the data over the whole range, the Chen and NATOF correlations predict a lower heat transfer coefficient.

Comparison of several correlations with the data of Ref 76 is given in Fig 5.7 where the parameters $h_{2\phi}$ and $h_{1\phi}$ are the heat transfer coefficient with boiling and without boiling at the same inlet mass flow. While the Chen correlation included both macroscopic and microscopic contributions to the wall heat transfer, the suggested correlation and the NATOF correlation included only the macroscopic contribution. The heat transfer coefficient in this experiment is lower than the Zeigarnick and Litvinov results. Furthermore, some data are seen to drop below the single-phase heat transfer coefficient. The Hoffman and Krakoviak (78) potassium data also showed that the heat transfer coefficient in unstable boiling is much lower than that in stable boiling and could be equal to the single-phase heat transfer coefficient, as are most of the data in Fig 5.7. Therefore, it can be concluded that most of the data of Ref 76 were obtained in the unstable boiling regime. While the NATOF correlation is generally in good

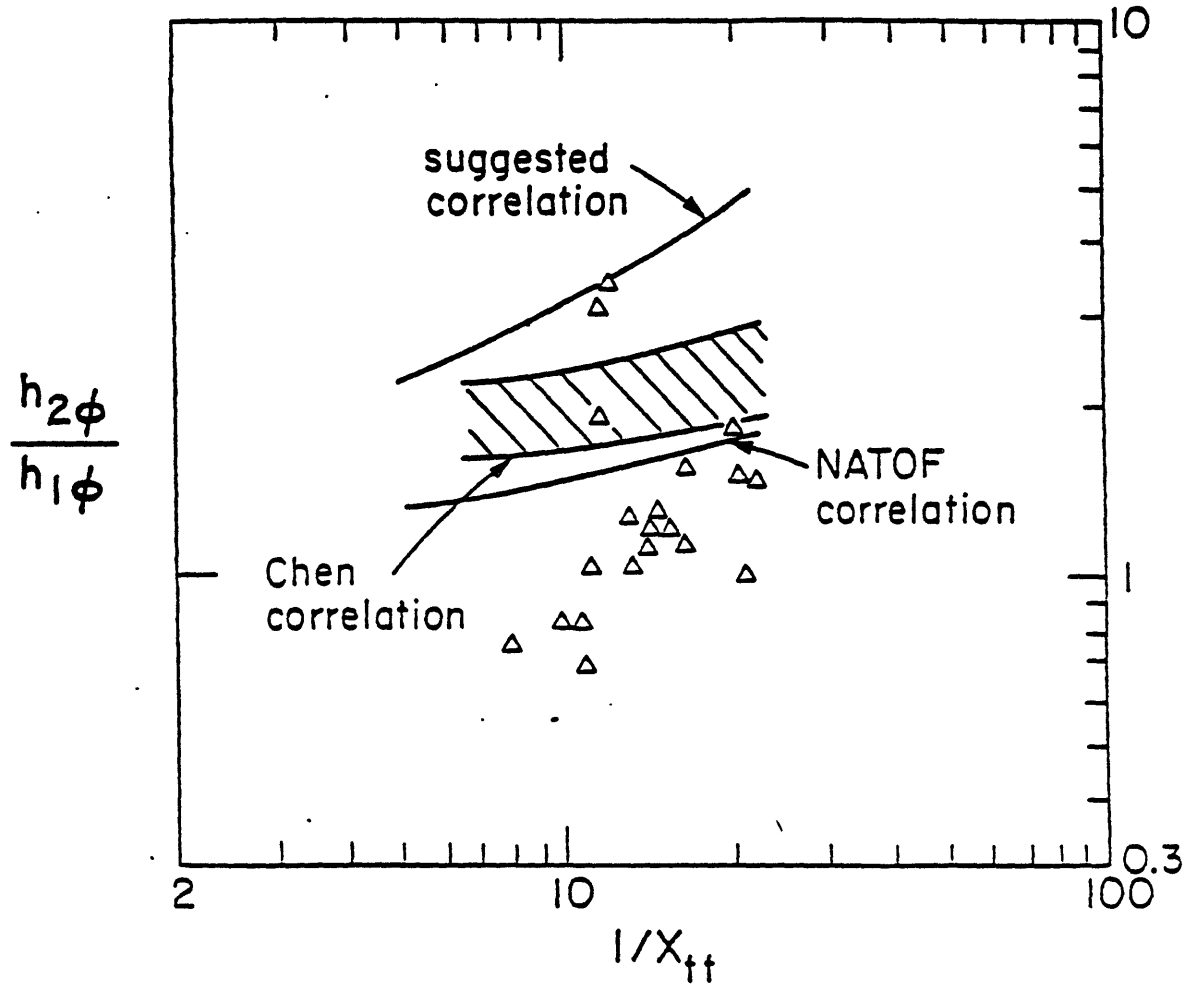

Fig. 5.7: Comparison of Correlations with GE Data

agreement with Ref 76, the suggested correlation is in good agreement with the high heat transfer coefficient of some of the latter.

To evaluate the suggested correlation, the correlation for E and the Wallis method for τ_i / τ_w were used. Sensitivity analysis showed that the effect of these parameters on the heat transfer coefficient is small. The change in the coefficient was within 10% when E and τ_i / τ_w were separately changed over the possible range of 0.0001 to 1.0 and 0.001 to 1, respectively.

5.2.4 Interfacial Mass and Energy Exchange

The exchange of mass, energy, and momentum across liquid-vapor interfaces must be explicitly given in the two-fluid model. As the interfacial exchange controls non-equilibrium phenomena, slip ratio, and mass transfer, accurate and reasonable physical models are very important in analysis of LMFBR transients.

A survey of the literature on models of mass and energy exchange is given. It is found that most of models, which have been developed for the analysis of non-metallic flows, must be modified for application to metallic flows. Here, it is assumed that mass and energy exchange at the interface is controlled either by the rate at which the latent heat for mass exchange is transported away from or into the interface, or by the rate at which vapor is supplied to the interface, whichever is smaller. The latter mechanism is described by a simple kinetic theory. The turbulent flux model is taken as the basis for description of the former mechanism, because of its easy generalization. The concept of modified mixing theory, which accounts for the energy loss of eddies, is introduced to generalize the turbulent flux model.

The proposed model is verified by two methods: one is the comparison of the predicted bulk liquid temperature to analytical results, and the other is the comparison of the void volume in the bundle estimated from experimental results with that according to the suggested model.

5.2.4.1 Literature Review

Among the models proposed to provide a basis for the mass exchange rate, the best known are the stagnant film model, the penetration model, the Reynolds analogy, and the turbulent flux model.

The main limitation of the stagnant film theory (79) lies in the assumed simple spatial dependence of parameters; the pressure, velocity, temperature, and composition depend only on the distance from the wall, and become constant when the distance exceeds the corresponding film thickness.

The penetration model, which was suggested by Higbie (80) in 1935, presents a picture of small fluid elements contacting the phase interface for brief periods during which the transient transport processes occur. Then, the fluid elements are replaced by fresh fluid from the reservoir. The penetration model leads us to the conclusion that the transport flux of properties should be proportional to the square root of the diffusivity of the material involved. This has been found to be approximately true in non-metallic flow systems.

The Reynolds analogy, based on Reynolds' postulate (65), was suggested by von Karmann (68) and established by Chilton and Colburn (81). It is well known that Reynolds' postulate breaks down for metallic flows.

The turbulent flux model developed by Spalding (82) adopted a simple visualization of the Prandtl mixing-length theory for turbulent motion in the neighborhood of an

interface. An eddy is visualized, which originates around the interface, travels transversely at a constant temperature over a distance of one mixing-length, and then is mixed with the fluid there. However, in sodium, it is expected that there are considerable energy losses from the eddies due to the high conductivity of sodium. Nevertheless, we shall use this model as the basis for a generalized model, because of its easy application and flexibility.

5.2.4.2 Model Development

The turbulent flux model assumes that mass exchange is determined by the effectiveness of energy transfer by eddies. This model uses a simple approach to describe the movement of an eddy around the vapor-liquid interface, as shown in Fig. 5.8. In Fig. 5.8, the solid lines, I.G. and I.L. represent the gas side interface and the liquid side interface. It is assumed that each eddy with bulk properties enters each region across the B.G. or B.L. lines, which are located at a distance of one mixing length in each phase, ℓ_g or ℓ_ℓ, from I.G. or I.L. Denote: h_{bg} and $h_{b\ell}$ are the bulk specific enthalpy in the gas and liquid regions, respectively.
T_g and T_ℓ are the bulk temperatures of the vapor and liquid regions, respectively.
h_{mg} and $h_{m\ell}$ are the specific enthalpy transported by eddies originated near the interface as they cross B.G. or B.L., respectively.

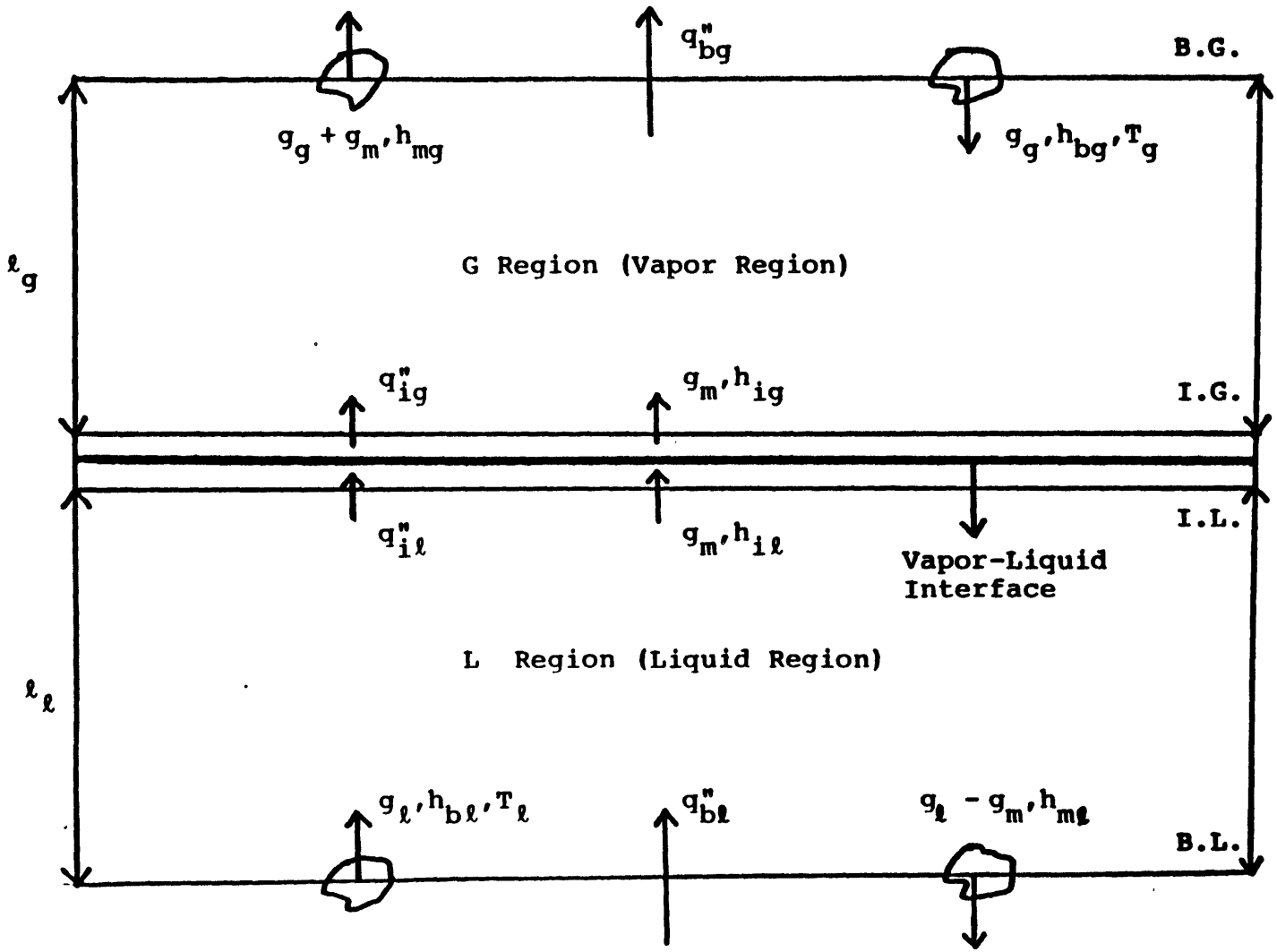

Fig. 5.8: Simple Representation of Mass and Heat Transfer around the Vapor-Liquid Interface

q''_{bg} and $q''_{b\ell}$, and q''_{ig} and $q''_{i\ell}$, are the heat flux through B.G and B.L, and through I.G and I.L, respectively. g_g and g_ℓ are the turbulent mass flux of each region, and g_m is the mass flux transferred from one phase to the other across the interface.

First, let us establish the relationship between the interface heat flux, $q''_{i\ell}$ and q''_{ig} , and the mass flux, g_m , by considering the steady state energy balance equation in the region surrounded by I.G and I.L.

$$g_m h_{i\ell} + q''_{i\ell} = g_m h_{ig} + q''_{ig} \qquad (5.2.4\text{-}1)$$

Assuming the saturation state at the interface and rearranging Eq (5.2.4-1), we obtain the relationship

$$g_m = (q''_{i\ell} - q''_{ig})/h_{fg} \qquad (5.2.4\text{-}2)$$

where h_{fg} is the latent heat of vaporization.
As the interfacial heat flux in the gas phase, q''_{ig} , is usually much smaller than $q''_{i\ell}$, a simplified expression of Eq (5.2.4-2) may be obtained by neglecting q''_{ig} .

$$g_m = q''_{i\ell}/h_{fg} \qquad (5.2.4\text{-}3)$$

This simplified equation enables us to focus on the evaluation of $q''_{i\ell}$.

The steady state liquid energy balance equation in the L region leads to the equation:

$$q''_{i\ell} = q''_{b\ell} + g_\ell (h_{b\ell} - h_{m\ell}) + g_m (h_{m\ell} - h_{s\ell}) \qquad (5.2.4\text{-}4)$$

where $h_{s\ell}$ is the specific liquid enthalpy corresponding to the saturation temperature of the above system, T_s .

Assuming a linear temperature distribution in the mixing length, ℓ_ℓ , $q''_{b\ell}$ can be expressed in terms of T_ℓ and T_s .

$$q''_{b\ell} = k_\ell (T_\ell - T_s)/\ell_\ell \qquad (5.2.4\text{-}5)$$

where k_ℓ is the molecular conductivity of liquid.

For non-metallic flows, there are negligible heat losses from eddies while they travel the distance ℓ_ℓ . Therefore, $h_{m\ell}$ is equal to $h_{s\ell}$. Then we get a simple relationship of $q''_{i\ell}$ for non-metallic flows by substituting Eq (5.2.4-5) in Eq (5.2.4-4):

$$q''_i = H_{i\ell}(T_\ell - T_s) \qquad (5.2.4\text{-}6)$$

where

$$H_{i\ell} = k_\ell/\ell_\ell + g_\ell C_{p\ell} \qquad (5.2.4\text{-}7)$$

and $C_{p\ell}$ is the specific heat of liquid

However, for metallic flows such as sodium, heat losses from eddies require a modification of the above treatment. Deissler's modified mixing-length theory (83) is taken to account for heat losses from eddies.

Fig 5.9 illustrates an eddy movement. An eddy of fluid originates at the surface 1, where its temperature is T_1 . It travels at the velocity v'_y , with the temperature T', to the surface 2, a distance ℓ_ℓ away, where T'_2 and T_2 are

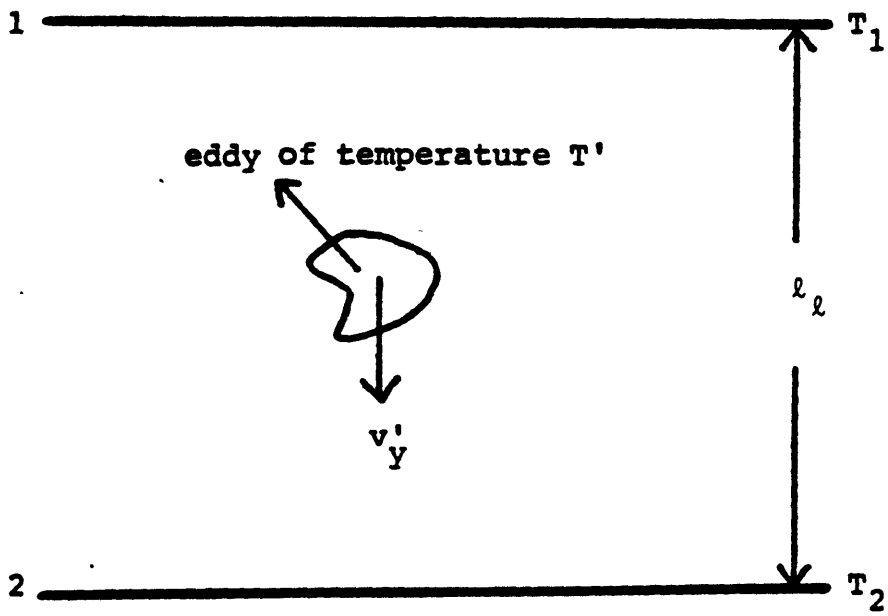

Fig. 5.9: Movement of an Eddy in a Fluid

the temperature of the eddy and of the fluid. Then the eddy breaks up and mixes with the fluid. As heat is conducted out of the eddy between the surfaces 1 and 2, T_2' is different from T_1. Based on the above picture, Deissler expressed the effectiveness of energy transfer by an eddy as E

$$E = \frac{T_2' - T_2}{T_1 - T_2} \qquad (5.2.4\text{-}8)$$

For the value of E the following simplified Rohsenow and Cohen correlation (75) is used.

$$E = 27.73\ Pr \qquad (5.2.4\text{-}9)$$

where Pr is the Prandtl number.

Now E can be expressed in terms of parameters defined in Fig 5.8.

$$h_{b\ell} - h_{m\ell} = E(h_{b\ell} - h_{i\ell}) \qquad (5.2.4\text{-}10)$$

Combining Eq (5.2.4-10) with Eq (5.2.4-4), $q''_{i\ell}$ can be expressed as follows:

$$q''_{i\ell} = k_\ell \frac{T_\ell - T_s}{\ell_\ell} + C_{p\ell}[g_\ell E + g_m(1-E)](T_\ell - T_s) \qquad (5.2.4\text{-}11)$$

Replacing Eq (5.2.4-3) with Eq (5.2.4-11) and rearranging the results, we get the equation.

$$g_m = \frac{(k_\ell/\ell_\ell + C_{p\ell} g_\ell E)(T_\ell - T_s)}{h_{fg} - C_{p\ell}(1 - E)(T_\ell - T_s)} \qquad (5.2.4\text{-}12)$$

Since h_{fg} is much greater than the value, $C_{p\ell}$ $(1-E)(T_\ell - T_s)$, for all practical purposes, Eq (5.2.4-12) can be simplified:

$$g_m = H_{i\ell}(T_\ell - T_s)/h_{fg}, \qquad (5.2.4\text{-}13)$$

where $H_i = k_\ell/\ell_\ell + C_{p\ell} g_\ell E$ (5.2.4-14)

Let us compare Eqs (5.2.4-6) and (5.2.4-7) with Eqs (5.2.4-13) and (5.2.4-14). We notice that the mass flux obtained by Eqs (5.2.4-13) and (5.2.4-14) is always less than that obtained by Eqs (5.2.4-6) and (5.2.4-7), because E is always less than 1. Physically this implies that energy loss from an eddy lessens the effectiveness of energy transfer by the eddy.

The unknown variables in Eq (5.2.4-14), g_ℓ and ℓ_ℓ, are defined by the Prandtl momentum transfer theory. The rate of momentum transfer by eddies per unit area, τ_t, and turbulent mass flux, g_ℓ, are expressed as follows:

$$\tau_t = \rho_\ell \ell_\ell \left(\frac{dV_z}{dy}\right)^2 \qquad (5.2.4\text{-}15)$$

$$g_\ell = \rho_\ell \sqrt{\overline{v_y'^2}} = \rho_\ell \ell_\ell \left(\frac{dV_z}{dy}\right) \qquad (5.2.4\text{-}16)$$

where ρ_ℓ and V_z are the liquid density and time averaged axial flow velocity, and $\sqrt{\overline{v_y'^2}}$ is the intensity of turbulence when it is divided by V_z. From Eq (5.2.4-15) and (5.2.4-16), g_ℓ can be expressed in terms of τ_t.

$$g_\ell = \sqrt{\rho_\ell \tau_t} \qquad (5.2.4\text{-}17)$$

τ_t can be approximated by the interfacial stress, τ_i . For an annular flow of sodium, the correlation of Eq. (5.2.5-19) can be used :

$$\tau_i = C_{fi} \frac{\rho_v V_r^2}{2} , \qquad (5.2.4\text{-}18)$$

where $C_{fi} = 0.005(1 + 234.3(1 - \sqrt{\alpha})^{1.15})$

$V = V_v - V_\ell$,

and α and ρ_v are the volumetric fraction of vapor and the vapor density.

The simplest relationship for ℓ_ℓ suggested by Prandtl (66) would be one of direct proportionality to the distance from the solid wall, y.

$$\ell_\ell = \xi\, y \qquad (5.2.4\text{-}19)$$

where ξ is a constant value.

In a turbulent pipe flow, he suggested 0.4 for ξ .

In summary the interfacial heat flux, $q''_{i\ell}$ and the mass

flux, g_m , can be calculated as follows:

$$q''_{i\ell} = H_i(T_\ell - T_s).$$

$$g_m = q''_{i\ell}/h_{fg}, \qquad (5.2.4\text{-}20)$$

where $H_{i\ell} = k_\ell/\ell_\ell + C_{p\ell} g_\ell E$

$$E = 27.73\ Pr$$

$$\ell_\ell = 0.4\delta$$

$$g_\ell = \sqrt{\rho_\ell \tau_i}$$

$$\tau_i = C_{fi} \frac{\rho_v V_r^2}{2}$$

$$C_{fi} = 0.005(1 + 234.3(1 - \sqrt{\alpha})^{1.15})$$

Kowalchuk and Sonin (84) reasoned that mass exchange in the interface is controlled either by the rate at which the latent heat for mass exchange is tranpsorted away from the interface, or by the rate at which the vapor is supplied to the interface, whichever is smaller. These two mechanisms are in competition with each other; when the amount of supplied vapor exceeds the capability to transport latent heat required for phase transformation into the bulk fluid, mass exchange is controlled by the former mechanism. These mechanisms are referred to as the latent heat transport

control mechanism and vapor supply control mechanism, respectively.

The vapor supply control mechanism can be viewed as the net effusive molecular flow between two quantities- a rate of arrival of molecules from the vapor space toward the interface and a rate of departure of molecules from the surface of liquid into the vapor space. While the turbulent flux model represents the latent heat transport mechanism, the vapor supply control mechanism can be described by a kinetic theory.

From a simple kinetic theory it can be shown that, in a stationary container of molecules, the mass rate of flow of molecules passing through an interface is given by

$$j = \left(\frac{M}{2\pi R}\right)^{\frac{1}{2}} \frac{P}{T^{\frac{1}{2}}} \qquad (5.2.4\text{-}21)$$

where j: efflux of molecules moving in one direction

M: molecular weight

R: universal gas constant

P and T: pressure and temperature

The net molecular flux through the interface of liquid-vapor is difference between the fluxes in the either direction

$$q_m = \left(\frac{M}{2\pi R}\right)^{\frac{1}{2}} \left(\frac{P_\ell}{T_\ell^{\frac{1}{2}}} - \frac{P_v}{T_v^{\frac{1}{2}}}\right) \qquad (5.2.4\text{-}22)$$

where v and ℓ denote vapor and liquid.

Following Schrage (85) who introduced γ to account for

the net motion of the vapor towards the surface which is superimposed on the assumed Maxwellian distribution, Eq (5.2.4-22) is rewritten in the form

$$g_m = \left(\frac{M}{2\pi R}\right)^{\frac{1}{2}} \left(\sigma_e \frac{P_\ell}{T_\ell^{\frac{1}{2}}} - \gamma\sigma_c \frac{P_v}{T_v^{\frac{1}{2}}}\right) \qquad (5.2.4\text{-}23)$$

where σ_e and σ_c are evaporation and condensation coefficients which are usually taken to be the same and are written generally as σ. γ is defined as that fraction of the molecules striking the surface which actually do condense. For a very small ratio of overall speed to a characteristic molecular velocity Silver and Simpson (86) suggested a simplified form of Eq (5.2.4-23).

$$g_m = \frac{\sigma}{2-\sigma} \left(\frac{M}{2\pi R}\right)^{\frac{1}{2}} \left(\frac{P_\ell}{T_\ell^{\frac{1}{2}}} - \frac{P_v}{T_v^{\frac{1}{2}}}\right) \qquad (5.2.4\text{-}24)$$

Assuming small differences in pressure and temperature and using the Clausius-Clapeyon relationship, we can arrive at a final form for a heat transfer coefficient, $H_{i\ell}$ for the vapor supply control mechanism

$$H_{i\ell} = \frac{\sigma}{2-\sigma} \left(\frac{M}{2\pi R}\right)^{\frac{1}{2}} \frac{\rho_v^2 \, h_{fg}^2}{P \sqrt{T_s}} \qquad (5.2.4\text{-}25)$$

Experiments with potassium and sodium vapor indicate a considerable reduction in the value of the condensation coefficient from near unity at low pressure to below 0.1 near atmospheric pressure. Wilcox and Rohsenow (87) have

considered the precision with which measurements of the condensation coefficient can be made. They conclude that the value should be unity and the reduction in the condensation coefficient with pressure is the result of increasing random errors with pressure. We adopt this here.

5.2.4.3 Model Validation

Two methods are designed for the validation of the suggested model. Numerical results for the methods are obtained by a 2-D numerical simulation of the P3A test (88) for which THERMIT-6S with the suggested model is used.

Indirect methods must be developed to verify the suggested model because of the lack of experimental data concerning the mass exchange of sodium. One of them is to compare the bulk liquid temperature from the suggested model with the values determined analytically. The analytical bulk liquid temperature can be predicted by using the definition of the bulk liquid temperature in the same way derived in Section 5.2.3. From Eq (5.2.3-25) we may approximate $(T_w - T_\ell)$ for the turbulent zone in terms of $(T_w - T_\delta)$ as follows:

$$T_w - T_\ell = 0.55(T_w - T_\delta) \qquad (5.2.4\text{-}26)$$

Fig 5.10 shows results, calculated from Eq (5.2.4-26), from THERMIT-6S with the suggested model, and according to the assumption of thermal equilibrium. In the equilibrium state, liquid temperature is forced to be equal to

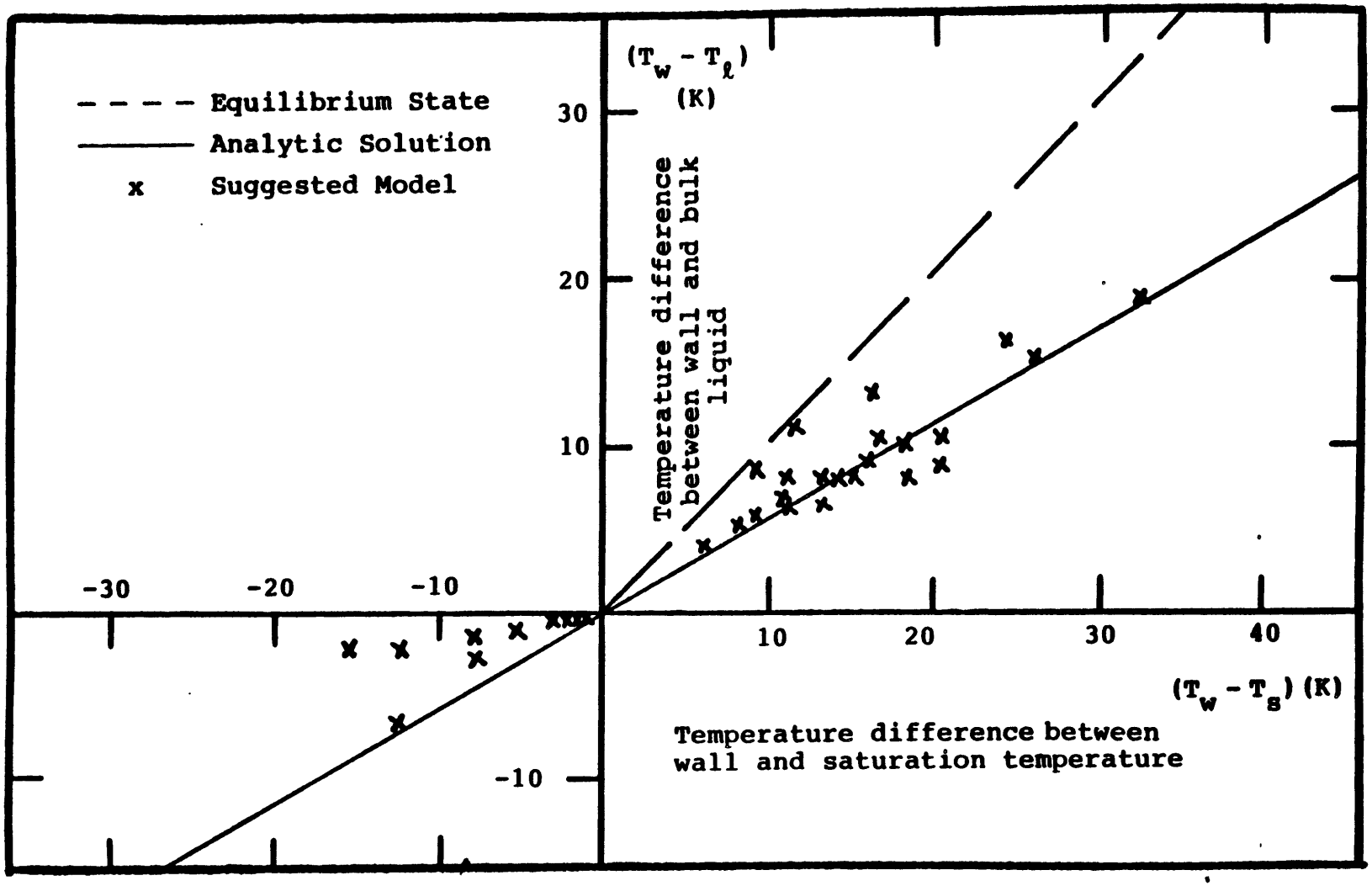

Fig. 5.10: Comparison between Analytic Solution and Results Calculated According to the Suggested Model

saturation temperature, if vapor temperature is assumed to be in the saturation state. As, in the equilibrium state, no vapor can exist in the subcooled region, that is, the region with the negative ($T_w - T_s$), the dashed line to represent the equilibrium state appears only in the evaporation region with positive ($T_w - T_s$) in Fig 5.10. In both the evaporation and subcooled regions, most results predicted by the suggested model fall between results from the equilibrium state and analytical results.

The second method to verify the suggested model is to compare the void volume in the bundle as a function of time after boiling. A comparison of inlet and outlet bundle flowmeter readings led to prediction of void volume production rates before the voids reached the exit flowmeter and upset further readings. To account for the bundle outlet flowmeter FE 2-1 reading 4% lower than the bundle inlet flowmeter FE 1-1 at the start of the P3A LOF transient, two normalization methods were used to obtain the void volume. (Ref 88) In method A, the two flowmeter readings were made to coincide at the 8.8 second boiling inception time by adjusting FE 2-1 gain to zero. In method B, the flowmeter zeros and flowmeter amplitudes at steady state were made to agree. These two methods should span the uncertainty in determination of the void volume, which is proportional to the enclosed area between the two flowmeter curves.

Fig 5.11 shows the void volumes in the bundle as a

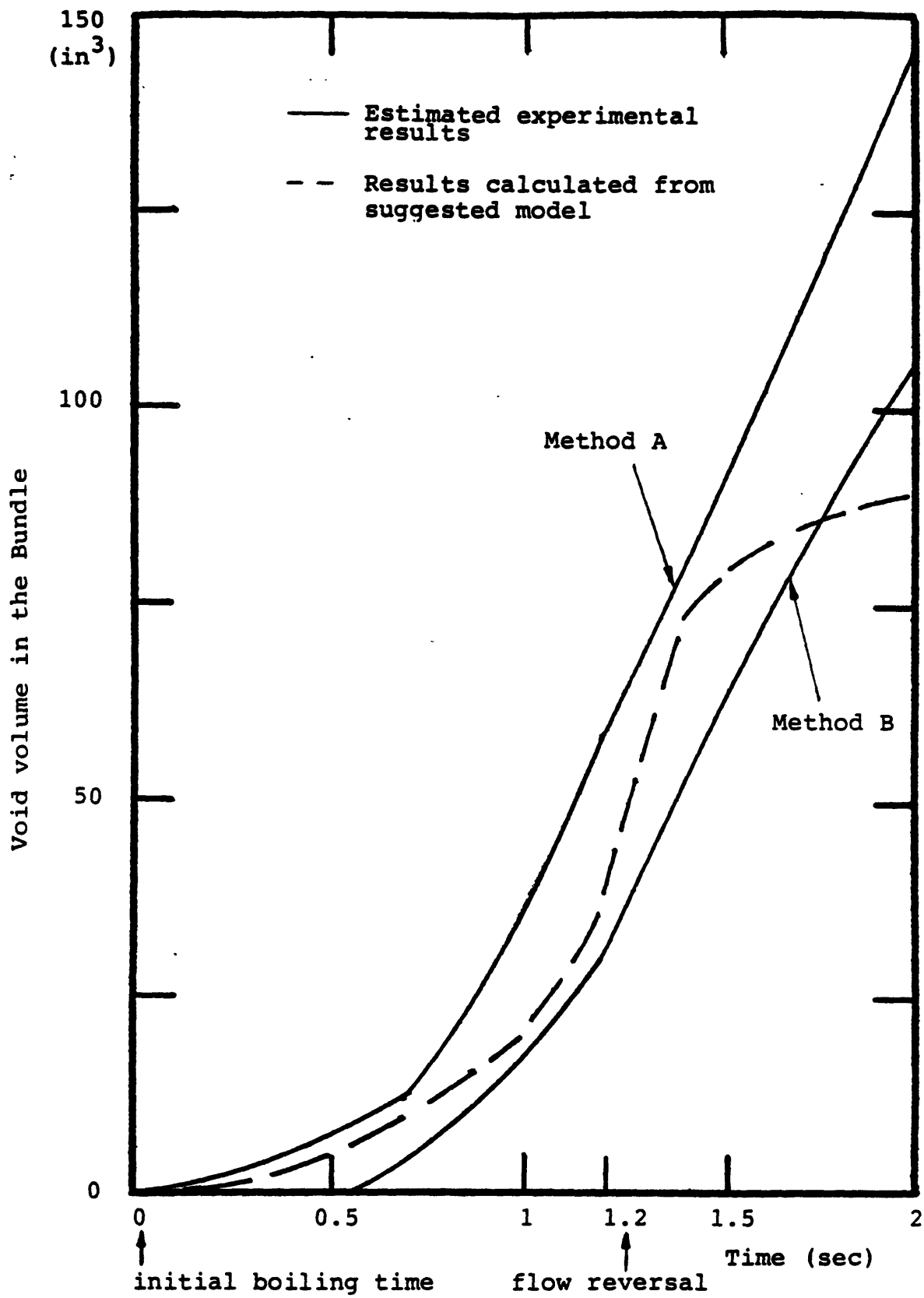

Fig. 5.11: Comparison of Void Volume in the Fuel Bundle between Estimated Experimental Results and Results from the Suggested Model

function of time after boiling, which are estimated from experimental and calculational results, respectively. The experimental estimation was given in Ref 88. Some of the void volume was undoubtedly sodium vapor, but an indeterminate amount was also fission gas released from rupturing of fuel pins. The void volume from the calculational results is less than that by method A, but greater than that by method B, up to 1.75 seconds, when failure of fuel pin clad and release of fission gas into the sodium vapor occurred.

At 1.1 seconds just before flow reversal takes place in the computation, as the test section is completely voided in the radial direction, a high rate of vapor generation is noted. As a result, pressure built up in the bundle causes the inlet flow to be reversed. These physical processes result in the rapid propagation of the void in the bundle in both the downward and upward directions until the void reaches the upper plenum. Afterwards, the void volume calculated by the present code is almost flattened.

5.2.5 Interfacial Momentum Exchange

Interfacial momentum exchange controls the slip ratio, which is one of the most important factors in the analysis of two-phase flow. Autruffe (89) derived a correlation for the vapor-liquid drag coefficient of sodium by using data from Ref 63. As his work included the effects of both liquid film and droplets for the evaluation of interfacial drag coefficient, his correlation predicts a much higher interfacial drag coefficient than other correlations. Here, methods to calculate momentum transfer by droplets will be presented so that the interfacial drag coefficient for liquid film can be derived. The results are compared to experimental data and correlations, for non-metallic flows.

5.2.5.1 Analytical Models

A one-dimensional, steady-state flow model is now to be developed for vertical upward adiabatic flow. For annular-dispersed flow, the vapor momentum balance equation should account for a momentum exchange between vapor and droplets, and can be stated as:

$$\frac{d}{dz}\left(\alpha_g \rho_g U_g^2\right) + \alpha_g \frac{dP}{dz} = -F_{fi} - F_{di} - \alpha_g \rho_g g, \qquad (5.2.5\text{-}1)$$

where F_{fi} and F_{di} are the momentum exchange rates, per unit volume, from vapor to liquid film and to droplets, respectively.

Assuming uniform dispersion of spherical droplets of the same diameter, D_d , F_{di} is expressed in an empirical form

as

$$F_{di} = A_i C_d \frac{\rho_g}{2} (U_g - U_{\ell d})^2 , \qquad (5.2.5\text{-}2)$$

where A_i is the interfacial area of droplets per unit volume, and C_d is the drag coefficient.

The quantity A_i can be expressed in terms of the droplet fraction, $\alpha_{\ell d}$ as

$$A_i = 6\ \alpha_{\ell d}/D_d \qquad (5.2.5\text{-}3)$$

An expression obtained by Carofano and McManus (90), who correlated the drag coefficient for falling droplets undergoing distortion of shape, is used for C_d :

$$C_d = 0.271\ Re_d^{0.217} , \quad 400 \leq Re_d \leq 10{,}000 \qquad (5.2.5\text{-}4)$$

where Re_d is the Reynolds number for a droplet.

$$Re_d = \frac{\rho_\ell U_{\ell d} D_d}{\mu_\ell}$$

As an appropriate description of the entrained droplet velocity and diameter as a function of the flow condition is not available, $U_{\ell d}$ is assumed to be one-half of U_g , and D_d is determined by the work of Smith (91) as

$$D_d = 0.0122 \text{ cm} \qquad (5.2.5\text{-}5)$$

The criterion used to establish a change in the droplet area is that used by Rabin et al. (92). Droplet break-up is considered to occur when the following expression is

satisfied:

$$\frac{We}{Re_d^{0.5}} > 1.0 \qquad (5.2.5\text{-}6)$$

where We is the Weber number.

It is also assumed that once droplet shatter occurs, the original droplet diameter will be reduced to one-third of the initial value, as Martindale and Smith suggested (93).

The liquid film momentum balance equation can be written as

$$\frac{d}{dz}(\alpha_{\ell f}\,\rho_\ell\,U_{\ell f}^2) + \alpha_{\ell f}\frac{dP}{dz} = F_{fi} - F_{w\ell} - \alpha_{\ell f}\,\rho_\ell\,g, \qquad (5.2.5\text{-}7)$$

where $F_{w\ell}$ is the liquid wall friction force per unit volume.

Equation (5.2.1-3) is used to calculate $U_{\ell f}$ for given G, x, and $\alpha_{\ell f}$, and F_{di} is obtained by adding Eq (5.2.5-1) to Eq (5.2.5-7):

$$F_{di} = -\frac{d}{dz}(\alpha_g\rho_g U_g^2) - \frac{d}{dz}(\alpha_{\ell f}\rho_\ell U_{\ell f}^2) - (\alpha_g + \alpha_{\ell f})\frac{dP}{dz} - (\alpha_\ell\rho_\ell + \alpha_g\rho_g)g - F_{w\ell} \qquad (5.2.5\text{-}8)$$

where $F_{w\ell} = \phi_\ell^2\,F_{wl\phi}$ (5.2.5-9)

$$F_{wl\phi} = f_\ell\,\frac{\rho_\ell(\alpha_\ell U_{\ell f})^2}{2D} \qquad (5.2.5\text{-}10)$$

$$f_\ell = 0.184/Re_\ell^{0.2} \qquad (5.2.5\text{-}11)$$

$$Re_\ell = \frac{D\rho_\ell\alpha_{\ell f}U_{\ell f}}{\mu_\ell} \qquad (5.2.5\text{-}12)$$

D: tube diameter

Using the definition of the liquid entrainment fraction, E, and the following relation for G', we obtain

$$G'=(1-E)(1-x)G \tag{5.2.5-13}$$

Eqs (5.2.5-10) and (5.2.5-12) can be rewritten in terms of G' as

$$F_{wl\phi} = f_{\ell} \cdot \frac{G'^2}{2D\rho_{\ell}} \tag{5.2.5-14}$$

$$Re_{\ell} = \frac{DG'}{\mu_{\ell}} \tag{5.2.5-15}$$

The two-phase multiplier, ϕ_{ℓ}^2 , was evaluated by the Lockhart-Martinelli correlation.

As, the liquid entrainment fraction, E, which is needed to calculate the acceleration loss of both vapor and liquid, and the wall friction loss, are functions of $\alpha_{\ell d}$ in Eq (5.2.1-6), $\alpha_{\ell d}$ is iterated until F_{di} in Eq (5.2.5-2) matches F_{di} in Eq (5.2.5-8). For given G, x, and $\alpha_{\ell f}$, F_{fi} can be calculated by the following procedure:

1. Guess $\alpha_{\ell d}$.
2. Calculate acceleration loss by both liquid and vapor and pressure loss by gravity and wall friction loss.
3. Calculate F_{di} from Eq (5.2.5-8).
4. Calculate $\alpha_{\ell d}$ from Eqs (5.2.5-2) and (5.2.5-3).
5. Reiterate the procedure until the change in $\alpha_{\ell d}$ is sufficiently small.
6. Calculate F_{fi} from Eq (5.2.5-7).

5.2.5.2 Model Validation

The above procedure is now applied to determine F_{fi} from the sodium boiling experiments of Kaiser et al. (63). The term F_{fi} in Eq (5.2.5-1) is related to the interfacial friction, τ_i , per unit area as

$$F_{fi} = \frac{4\sqrt{\alpha_g}}{D} \tau_i, \qquad (5.2.5\text{-}16)$$

where $$\tau_i = C_{fi} \frac{1}{2} \rho_g (U_g - U_{\ell f})^2 \qquad (5.2.5\text{-}17)$$

In Fig 5.12, data for C_{fi} in Eq (5.2.5-17) obtained from our analysis of Kaiser et al. (63) are compared to those for C_{fi} of Wallis (62) and of Moeck (94), which were derived from air-water experiments. Moeck obtained the air-water data in Fig 5.12 by using his film flow model and droplet interchange model to analyze three sets of data (95-97). He calculated C_{fi} by subtracting droplet drag, acceleration of net entrainment, vapor acceleration, and vapor static head from the overall vapor pressure drop. The important result that we note is that the data cluster into a single band, regardless of

1. vapor Reynolds number
2. tube diameter
3. total liquid flow rate.

Earlier work by Autruffe included the effects of both liquid film and droplets for the evaluation of C_{fi} :

$$F_i = F_{fi} + F_{di} \qquad (5.2.5\text{-}18)$$

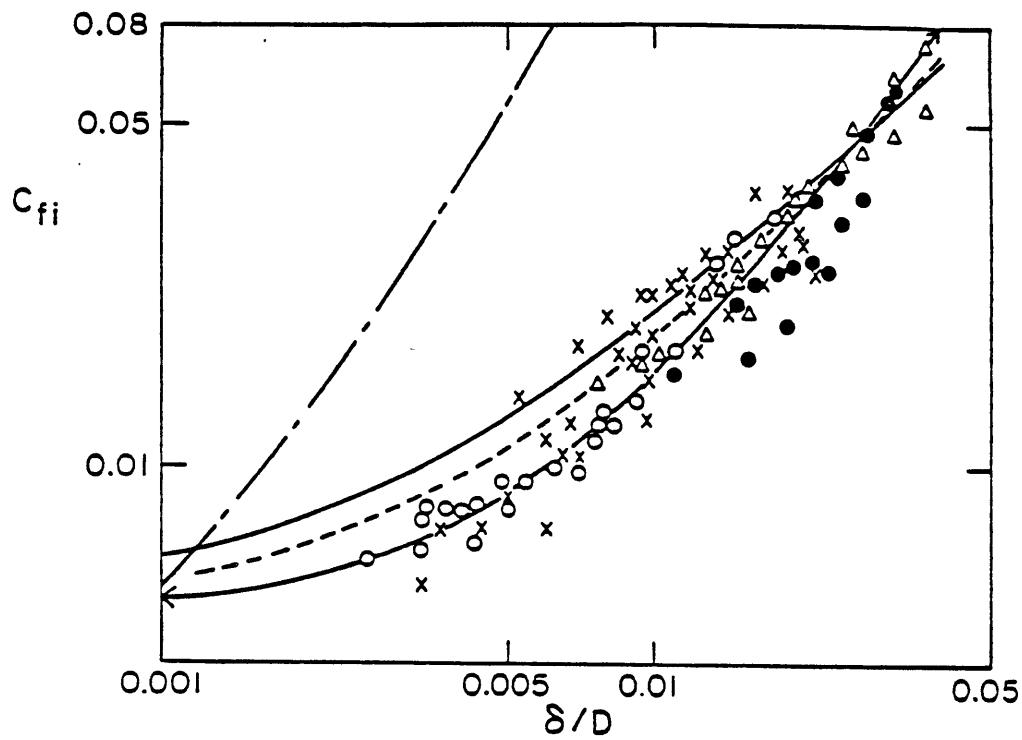

Wallis correlation $C_W = 0.005\,(1 + 300\,\frac{\delta}{D})$ ——

Moeck correlation $C_M = 0.005\,(1 + 1458\,(\frac{\delta}{D})^{1.42})$ ⟷

Suggested correlation $C_S = 0.005\,(1 + 520\,(\frac{\delta}{D})^{1.15})$ ----

Autruffe correlation $C_A = 4.36\,\frac{\delta}{D}\,(1 + 300\,\frac{\delta}{D})^{0.95} / (1 - \frac{2\delta}{D})$ ——

Air-Water Flow Data	Sodium Data
○ 31.75 mm tube (Ref.(95))	× 9 mm tube (Ref.(63))
● 9.53 mm tube (Ref.(96))	
△ 12.7 mm tube (Ref.(97))	

Fig. 5.12: Interface Drag Coefficient to Dimensionless Film Thickness

where F_i is total momentum exchange between liquid and vapor.

As a result, his correlation predicts a much higher interfacial drag coefficient than other correlations. Several problems can be raised when Autruffe's correlation is applied. First, as his correlation is derived for annular-dispersed, two-phase flow of sodium, it may not be appropriate for the early stage of boiling transients, especially low-flow/low-power LMFBR accidents where pure annular flow is dominant. Second, since his correlation predicts an average liquid velocity that is much higher than the real liquid film velocity, the wall heat transfer coefficient, which is a function of the liquid film velocity, will be mispredicted.

As the sodium data lead to values of C_{fi} that have an upper bound represented by the Wallis correlation and a lower bound represented by the Moeck correlation, an intermediate correlation is recommended for C_{fi} of sodium:

$$C_{fi} = (0.005(1 + 520 \left(\frac{\delta}{D}\right)^{1.15}) \qquad (5.2.5\text{-}19)$$

5.3 Constitutive Relations in Post-Dryout Region

After flow reversal the subcooled inlet is prevented from entering channels. Then, the liquid film remaining on the hot wall is rapidly evaporated and eventually dryout will occur. Especially, in the low flow/high power transients, the region and period of dryout are extensive and long enough to have considerable effects on system behavior. Unfortunately, few studies have been done on the post-dryout region. Therefore, a simple dryout criterion and post-dryout models are implemented in the present code.

The experiments analyzed by Autruffe (89) indicated that vapor did not come into contact with the wall until the void fraction exceeded 0.957. This value of void fraction 0.957 is used for a dryout criterion. It is assumed that for a void fraction below 0.957 the entire surface of the rod is coated with liquid. As the void fraction increases from 0.957 to 1.0, the liquid contact fraction decreases linearly from 1.0 to 0.0, while the vapor contact fraction goes from 0.0 to 1.0. Therefore, the wall contact areas of liquid and vapor after dryout are estimated in terms of the void fraction and the criterion of dryout 0.957.

$$Cf_\ell = 1.0, \quad Cf_v = 0.0, \quad \text{for } 0 \le \alpha \le 0.957 \qquad (5.3.1)$$

$$Cf_\ell = \frac{1.0 - \alpha}{0.043}, \quad Cf_v = \frac{\alpha - 0.957}{0.043}, \quad \text{for } 1.0 \ge \alpha \ge 0.957 \qquad (5.3.2)$$

where Cf_ℓ and Cf_v are the fractions of the wall contact area of liquid and vapor, respectively.

These contact area fractions multiplied by the total wall area A_w in a cell become the liquid contact area $A_{w\ell}$ and vapor contact area A_{wv} . If these contact areas are divided by the fluid volume, we obtain the wall contact area density $\frac{1}{L_w}$ for the LMFBR geometry.

$$\frac{1}{L_{w\ell}} = \frac{A_{w\ell}}{V_f} = Cf_\ell \frac{1}{L_w} \tag{5.2.3}$$

$$\frac{1}{L_{wv}} = \frac{A_{wv}}{V_f} = Cf_v \frac{1}{L_w} , \tag{5.2.4}$$

where $$\frac{1}{L_w} = \frac{A_w}{V_f} = \frac{4}{D_e} = \frac{4}{D[2\sqrt{3}(P/D)^2 - \pi]} \tag{5.2.5}$$

The total heat flow Q_{wt} through the fuel surface area A_w per unit volume is contributed by the heat transferred to or from liquid and vapor, $Q_{w\ell}$ and Q_{wv} .

$$Q_{wt} = Q_{w\ell} + Q_{wv} \tag{5.2.6}$$

Using Eqs (5.2.3) and (5.2.4) each component can be expressed as follows:

$$Q_{w\ell} = \frac{1}{L_{w\ell}} q''_{w\ell} \tag{5.2.7}$$

$$Q_{wv} = \frac{1}{L_{wv}} q''_{wv} \tag{5.2.8}$$

The heat transfer coefficient for the liquid film in two-phase flow, which is described in Sections 5.2.3.2, is used for $q''_{w\ell}$. For q''_{wv} the Dittus-Boelter correlation

is used.

$$q''_{w\ell} = Nu_\ell \frac{k_\ell}{D_e} (T_w - T_\ell) \tag{5.3-9}$$

$$q''_{wv} = Nu_v \frac{k_v}{D_e} (T_w - T_v) \tag{5.3-10}$$

where $$Nu_\ell = 0.152 \frac{F_2}{F_1} Pr_\ell \, Re_\ell^{0.9} \, \phi_\ell \tag{5.3-11}$$

$$Nu_v = 0.023 \, Re_v^{0.8} \, Pr_v^{0.4} \tag{5.3-12}$$

$$Re_\ell = G(1 - x) D_e / \mu_\ell$$

$$Re_v = G \, x \, D_e / \mu_v$$

Refer to Eqs (5.2.3-30) and (5.2.3-31) for F_1, F_2, and ϕ_ℓ

For the axial wall liquid friction in the post-dryout region, the correlation of the wall friction factor for annular flow is assumed to hold true. Accounting for the reduced contact area, we have

$$F_{wz\ell d} = Cf_\ell \, F_{wz\ell a} \tag{5.3-13}$$

where $F_{wz\ell d}$ and $F_{wz\ell a}$: liquid axial wall friction force per unit volume for post-dryout and annular flow,

respectively.

$$F_{wz\ell a} = \phi_\ell^2 \, f_\ell \, \frac{\rho_\ell j_\ell^2}{2D_e} , \qquad (5.3\text{-}14)$$

where $\phi_\ell = (1 + \frac{20}{X_{tt}} + \frac{1}{X_{tt}^2})^{0.88}$

$j_\ell = \alpha_\ell v_\ell$

In Eq (5.3.14) f_ℓ is calculated by using correlations described in Section 5.1.1, but Re_ℓ is defined as

$$Re_\ell = \frac{\rho_\ell D_e j_\ell}{\mu_\ell}$$

In the post-dryout region, we can consider the region in which vapor contacts the wall as a single-phase region. Therefore, for this contacting area, we have

$$F_{wzvd} = Cf_v \, F_{wzv} \qquad (5.3\text{-}15)$$

where F_{wzvd} is vapor axial wall friction force per unit volume for post-dryout, and F_{wvz} is the single phase vapor flow friction force given by

$$F_{wzv} = f_v \, \frac{\rho_v U_v^2}{2D_e} \qquad (5.3\text{-}16)$$

Here, f_v is calculated by the same correlation in Section 5.2.2, but Re_v is defined as

$$Re = \rho_v D_e U_v / \mu_v$$

For the transverse friction factor in post-dryout flows with both liquid and vapor Reynolds numbers in the laminar regime, Eq (5.2.2-1) is multiplied by the wall contact areas, respectively.

$$\Delta p_\ell = Cf_\ell \cdot f_\ell \frac{\Delta t}{D_v} \frac{\rho_\ell U^2_{\ell max}}{2} \qquad (5.3\text{-}17)$$

$$\Delta p_v = Cf_v \; f_v \frac{\Delta t}{D_v} \cdot \frac{\rho_v U^2_{v max}}{2} \; , \qquad (5.3\text{-}18)$$

where $f_\ell = \frac{180}{Re_\ell}$, $Re_\ell = \alpha_\ell \rho_\ell |U_{\ell max}| D_v / \mu_\ell$

$f_v = \frac{180}{Re_v}$, $Re_v = \alpha_v \rho_v |U_{vmax}| D_v / \mu_v$

If either liquid or vapor is in the turbulent flow regime, the Ishihara correlation (64) is used, which was described in Section 5.2.2.

$$F_{wt\ell a} = f \frac{1}{D_v} \frac{G^2}{2\rho_\ell} \phi^2_{\ell o} \qquad (5.3\text{-}19)$$

where G and f are the total mass flow rate and friction factor, respectively.

For the transverse friction factor in post-dryout flows Eq (5.3.19) is split into two components in such a way that the proper limits are maintained as the void fraction

approaches zero or one. Thus we have

$$F_{wt\ell d} = Cf_\ell \; f \frac{1}{D_v} \frac{G^2}{2\rho_\ell} \left(1 + \frac{8}{X_{tt}}\right) \tag{5.3-20}$$

$$F_{wtvd} = Cf_v \; f \frac{1}{D_v} \frac{G^2}{2\rho_\ell} \frac{1}{X_{tt}^2} \tag{5.3-21}$$

In the same manner, the interfacial area can be corrected by the fraction of Cf_ℓ , if we assume that a very thin and smooth liquid film after dryout remains on the wall.

$$A_i = A_{it} \, Cf_\ell \tag{5.3-22}$$

where A_i and A_{it} : corrected interfacial area, and interfacial area for a given void fraction when the wall is totally covered by liquid.

The complexity of the interfacial structure makes it difficult to determine the interfacial area, A_{it} . Therefore, a simple slug model of the interfacial area is implemented in THERMIT-6S. In the slug model void is assumed to be in the shape of cylinder which fills up a channel. By this assumption the void fraction can be the functions of axial length of the control volume Δz and the axial length filled up with vapor, Δz_v .

$$\alpha = \frac{V_v}{V_f} = \frac{A_f \, \Delta z_v}{A_f \, \Delta z} = \frac{\Delta z_v}{\Delta z} \tag{5.3-23}$$

where V_v and V_f : vapor and total flow volume

A_f : total flow area

Then, the area density $\frac{1}{L_a}$ can be expressed in terms of geometry and void fraction.

$$\frac{1}{L_a} = \frac{A_{it}}{V_f} = \frac{0.5\ \pi D}{A_f}\ \alpha, \tag{5.3-24}$$

where $$A_f = \frac{D^2}{8}\ [2\sqrt{3}\ (\frac{P}{D})^2 - \pi] \tag{5.3-25}$$

The area density of post-dryout $\frac{1}{L_{ap}}$ is expressed in terms of the contact area fraction, Cf_ℓ :

$$\frac{1}{L_{ap}} = \frac{1}{L_a}\ Cf_\ell \tag{5.3-26}$$

This area density $\frac{1}{L_{ap}}$ will be multiplied by interfacial mass and energy flux to get the rates of interfacial mass and energy exchange per unit volume, respectively. After dryout, most of liquid is in the form of droplets which are almost homogenized with vapor. In order to implement this condition, momentum exchange after dryout is not accounted for by the interfacial area fraction. For complete equations refer to Table 5.3 and 5.4. Note that most physical models for post-dryout are based on the liquid film models which are developed for pre-dryout. However, when the wall is hot enough, there is little liquid left on the wall and the droplets play an important role in transferring mass and energy. As, presently, effects of droplets are not

considered in most of models for the present code, future work for them is recommended.

TABLE 5.3

THERMIT-6S Wall Friction and Heat Transfer Models

		Single Phase Liquid Region ($\alpha=0$)		Pre-Dryout Region ($0<\alpha<0.957$)		Post-Dryout Region ($0.957<\alpha<1$)		Single Phase Vapor Region ($\alpha=1$)	
Wall Contact Area Fraction (Cf) and Wall Contact Area Density ($1/L_w$)	Liquid	$Cf_\ell=1$	$1/L_{w\ell} = 1/L_w = \frac{4}{D_e} = \frac{4\pi}{D[2\sqrt{3}(\frac{P}{D})^2-\pi]}$	$Cf_\ell=1$	$1/L_{w\ell}=1/L_w$	$Cf_\ell = \frac{1-\alpha}{1-0.957}$	$1/L_{w\ell} = Cf_\ell/L_w$	$Cf_\ell=0$	$1/L_{w\ell} = 0$
	Vapor	$Cf_v=0$	$1/L_{wv}=0$	$Cf_v=0$	$1/L_{wv}=0$	$Cf_v = 1-Cf_\ell$	$1/L_{wv} = Cf_v/L_w$	$Cf_v=1$	$1/L_{wv} = 1/L_w$
	Liquid	$F_{wz\ell1} = f_{\ell1}\frac{\rho_\ell v_\ell^2}{2D_e}$		$F_{wz\ell2} = \phi_\ell^2 f_{\ell2}\frac{\rho_\ell j_\ell^2}{2D_e}$		$F_{wz\ell3} = Cf_\ell F_{wz\ell2}$		$F_{wz\ell4} = 0$	
	Vapor	$F_{wzv1} = 0$		$F_{wzv2} = 0$		$F_{wzv3} = Cf_v F_{wv4}$		$F_{wzv4} = f_{v4}\frac{\rho_v v_v^2}{2D_e}$	
Axial Wall Friction Force per unit volume $F_{wz} = \frac{\Delta p_z}{\Delta z}$		i) For $Re_\ell \le 400$ $f_{\ell1}=f_L = \frac{32}{\sqrt{H}}\left(\frac{D}{P}\right)^{1.5}\frac{1}{Re_\ell}$ ii) For $Re_\ell \ge 2600$ $f_{\ell1}=f_T = \frac{0.316M}{Re_\ell^{0.25}}$ $M = \left[\frac{1.034}{\left(\frac{P}{D}\right)^{0.124}} + \frac{29.7\left(\frac{P}{D}\right)^{6.9}}{\left(\frac{H}{D}\right)^{2.239}} \times Re_\ell^{0.086}\right]^{0.885}$ iii) For $400<Re_\ell<2600$ $f_{\ell1}=f_{Tt} = f_T\sqrt{\Psi} + f_L\sqrt{1-\Psi}$ $\Psi = \frac{Re_\ell-400}{2200}$		$\phi_\ell = 1+\frac{20}{X_{tt}}+\left(\frac{1}{X_{tt}^2}\right)^{0.88}$ $\frac{1}{X_{tt}} = \left(\frac{x}{1-x}\right)^{0.9}\left(\frac{\rho_\ell}{\rho_g}\right)^{0.5} \times \left(\frac{\mu_g}{\mu_\ell}\right)^{0.1}$ $j_\ell = v_\ell \alpha_\ell$ $Re_\ell = \frac{\rho_\ell D\lvert j_\ell\rvert}{\mu_\ell}$ i) For $Re_\ell \le 400$ $f_{\ell2}=f_L$ ii) For $Re_\ell \ge 2600$ $f_{\ell2}=f_T$ iii) For $400<Re<2600$ $f_{\ell2}=f_{Tt}$				$Re_\ell \to Re_v$ $\rho_\ell \to \rho_v$ $v_\ell \to v_v$ i) For $Re_v \le 400$ $f_{v4} = f_L$ ii) For $Re_v \ge 2600$ $f_{v4} = f_T$ iii) For $400<Re_v<2600$ $f_{v4} = f_{Tt}$	

TABLE 5.3 (continued)

	Liquid	$F_{w\ell 1}=f_{\ell 1}\frac{v_{\ell max}^2}{2D_v}$	$F_{wt\ell 2}$	$F_{wt\ell 3}$	$F_{wt\ell 4}=0$
	Vapor	$F_{wtv1}=0$	$F_{wtv2}=0$	F_{wtv3}	$F_{wtv4}=f_{v4}\frac{\rho_v v_{v\,max}^2}{2D_v}$
Transverse Wall Friction Force per unit volume $F_{wt}=\frac{\Delta P_t}{\Delta t}$		i) For $Re_\ell \leq 202.5$ $f_{\ell 1}=f_L=180/Re_\ell$ ii) For $Re > 202.5$ $f_{\ell 1}=f_T=\frac{1.92}{Re_\ell^{0.145}}$ $Re_\ell=\frac{\rho_\ell \lvert v_{\ell max}\rvert D_v}{\mu_\ell}$	i) For $Re_\ell<202.5$ $F^a_{wt\ell 2}=f_{\ell 2}\frac{\rho_\ell v_{\ell max}^2}{2D_v}$ $f_{\ell 2}=f_L$ $Re_\ell=\alpha_\ell\rho_\ell\lvert v_{\ell max}\rvert\frac{D_v}{\mu_\ell}$ ii) For $Re > 202.5$ $F^b_{wt\ell 2}=\phi^2_{\ell 0}\, f_{\ell 2}\frac{\rho_\ell v_{\ell max}^2}{2D_v}$ $G=\alpha_\ell\rho_\ell v_{\ell max}+\alpha_v\rho_v v_{vmax}$ $\phi^2_{\ell 0}=1+\frac{8}{X_{tt}}+\frac{1}{X_{tt}^2}$ $\frac{1}{X_{tt}^2}=\left(\frac{x}{1-x}\right)^{1.855}\left(\frac{\rho_\ell}{\rho_v}\right)\times\left(\frac{\mu}{\mu_\ell}\right)^{0.145}$ $f_{\ell 2}=f_T$ $Re_\ell=\frac{GD_v}{\mu_\ell}$	i) For $Re_\ell<202.5$ and $Re_v<202.5$ $F_{w\ell 3}=Cf_\ell F^a_{w\ell 2}$ $F_{wv3}=Cf_v\cdot F_{wtv4}$ $f_{v4}=f_L$ $Re_v=\alpha_v\rho_v\lvert v_{vmax}\rvert\times\frac{D_v}{\mu_v}$ ii) For $Re_\ell>202.5$ or $Re_v>202.5$ $F_{w\ell 3}=Cf_\ell(1+\frac{8}{X_{tt}})\times f_{\ell 2}\frac{G^2}{2D_v\rho_\ell}$ $F_{wv3}=Cf_v(\frac{1}{X_{tt}^2})\times f_{\ell 2}\frac{G^2}{2D_v\rho_\ell}$	$Re_\ell\rightarrow Re_v$ $\rho_\ell\rightarrow\rho_v$ $v_{\ell max}\rightarrow v_{v\,max}$ i) For $Re_v\leq 202.5$ $f_{v4}=f_L$ ii) For $Re_v>202.5$ $f_{v4}=f_T$

	Liquid	$Q_{w\ell 1}=q''_{w\ell 1}/L_{w\ell}$	$Q_{w\ell 2}=q''_{w\ell 2}/L_w$	$Q_{w\ell 3}=q''_{w\ell 2}/L_{w\ell}$	$Q_{w\ell 4}=0$
	Vapor	$Q_{wv1}=0$	$Q_{wv2}=0$	$Q_{wv3}=q''_{wv4}/L_{wv}$	$Q_{wv4}=q''_{wv4}/L_{wv}$
Rate of Wall Heat Transfer per unit volume $Q_w=q''_w/L_w$		$q''_{w\ell 1}=h_\ell(T_w-T_\ell)$ $h_{\ell 1}=Nu_1\cdot\frac{k_\ell}{D_h}$ i) For $1.15\le\frac{P}{D}\le 1.3$ and $10\le Pe\le 5000$ $Nu_1=4.0+0.33\left(\frac{P}{D}\right)^{3.8}\left(\frac{Pe}{100}\right)^{0.86}+0.16\left(\frac{P}{D}\right)^{5.0}$ ii) For $1.05\le\frac{P}{D}<1.15$ and $150\le Pe\le 1000$ $Nu_1=Pe^{0.3}[-16.15+24.96(\frac{P}{D})-8.55(\frac{P}{D})^2]$ iii) For $Pe\le 150$ $Nu_1=4.50[-16.15+24.96(\frac{P}{D})-8.55(\frac{P}{D})^2]$	$q''_{w\ell 2}=h_{\ell 2}(T_w-T_\ell)$ $h_{\ell 2}=Nu_2\cdot\frac{k_\ell}{D_h}$ $Nu_2=0.152\,\frac{F_1}{F_2}Pr_\ell Re_\ell^{0.9}\phi_\ell$ i) For $Re_\ell<50$ $F_1=1.5$ $F_2=0.7071\,Re_\ell^{0.5}\,Pr_\ell$ ii) For $50<Re_\ell<1125$ $F_1=1.563$ $F_2=5Pr_\ell+\frac{5}{E}\ln[1+E\,Pr_\ell(\frac{\delta^+}{5}-1)]$ $E=27.73\,Pr_\ell$ $\delta^+=0.4818\,Re_\ell^{0.585}$ iii) For $Re_\ell>1125$ $F_1=1.818$ $F_2=5Pr_\ell+\frac{5}{E}(1+5EPr_\ell)+\frac{6}{E\gamma}\ln(\frac{2M+\gamma-1}{1+\gamma-2M}\times\frac{1+\gamma-\beta}{\beta+\gamma-1})$ $\beta=60\,\frac{M}{\delta^+}$, $M=1-\sqrt{\alpha}$ $\delta^+=0.133\,Re_\ell^{0.7614}$ $\phi_\ell=(1+\frac{20}{X_{tt}}+\frac{1}{X_{tt}^2})^{0.88}$	$q''_{w\ell 3}=h_{\ell 2}(T_w-T_\ell)$ $q''_{wv3}=h_{v4}(T_w-T_v)$	$q''_{wv4}=h_{v4}(T_w-T_v)$ $h_{v4}=Nu_4\cdot\frac{k_v}{D_h}$ $Nu_4=0.023\times Re_v^{0.8}Pr_v^{0.4}$

TABLE 5.4

THERMIT-6S Interfacial Exchange Models

	Pre-Dryout Regime ($0 < \alpha < 0.957$)	Post-Dryout Regime ($1 > \alpha > 0.967$)
Interfacial Area Density $(\frac{1}{L_a})$	$\frac{1}{L_{a1}} = \frac{4\pi\alpha}{D[2\sqrt{3}\,(\frac{P}{D})^2 - \pi]} = \frac{4\alpha}{D_e}$	$\frac{1}{L_{a2}} = \frac{1}{L_{a1}} \frac{(1.0-\alpha)}{(1.0-0.957)}$
Interfacial Mass Flux $q_m = \frac{H_{i\ell}}{h_{fg}} (T_\ell - T_s)$ Rate of Mass Exchange per unit volume $\Gamma = \frac{1}{L_a} q_m$	$H^a_{i\ell} = \frac{k_\ell}{l_\ell} + C_{p\ell} g_\ell E$ $l_\ell = \frac{D_e}{4}(1-\alpha)$ $E = 27.73\ Pr_\ell$ $g_\ell = \sqrt{\rho_\ell \tau_i}$ $\tau_i = C_{fi} \frac{\rho_v}{2}(v_v - v_\ell)^2$ $C_{fi} = 0.005(1+234.3\ (1-\sqrt{\alpha})^{1.15})$ $H^b_{i\ell} = (\frac{M}{2\pi R})^{1/2} \frac{(\rho_v\ h_{fg})^2}{p\sqrt{T_s}}$ If $H^b_{i\ell} > H^a_{i\ell}$, $H_{i\ell 1} = H^a_{i\ell}$ If $H^a_{i\ell} > H^b_{i\ell}$, $H_{i\ell 1} = H^b_{i\ell}$ $q_m = \frac{H_{i\ell 1}}{h_{fg}} (T_\ell - T_s)$ $\Gamma = \frac{1}{L_{a1}} q_m$	$\Gamma_2 = \frac{1}{L_{a2}} q_m$

TABLE 5.4 (continued)

Interfacial Heat Flux $q''_i = H_{i\ell}(T_\ell - T_v)$ Rate of Interfacial Energy Exchange per unit volume $Q_i = \frac{1}{L_a}\frac{h_g}{h_{fg}} q''_{i\ell}$	$q''_{i\ell} = H_{i\ell 1}(T_\ell - T_v)$ $Q_{i1} = \frac{1}{L_{a1}}\frac{h_g}{h_{fg}} q''_{i\ell}$	$Q_{i2} = \frac{1}{L_{a2}}\frac{h_g}{h_{fg}} q''_{i\ell}$
Rate of Interfacial Momentum Exchange per unit volume $F_i = F_s + F_v$		
Standard Drag Force $F_s = K\lvert v_v - v_\ell \rvert$ $= \frac{1}{L_a}\tau_i$	$\tau_i = C_{fi}\,\frac{1}{2}\rho_v (v_v - v_\ell)^2$ $C_{fi} = 0.005(1 + 234.3(1-\sqrt{\alpha})^{1.15})$ $K = \frac{1}{L_{a1}} C_{fi}\,\frac{1}{2}\rho_v \lvert v_v - v_\ell \rvert$ $F_{s1} = K(v_v - v_\ell)$	$F_{s2} = F_{s1}$
Virtual Mass Force F_v	$F_{v1} = \alpha\rho_g C_v \left(\frac{\partial v_v}{\partial t} - \frac{\partial v_\ell}{\partial t} + v_v \cdot \nabla(v_v - v_\ell)\right.$ $\left. + (v_v - v_\ell)\cdot[(\lambda-2)\nabla v_v + (1-\lambda)\nabla v_\ell]\right)$	$F_{v1} = F_{v2}$

Chapter 6. CODE ASSESSMENT

The code assessment is defined as the task of ascertaining how well the code can simulate the physical processes measured in experiments, quantifying the error within which the code is capable of predicting certain key parameters, and determining the code's limitations.

In LMFBR analysis, the important physical processes are temperature transients, incipient boiling, vapor propagation in the axial and radial directions, flow coastdown, flow reversal, flow oscillation, and dryout. The key parameters to affect reactor behavior are therefore the times of incipient boiling, of flow reversal, and of initial dryout, wall and fluid temperature distribution, and inlet and outlet flow rate.

The capability of the code is restricted by the validation range of the constitutive equations implemented in THERMIT-6S. Most of the constitutive equations were derived for forced convection flow, based on an assumption of the predominance of the cocurrent annular flow regime. Although it is questionable whether these constitutive equations can be applied to natural convection flow, it is expected that the differences in the local processes between two-phase flow under natural convection and forced convection may be much smaller than those in single phase flow. Also, the code can only be applied to predictions of phenomena before fuel melting occurs. The code was

originally designed to be applicable to a component system but it can be extended to the analysis of a whole loop system in the future in order to account for the effect of loop system and to obtain accurate boundary conditions (98).

Additionally, an assessment of 1-D vs 2-D model predictions of sodium boiling in LMFBR subassemblies in relation to experimental results will be given. This was motivated by the need to determine whether two-dimensional voiding behavior and temperature distribution in large pin bundles are important. This work includes comparison with predictions by SAS (7 and 8) and NATOF (16 and 99). SAS is considered to be one of the best 1-D codes developed so far. Comparison between the present code and SAS will give some insight into 2-D effects and future development needs. Also, comparison with NATOF-2D, which uses the same solution scheme but different physical models, will illustrate the effect of improvement in the physical models of the present code. A brief description of experiments selected for assessment is shown in Table 6.1.

6.1 W-1 Experiments

The Sodium Loop Safety Facility (SLSF) W-1 Experiments (100) were 19-pin bundle in-pile tests performed by Hanford Engineering Development Laboratory and coordinated with the Argonne National Laboratory P series. The W-1 Experiments utilized SLSF as a packaged testing facility in the Engineering Test Reactor (ETR).

TABLE 6.1

Experiments and Codes Selected for THERMIT-6S Code Assessment and Comparison

Types of Accident \ # of Pins in Assembly	19	37	61
Low Flow/ High Power (LOF)	W-1 (W-7b')	P3A	OPERA -15 Pin
	* * * NATOF-2D SAS-3D	— * * NATOF-2D SAS-3A	— * * — — (Pre-test)
Low Flow/ Low Power (LOPI)	THORS (test 72B, run 101)		
	* * SAS-3A		

*: 1-D Analysis by THERMIT-6S

**: 2-D Analysis by THERMIT-6S

NATOF-2D: 2-D Code

SAS-3D and SAS-3A: 1-D Codes

The W-1 Experiments consisted of many individual tests to provide experimental data on sodium boiling and boiling stability in a fuel pin bundle during flow transients in the LMFBR. The W-1 tests were also designed to provide fundamental information: the rate at which sodium boiling develops, the time required to establish dryout in local coolant channels, the time fuel pins can sustain without cladding failure, the operating conditions (fuel pin power and flow) which produce stable boiling in a pin array.

The tests were divided into two parts. The first was the protected LMFBR Loss-Of-Piping Integrity (LOPI) accident simulation to determine the heat transfer characteristics from fuel pins to coolant and boiling behavior. The second phase was the Boiling Window Tests (BWT) to establish flow-power combinations which will produce incipient and stable boiling zones in the bundle for a given inlet temperature. The BWT tests were subdivided into three phases: approach to boiling, incipient boiling, and dryout with fuel pin failure.

6.1.1 Test Apparatus and Procedures

The test train includes the test subassembly, bypass flow channel, flow divider, and test instrumentation. Downward coolant flow in the loop is outside the test train flow divider, which is insulated over much of its length to minimize radial heat transfer. Upward flow in the lower portion of the test train occurs in parallel through the

test assembly and the bypass channel. Test subassembly coolant flow is metered at both the test subassembly inlet and outlet. The two parallel coolant streams mix above the test subassembly outlet flowmeter and upward flow continues through two loop flowmeters prior to reaching the heat exchanger inlet.

The BWT tests were initiated at a steady state flow of 1.95 Kg/sec. The flow was linearly reduced to its low flow value in 0.5 seconds, where it was held for a specific time, and then linearly returned to its initial state in 0.5 seconds. Among the BWT tests, BWT-7b' (simply called as W-7b') is selected for numerical simulation. The W-7b' is the most interesting and demanding test to be run by the code, because flow reversal, 2.0 seconds of flow oscillation, and dryout occurred in this test. Boiling occurred at a pin power of 14.4 Kw/ft before clad dryout. The test section had 38% of full flow for a period of 3.0 seconds. This test simulates a high power/low flow sodium boiling accident. The thermal and hydraulic operating conditions in W-7b' are shown in Fig 6.1.

6.1.2 Numerical Simulation of W-7b'

6.1.2.1 2-D Analysis of W-7b'

To save computer time and probe the two-dimensional nature of sodium boiling, a 2-D analysis instead of a 3-D analysis is done by considering one-sixth of the test fuel

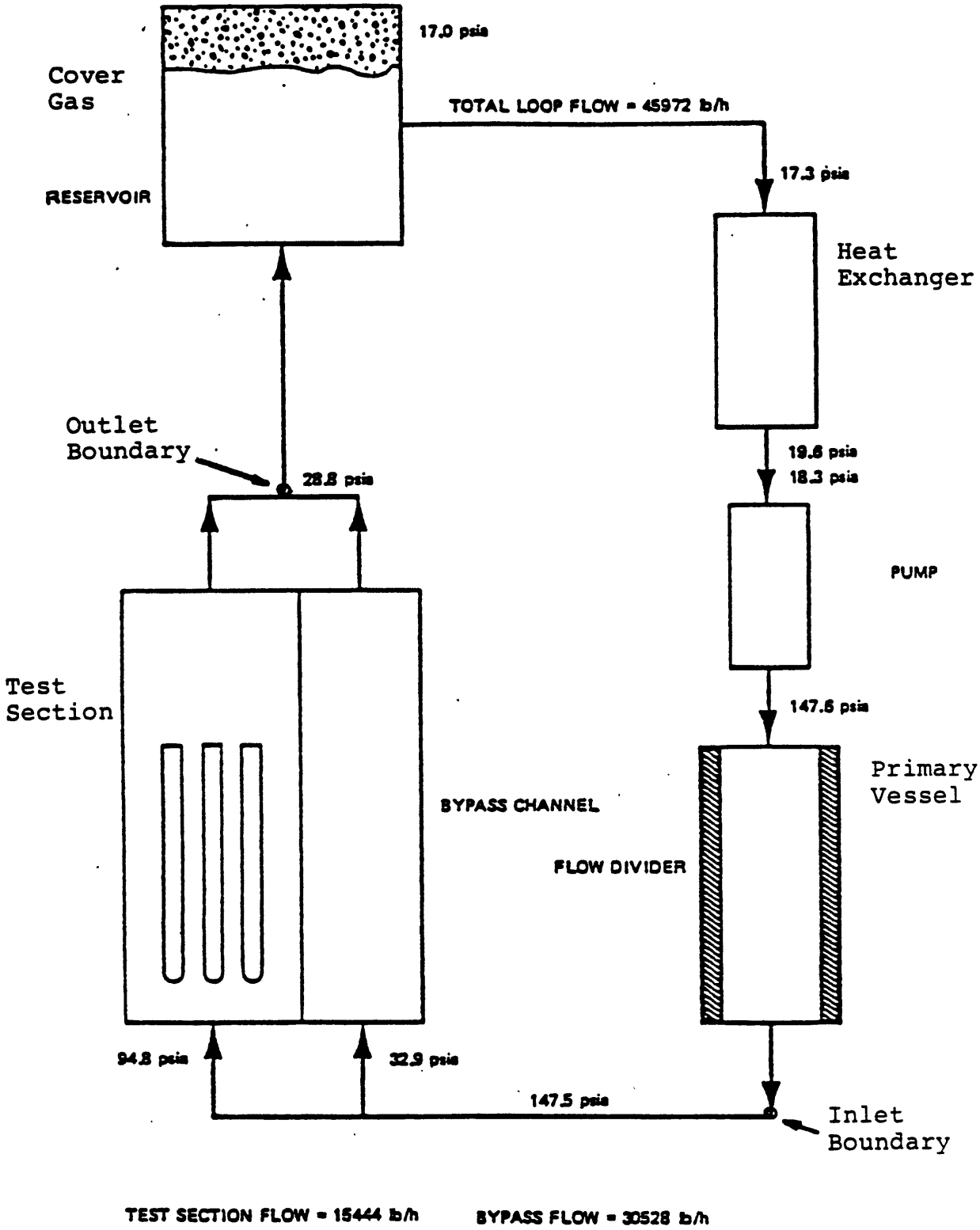

Fig. 6.1: SLSF Loop Steady-State Hydraulics at 145 MW ETR Power and 4.29 lb/sec Test Section Sodium Flow (Fuel Pin Peak Linear Power of 14.4 kW/ft)

bundle. Since the present code uses a x-y-z coordinate, the assumption adopted for the 2-D analysis is that there are no net mass, energy, or momentum exchange in the y direction, which can be achieved by assigning a zero flow area in the y direction. Then the x-z coordinate will be transformed into the r-z coordinate. As a result, uniform power in the θ direction is assumed and swirl flow is not considered. As shown in Fig 6.2, the fuel bundle consists of three meshes in the radial direction. Seventeen meshes in the axial direction are considered: one in the lower blanket (each 8"), nine in the fuel (each 4"), two in the upper blanket (each 6"), and five in the gas plenum (each 8").

Up to 1.5 seconds into transients, the measured inlet flow is used for the inlet boundary condition. After boiling starts, the pressure-pressure boundary condition is needed in order to predict flow coastdown and flow oscillation. Unfortunately, as there are no data for the inlet and outlet pressures of the test section, an estimation of the pressures is inevitable. The positions of the inlet and outlet boundary are shown in Fig 6.1. The reason for selecting these positions as the inlet and outlet boundary positions is that, while the mass flow rate in the test section is varied substantially with time after boiling, change in the total mass flow rate in the loop is relatively small. Therefore, the variation of pressures with time at the positions selected for the boundary conditions is relatively small. The cover gas region is not

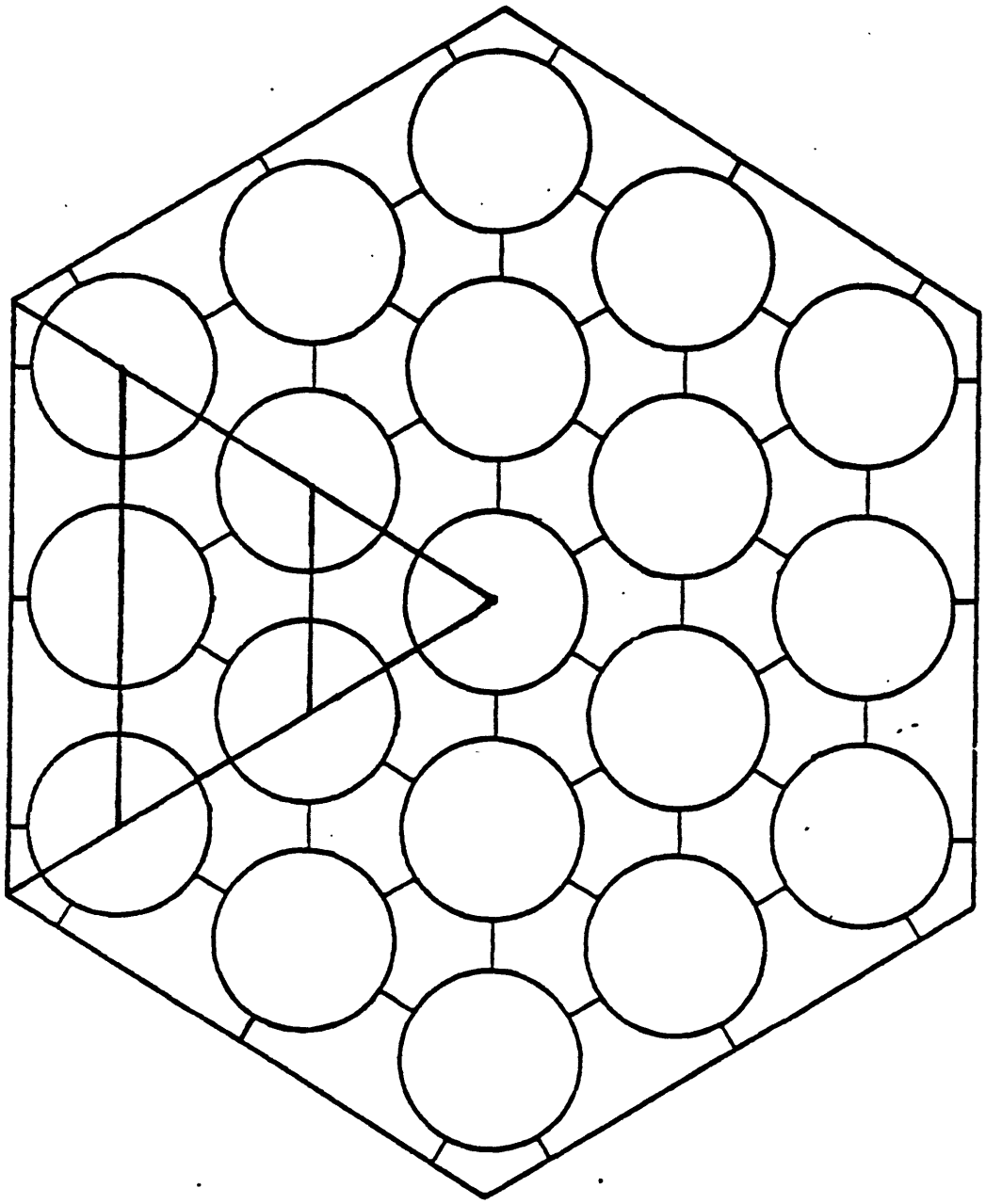

Fig. 6.2: Radial Meshes of the Fuel Bundle for the 2-D Numerical Simulation of W-7b'

selected as the outlet boundary because the pressure drop between the outlet of the test section and the cover gas region requires information on the total mass flow rate in the loop which can not be predicted in the present code. To account for pressure drops between the inlet boundary and outlet of the test section, and between the outlet boundary and outlet of test section, a valve model is designed and described in Appendix D. The importance of the boundary positions will be discussed in detail in Section 6.5.3. As the velocity-pressure boundary condition is used before boiling, it is not necessary to know the exact inlet and outlet pressures. However, use of the pressure-pressure boundary condition after boiling requires information on the values of inlet and outlet pressures. Therefore, the inlet pressure is estimated so as to give the saturation temperature in the last cell of the heated section at boiling inception, which can be estimated by experimental data. Note that the fluid temperature ultimately reaches a saturation temperature which is fairly constant over a time span. Then the outlet pressure is determined so as to give the experimental inlet flow at 1.5 seconds. Figure 6.3 shows the forcing function used for the boundary conditions; the solid line represents the pressure-pressure boundary condition and the velocity-pressure boundary condition is used in the time period of the dashed line, 1.5 seconds.

In order to obtain the correct inlet and outlet pressures, it is inevitable to use some iteration.

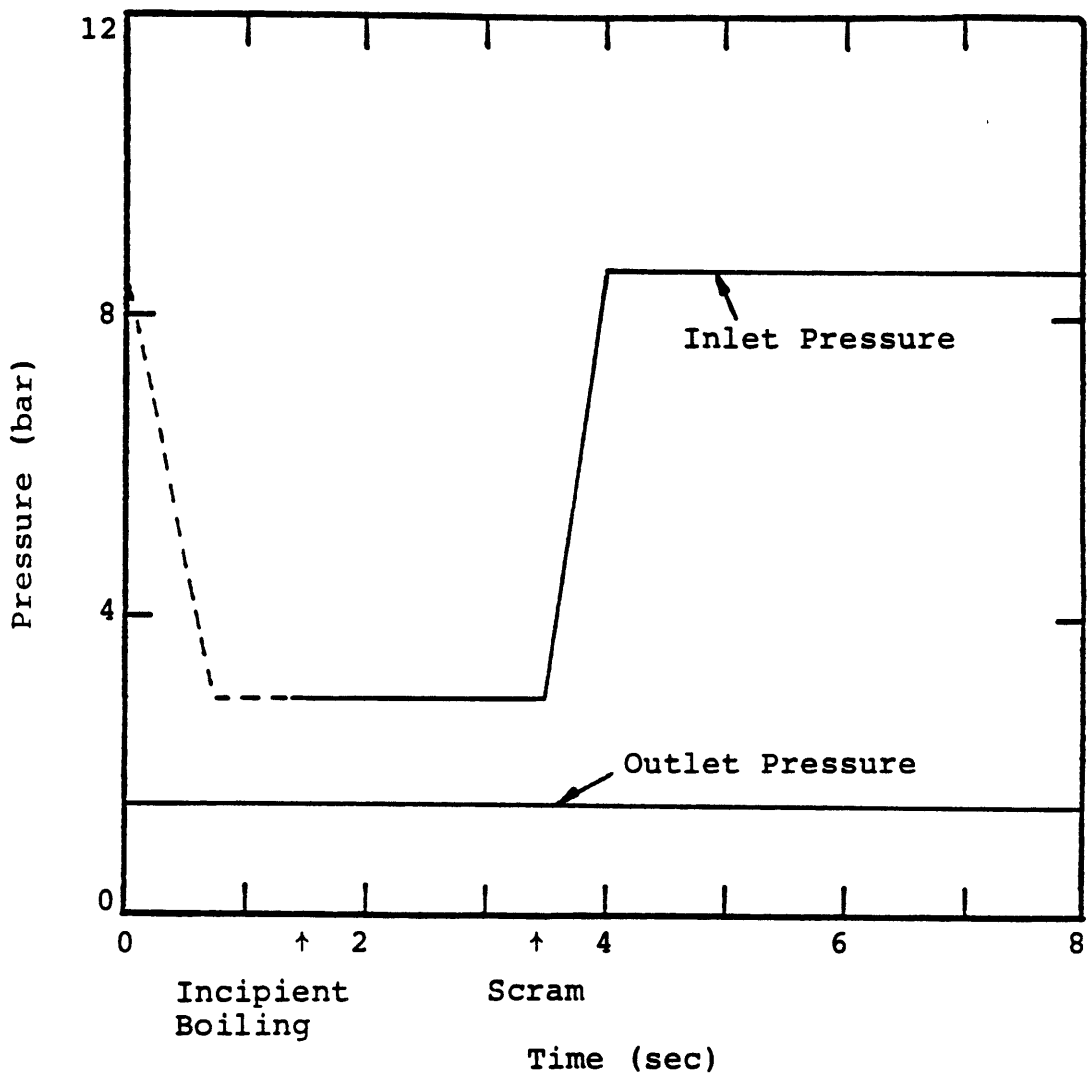

Fig. 6.3: Forcing Function for W-7b' Numerical Simulation (Dashed line represents the period when the inlet velocity boundary condition was used)

Therefore, loop simulation is recommended for future work to eliminate the uncertainties in estimating the inlet and outlet pressures.

Uniform power distribution in the radial direction is used for the numerical simulation during transients. The constant Nusselt number for liquid thermal conduction during transients is taken to equal 22 as recommended by Zielinski (99). Various types of fuel rods for the W-1 tests were used to obtain uniform radial power. To account for the different radial geometries, a generalized normalization of heat source is needed. (See Appendix E) The importance of this normalization of heat source will be discussed in Section 6.5.4.

6.1.2.2 Results

The numerical results for the W-7b' are shown in Fig 6.4-6.10. In the computation, incipient boiling starts at 1.55 seconds and inlet flow reversal occurs at 2.65 seconds. Dryout occurs within 0.15 seconds after flow reversal.

All temperature predictions (Figs 6.4-6.6) by the present code are higher than experimental data. Especially, it is observed that temperature differences between data and predictions are very large at the midplane of the heated section. (See Fig 6.6) One of the plausible explanations of these large temperature differences is geometry distortion due to high power. Also there is a time delay between the actual events and measurement of events by thermocouples,

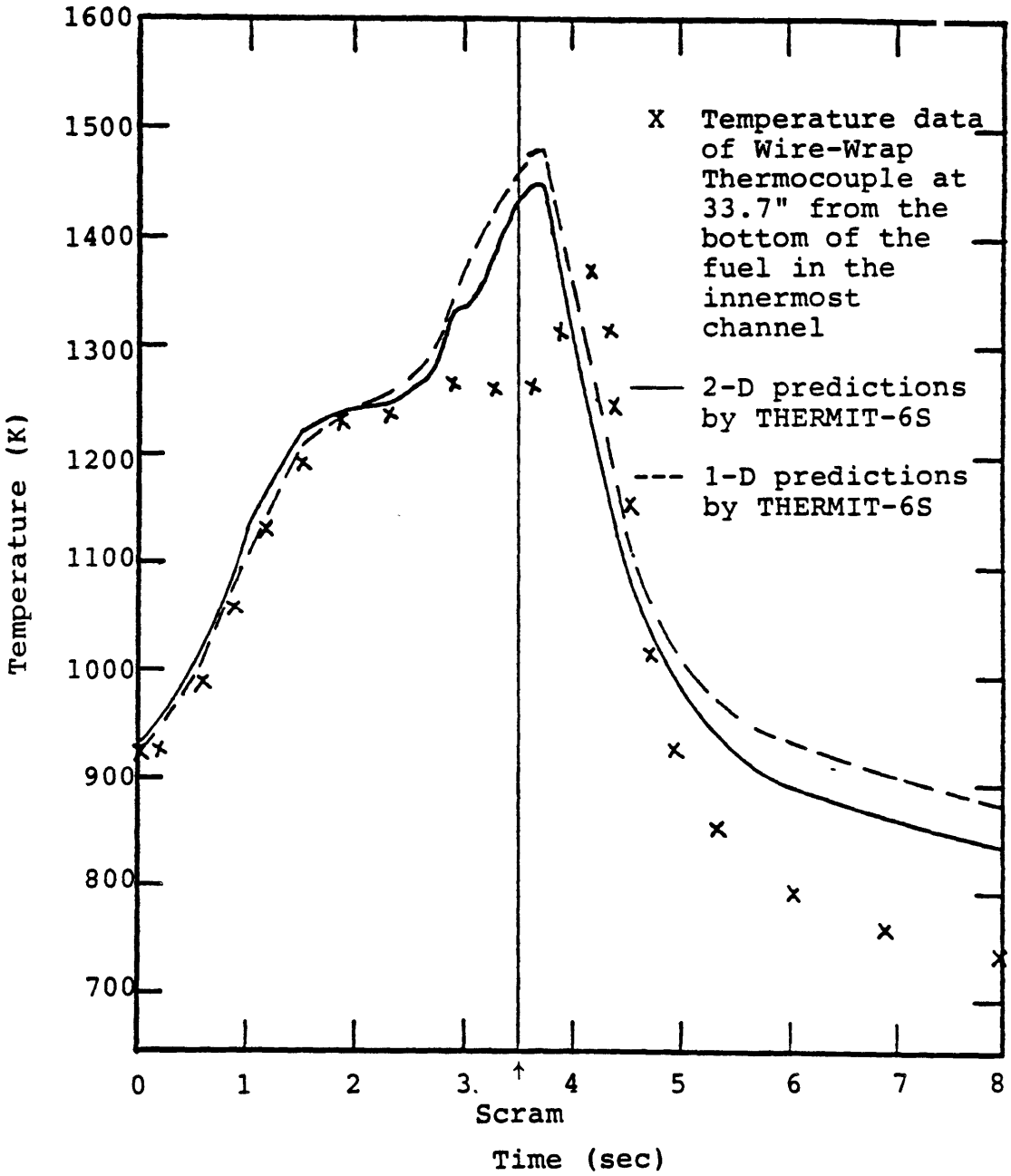

Fig. 6.4: Comparison between Temperature Data, and 1-D and 2-D Predictions by THERMIT-6S at 33.7" (from the bottom of the fuel) in the Innermost Channel for the W-7b' Test

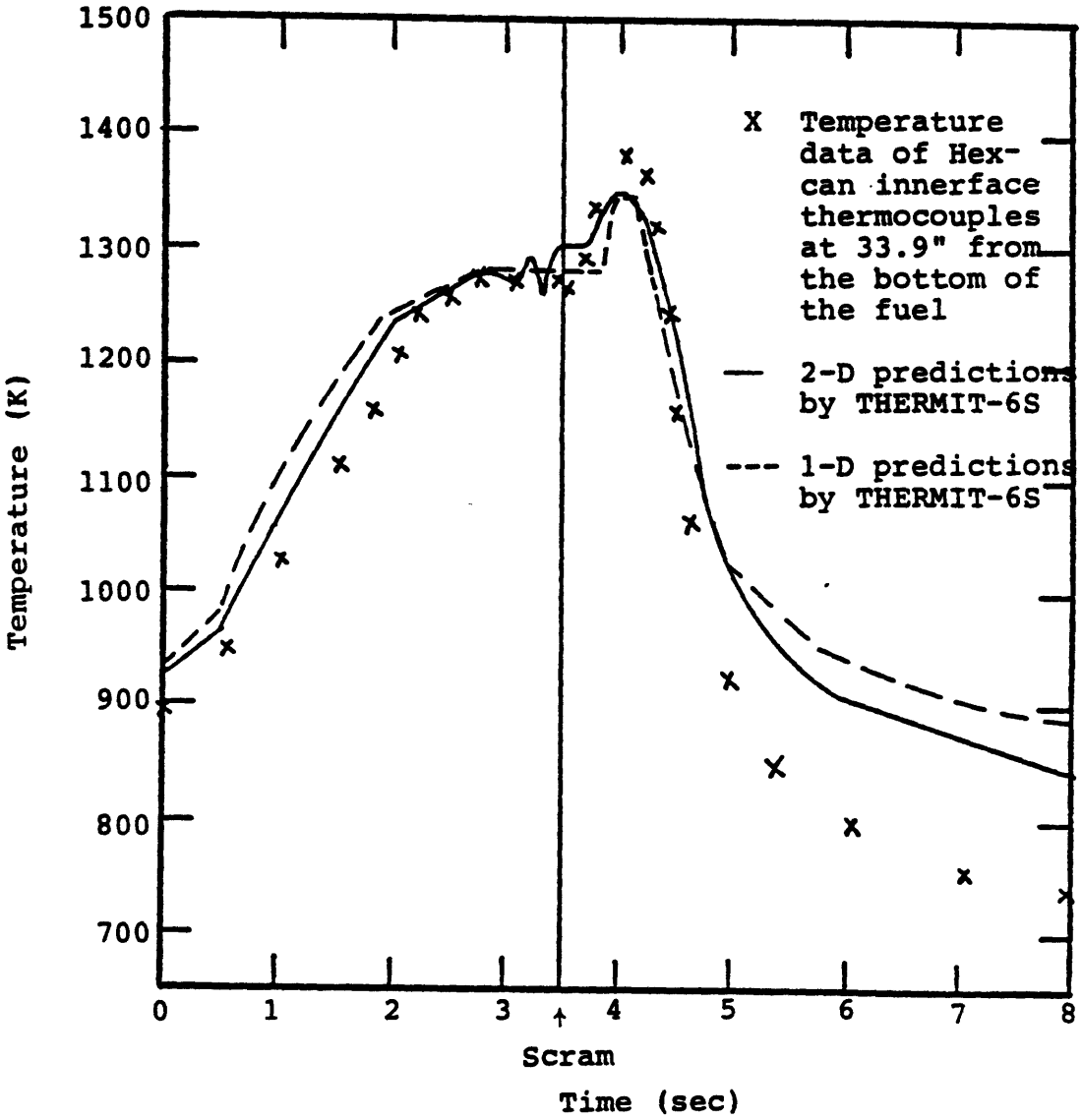

Fig. 6.5: Comparison between Temperature Data of Hex-Can Innerface, and 1-D and 2-D Predictions by THERMIT-6S at 33.9" (from the bottom of the fuel) for the W-7b' Test

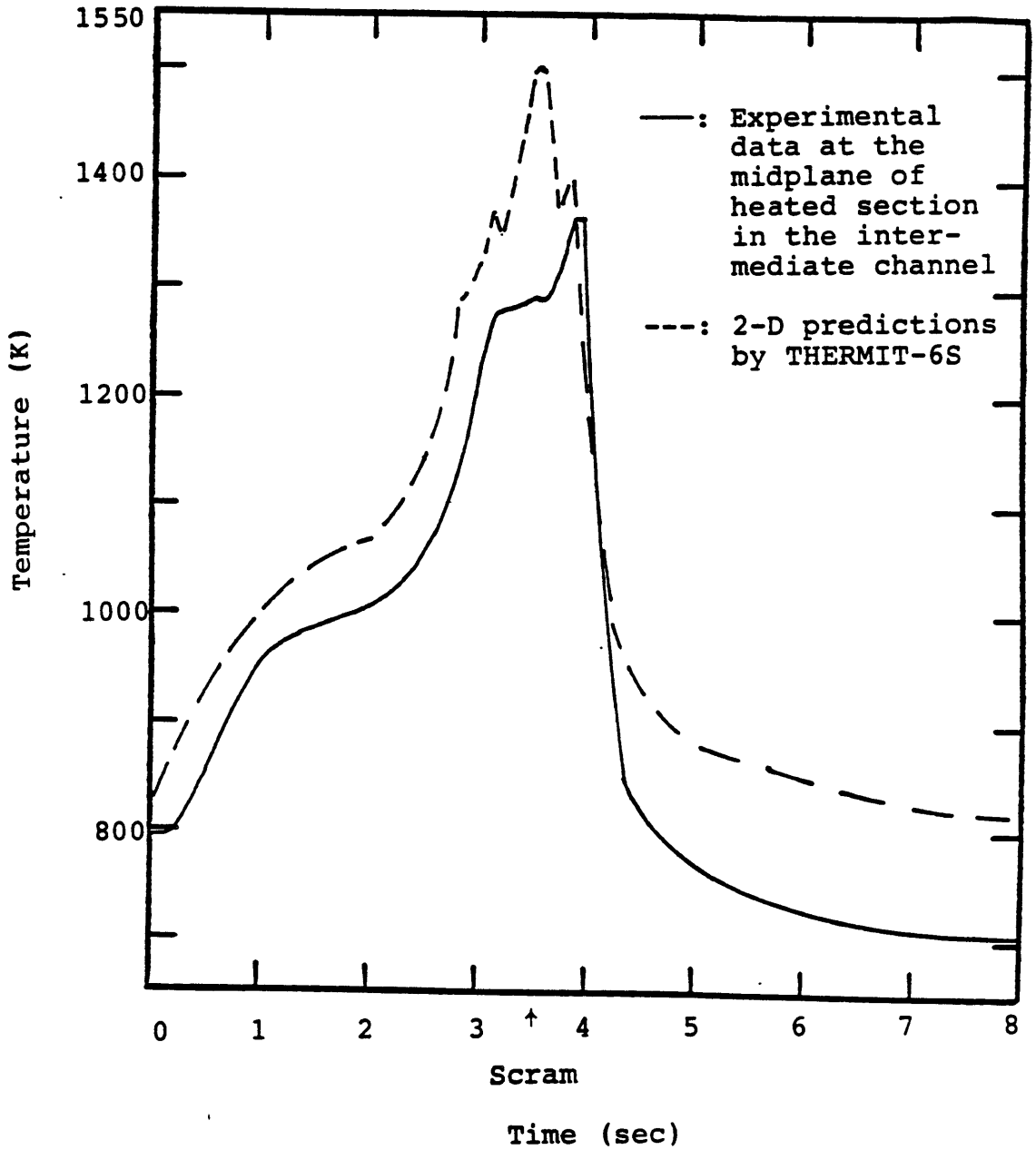

Fig. 6.6: Comparison between Temperature Data and 2-D Predictions by THERMIT-6S at the Midplane of Heated Section in the Intermediate Channel for the W-7b' Test

which is not mentioned in Ref 100.

After boiling inception, rapid vapor production in the saturated region occurs due to the high density ratio of liquid to vapor, and vapor is transferred radially and axially from the saturated region to the subcooled region surrounding the saturated region. This transferred vapor is condensed in the subcooled region. Some of the vapor produced is trapped in that cell for a short time due to the interfacial drag force between liquid and vapor. The trapped vapor increases void fraction and pressure in that cell. This causes rapid inlet flow coastdown and strong radial fluid transfer from the center channel to the outer channel. Rapid inlet flow coastdown increases power-flow mismatch and in turn fluid temperature in the subcooled region. The large radial velocity escalates energy transfer due to vapor transferred from the inner channel to the outer channel.

If the homogenous model, which assumes that an infinite interfacial drag force exists, is used, more vapor produced in the saturation region is trapped in that region. This more trapped vapor results in more rapid increase in void fraction and pressure. This is the main reason that the homogeneous model often brings about failure of convergence of the Newton iteration. The reduction of the time step size to achieve the convergence of the Newton iteration requires much larger CPU time. Even though it is assumed that the computation may be successful, much more rapid

inlet flow coastdown and earlier flow reversal is expected. For details refer to Section 6.5.2.

At 1.0 seconds after boiling inception, the fluid in the last mesh of the heated section in the outmost channel reaches saturation temperature and vapor production in that cell occurs instead of vapor condensation. As a result, the rate of vapor generation and pressure build-up around the end of the heated section increase. Flow coastdown accelerated by this sharp increase in pressure and vapor generation can be seen in Fig 6.7. As shown in Fig 6.7, the rate of inlet flow coastdown is more rapid than that in the experiment. This can be explained by the following reasons:

1. While the constant pressure boundary condition is used in the computation, rapid inlet flow coastdown, in reality, may cause an increase in the inlet pressure due to the hydraulic resistance of the loop.
2. The condensation rate may be higher in the experiment due to shattered droplets around interfaces produced by Kelvin-Helmholtz instability and Taylor instability. Slower flow coastdown can be predicted if a model to account for this effect is implemented in the present code.

As a result, flow reversal occurs 0.2 seconds ahead of that in the experiment.

Voiding of the rest of the bundle proceeds rapidly from this time on, with the whole bundle indicating a single channel response. As the gas plenum region of the bundle is

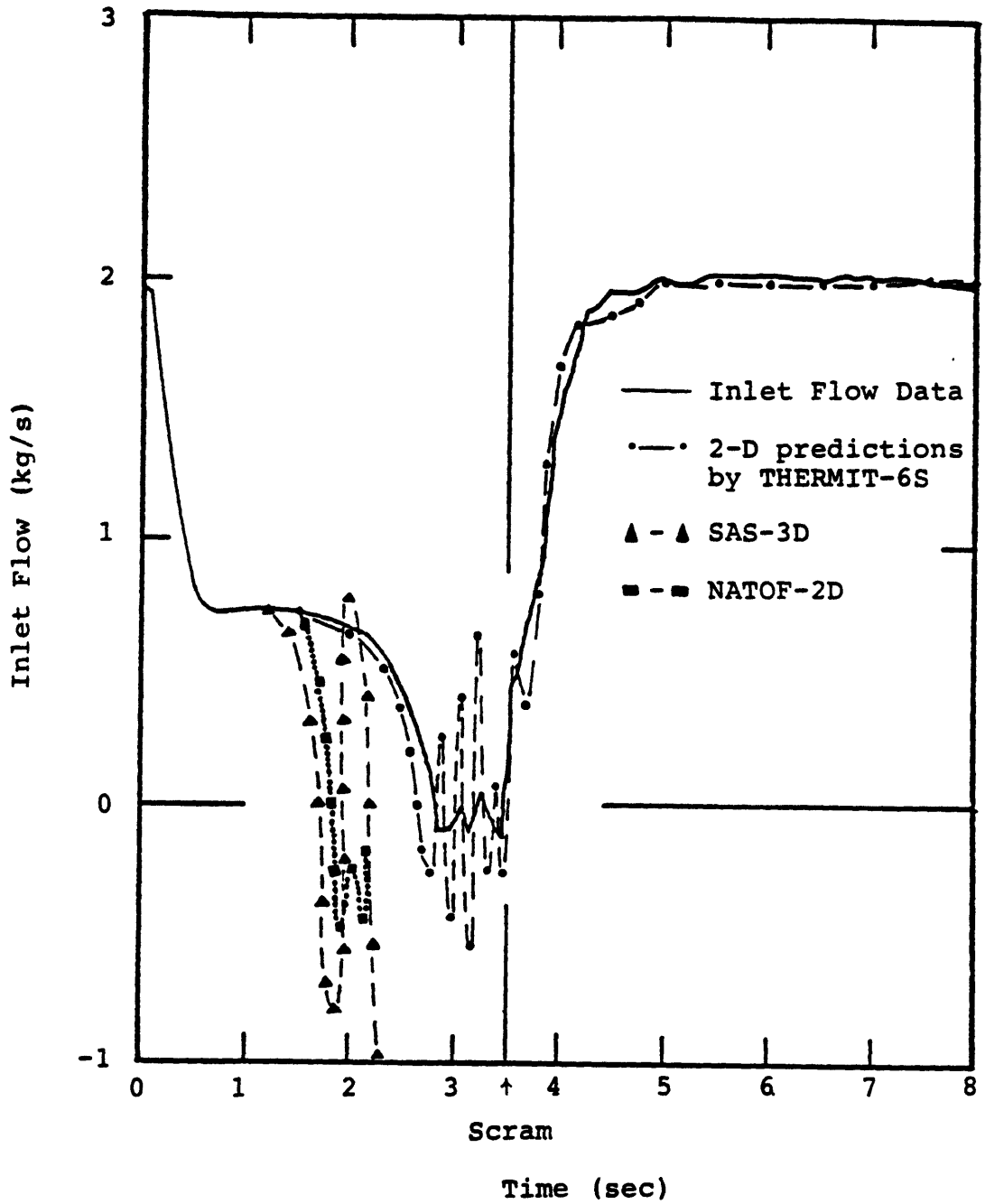

Fig. 6.7: Comparison between Inlet Flow Data and Predictions by THERMIT-6S, SAS-3D, and NATOF-2D for the W-7b' Test

mildly subcooled due to a lower heat capacity than those in the heated section and blanket region, more rapid vapor propagation in the gas plenum occurs until vapor reaches the end of pin at around 2.8 seconds. Within 0.15 seconds after flow reversal, dryout occurs. It seems that the incidence of flow reversal may be the most important single factor in the occurrence of dryout in low flow/high power accidents.

After flow reversal the liquid film remaining on the hot wall is rapidly evaporated due to high power and little liquid supply from subcooled liquid and eventually dryout occurs. Dryout dramatically reduces the heat transfer coefficient and as a result, sharp rise in the cladding temperature takes place. The temperature data in the experiment were obtained from wire-wrap thermocouples. After dryout, temperature measured by the wire-wrap thermocouples may be closer to wall temperature than to vapor temperature due to the low heat transfer coefficient. Thus, predictions before and after boiling in Figs 6.4-6.6 represent fluid and wall temperature, respectively. After dryout, vapor is rapidly accelerated due to high void fraction and this high vapor velocity dramatically reduces the time step size, and in turn increases CPU time. For this reason development of an advanced numerical scheme is recommended as future work.

Liquid reentry occurs at 0.2 seconds after flow reversal, followed by inlet flow oscillation. Figures 6.8-6.9 show voiding oscillation at the lower boundary of

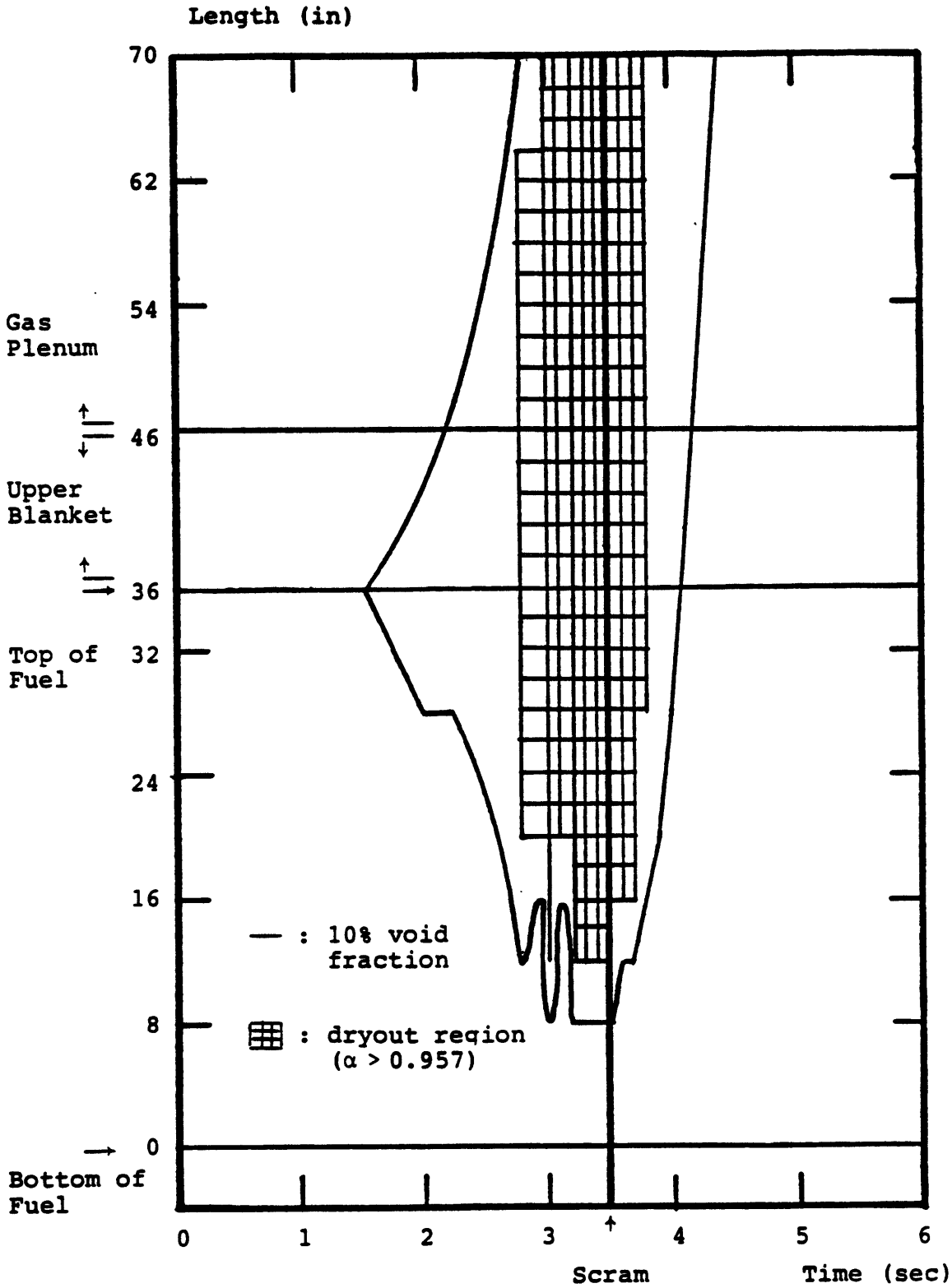

Fig. 6.8: Profile of Voided Region in the Innermost Channel for the W-7b' Test (2-D Simulation)

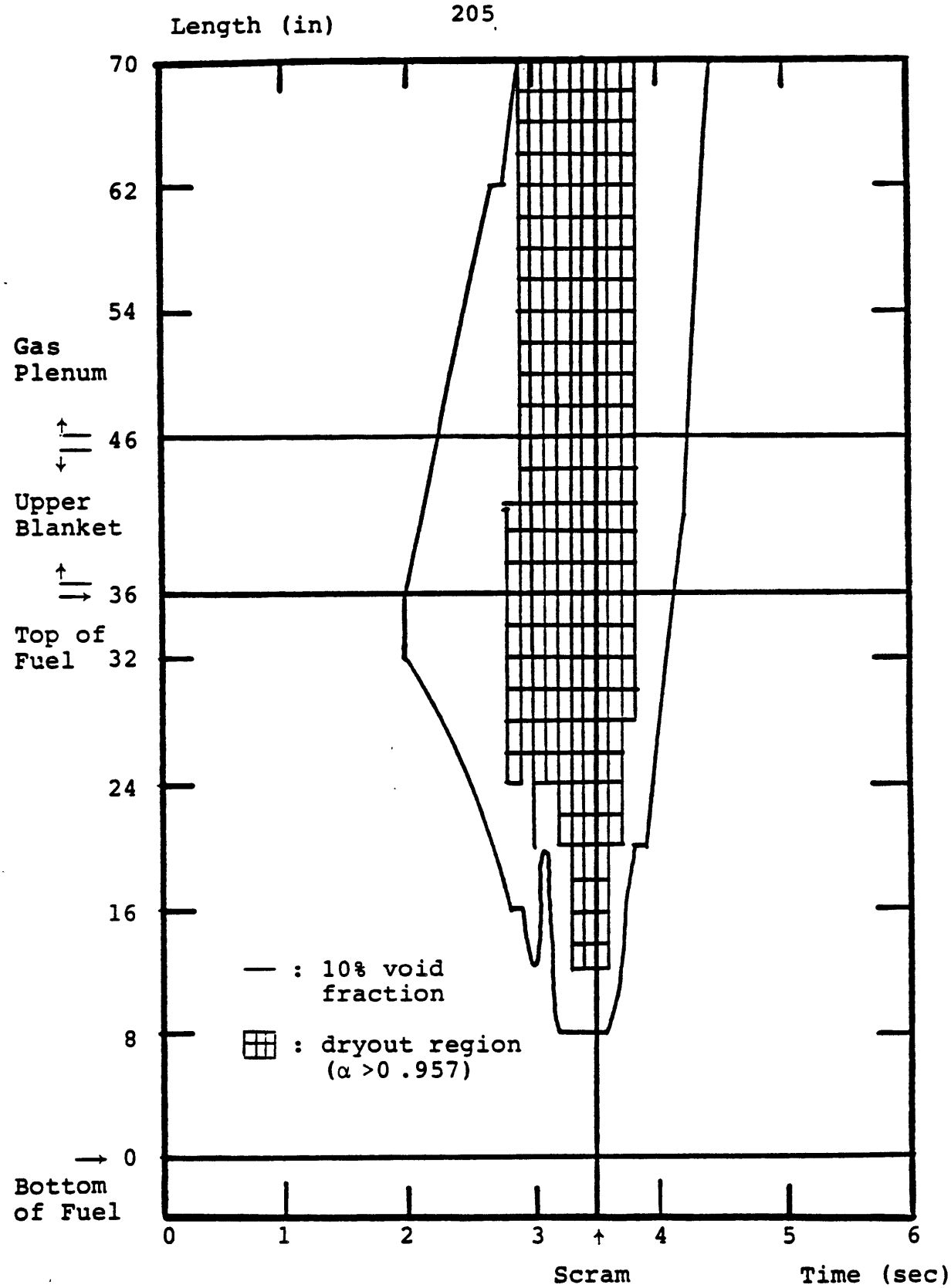

Fig. 6.9: Profile of Voided Region in the Outermost Channel for the W-7b' Test (2-D Simulation)

void by liquid reentry. The frequency of the flow oscillation is 5 cycles/sec, compared to 3 cycles/sec in the experiment and the amplitude is much larger than that in the experiment. It is hard to identify the reasons for these results, but several reasons can be considered.

1. Here again, changes in the inlet and outlet pressures are expected during flow oscillation, in contrast with the constant boundary condition in the computation.

2. The constitutive relations after dryout are highly questionable. In our model, effects of droplets are neglected. However, the region and duration of post-dryout are large enough to affect the flow behavior as shown in Figs 6.8 and 6.9.

3. Large radial velocities have a multi-dimensional effect on the control of the time step size for numerical stability. This may cause some error accumulation.

Scram and flow recovery are simulated at 3.5 seconds. Due to lack of information on the scram, it is assumed that the scram causes a negative reactivity of -0.13 corresponding to about twenty dollars worth of negative reactivity which gives a prompt drop of power:

$$q(t) = 0.054 \times q(t_o)$$

After this prompt drop in power, the test section goes on power decay with a period with 80 seconds. With rapid flow recovery, vapor condensation takes place starting from the

lower cells into which subcooled liquid is directly transported. Then the hot walls are rewetted by liquid and the dryout region is rapidly reduced as shown in Figs 6.4-6.6.

At about 4.6 seconds vapor in the innermost channel disappears and 0.13 seconds later is quenched in the outmost channel. This delay results from heat transfer from the hex can to fluid in the outmost channel. The wall temperature drop does not occur immediately after the scram. The cladding temperature continuously increase up to 0.25 seconds after the scram and then is sharply lessened. This delayed time can be a measure of how fast the cladding temperature will respond to the scram.

Fig 6.7 shows predictions by SAS-3D, NATOF-2D, and THERMIT-6S as well as the experimental inlet flow transient. Results by SAS are characterized by early flow reversal (1.7 seconds) and large flow oscillation. The NATOF code, which has the same numerical logic but different physical models, predicts that cladding dryout at 1.76 seconds and early flow reversal (1.95 seconds) occurs. Note that NATOF-2D predicts the occurrence of dryout before flow reversal unlike the experimental results and present predictions. This was primarily caused by use of the Autruffe correlation for the interfacial drag coefficient which predicts much higher intefacial force than the present model does. As a result, more vapor is trapped in the cell and then rapid increase in void fraction takes place. NATOF-2D calculation stopped at

2.2 seconds due to failure of convergence of the Newton iteration.

Comparison between 1-D and 2-D predictions is an interesting subject. Both predictions were done by the present code. 1-D analysis predicts 0.28 second delay of incipient boiling. (Fig 6.10) This can be understandable because fluid temperature in the 1-D calculation is averaged over the x-y plane. Therefore, at the same axial position, temperature predicted in 1-D analysis is lower in the innermost cell but higher in the outmost cell than predictions in 2-D analysis. As boiling is initiated in the innermost cell, time delay of incipient boiling in the 1-D calculation is quite natural. In the numerical simulation of experiments with steep radial temperature gradients, incipients boiling in the 1-D analysis can be substantially delayed. As radial temperature gradients in transients will be much steeper than at steady states, caution is required when 1-D simulation is performed. Initial dryout in the 1-D analysis occurs at 1.78 seconds after boiling, compared to 1.55 seconds in the 2-D analysis. In the 1-D analysis there is no room to condense vapor transferred in the the r direction. However, in the 2-D analysis strong cross flow caused by an increase in pressure in inner cells reduces pressure build-up. The frequency and amplitude of inlet flow oscillation in the 1-D analysis are higher than in the 2-D case; the frequency in the 1-D is about 6 cycles/sec, compared to 5 cycles/sec in the 2-D.

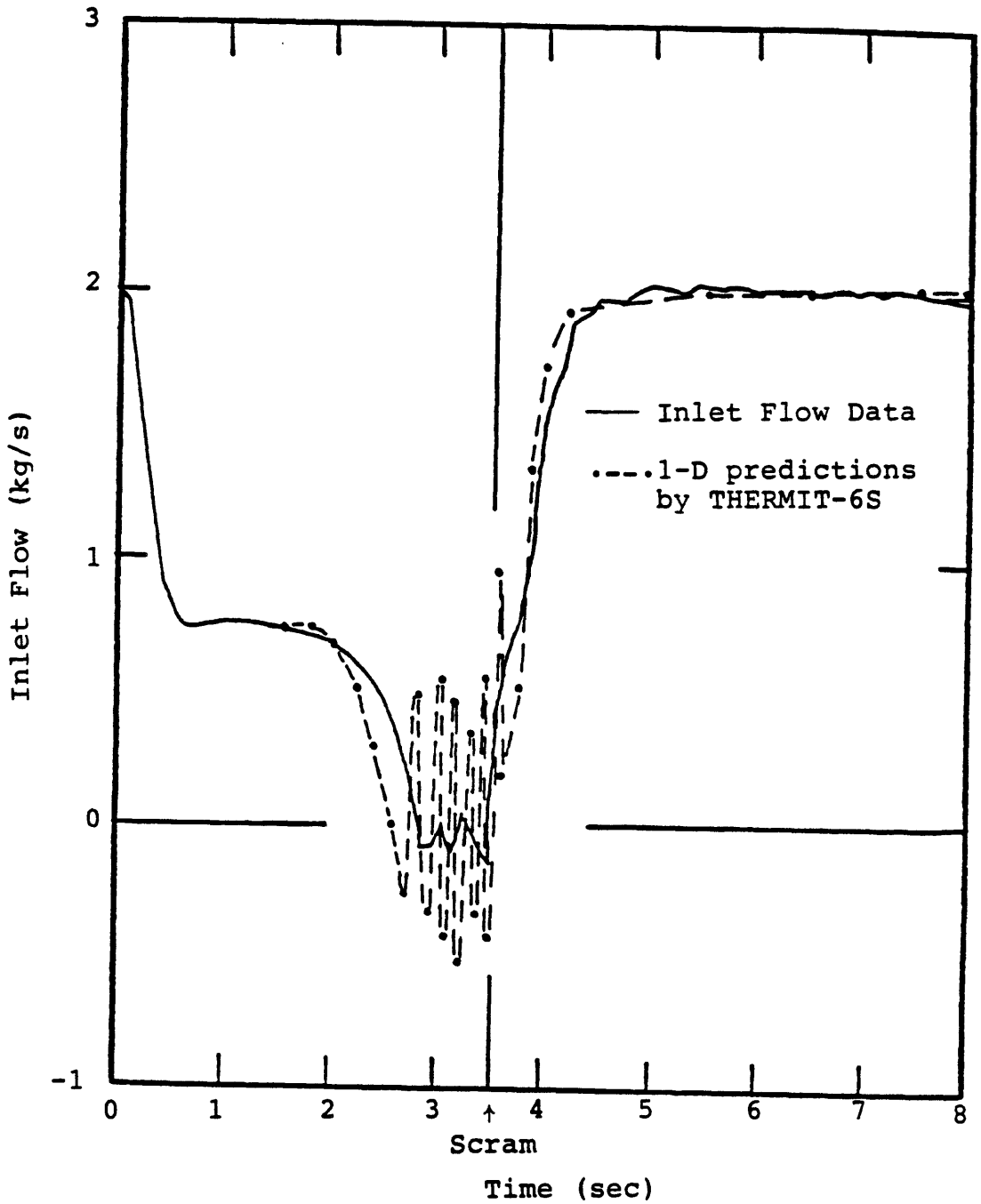

Fig. 6.10: Comparison between Inlet Flow Data and 1-D Predictions by THERMIT-6S for the W-7b' Test

6.2 P3A Experiment

The Sodium Loop Safety Facility (SLSF) P3A experiment (88) was an in-pile test performed by Argonne National Laboratory in 1977. Coolant boiling was detected by test section flowmeters and acoustic sensors at 0.8 seconds. Inlet flow reversal occurred at 10 seconds, followed by inlet flow oscillation. Gas passing through the bundle exit flowmeter at 10.8 seconds, was indicative of clad failure. Extensive clad melting and motion occurred at 12 seconds. ETR scram occurred at 12.9 seconds, as planned.

6.2.1 Test Apparatus and Procedures

SLSF test apparatus has already been described in Section 6.1.1.

The P3A experiment was designed to operate at coolant flow rates of 9.2 lb/sec in the test subassembly and 19.3 lb/sec in the loop while removing 1240 Kw of test assembly power at bundle inlet and exit temperatures of 720 F and 1216 F, respectively. These operating conditions simulate the design, center subassembly, beginning-of-life operating conditions in the FFTF core. A temperature gradient in the radial direction was observed which did not agree with the predicted values. This discrepancy was attributed to a non-uniform radial power distribution in the bundle. An estimated radial power profile is as follows:

Fuel Pins		Power Factor
center pin	:	0.9

1st row	:	0.95
2nd row	:	1.07
3rd row	:	1.156

The unprotected pump trip caused to start flow coastdown at t = 0 second, while the reactor power was maintained at the initial full power, 1240 Kw. The inlet mass flow rate reached 42% of the initial value at 8.8 seconds when boiling started. Without boiling the flow decay curve in the condition was designed to follow the projected ETR LOF curve up to 13 seconds. Afterwards, the flow was held constant at 2.76 lb/sec corresponding to 30% of the initial value.

6.2.2 Numerical Simulation of P3A

6.2.2.1 2-D Analysis of P3A

In the 2-D analysis of the P3A test, the central two subchannel rings are agglomerated into one mesh. This can be justified by Fig 6.11 which shows very uniform radial temperature gradients in the central two rings. As shown in Fig 6.12, the fuel bundle consists of three mesh zones in the radial direction. Seventeen mesh zones in the axial direction are considered: one in the lower blanket (each 8"), nine in the fuel (each 4"), two in the upper blanket (each 6"), and five in the gas plenum (each 8"). In effect, the upper blanket in the W-1 test is replaced by the gas plenum in the P3A test. Up to 8.8 seconds into the

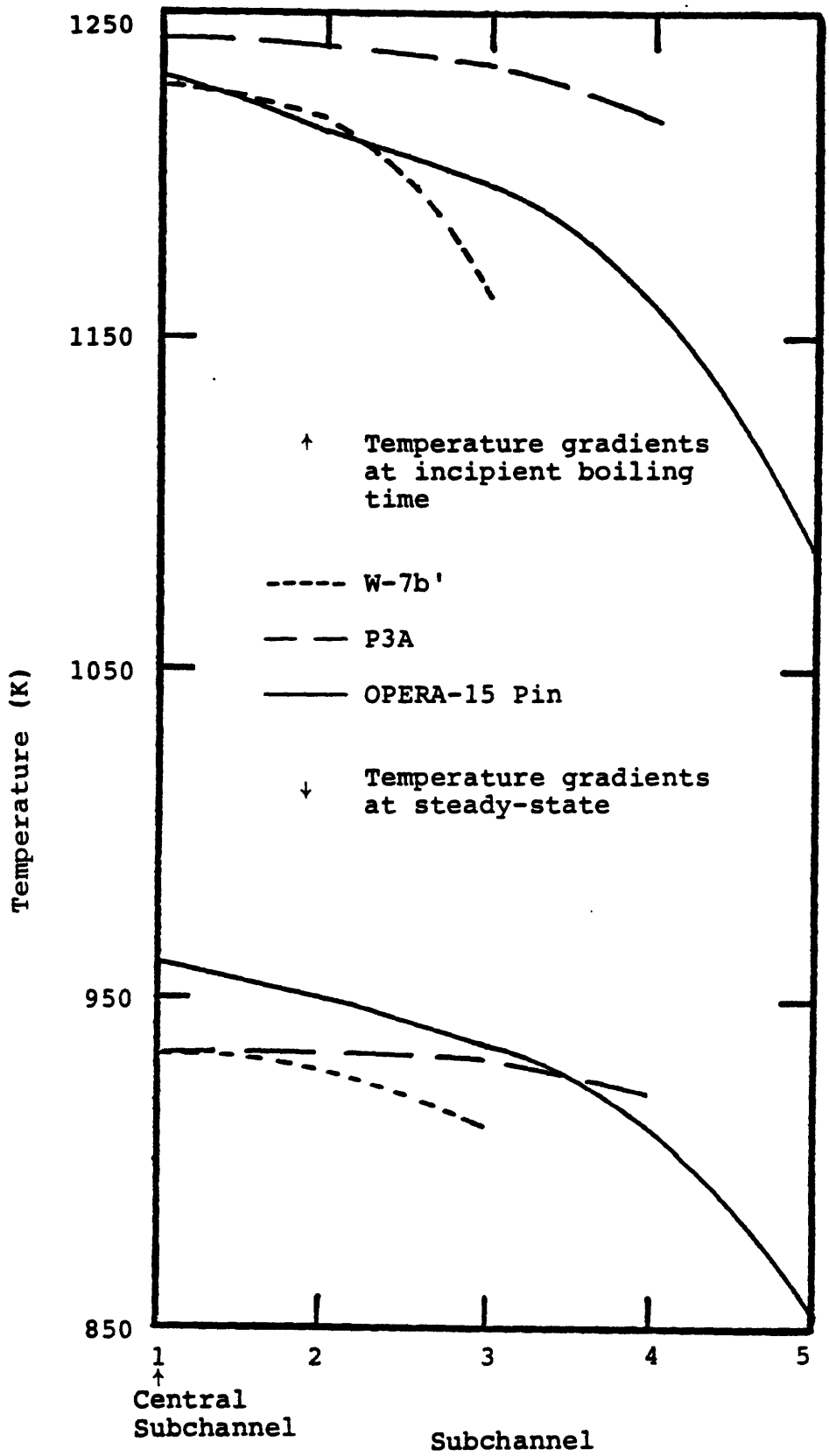

Fig. 6.11: Radial Temperature Gradients at the Last Cell of Heated Section Predicted by THERMIT-6S for the W-7b', P3A, and OPERA-15 Pin

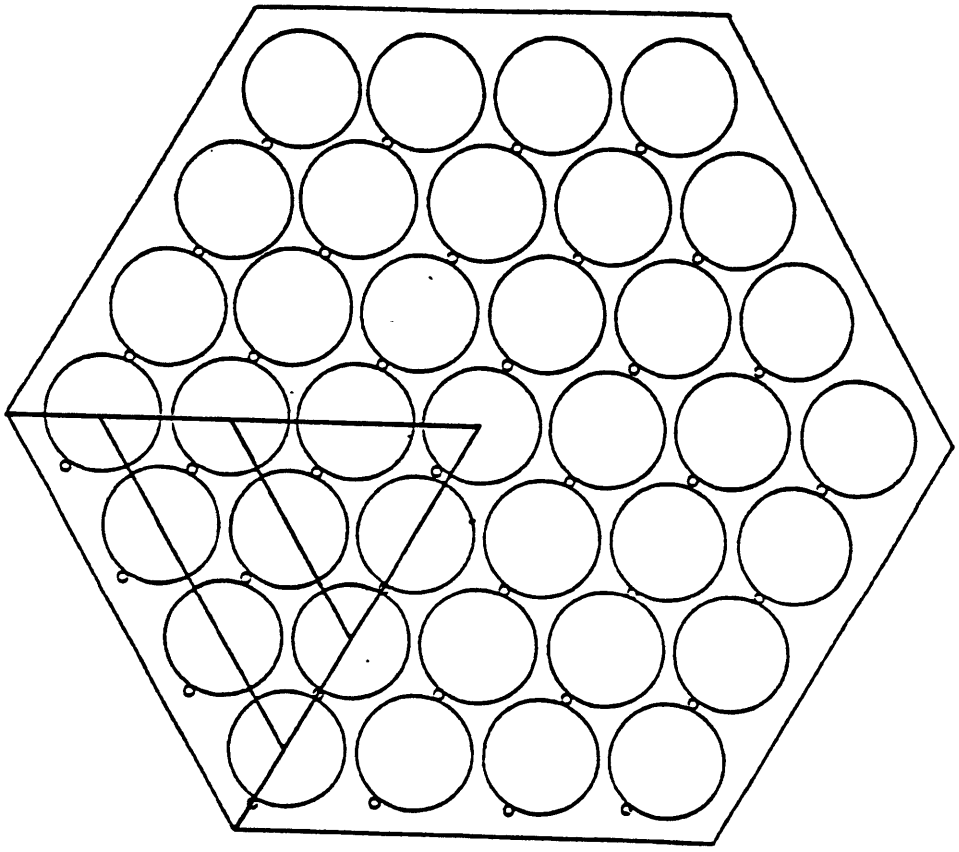

Fig. 6.12: Radial Meshes of the Fuel Bundle for the 2-D Numerical Simulation of P3A

transients when boiling started, the measured inlet flow is used for the inlet boundary condition. Similar to the W-7b', the inlet and outlet boundaries are positioned as shown in Fig 6.1. The inlet and outlet pressures are estimated so as to give the same inlet mass flow rate and saturation temperature as those measured at the end of the heated section at 8.8 seconds. After 8.8 seconds the constant pressure drop between the boundaries is used to observe flow coastdown and flow oscillation. The estimated nonuniform power distribution and constant Nusselt number for liquid thermal conduction, Nu=22, are used for the numerical simulation during transients.

6.2.2.2 Results

Numerical results for the P3A are shown in Figs 6.13-6.15. Incipient boiling starts at 9.4 seconds and inlet flow reversal occurs at 10.6 seconds. Dryout occurs within 0.2 seconds after flow reversal. Figs 6.13-6.14 show temperature transients predicted by THERMIT-6S and COBRA-3M (12) as well as data at various positions with time. The COBRA-3M predictions were obtained by using uniform power distribution. The predictions by THERMIT-6S are in closer agreement with experimental results, partly because of use of uniform power distribution for COBRA-3M analysis.

Incipient boiling starts in the last cell of the heated section of the central channel, delayed 0.6 seconds in comparison with experimental incipient boiling time. In the

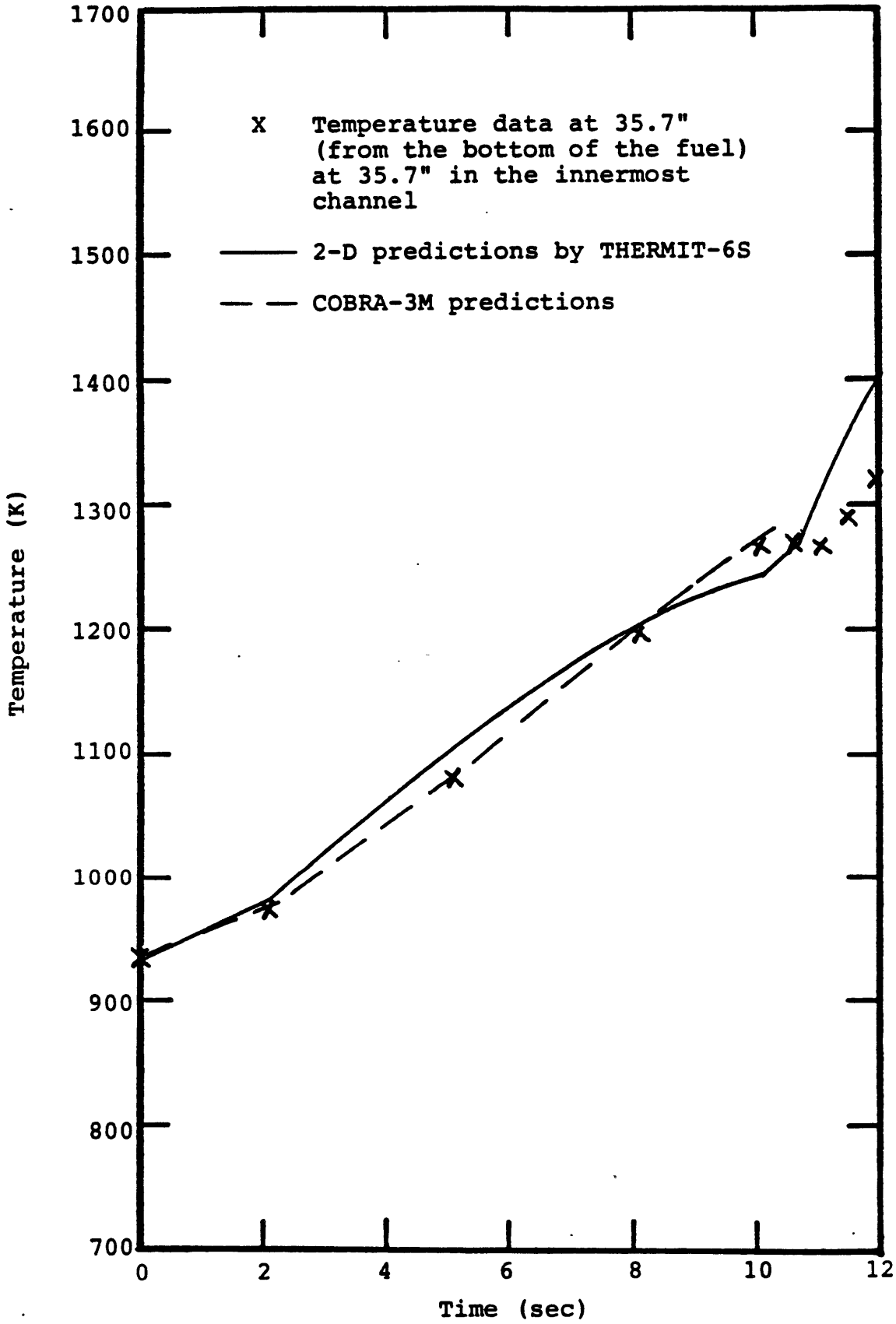

Fig. 6.13: Comparison among Temperature Data, COBRA-3M Predictions, and 2-D Predictions by THERMIT-6S at 35.7" (from the bottom of the fuel) in the Innermost Channel for the P3A Test

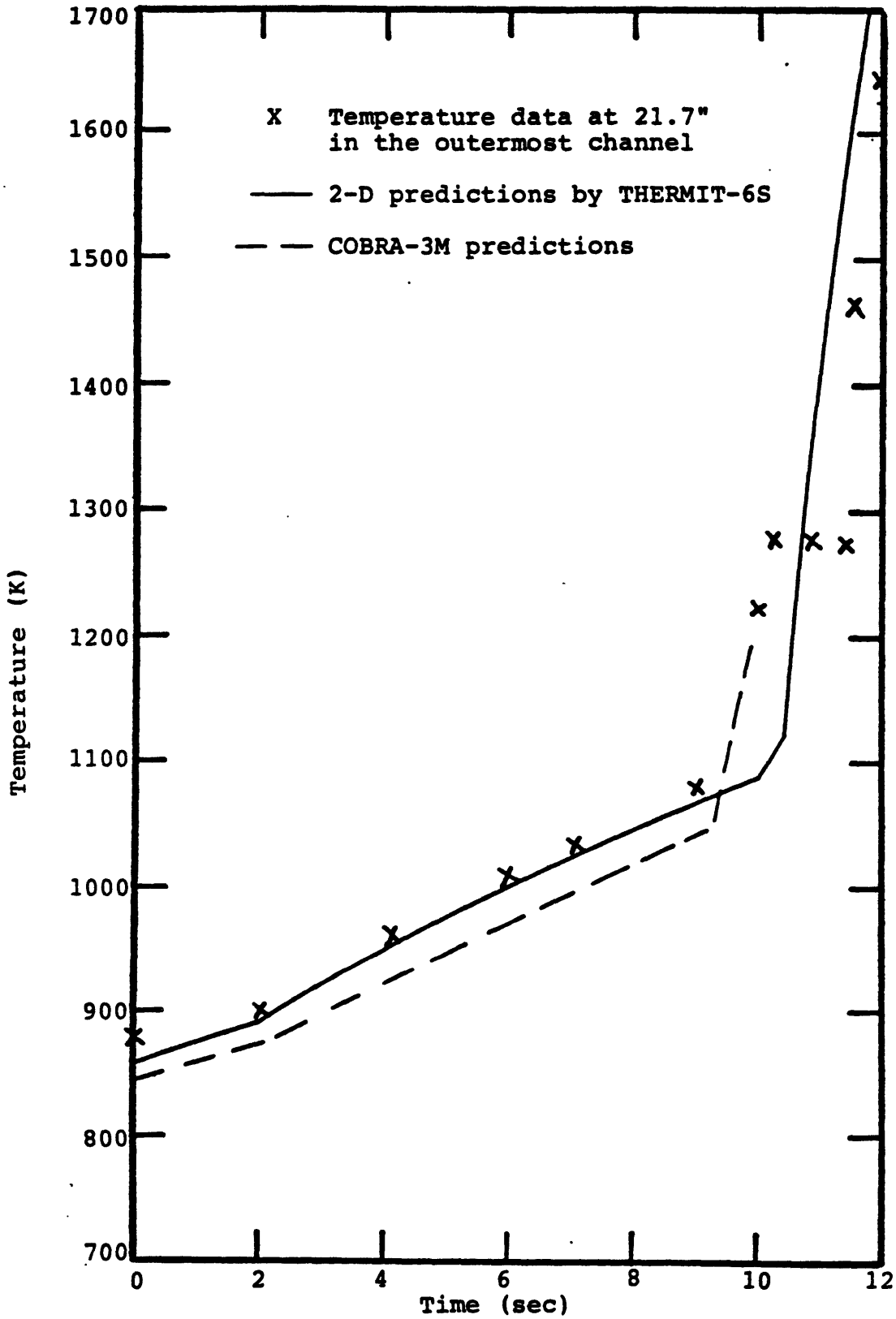

Fig. 6.14: Comparison among Temperature Data, COBRA-3M Predictions by THERMIT-6S at 21.7" (from the bottom of the fuel) in the Outermost Channel for the P3A Test

initial stage of boiling, THERMIT-6S predicts a higher inlet flow rate than the experiment because, while pump power was preset to decrease slowly up to 13 seconds, a constant pressure drop boundary condition is used in the numerical simulation. As shown in Fig 6.15, the rate of inlet flow coastdown in the computation after 0.8 seconds is more rapid than that in the experiment. This can be explained by the reasons described in Section 6.1.2.2.

As initial slower flow coastdown is followed by more rapid flow coastdown than the data, flow reversal occurs almost at the same time as that in the experiment. Within 0.2 seconds after flow reversal, dryout occurs. This confirms the conclusion from the W-7b' simulation that the incidence of flow reversal is the most important single factor in the occurrence of dryout in low flow/high power accidents. After dryout, vapor is rapidly accelerated due to high void fraction and this high vapor velocity dramatically reduces the time step size.

Liquid reentry occurs at 0.2 seconds after flow reversal, followed by inlet flow oscillation. The frequency of flow oscillation is 6 cycles/sec, compared to 3 cycles/sec in the experiment and the amplitude is much larger than that in the experiment due to the plausible reasons described in Section 6.1.2.2.

Fig 6.15 shows predictions by the NATOF-2D code (Ref 16) and the present code as well as the experimental inlet flow rates. The predictions by NATOF-2D are highly

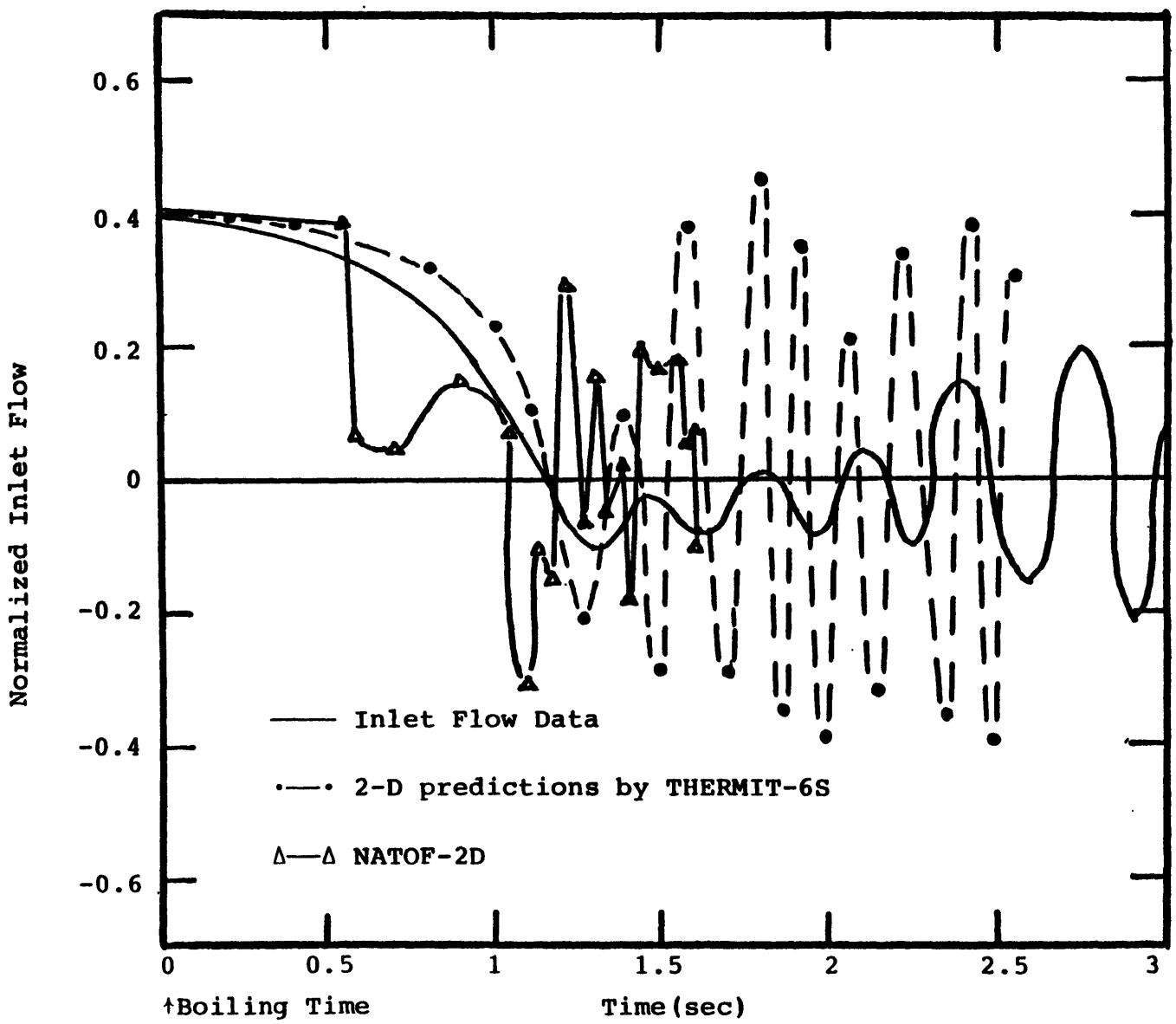

Fig. 6.15: Comparison between Inlet Flow and Predictions by NATOF-2D and THERMIT-6S for the P3A Test

irregular and terminated at around 1.6 seconds. In Ref 88 the predictions by SAS-3A were reported to be in good agreement with data.

6.3 OPERA 15-Pin Experiment

OPERA is an Out-of-Pile expulsion and Reentry Apparatus at ANL. OPERA 15-Pin (101) is a sodium experiment which simulates the initiating phase of a pump coastdown without the scram of a LMFBR, specifically, the FFTF. The objective of the OPERA 15-Pin pump-coastdown test is to investigate sodium boiling initiation and the subsequent two-dimensional nature of sodium voiding in large pin bundles approaching the size of current LMFBR subassemblies. In a large pin bundle the steep radial coolant temperature profile will affect the behavior of vapor generation, vapor condensation, onset of flow reversal, radial voiding, clad dryout, and the axial void oscillations.

This experiment utilized 15 electric fuel pin simulators in a triangular thin walled duct to represent a high powered sub-assembly in which each pin produces 33 Kw. The 15-Pin triangular test bundle was fabricated to simulate the one-sixth sector of a 61-pin hexagonal bundle.

6.3.1 Test Apparatus and Procedures

The OPERA facility is a once-through sodium system. Steady-state coolant flow with the inlet temperature 588 K through the test section is generated by first pressurizing

the blowdown vessel with argon gas, opening the sodium control valves at the inlet to the test section, and at the same time venting the receiver vessel to atmosphere. The pump-coastdown flow transient is generated by depressurizing the blowdown vessel through a valve and two nozzles, which can be preset by calibration procedures, to give the desired flow decay.

The pin power is maintained at 33 Kw until 3 heater pins fail or their power output varies 10% from the full 33 Kw at which time all pin power is terminated.

Full size wire wraps (0.0142cm O.D.) are on the interior pins and the pins on the one side of the bundle where the outside wall conditions are to be simulated. Small wire wraps (0.079 cm O.D.) and fillers (0.158 cm O.D.) are used on the pins and walls at the other two sides of the bundle where the interior part of the 61-pin bundle is to be simulated. This arrangement ensures that the power to flow ratio of each subchannel is the same as the corresponding subchannel in a 61-Pin hexagonal bundle. The thermal capacitance of the wall is minimized by using a thin wall of 0.5 mm thickness.

6.3.2 Numerical Simulation of OPERA-15 Pin

6.3.2.1 2-D Analysis of OPERA-15 Pin

A 2-D analysis is performed for the OPERA-15 Pin numerical simulation. As shown in Fig 6.16, the test section consists of five mesh zones in the radial direction.

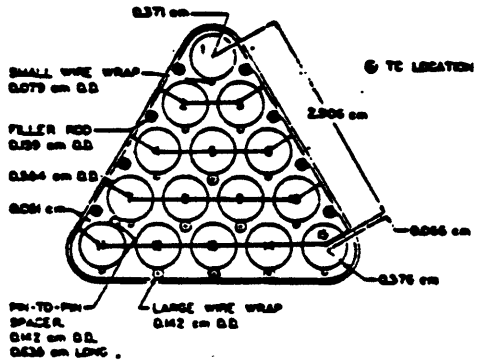

Fig. 6.16: Geometry of OPERA-15 Pin Bundle

Twenty nine mesh zones in the axial direction are considered: 18 in the heated section (each 2") and 11 in the unheated section (each 2" for low 3 mesh zones and each 6" for the next 8 mesh zones).

Inlet and outlet boundaries are positioned at the outlet of the blowdown vessel and inlet of the receiver vessel, respectively. As the receiver vessel is connected to the atmosphere, the outlet pressure is set to be equal to one atmosphere over the transients. The inlet velocities measured in the experiment are used for the inlet boundary condition up to 9 seconds into the OPERA-15 Pin flow transients when boiling starts in the numerical simulation. After boiling the outlet pressure estimated by the figure of blowdown vessel depressurization given in Ref 101 is used for the outlet boundary condition. Uniform radial and axial power distributions, and constant Nusselt number for liquid heat conduction, Nu=22, are used.

6.3.2.2 Results

The results by the present code were obtained by using the pretest information package for the OPERA-15 Pin, which contains only experiment apparatus, test section description, and operating procedures. Therefore, it is interesting to compare predictions by the present code to experimental data (102) which were published later.

Boiling first starts at 9 seconds into transients in the hottest channel, compared to 9.4 seconds in the test.

Fig 6.17 illustrates one of the primary reasons for the prediction of this earlier boiling: temperature predicted by the present code is higher than data over transients.

Up to 2 seconds after boiling starts, flow coastdown is very slow. Figs 6.18 and 6.19 reveal the reason of this slow flow coastdown: it takes about 1.8 seconds for vapor to reach the outermost channel due to the large bundle size, large inlet hydraulic resistance, and large radial temperature gradients shown in Fig 6.11. In the test it was estimated that the sodium void progresses from the innermost channel to the outermost channel in about 1.5 seconds.

Rapid flow coastdown follows and flow reversal at the inlet occurs at 3.1 seconds from incipient boiling, compared to 2.6 seconds in the experiment. (See Fig 20) This delay of flow reversal is attributed to larger temperature drop laterally across the bundle in the computation which is 144 K at boiling inception, compared to 109 K in the experiment. Note that for all three experiments simulating the low flow/high power accidents, the W-7b', P3A, and OPERA-15 Pin, rapid flow coastdown occurred when the outmost channel reaches around saturation temperature and vapor production in some cells of the outmost channel takes place instead of vapor condensation.

The outlet flow is almost constant up to 3.2 seconds when vapor reaches the end of the test section. Afterwards, the outlet flow rapidly drops due to high void fraction at the end of the test section, but never becomes the negative

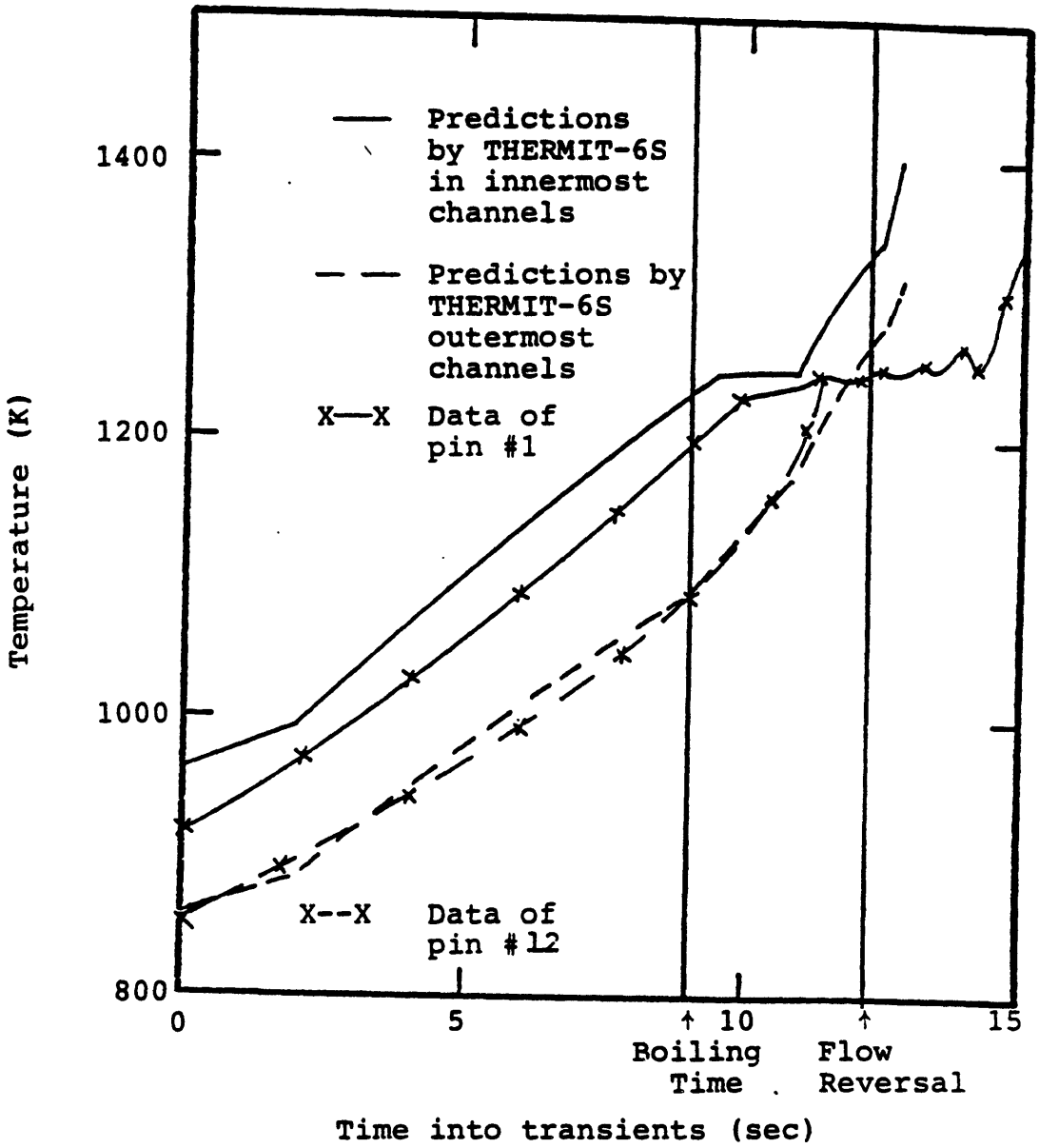

Fig. 6.17: Comparison of Temperature Transients of OPERA-15 Pin with Pretest Predictions by THERMIT-6S at 35.5" (above fuel bottom) in Innermost and Outermost Channels

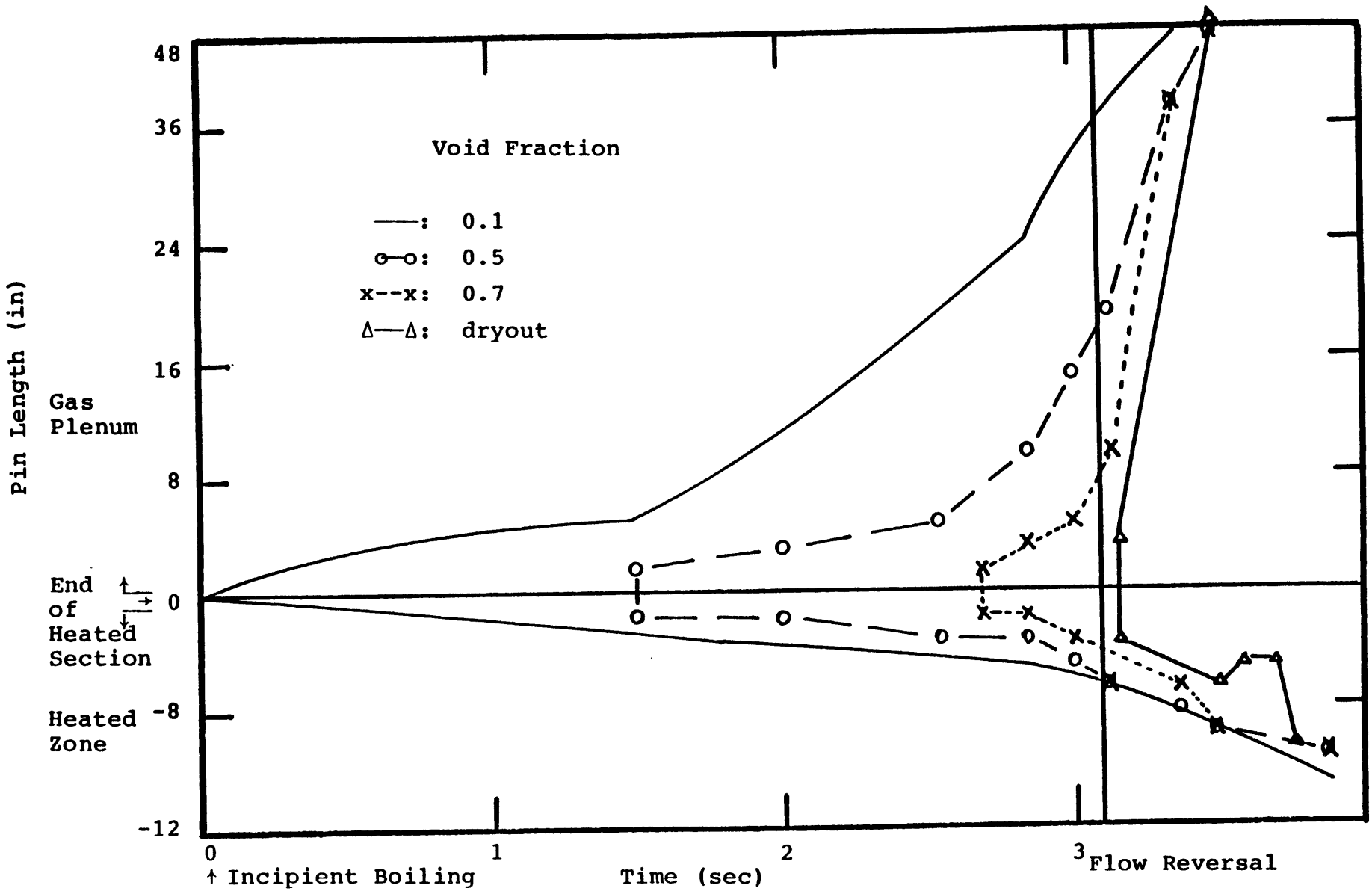

Fig. 6.18: Axial Void Profile in Innermost Channel Predicted by THERMIT-6S for the OPERA-15 Pin Test

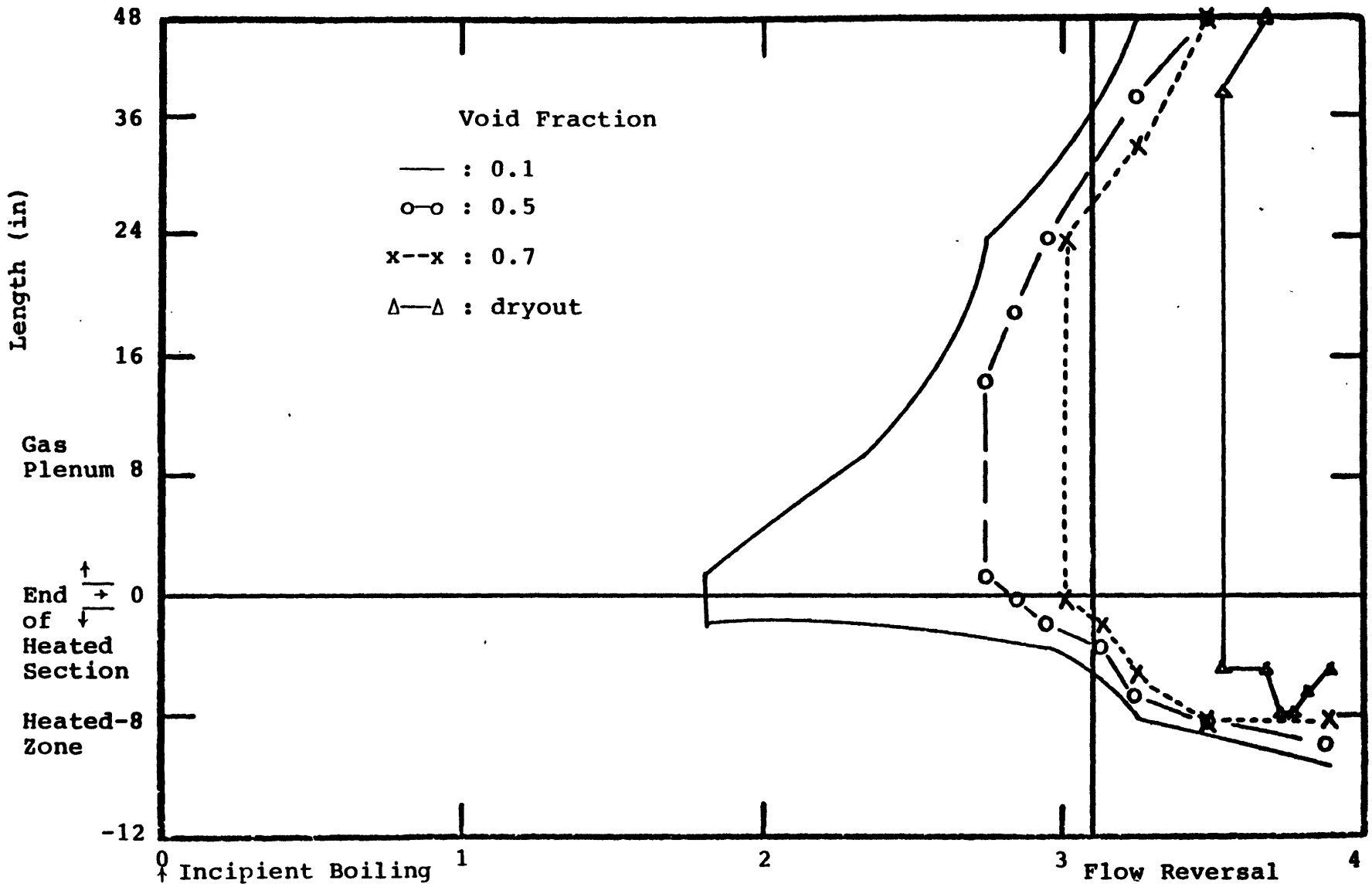

Fig. 6.19: Axial Void Profile in Outermost Channel Predicted by THERMIT-6S for the OPERA-15 Pin Test

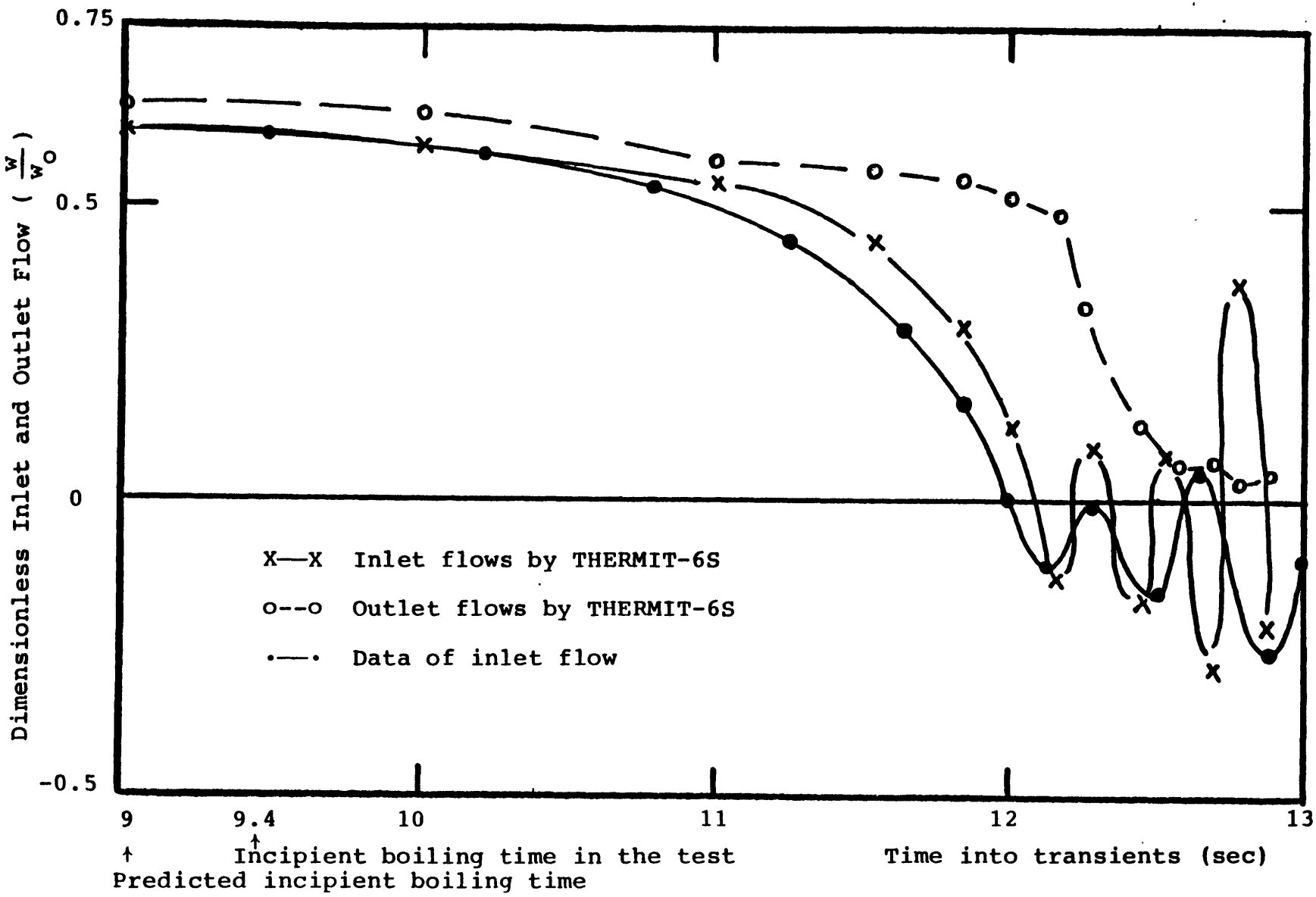

Fig. 6.20: Comparison of Flow Transients of OPERA-15 Pin with Pretest Predictions by THERMIT-6S

flow because the interfacial force by high vapor velocities drags the liquid along.

Within 0.05 seconds after flow reversal, dryout is predicted. However, the occurrence of dryout in the experiment was substantially delayed; elasped time from inlet flow reversal to dryout is around 2 seconds. In the computation liquid reentry occurs at 0.14 seconds after flow reversal and is followed by inlet flow oscillation of which the frequency is 3.5 cycles/sec, compared to 2 cycles/sec in the experiment.

6.4 THORS

During certain postulated loss-of-pipe-integrity transients in a loop-type liquid-metal fast breeder reactor (LMFBR), the flow-power mismatch, even with reactor scram, may be conducive to boiling conditions of several seconds duration in the reactor core. Experimental and analytical studies of sodium boiling in an electrically heated 19-pin simulated fuel assembly have been made at the Oak Ridge National Laboratory (ORNL) to investigate the extent of boiling stability at the low flow/low power transient condition.

6.4.1 Test Apparatus and Procedures

The THORS Bundle 6A experiments (40) were performed in 1978 at ORNL. The test section used was a full-length simulated LMFBR fuel assembly. It consists of 19

electrically heated pins. The bundle hexcan is a 0.02" thick 316 stainless steel backed by 1" of Marimet insulation contained in a stainless steel jacket.

Early in the test program, a comparison of experimental duct-wall temperatures with analytical predictions indicated higher values for hexcan thermal inertia than anticipated, and it was suggested that some sodium leakage into the insulation may have occurred. Posttest examination revealed that sodium had indeed penetrated the entire region.

The heated length of Bundle 6A is 36" with variable pitch heater windings to produce a 1.3 axial peak-to-mean chopped-cosine power distribution. The core inside the winding and the insulation between the winding and the type 316 stainless steel sheath is of compacted boron nitride. Downstream of the heated length, a nickel reflector and a simulated fission-gas plenum have the same length and thermal inertia as a FFTF fuel assembly.

The test-section inlet value was set to simulate the nominal-flow pressure drop of the reactor inlet configuration. The test-section sodium inlet temperature was set at 730 F. For each run, at a specified constant bundle power, a sodium flow was established to give a test-section bulk outlet temperature of 1300 F.

The test 72B, run 101 is selected for the numerical simulation because predictions by SAS-3A for this test are available in Ref 40. This test was a dryout run with the power 10.0 kw/pin. Before flow reduction began at 3

seconds, the flow was about 9.3 gpm (0.58 l/s) and the flow was reduced up to 3.7 gpm (0.23 l/s). Incipient boiling occurred at 12 seconds and afterwards, stable boiling lasted until 22 seconds, when a period of dryout and rewet began. At 30 seconds, permanant dryout began and power was cut at 31.5 secondss

6.4.2 Numerical Simulation of the test 72B, run 101

6.4.2.1 2-D Analysis of the test 72B, run 101

A 2-D analysis of THORS was performed, with the test section divided in the same way as the W-7b' analysis.

Inlet and outlet boundaries are positioned at the inlet and outlet of the test section because the inlet and outlet pressures of the test section were measured and kept constant after boiling. Up to 12 seconds into transients, when boiling started, the velocity-pressure boundary condition is used. After boiling the pressure-pressure boundary condition is used and the inlet and outlet pressures are kept at a constant value which gives the same mass flow rate as the experimental value at 12 seconds. The 1.3 axial peak-to-mean chopped-cosine power distribution, uniform radial power distribution, and constant Nusselt number for liquid heat conduction, Nu=22, are used. The properties of Marimet insulation degraded by leakage of sodium, which were estimated in Ref 40 by assuming that all the void space was full of sodium, are used. (Refer to Appendix B)

6.4.2.2 Results

Strong radial temperature gradients in the test are evident in Fig 6.21. The temperature difference between the centerline and periphery of the bundle is almost 160 K just before boiling. On the other hand, milder radial temperature gradients are predicted by the present code as shown in Fig 6.21. One of the plausible explanation on this discrepancy is the use of a high Nusselt number for the liquid conduction model. The Nusselt number 22 was obtained by comparison to a steady state experiment with high liquid velocity (99). As the test 72 B, run 101 is a low flow transient, it is expected that turbulent contribution on the effective liquid conduction will be reduced. In Fig 6.22, the predictions are in good agreement with the data inspite of the strong radial temperature gradients, because the temperature difference between the predictions and the data in the intermediate channel is relatively small, compared to that in the outermost and innermost channels.

This mild predicted radial temperature gradient can be one of the reasons for the 1.5 second delay of incipient boiling. Strong radial temperature gradients highly influence the prediction of incipient boiling time for 1-D simulation as explained in Section 6.1.2.2. Actually SAS-3A, with 100% of structure heat capacities which implies that all the void space in the Marimet insulation was filled with liquid sodium, predicted that boiling and dryout inceptions were delayed 11 seconds and 24-26 seconds,

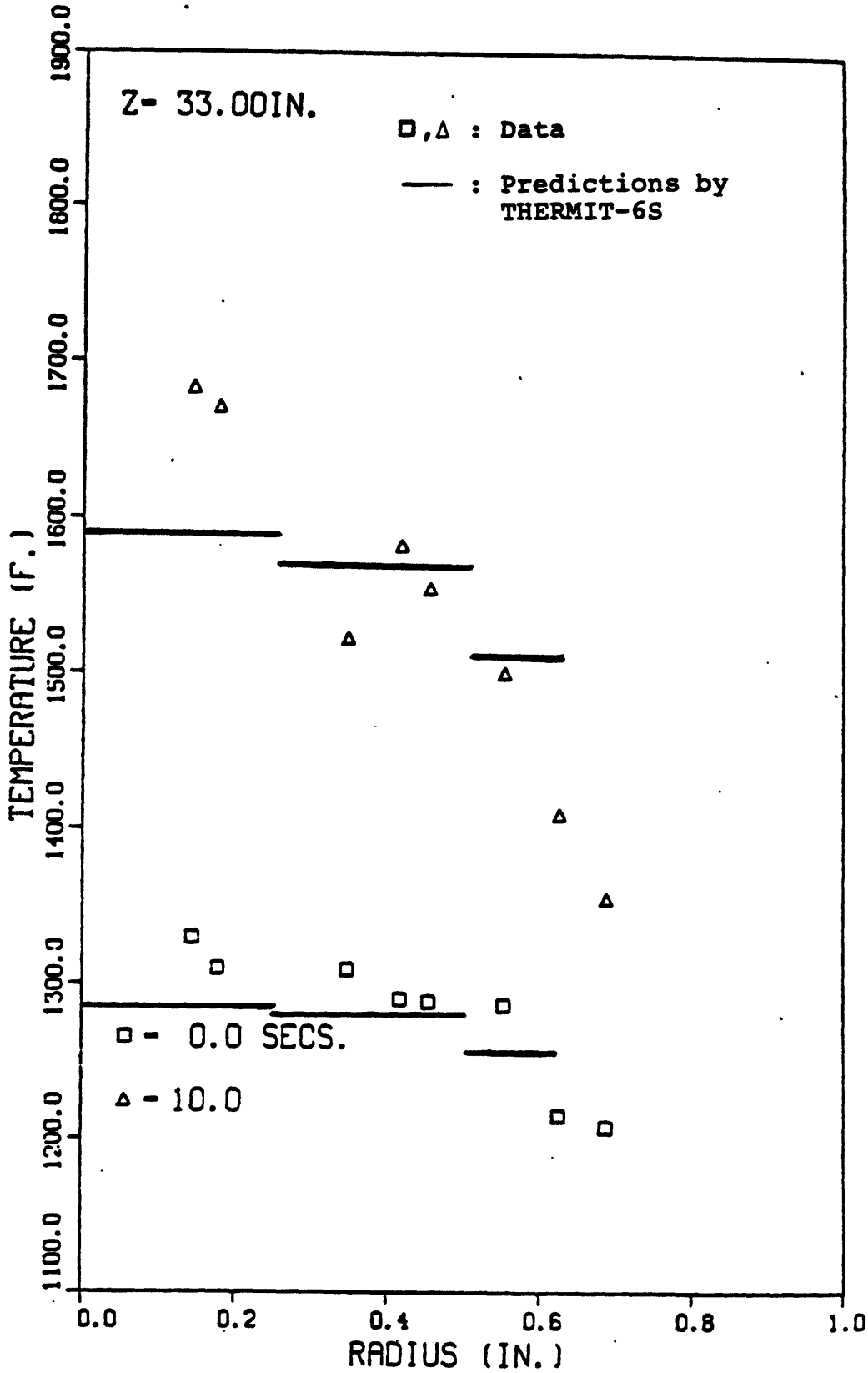

Fig. 6.21: Temperature vs. Radius with Time as a Parameter at Z = 33" (test 72B, run 101 of THORS)

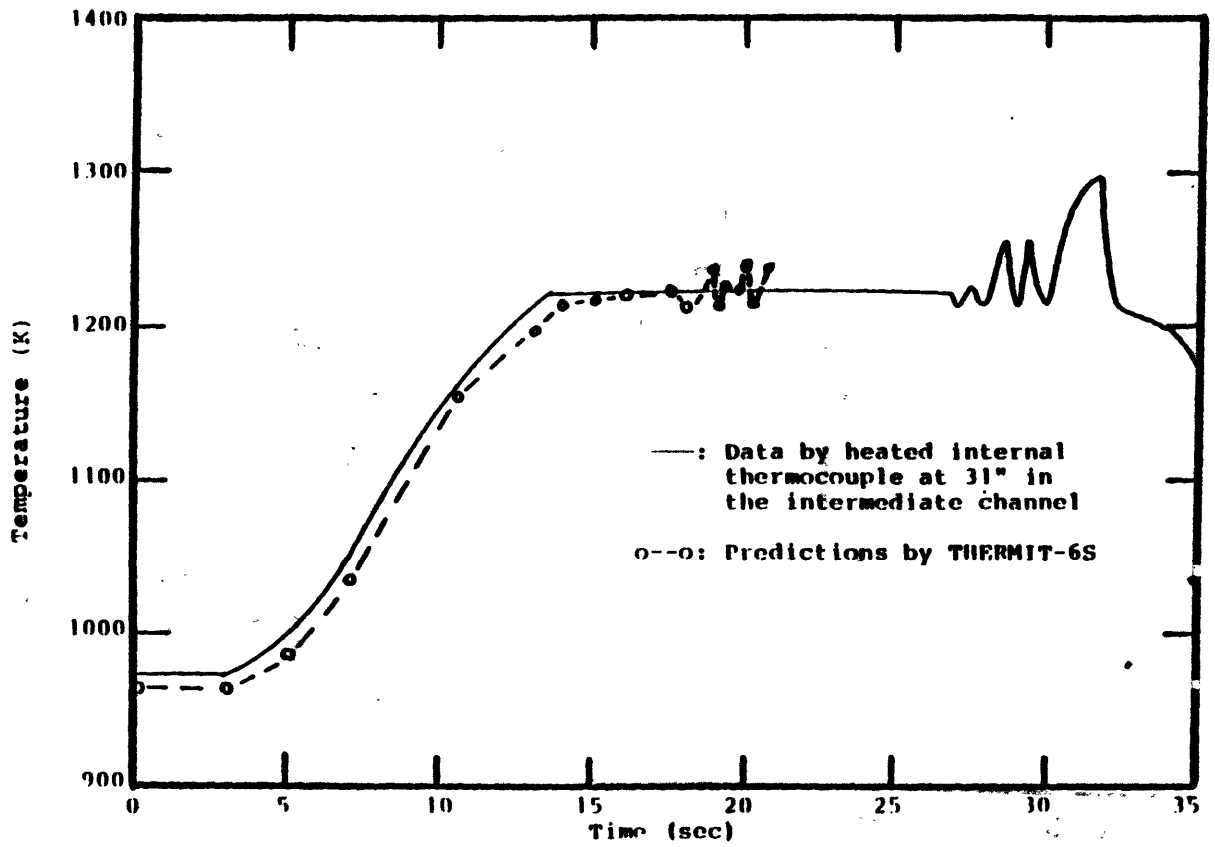

Fig. 6.22: Comparison between Predictions by THERMIT-6S and Temperature Data at 31" (from the bottom of the fuel) in the Intermediate Channel for the test 72B, run 101 of THORS

respectively. With 0% of structure heat capacities SAS-3A was satisfactory in predicting boiling inception.

In the initial stage of boiling, large inlet flow oscillation in the test takes place due to large superheat and low inlet hydraulic resistance. Unlike in-pile experiments which have a source such as fuel to provide enough non-condensible gas for nucleation of boiling, out-of-pile experiments such as THORS are likely to have little non-condensible gas and as a result, large superheat is possible in out-of-pile experiments. As no superheat for incipient boiling in the present analysis is assumed, Fig 6.23 shows the small amplitude of inlet flow oscillation in the initial stage of boiling. Figs 6.23 and 6.24 present approximate boundaries of the inlet mass flow rate in the experiment because of a difficulty in reading data. The SAS-3A predicted much larger oscillation than the present code does.

While dryout in low flow/high power accidents such as the W-7b', P3A, and OPERA-15 Pin occurred immediately after flow reversal, dryout in the test 72 B, run 101 occurred after 3 seconds from flow reversal. (see Fig 6.25) Another distinctive characteristic of the test 72 B, run 101 is the periodical occurrence of dryout and rewet over the whole bundle. (See Figs 6.21, 6.25, and 6.26) In low flow/high power accidents this phenomenon did not occur or lasted for a very short time.

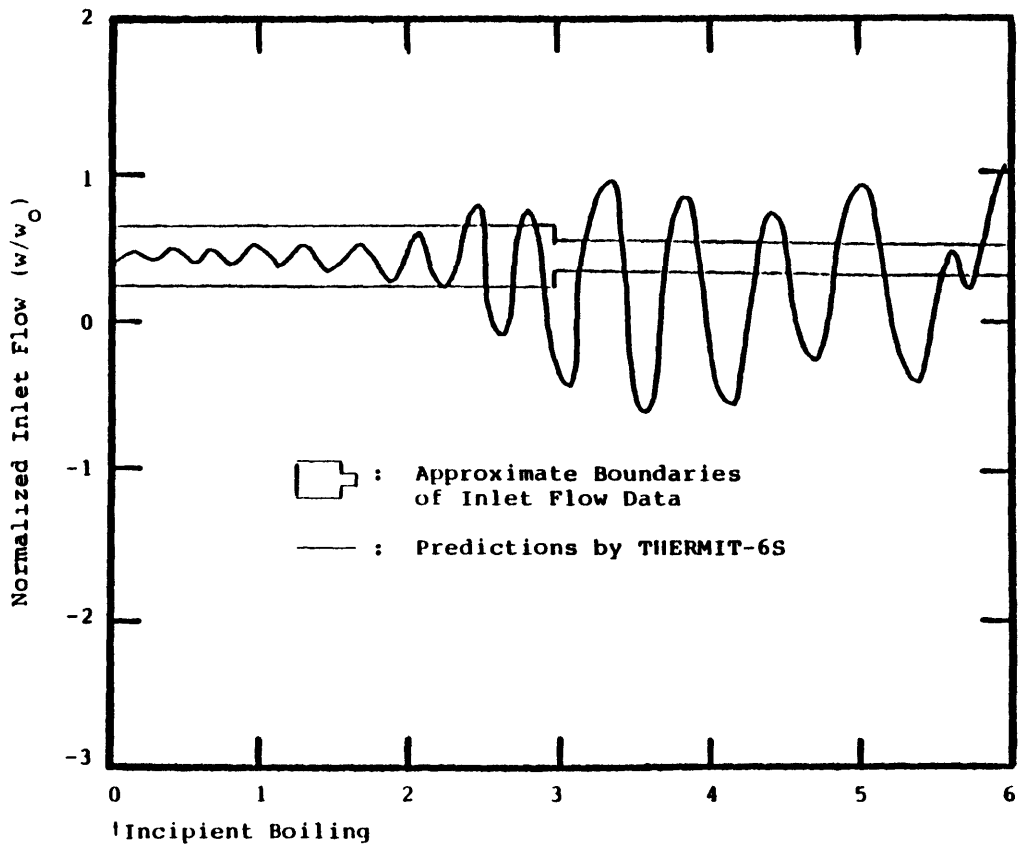

Fig. 6.23: Comparison between Inlet Flow Data and Predictions by THERMIT-6S for the Test 72B, Run 101 of THORS

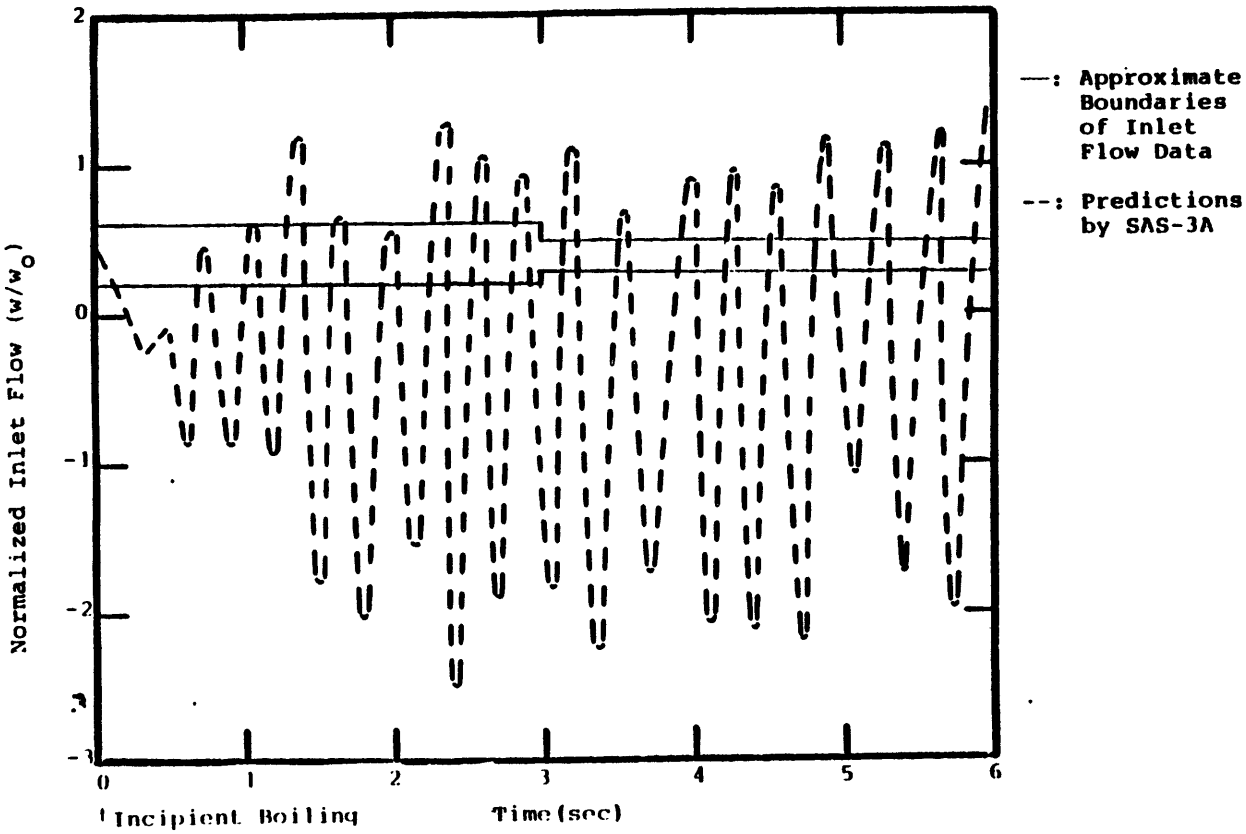

Fig. 6.24: Comparison between Inlet Flow Data and Predictions by SAS - 3A for the Test 72B, Run 101 of THORS

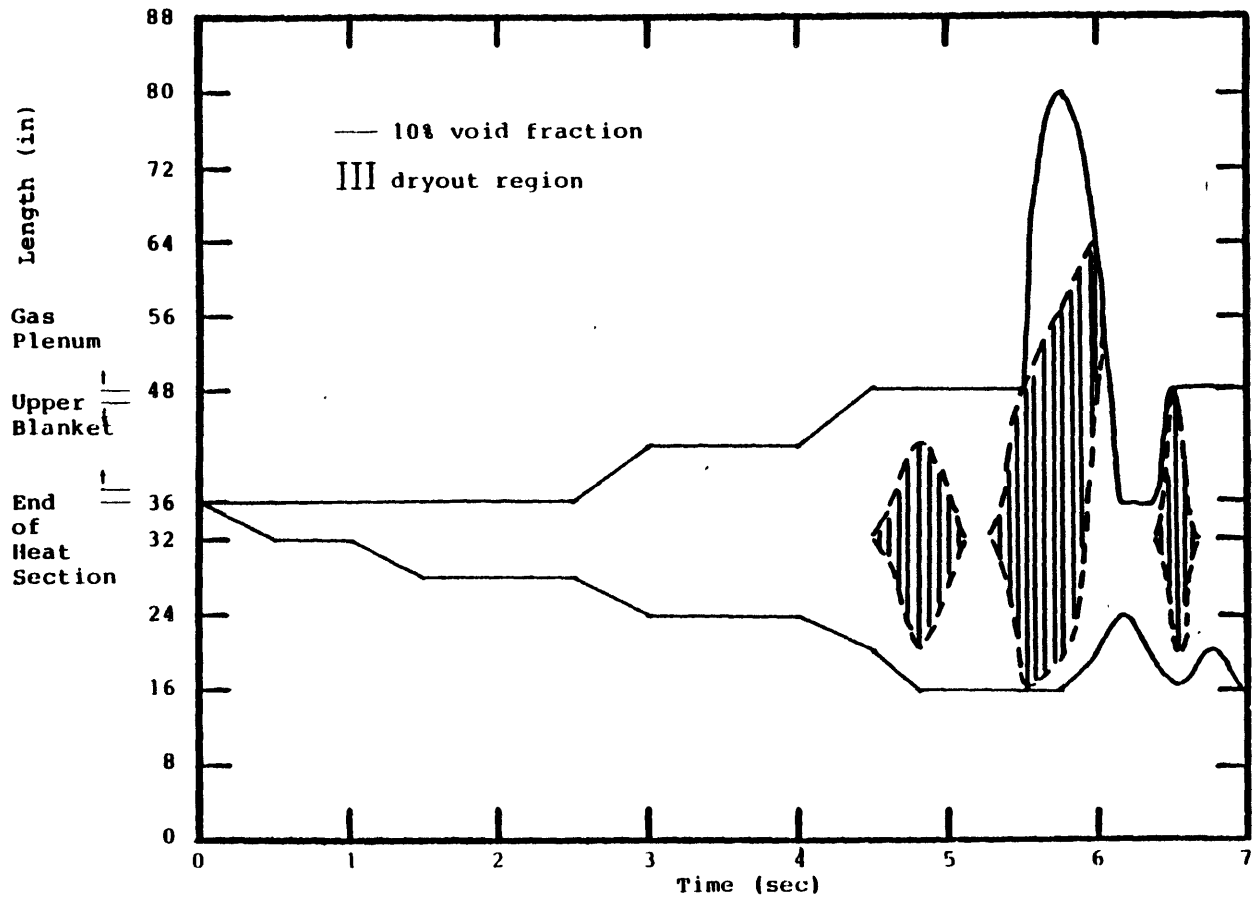

Fig. 6.25: Axial Void Profile in the Innermost Channel Predicted by THERMIT-6S for the Test 72B, Run 101 of THORS

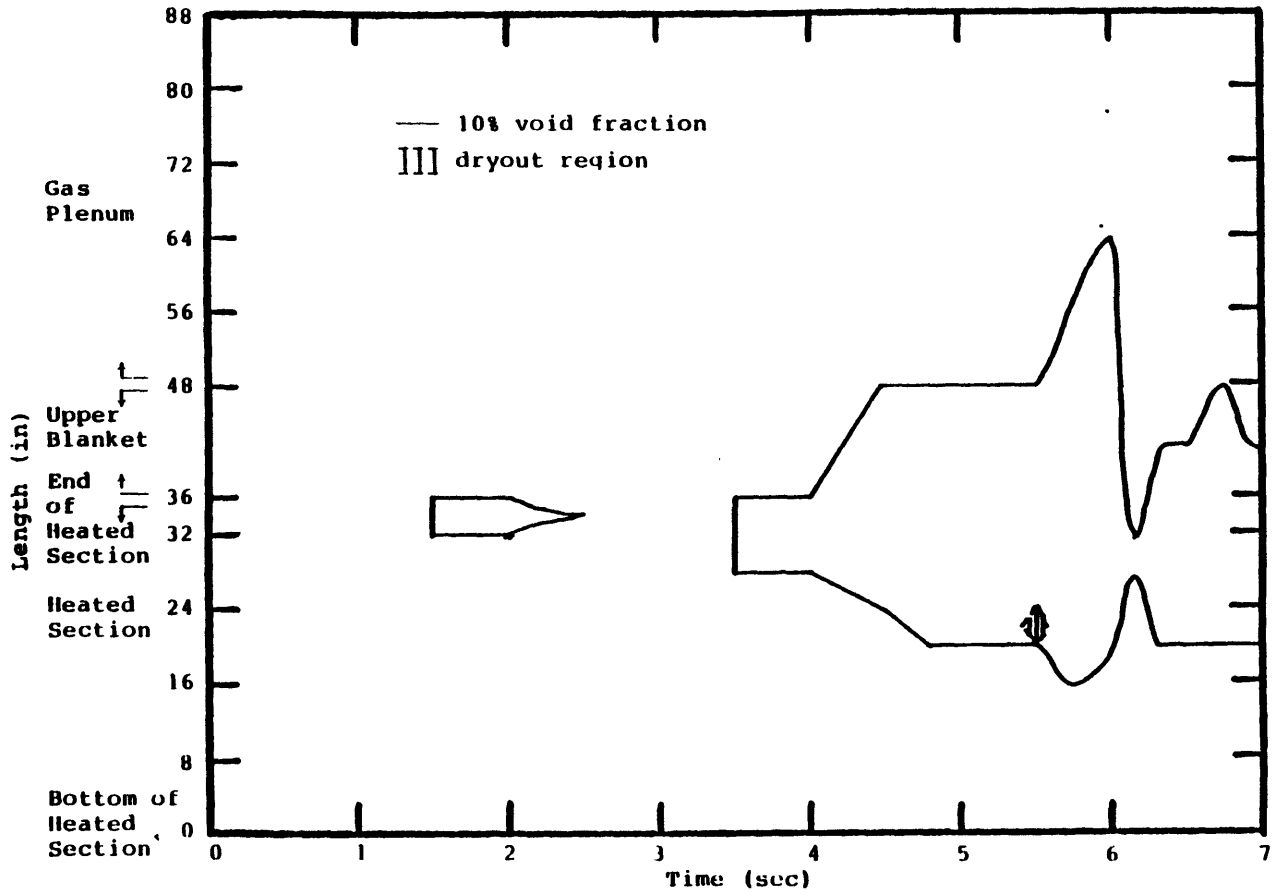

Fig. 6.26: Axial Void Profile in the Outermost Channal Predicted by THERMIT-6S for the Test 72B, Run 101 of THORS

6.5 Sensitivity Analysis

The sensitivity analysis reported here is done for the W-7b' simulation.

6.5.1 Interfacial Mass and Energy Exchange Models

For comparison with the present mass exchange model, described in Section 5.2.4, the equilibrium model and kinectic model are considered. The kinetic model is the model adopted in NATOF-2D based on a simple kinetic theory with the condensation coefficient set to unity.

The equilibrium model assumes that there is no temperature difference between vapor and liquid. With an infinite heat transfer coefficient assumed in THERMIT (17), both vapor and liquid are forced to have the saturation temperature. While the liquid film at a saturated boiling zone is in reality at a superheated state, in the equilibrium model it is always at a saturated state. Therefore, the superheat energy contained in the liquid film has to be transferred to vapor by mass exchange to achieve the saturation state. Note that mass exchange is driven by the difference between liquid and saturation temperatures. Then in the heated section with high heat flux, or high temperature gradient in the liquid film, the equilibrium model predicts higher mass exchange rates. Also all vapor transferred from the saturated region to the subcooled region will be condensed. The kinetic model produces almost the same results as the equilibrium model.

As a result, the equilibrium model and kinetic model predict higher condensation and evaporation rates than the present model, which allows a nonequilibrium state between vapor and liquid. (See Fig 5.10) These larger condensation and evaporation rates induce greater pressure fluctuation which may cause failure of convergence of the Newton iteration. As expected, severe numerical difficulties are encounted; calculation with both the homogeneous and kinectic models stopped within 0.1 seconds after incipient boiling due to failure of convergence of the Newton iteration.

6.5.2 Interfacial Momentum Exchange Models

The present model described in Section 5.2.4 is compared with the homogeneous model and the Autruffe model which was implemented in the old version of THERMIT. In the homogeneous model vapor and liquid velocities are forced to be equal by an infinite momentum exchange. The Autruffe model was developed with data obtained in annular flow with large amount of droplets and this included the interfacial momentum exchange by both the liquid film and droplets. As a result, his model predicts much larger drag coefficients than the present model does.

The larger interfacial drag force, the more vapor will be trapped in the cells. Therefore, the homogeneous model predicts the largest void fraction as seen in Fig 6.27. Notice that the homogeneous and Autruffe models predict the

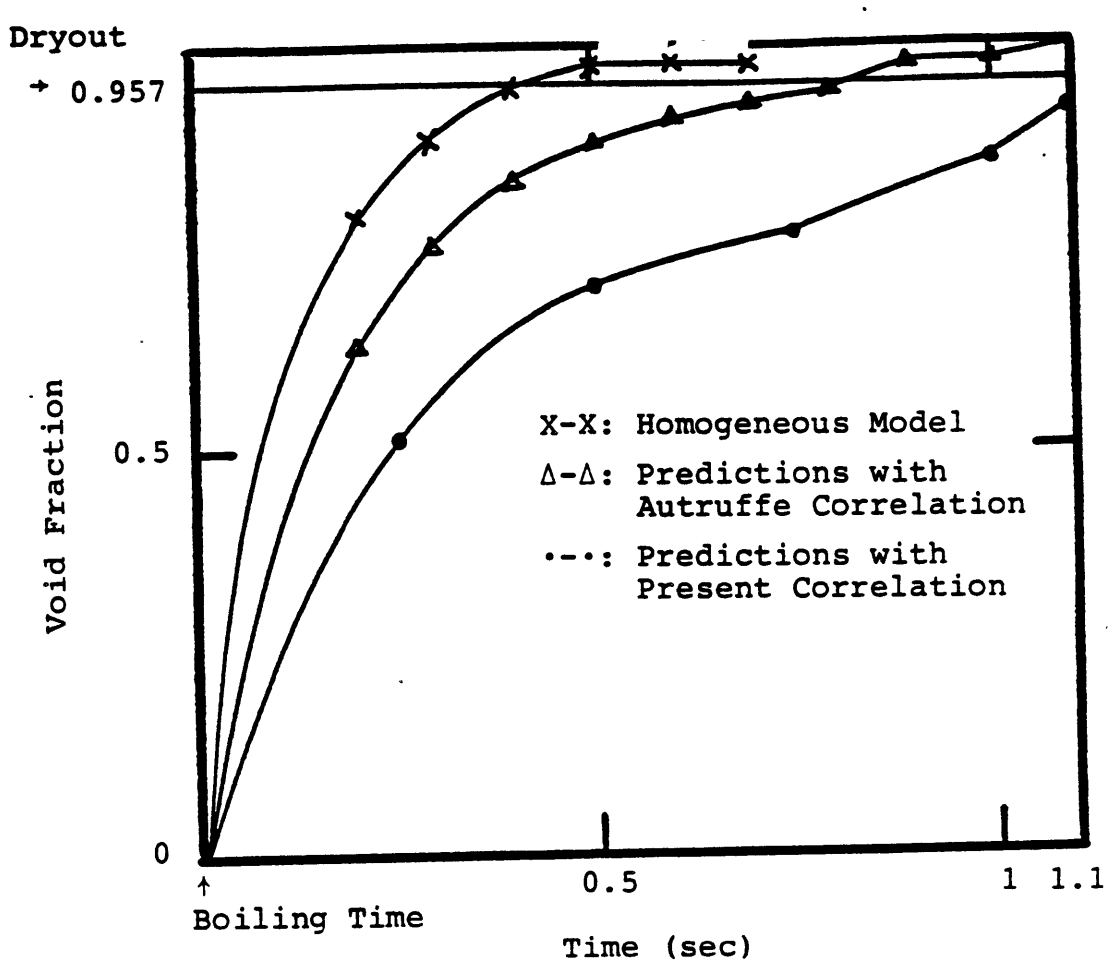

Fig. 6.27: Comparison of Void Fraction in the Last Cell of Heated Section Predicted with Various Interfacial Momentum Exchange Models

occurrence of dryout before flow reversal. Also this more trapped vapor causes larger pressure build-up in channels, and in turn more rapid flow coastdown and earlier flow reversal. This large void fraction drives vapor and liquid to have large velocities. (See 6.28) Also the large velocities dramatically reduce time step sizes and increase CPU time as illustrated in Fig 6.29. The computation with the homogeneous model stopped at around 0.7 seconds due to failure of convergence of the Newton iteration.

6.5.3 Boundary Positions

Let us investigate the importance of selecting boundary positions by comparing inlet flow rates of W-7b' predicted with two choices of boundary positions: the inlet and outlet of the test section (called A boundary) and the boundary positions shown in Fig 6.1 (called B boundary). In both cases the pressure drops between the inlet and outlet boundaries are set to give the same inlet mass flow rate as the experimental value at 1.5 seconds and kept constant up to 3.5 seconds. In the B boundary case the hydraulic resistances between the inlet boundary and inlet of the test section, and between the outlet of the test section and outlet boundary are estimated by the valve model described in Appendix D.

In the B boundary case flow coastdown decreases pressure drops between the inlet boundary and inlet of the test section and between the outlet of the test section and

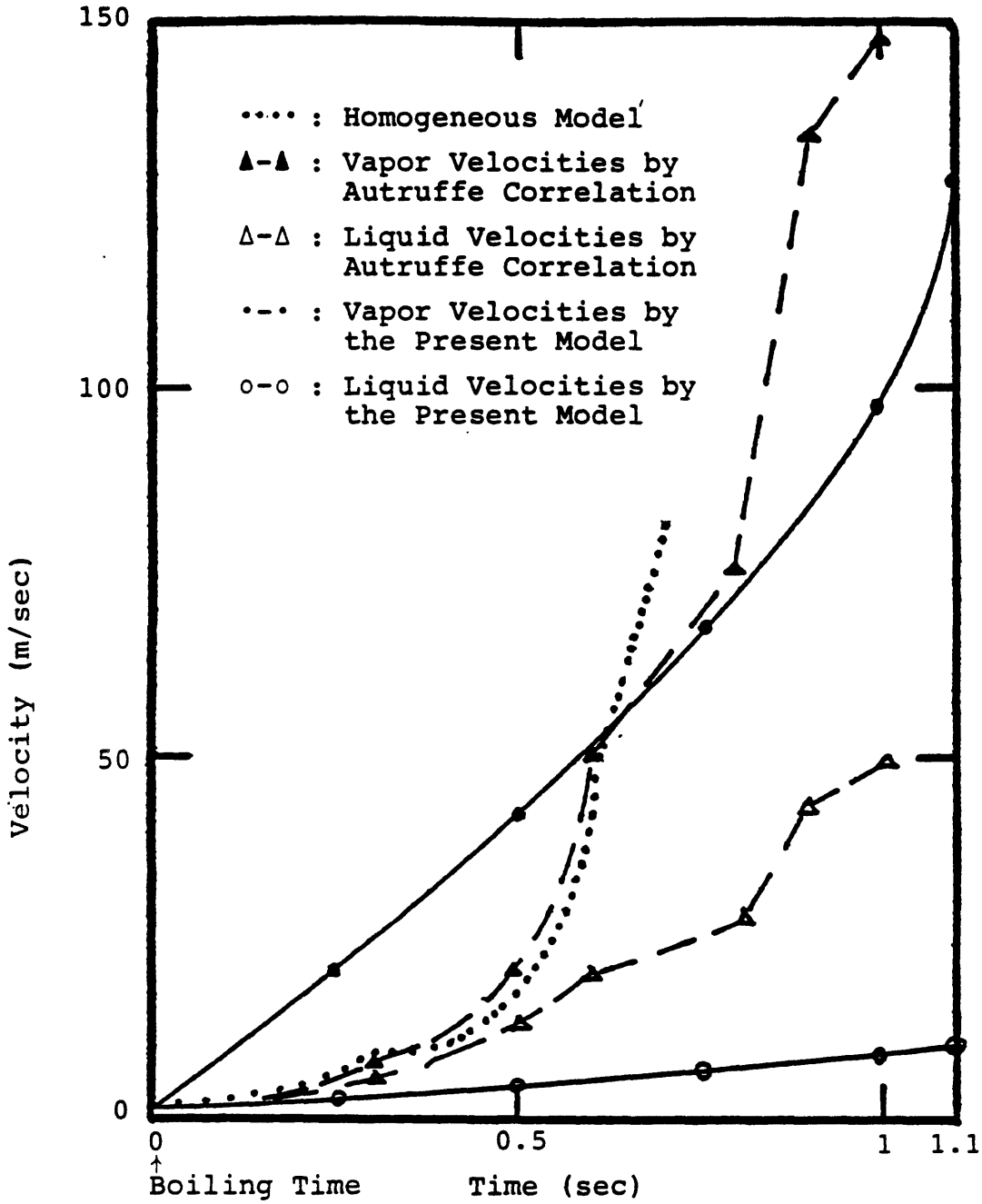

Fig. 6.28: Comparison of Vapor and Liquid Velocities Predicted at the Last Cell of the Heated Section with Various Interfacial Momentum Exchange Relations

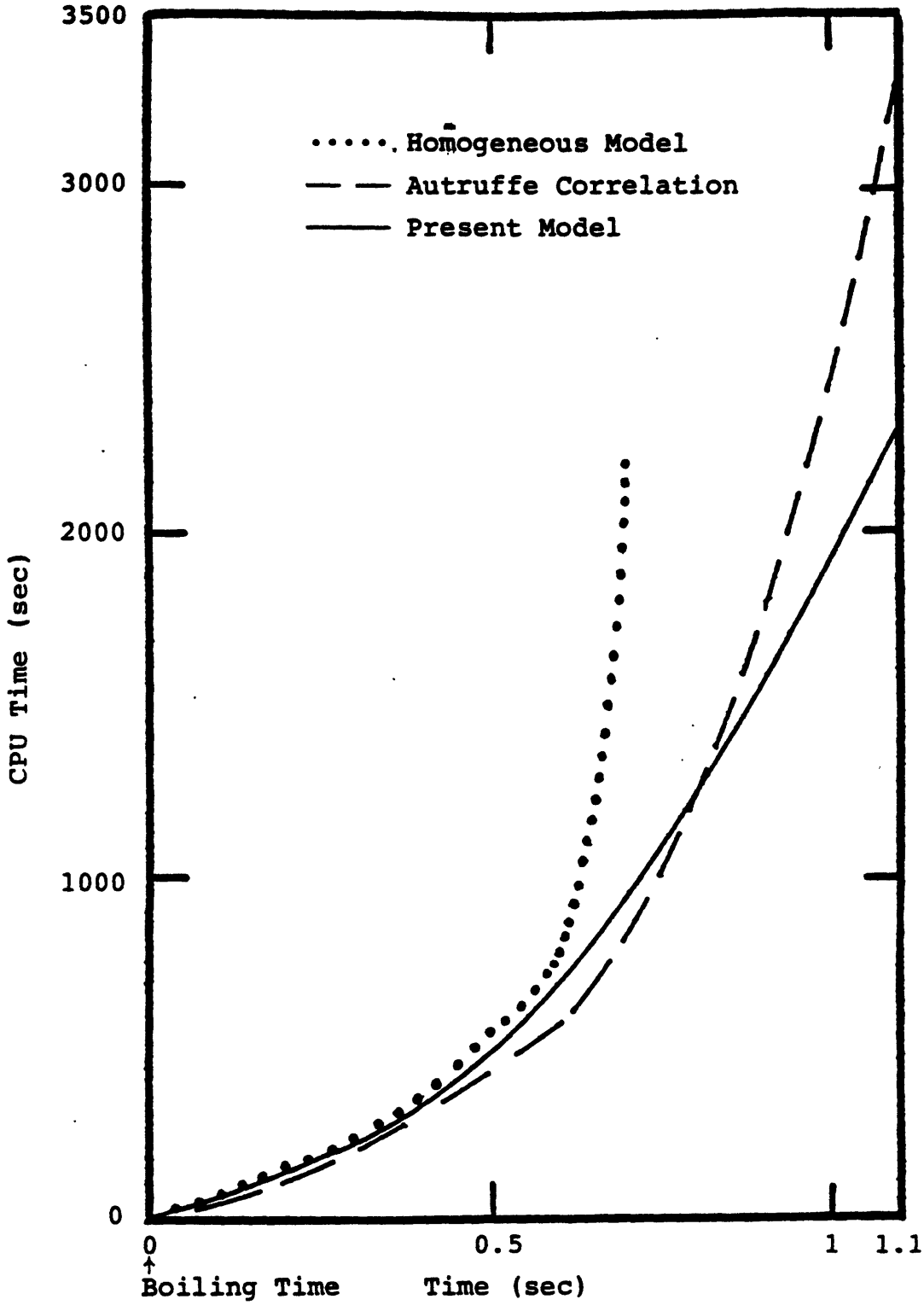

Fig. 6.29: Comparison of CPU Time for the W-7b' Test Using the MULTICS Computer

outlet boundary. As a result, flow reduction increases pressure at the inlet of the heated section but decreases pressure at the outlet of the heated section, while the inlet and outlet pressures in the A boundary case are kept constant. This increase in the pressure drop between the inlet and outlet of the test section substantially retards flow reversal as shown in Fig 6.30.

6.5.4 Normalization of Heat Source

In order to partition the total power Q(t) into each mesh in the fuel rods, the volumetric heat generation rate q''' in THERMIT is obtained by using the following equation

$$q'''(i,j,k) = Q(t)\,\frac{q_z(j)\;q_t(i)\;q_r(k)}{N_z\;N_t\;N_r} \tag{6.1}$$

where q_z , q_t , and q_r : axial and transverse power distribution in the reactor, and radial power distribution within a fuel rod

N_z, N_t and N_r: normalization factors

$$\begin{aligned} N_z &= \sum_j q_z(j)\;dz(j+1) \\ N_t &= \sum_i q_t(i)\;rn(i) \\ N_r &= \sum_k q_r(k)a(k) \end{aligned} \tag{6.2}$$

dz, rn, and a in Eq (6.2) are mesh spacing of j+1'th cell in the z direction, number of fuel rods in the i'th channel,

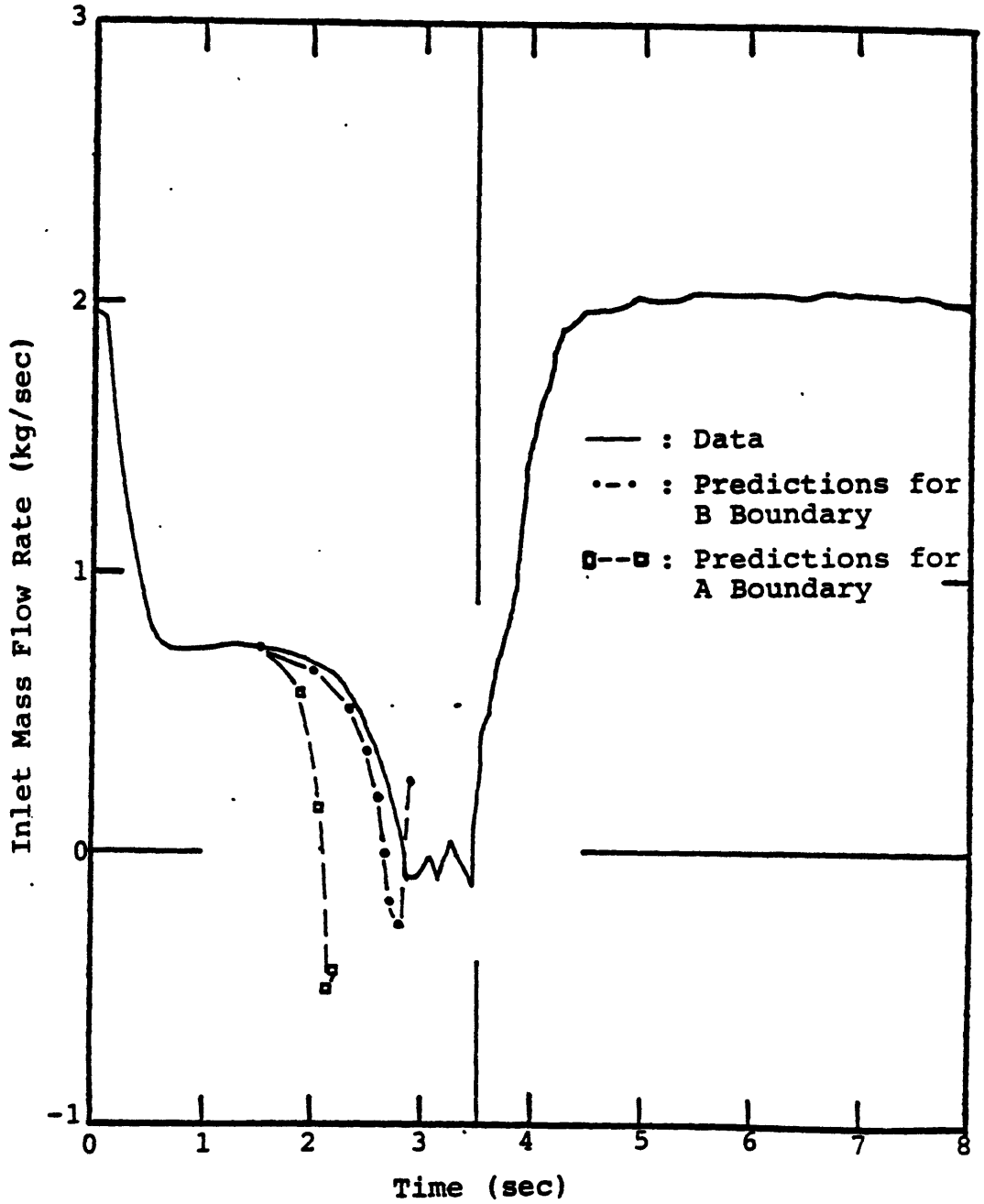

Fig. 6.30: Comparison between Inlet Flow Data and Predictions for A Boundary and B Boundary

and horizontal plane cross-sectional area of the k'th mesh cell in the fuel rod, respectively.

The assumption involved in Eq (6.1) is that all fuels at the same positions have the same geometry, that is, the same thickness of cladding, gap distance and radius of the center fuel void region. The actual geometry of fuels is different. Therefore, the general normalization of heat source described in Appendix E is needed.

Let us investigate the importance of this general normalization by comparing it (called as Case A) with Eq (6.1) (called as Case B). The W-7b' test, in which several gap distances were used, is selected for comparison between Case A and Case B. In the real geometry of the W-7b' test, gap distances and radii of center fuel void were 0.05588 mm and 0.8763 mm for the center fuel, and 0.07974 mm and 0.0 mm for seven fuels in the second ring, respectively. In Case B, 0.07974 mm for the uniform gap distance and 0.0 mm for the uniform radius of center fuel void are used for all channels. On the other hand, we can take different gap distances and radii of center fuel void for different channels in Case A; 0.05588 mm and 0.8763 mm in the innermost channel, and 0.07974 mm and 0.0 mm in the intermediate channel. Then the wall heat flux for both cases at the same positions are different due to the different volumes of fuel. Fig 6.31 verifies the above explanation; Case B has the larger amount of fuel and higher heat flux than Case A does.

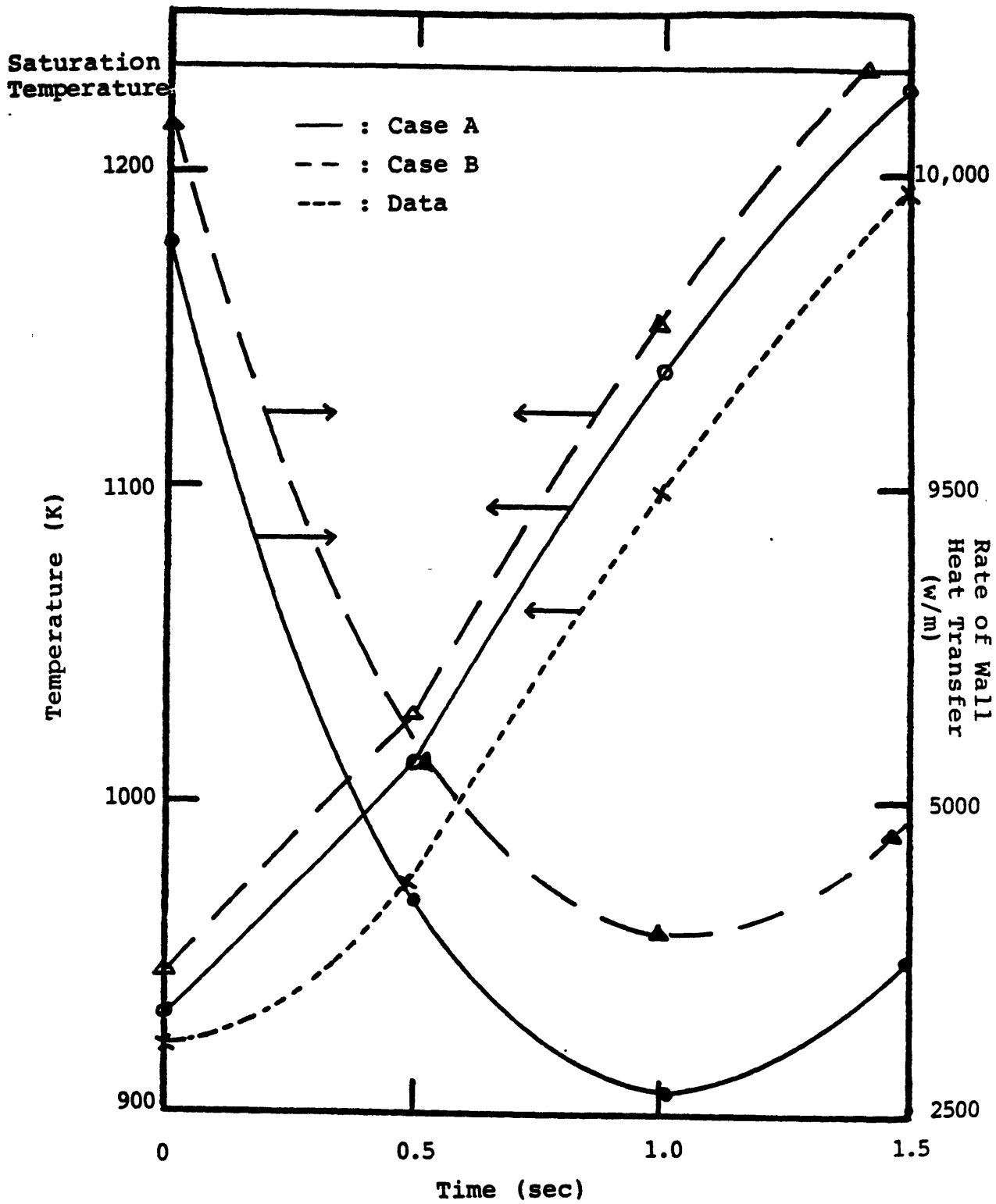

Fig. 6.31: Comparison of Temperature and the Rate of Wall Heat Transfer in the Last Cell of the Innermost Channel for Case A and Case B of Power Normalization

Also as expected, the centerline fuel temperature with the larger gap distance is higher by about 400 K than that with the smaller gap distance. (Fig 6.32) The wall heat flux of the last cell of the heated section in the innermost channel for Case B is higher than that for Case A. As a result, Case B predicts higher fluid temperature and earlier boiling inception.

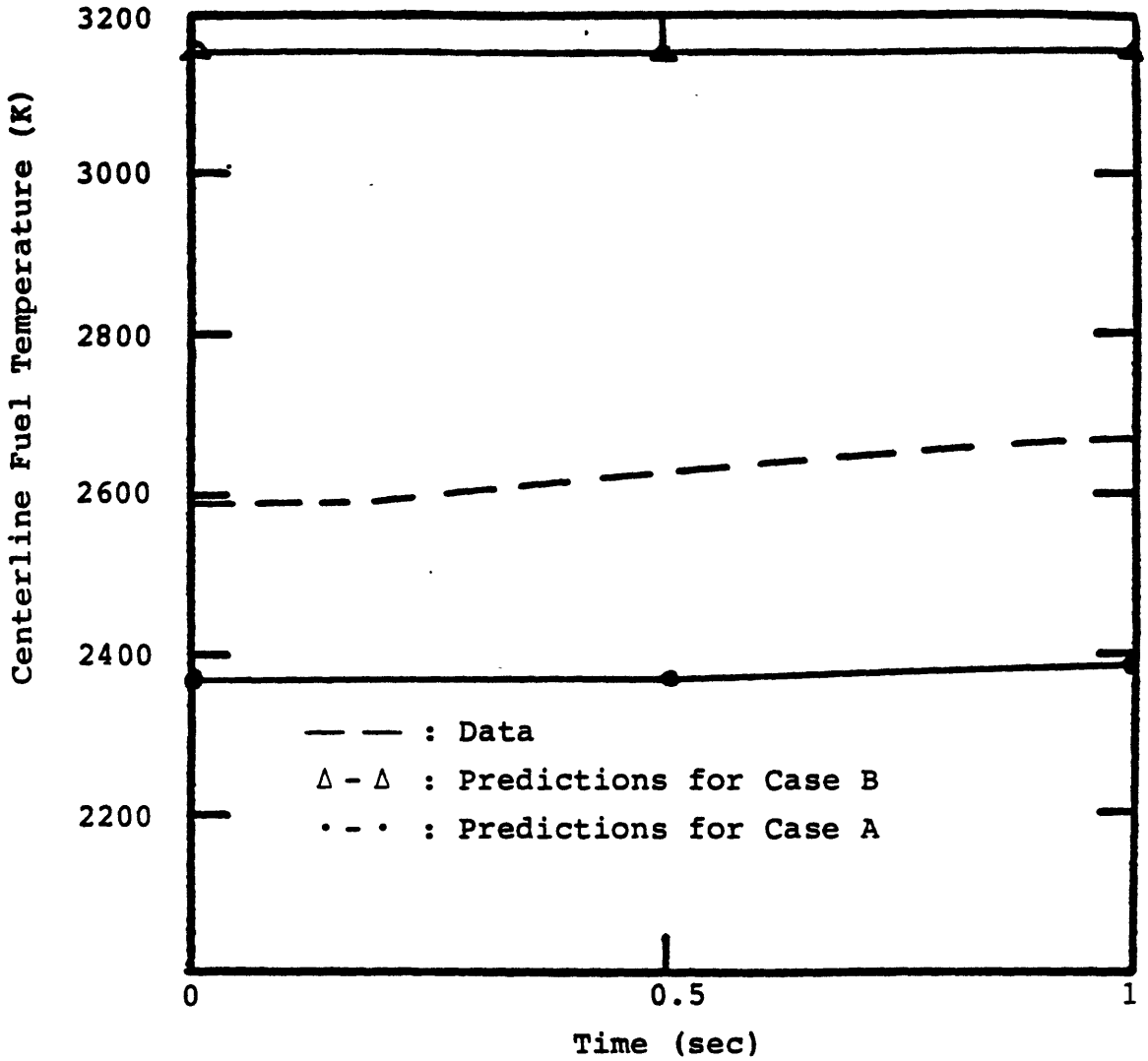

Fig. 6.32: Comparison between Centerline Fuel Temperature Data in the Last Cell of Innermost Channel and Predictions for Case A and Case B of Power Normalization

Chapter 7 SUMMARY AND RECOMMENDATIONS

7.1 Summary

Review of previous work reveals the limitations of models involved in several codes which were designed for the analysis of sodium boiling in the LMFBR. These limitations can be attributed to the characteristics of sodium itself such as the high density ratio of liquid to vapor, and of the LMFBR such as the existence of the highly subcooled region, flow reversal, and sharp radial temperature gradients.

The high density ratio induces high slip between liquid and vapor and, as a result, eliminates the possibility of use of the homogeneous model which assumes no slip. The existence of highly subcooled region in the bundle of the LMFBR, where vapor is condensed, causes numerical difficulties due to large pressure fluctuations. Use of the equilibrium approach, in which vapor must be completely condensed in the subcooled region, enlarges pressure fluctuations and in turn numerical difficulties. Therefore, the non-equilibrium approach instead of the equilibrium approach is needed to represent the physical conditions. As correlations for slip in annular or reversed flow are not readily available, the slip model is difficult to apply.

Sharp radial temperature gradients and multi-dimensional voiding behavior lead us to favor the multi-dimensional model. The 3-D representation is chosen

because a 3-D model can be used to simulate 1-D or 2-D geometries.

According to the above brief review, the two-fluid 3-D model is more suitable for the analysis of sodium boiling in the LMFBR. The THERMIT code (17) is taken as the basic tool for the development of the two-fluid 3-D code due to its following features:

1. It is based on a two-fluid 3-D geometry
2. It has an advanced numerical scheme
3. It allows flexible boundary conditions

Although cylindrical (r, θ, z) coordinates are better fitted for the geometry of the hexagonal bundle of the LMFBR, rectangular (x, y, z) coordinates are used for the present code due to the easy adoption of the original THERMIT code.

To investigate the main assumptions involved in the differential equations of THERMIT-6S, mathematically rigorous derivations of time-volume averaged conservation equations for the two-fluid model were done by starting from the integral general balance equation. It was found that THERMIT-6S includes all terms to dominantly contribute to the analysis of sodium boiling.

The THERMIT-6S differential equations were then discretized in the same way as THERMIT to obtain difference equations. Spatial discretization is characterized by a first-order spatial scheme, donor cell method, and staggered mesh layout. For time discretization, a first-order semi-implicit scheme treats implicitly sonic terms and terms

related to local phenomena, and treats explicitly convective terms. Therefore, the time step size in THERMIT-6S is limited by the convective limit:

$$\Delta t \leq \frac{\Delta z}{|v_z|_{max}}$$

The most important characteristic of the present difference equations lies in the treatment of coupling terms. Coupling between mesh cells at the new time level is through the pressure variable. Hence, we need only to solve the reduced pressure equations which form a NxN matrix (N is the total number of fluid cells) in 3-D, compared to a 10N x10N matrix of equations obtained by the ordinary implicit .method. A crucial property of the reduced pressure problem is its diagonal dominance.

It is known that the typical two-fluid model such as THERMIT possesses complex characteristics, exhibits unbounded instabilities in the short-wavelength limit and constitutes an ill-posed problem. To overcome these difficulties, a virtual mass term was studied here because the virtual mass represents real physical effects to accomplish dissipation for numerical stability. It was found that the virtual mass has a profound effect on the mathermatical characteristic and numerical stabiliy as well as a real physical effect. Quantitative bounds on the coefficients of the virtual mass terms in a model proposed by Drew et al. (33) were suggested for mathermatical

hyperbolicity, numerical stability, and satisfaction of the thermodynamics second law.

For the closure of the conservation equations, the functions, which represent the transfer of mass, energy, or momentum at solid-fluid and vapor-liquid interfaces, must be explicitly expressed in terms of primary variables and properties. While the two-fluid model provides wider applicability and flexibility in the analysis of two-phase flow than other models do, its accuracy strongly depends on these constitutive equations.

The constitutive relations for pre-dryout were derived, based on two assumptions:

1. The exchange mechanism is dominantly controlled by local phenomena.
2. The cocurrent annular flow regime in two-phase flow of sodium is dominant on the scale of the subchannel.

These two assumptions lead to a simplified flow regime which facilitates not only developing physical models but also obtaining convergence of the Newton iteration. Significant obstacles to obtaining constitutive equations lie in discrepancies between data of different authors as well as limited experimental data available for two-phase flow of sodium. Here, the main reasons of these discrepancies were clarified and physical models were derived within the present capabilities, based on the above two assumptions.

By reviewing several publications on frictional pressure drop in the two-phase flow of liquid metals, it was found

that discrepancies between data of different authors become evident. The review indicates that the data can be divided into two groups, which are characterized by the flow pattern: pure annular or annular-dispersed flow. It is argured that the difference between the two groups is caused by the acceleration pressure drop of droplets, which was commonly neglected in the evaluation of the frictional pressure drop in annular-dispersed flow. While most of data for adiabatic annular flow fall between the Lockhart-Martinelli correlations for viscous-viscous and turbulent-turbulent flow, data for diabatic annular flow fall much below the Lockhart-Martinelli correlation for turbulent-turbulent flow.

Discrepancies between data of different authors have been reported due to boiling instability. Recently Zeigarnick and Litvinov provided data for wall heat transfer which were obtained with complete boiling stability. Their data were used to validate wall heat transfer coefficients for both boiling and condensation in the forced convective flow of sodium. The wall heat transfer coefficient in two-phase flow was derived by using momentum-heat transfer analogy and logarithmic law for velocity distribution in the liquid film. Only one constant in the logarithmic form needs to be empirically determined. The results from the suggested correlation were found to be in good agreement with their data over a broad range of parameters. The proposed correlation predicts higher heat transfer

coefficients than previous correlations do.

Two control mechanisms, "vapor supply" and "latent heat transport", were proposed for the models of mass and energy exchange. The rate of exchange was assumed to be controlled by whichever mechanism yields smaller values. The former mechanism is described by a simple kinectic theory approach. The turbulent flux model is taken as the basis for a model of the latter mechanism. A modified mixing theory is introduced to account for the energy losses of eddies. When the bulk liquid temperature calculated according to the proposed model was compared with analytically predicted values, they were found to be in close agreement. In a comparison of the void volume in a 19 pin bundle as a function of time, calculational results fall around experimental results until release of fission gas into the sodium vapor from the pins occurred in the test.

A one-dimensional steady-state model was developed for vertical upward annular-dispersed flow to account for momentum tranfer by droplets. It was shown that results obtained from the suggested model fall near the Wallis correlation and the Moeck correlation which were derived from air-water data.

Pre-dryout predictions by the present code were generally in good agreement with data. Discrepancies between data and predictions emerge after dryout. The higher frequency and larger amplitude of flow oscillation than data were predicted. Actually, the present physical models for

post-dryout are highly questionable because they have been derived by a simple extension of liquid film models for pre-dryout. Therefore, development of physical models for post-dryout is recommended.

A code assessment was performed to determine how well the code can simulate the physical process measured in experiments and to assess the code's capability. The capability of the present code is restricted by the followings:

1. The validation range of constitutive equations implemented in the code -- Most of the constitutive equations for two-phase flow are derived, based on the forced convective annular flow. Though it is questionable whether these constitutive equations can be applied to natural convection flow, it is expected that the differences in the local processes between two-phase flow under natural convection and forced convection may be much smaller than those in single phase flow.
2. No fuel melting model -- The code can be applied to predictions of phenomena before fuel melting.
3. A component code -- However, a loop simulation is possible, if the code is slightly modified.

The W-7b' (in-pile 19 pin bundle), P3A (in-pile 37 pin bundle), and OPERA-15 Pin (out-of-pile simulator of 61 bundle) were chosen for the numerical simulation of low flow/high power accidents. These three numerical simulations present a series of following physical

phenomena:

1. After incipient boiling rapid vapor production in the saturated region occurs due to high power and the high density ratio, and vapor is transferred radially and axially from the saturated region to the subcooled region. Strong cross flow caused by rise in pressure in inner cells reduces pressure build-up. As a result, mild flow coastdown in the initial stage of boiling occurs.

2. When fluid in the outermost channel reaches saturation temperature, vapor expulsion and rapid pressure build-up take place. Flow coastdown is accelerated by these sharp increases in vapor generation and pressure.

3. Rapid flow coastdown leads to flow reversal. From this time on voiding of the rest of the bundle proceeds rapidly, with the whole bundle indicating a single channel response.

4. In a short time after flow reversal, dryout occurs. It turns out that the incidence of flow reversal is the most important single factor in the occurrence of dryout in the low flow/high power accidents. Dryout dramatically reduces wall heat transfer coefficients and sharp rise in the cladding temperature takes place. Then, vapor is rapidly accelerated due to high void fraction, and this high vapor velocity reduces time step sizes and in turn increases CPU time.

5. Liquid reentry occurs in a short time after flow

reversal, followed by inlet flow oscillation. The higher frequency and larger amplitude of the flow oscillation than data are predicted.

For the numerical simulation of low flow/low power accidents, the test 72B, run 101 of THORS was chosen. The distinctive characteristics of this type accidents are as follows:

1. While dryout in the low flow/high power accidents was predicted to occur immediately after flow reversal, dryout in THORS was significantly delayed.
2. The periodical dryout and rewet over the whole bundle occurred for a long time until a sustained dryout began.

Comparison between 1-D and 2-D analysis performed by the present code reveals the following facts:

1. Incipient boiling in 1-D analysis can be substantially delayed when experiments with steep radial temperature gradients are simulated.
2. 1-D analysis predicts more rapid flow coastdown than 2-D analysis does. While in 1-D analysis there is no room to condense vapor transferred in the r direction, strong cross flow caused by rise in pressure in inner cells in 2-D analysis reduces pressure build-up.

Sensitivity analysis confirms the review of the limitations of the models described at the beginning of this chapter. Severe numerical difficulties in the equilibrium model were encounted; calculation stopped within 0.1 seconds after incipient boiling due to failure of convergence of the

Newton iteration. The homogeneous model predicts higher void fraction and larger pressure build-up, and as a result, earlier dryout and flow reversal than the present model does.

7.2 Recommendations

Based on the present experience, the following recommendations for future work are made:

1. The development of a loop simulation capability is recommended to account for the effect of a loop system and to obtain accurate boundary conditions. As shown in Section 6.5.3, boundary conditions have great effects on flow transients. As the code is originally designed to be applicable to a component system, boundary values have to be provided by data or estimation. Since few experiments measured the inlet and outlet pressures of the test section, rough estimation by iteration was usually needed, which leaves uncertainties in the boundary values. To eliminate these uncertainties, a simple loop model is needed to account for the loop hydraulic resistance, including a simple pump model for pump trip.
2. Development of an advanced numerical scheme is recommended to reduce CPU time. After dryout vapor is rapidly accelerated due to high void fraction. As time step sizes are limited by the convective stability condition, this high vapor velocity (more than 100 m/sec)

dramatically reduces time step sizes (often less than 10^{-3} seconds) and in turn increases CPU time. Moreover, if we consider a multidimensional effect on the control of time step sizes for numerical stability, time step sizes will be reduced up to 10^{-4} seconds, which is totally unacceptable. Therefore, unless an advanced numerical scheme is developed, the capability of the present code is limited to a few second predictions after dryout. Studies of the two-step method or fully implicit method are suggested.

3. The present physical models for post-dryout are highly questionable. They are based on the liquid film models which were developed for pre-dryout. However, when the wall is hot enough, there is little liquid left on the wall. Then, droplets would play an important role in transferring mass, momentum, and energy. Moreover, the region and duration of post-dryout are large enough to affect flow behavior. Therefore, development of physical models for post-dryout is recommended. Because there are little data for post-dryout, it is inevitable that physical model for the LWR would be used, based on analogy of dryout mechanisms between water and sodium.

4. The liquid conduction model is important in prediting accurate radial temperature gradients, incipient boiling time, and flow reversal time. A constant Nusselt number, which was obtained from a high flow test, was used for liquid radial conduction. In the numerical simulation of

THORS, which are low flow experiments, milder radial temperature gradients than the data were predicted due to use of the high Nusselt number. Therefore, a study of an improved liquid conduction model is recommended to account for effects of various flow variables on liquid conduction.

References

1. W.D. Hinkle, "LMFBR Safety and Sodium Boiling, A State of the Art Report," draft, M.I.T. (Dec. 1977)

2. R.C. Noyes, J.G. Morgan, and H.H. Cappel, "Transfugue-1, A Digital Code for Transient Two-Phase Flow and Heat Transfer," NAA-SR-11008 (July 1965)

3. J.E. Meyer, "Hydrodynamic Models for the Treatment of Reator Thermal Transients," Nuclear Sci. and Eng., 10 (1961)

4. J.A. Landomi, "Transfugue-IIa, A Digital Code for Transient Two-Phase Flow in Single Heated Channels," NAA-SR-12503 (March 1968)

5. D.R. MacFarlane, Ed. "SAS1A, A Computer Code for the Analysis of Fast Reator Power and Flow Transients," Argonne Nat. Lab., ANL-7607 (1970)

6. F.E. Dunn, et.al., "The SAS2A LMFBR Accident Analysis Computer Code," Argonne Nat. Lab., ANL-8138 (1975)

7. M.G. Stevenson, et.al., "Current Status and Experimental Basis of the SAS LMFBR Assident Analysis Code System," Proc. ANS Conf. Fast Reator Safety, Beverly Hills, California, USAEC-CONF 740401, p.1303 (1974)

8. J.E. Cahalan, et.al., "SAS3D LMFBR Accident Analysis Computer Code," ANL

9. J.E. Cahalan, et.al., "The Status and Experimental Basis of the SAS4A Accident Analysis Code System," Proc. Int. Mtg. on Fast Reator Safety Technology, Seattle, Vol.II, p.603-614 (1979)

10. P. Wirtz, "Ein Beitrag zur theoretischen Beschreibung des Siedens unter Storfallbedingungen in natriumgekuhlten Schnellen Reaktoren," KFK 1858 (Oct. 1973)

11. E.R. Siegmann, "Theoretical Study of Transient Sodium Boiling in Reator Coolant Utilizing a Compressible Flow Model," Argonne Nat. Lab. ANL-7842, (1971)

12. W.W. Marr, "COBRA-3M: A Digital Computer Code for Analyzing Thermal Hydraulic Behavior in Pin Bundles," Argonne Nat. Lab. ANL-8131 (Mar. 1975)

13. C.W. Stewart, et.al., "COBRA-IV : The Model and the Method," BNWL-2214, NRC-4 (July 1977)

14. G. Basque, D. Grand, and B. Menant, "Theoretical Analysis and Experimental Evidence of Three Types of Thermohydraulic Incoherency in Undisturbed Cluster Geometry," IAEA Specialists Meeting on Thermodynamics of Fast Breeder Reator Fuel Sub-Assemblies under Nominal and non-Nominal Operating Conditions, Karlsruhe (Feb. 1979)

15. A. L. Schor, "A Four-Equation Two-Phase Flow Model for Sodium Boiling Simulation of LMFBR Fuel Assemblies," Ph. D. Thesis in Department of Nuclear Engineering, M.I.T. (1982)

16. M.R. Granziera and M.S. Kazimi, "A Two-Dimensional, Two-Fluid Model for Sodium Boiling in LMFBR Fuel Assemblies," MIT-EL-80-011 (May 1980)

17. W.H. Reed and H.B. Stewart, "THERMIT--A Computer Program for Three-Dimensinal Thermal Hydraulic Analysis of Light Water Reator Codes," M.I.T.

18. M. Ishii, Thermo-fluid Dynamic Theory of Two-Phase Flow, Eyrolles, France (1975)

19. S. Banerjee and A.M.C. Chan, "Seperated Flow Models-1," Int. J. Multiphase Flow, Vol.6 (1980)

20. M. Ishii, "Foundation of Various Two-phase Models and Their Limitations," Electric Power Reseach Institute, EPRI-WS-81-212 (May 1981)

21. R. Aris, Vectors, Tensors and the Basic Equations of Fluid Mechanics, Prentice-Hall (1962)

22. F.B. Hildebrand, Advanced Calculus for Applications, Prentice-Hall (1963)

23. J.T. Delhaye and J.L. Achard, Invited paper presented at OECD/NEA Specialists Meeting on Transient Two-Phase Flow, Toronto (Aug. 1976)

24. S. Javis, Jr., "On the Formulation and Numerical Evaluation of a Set of Two-Phase Flow Equations Modelling the Cooldown Process," Technical Note 301, National Bureau

of Standards, Boulder, Colorado (1965)

25. R.D. Richtmyer and K.W. Morton, Difference Methods for Initial-Value Problem, Interscience Publishers, Inc., New York (1967)

26. J.A. Boure, "GEVATRAN: A Computer Program to Study Two-Phase Flow Dynamics," CONF-720686-3 (June 1972)

27. D. Gidaspow, Proc. 5th Int'l. Heat Trensfer Conference, Tokyo, Japan, CONF-740925, V.II (1974)

28.W.R. Bryce, "Determination of the Hyperbolic Regime of the Hydrodynamic Equations Modeled in the LOCA Code RELAP-UK," OECD/NEA Specialists Meeting on Transient Two-Phase Flow, Toronto (Aug. 1976)

29. R.W. Lyczkowski, D. Gidaspow, C.W. Solbrig, and E.D. Hughes, "Characteristics and Stability Analyses of Transient One-Dimensional Two-Phase Flow Equations and Their Finite Difference Approximations," NSE 66, p378-396 (1978)

30. P.S. Anderson, P. Astrup, L. Eget, and O. Rathmann, "Numerical Experience with the Two-Fluid Model RISQUE," Proc. Topical Meeting, Thermal Reator Safety, Sun Vally, Vol. 2 (1978)

31. W.C. Rivard and J.R. Travis, "A Nonequilibrium Vapor Production Model for Critical Flow," NSE 74, p40-78 (1980)

32. R.T. Lahey, Jr., L.Y. cheng, D.A. Drew, and J.E. Flaherty, "The Effect of Virtual Mass on the Numerical Stability of Accelerating Two-phase Flows," Int. J. Multiphase Flow, Vol. 6 (1980)

33. D.A. Drew, L.Y. Cheng, and R.T. Lahey, Jr., "The Analysis of Virtual Mass Effects in Two-Phase Flow," Int. J. Multiphase Flow, Vol.5 (1979)

34. H. Lamb, Hydrodynamics, Dover, New York (1945)

35. J. Hadamard, Lectures on Cauchy's Problem in Linear Partial Differential Equations, Yale University Press, New Haven (1923)

36. P.D. Lax, "Differencial Equations, Difference Equations and Matrix Theory," Comm. on Pure and Applied Math., Vol.XI, p.174-194 (1958)

37. J.D. Ramshaw and J.A. Trapp, "Characteristics, Stability, and Short-Wavelength Phenomena in Two-Phase Flow Systems," Nuclear Sci. and Eng., 66, p 93 (1978)

38. D.A. Drew and R.T. Lahey, Jr., "Application of General Constitutive Principles to the Derivation of Multidimensional Two-Phase Flow Equations," Int. J. Multiphase Flow, Vol.5 (1979)

39. D.A. Drew and R.T. Lahey, Jr., "Interfacial Dissipation in Two-Phase Flow," Symposium on Basic Mechanisms in Two-Phase Flow and Heat Transfer presented at the Winter

Annual Meeting of ASME, Chicago, Illinois (Nov. 1980)

40. R.J. Ribando, "Sodium Boiling in a Full-Length 19 -Pin Simulated Fuel Assembly (THORS BUNDLE 6A)," Oak Ridge Nat. Lab., ORNL/TM-6553 (Jan. 1979)

41. W.T. Hancox, R.L.Ferch, W.S. Lin, and R.E. Nieman, "One-Dimensional Models for Transient Gas-Liquid Flows in Ducts," Int. J. Multiphase Flow, Vol.6, p.25-40 (1980)

42. H.B. Stewart, "Stability of Two-Phase Flow Calculation Using Two-Fluid Models," J. of Computational Physics 33, p.259-270 (1979)

43. K.H. Ardron, "One-Dimensional Two-Fluid Equations for Horizontal Stratified Two-Phase Flow," Int. J. Multiphase Flow, Vol.6, p.295-304 (1980)

44. R.E. Henry, "Two-Phase Compressible Flow," Int. J. Multiphase Flow, Vol.2, p.9-67 (1979)

45. G. Wilson and M.S. Kazimi, "Development of Models for the Sodium Version of the Two-Phase, Three Dimensional Thermal Hydraulic Code THERMIT," MIT-EL-80-010 (1980)

46. R.A. Markely and F.C. Engel, "LMFBR Blanket Assembly Heat Transfer and Hydraulic Test Data Evaluation," Westinghouse Electric Corp. Advanced Reactors Division, US/DOE Contract No. EY-76-C-02-3045-004 (1976)

47. E.H. Novendstern,"Turbulent Flow Pressure Drop Model for Fuel Rod Assemblies Utilizing a Helical Wire-Wrap Spacer System," Nuclear Eng. and Design, 22, (1972).

48. A.Y. Gunter and W. A. Shaw, "A General Correlation of Friction Factors for Various Types of Surfaces in Crossflow," ASME Transactions, 67, (1945).

49. M.S. Kazimi and M.D. Carelli, "Heat Transfer Correlations for Analysis of CRBRP Assemblies," CRBRP-ARD-0034, U.S. Energy Research and Development Administration, (1976).

50. R.W. Lockhart and R.C. Martinelli, "Proposed Correlation of Data For Isothermal Two-Component Flow in Pipes," Chem. Eng. Prog. Symp. Series, No.1, Vol. 45, (1949).

51. H. Lurie, "Sodium Boiling Heat Transfer and Hydrodynamics," Proc. Conference on Application of High Temperature Instrumentation to Liquid Metal Experiments, ANL-7100, P. 549-571, (Sept. 1965).

52. H.K. Fauske and M.A. Grolmes, "Pressure Drop for Forced Convection Flashing Sodium," Liquid-Metal Heat Transfer and Fluid Dynamics, ASME (Nov. 1970)

53. I.T. Alad'yev et al., "Hydrodynamics of a Two-Phase Flow of Potassium in Tubes," ASME, Heat Transfer, Soviet Research, Vol. 1, No. 4,(JUly 1969).

54. L.R. Smith, M. Rasin Tek, and R.E. Balzhiser, "Pressure Drops and Void Fractions in Horizontal Two-Phase Flows of Potassium," AIChE Journal, Vol. 12, No. 1, p. 50, (Jan. 1966).

55. C.J. Baroczy, "Pressure Drop for Two-Phase Potassium Flowing through a Circular Tube and an Orifice," Chem. Eng. Prog. Symp. Series, No. 82, Vol. 64, (1968).

56. C.J. Baroczy, "A Systematic Correlation for Two-Phase Pressure Drop," Chem. Eng. Prog. Symp. Series, No.64, Vol.62 (1966).

57. Y.A. Zeigarnick and V.D. Litvinov, "Heat Transfer and Pressure Drop in Sodium Boiling in Tubes," Nucl. Sci. Eng., 73 (1980)

58. J.C. Chen and S. Kalish, "An Experimental Investigation of Two-Phase Pressure Drop for Potassium with and without Net Vaporization," Fourth International Heat Transfer Conference, Paris-Versailles, (Aug.-Sept. 1970).

59. A. Kaiser, F.W. Peppler and L. Voross, "Type of Flow, Pressure Drop, and Critical Heat Flux of a Two-Phase Sodium Flow," Nucl. Eng. and Design 30, p. 305-315 (1974).

60. A. Kaiser and F.W. Peppler, "Sodium Boiling Experiments in a Seven-Pin Bundle; Flow Patterns and Two-Phase Pressure Drop," Nuc. Eng. and Design 43, p. 285-293 (1977).

61. J.M. Turner and G.B. Wallis, "An Analysis of the Liquid Film in Annular Flow," NYO-3114-13, U.S. Atomic Energy Commision (1965)

62. G.B. Wallis, One-Dimensional Two-Phase Flow,McGraw Hill (1969)

63. A. Kaiser, F.W. Peppler and L. Voross, "Untersuchungen der Stromungsform, des Druckabfalls und des Kritischen Warmeflusses einer Zweiphasenstromung mit Natrium," KFK 2085, (Apr. 1975).

64. K. Ishihara, J.W. Palem, and J. Taborek, "Critical Review of Correlations for Predicting Two-Phase Flow Pressure Drop across Tube Banks," ASME paper, 77-WA/HT-23 (1977)

65. O. Reynolds, Proc. Manchester Lit. Phil. Soc., 8 (1874), reprinted in Scientific Papers of Osborne Reynolds, Vol. , Cambridge, London (1901)

66. L.Z. Prandtl, Physik, , 1072 (1910)

67. G.I. Taylor, "Conditions at the Surface of a Hot Body Exposed to the Wind," reports and memoranda, No.272 (May 1916), in Technical Reports of the Advisory Committee for Aeronautics for the Year 1916-17, Vol.2, p.423, London (1920)

68. TH. von Karmann, Trans. ASME, 61, p. 705 (1939)

69. R.C. Martinelli, Trans.Am.Soc.Mech.Eng., 69 947 (1947)

70. A.E. Dukler, Chem.Eng.Prog.Symp.Series, 56, 301 (1960)

71. D.P. Traviss, W.M. Rohsenow, and A.B. Baron, "Forced convection Condensation Inside Tubes: A Heat Transfer Equation for Design," ASHARE No.2272, RP-63 (1972)

72. R.M. Bjorge, "Recent Developments in Boiling Heat Transfer," MS Thesis in Mechanical Engineering, M.I.T. (1979)

73. J.C. Chen, "A Correlation for Boiling Heat Transfer to Saturated Fluids in Convective Flow," ASME paper 63-HT-34 (1963)

74. J.C. Chen, "A Proposed Mechanism and Method of Correlation for Convective Boiling Heat Transfer with Liquid Metals," BNL-7419 (1963)

75. W.M. Rohsenow and L.S. Cohen, M.I.T. Heat Transfer Laboratory Report (June 1960)

76. J. Longo, Ed., "Akali Metals Boiling and Condensing Investigations," Quarterly Progress Reports 2 and 3, Space power and Propulsion Section, General Electric Company (1963)

77. I.T. Aladjev, I.G. Gorlov, and L.D. Dodonov, "Potassium Boiling Heat Trasfer in Tubes with Uniform Heat Flux," Investigations of heat Transfer, Hydrodynamics and Material

Thermophysical Properties, Nauka, Moscow (1968)

78. H.W. Hoffman and A.I. Krakoviak, "Forced Convection Saturation Boiling of Potassium at Near-Atmosperic Pressure," Proc. 1962 Mtg. High Temperature Liquid Metal Heat Transfer Technology, Upton, New york, BNL-756 (1962)

79. R.B. Bird, W.E. Stewart, and E.N. Lightfort, Transport Phenomena, John Wiley & Sons, Inc. (1960)

80. R. Higbie, Trans. A.I.Ch.E., 31, p. 365-389 (1935).

81. T.H. Chilton and A.P. Colburn, "Mass Transfer (Absorption) Coefficients," Int. Eng. Chem., 26, p. 1183 (1934).

82. D.B. Spalding, Convective Mass Transfer, Edward Arnold, London (1963).

83. R.G. Deissler, "Analysis of Fully Developed Turbulent Heat Transfer at Low Peclet Numbers in Smooth Tubes with Application to Liquid Metals," NACA RM E52F05 (1952).

84. W. Kowalchuk. and A.A. Sonin, "A Model for Condensation Oscillations in a Vertical Pipe Discharging Steam into a Subcooled Water Pool," NUREG/CR-0221, (1978).

85. R.W. Schrage, "A Theoretical Study of Interphase Mass Transfer," Columbia University Press, N.Y. (1953).

86. R.S. Silver and H.C. Simpson, "The Condensation of Superheated Steam," Proc. of Nat.Engrg. Lab. Conf., Glasgow,

Scotland (1961).

87. S.J. Wilcox and W.M. Rohsenow, "Film Condensation of Liquid Metals-Precision of Measurement," M.I.T. Report D.S.R. 71475-62 (1969).

88. Edited by D.H. Thompson, "SLSF In-Reactor Experiment P3A," Argonne Nat.Lab. ANL/RAS 77-48, (Nov. 1977).

89. M.A. Autruffe, "Theoretical Study of Thermohydraulic Phenomena for LMFBR Accident Analysis," M.S. Department of Mechanical Eng., M.I.T., Sept. (1978).

90. G.C. Carofano and H.N. McManus, Jr., "An Analytical and Experimental Study of the Flow of Air-Water and Steam-Water Mixtures in a Converging-Diverging Nozzle," Prog. Heat and Mass Transfer, Vol.2, p.395-417, (1969).

91. R.V. Smith, "Two-Phase Two-Component, Critical Flow in a Venturi," Ph.D. Thesis, University of Oxford, (1968).

92. E. Rabin, A.R. Schellenmuller and R.B. Lowhead, "Displacement and Shattering of Propellant Droplets." AFSOR TR 60-75, Rocketdyne, Division of North Americal Aviation, Inc., (March 1960).

93. W.R. Martindale and R.V. Smith, "Two-Phase Two-Component Interface Drag Coefficients in Seperated Phase Flows," Int. J. Multiphase Flow, Vol.7, p.211-219, (1981).

94. E.O. Moeck, "Annular-Dispersed Two-Phase Flow and Critical Heat Flux," AECL-3656 (1970).

95. L.E. Gill, G. F. Hewitt and P.M.C. Lacey, "Sampling Probe Studies of the Gas Core in Annular Two-Phase Flow," AERE-R 3955, UKAEA, Harwell, England, (June 1963).

96. L.B. Cousins, W.H. Denton and G.F. Hewitt, "Liquid Mass Transfer in Annular Two-Phase Flow," AERE-R 4926, UKAEA,Harwell, England, (May 1965).

97. W.D. Hinkle, "A Study of Liquid Mass Transport in Annular Air Water Flow," Sc.D. Thesis, Department of Nuclear Eng., M.I.T., (June 1967).

98. K.Y. Huh, "Simulation of Sodium Boiling Experiments with THERMIT Sodium Version," M.S. Thesis, Department of Nuclear Eng., M.I.T. (1982)

99. R.G. Zielinski, "Development of Models for the Two-Dimensional, Two-Fluid Code for Sodium Boiling NATOF-2D," M.S. Thesis, Department of Nuclear Eng., M.I.T. (1981)

100. Edited by A.N. Baker, "SLSF W-1 Experiment Test Predictions," General Electric, GEFR-00047-9(L) (1977)

101. T.J. Scale, "Pretest Information Package for OPERA 15-Pin Experiment," Argonne Nat. Lab., ANL/RAS 81-32, (1981)

102. T.J. Scale, et al., "OPERA 15-Pin Sodium Expulsion Test," ANS Trans., Vol. 43, p 495 (Nov. 1982)

103. O.E. Dwyer, "On the Transfer of Heat to Fluids Flowing through Pipes, Annulii, and Parallel Plates," Nuclear Sci. and Eng., 17, p 336 (1963)

104. J.E. Meyer, " Some Physical and Numerical Considerations for the SSC-S Code," NUREG/CR-0451, BNL-NUREG-50913, Brookhaven Nat. Lab. (1978)

105. F.C. Engel, R.A. Markley, and B. Minushkin, "The Effect of Heat Input Patterns on Temperature Distributions in LMFBR Blanket Assemblies," Westinghouse Electric Corp. Advanced Reator Division (11058)

106. G.H. Golden and J.V. Toker, "Thermophysical Properties of Sodium," Argonne Nat. Lab., ANL-7323 (1967)

107. Edited by P.E. MacDonald and L.B. Thomson, "MATRO-VERSION09, A Hand Book of Materials Properties for Use in the Analysis of Light Water Reator Fuel Rod Behavior," TREE-NUREG-1005 (Dec. 1976)

108. Y.S. Tang, R.D. Coffield, Jr., and R.A. Markley, Thermal Analysis of Liquid Metal Fast Breeder Reators, American Nuclear Society (1978)

109. R.S. Brokaw, "Alignment Charts for Transport Properties, Viscosity, Thermal Conductivity, and Diffusion Coefficients for Nonpolar Gases and Gas Mixtures at Low

Density," Lewis Reseach Center, NASA-TR-R-81 (1960)

110. A. Goldsmith, T.E. Waterman, H.J. Hirschhorn, Handbook of Thermophysical Properties of Solid Materials, The Macmillan Company, New York (1961)

111. C.S. Kim, "Thermophysical Properties of Stainless Steels," Argonne Nat. Lab., ANL-75-55 (1961)

Appendix A CONDUCTION MODELS

A.1 Fuel Conduction Model

The fuel conduction model in THERMIT-6S is based on the water version THERMIT (17). Only radial heat conduction is considered:

$$\rho C_p \frac{\partial T}{\partial t} - \frac{1}{r}\frac{\partial}{\partial r}\left(rk\frac{\partial T}{\partial r}\right) = q''' \qquad (A.1)$$

The fuel and clad are divided into mesh cells and one cell is assumed for the gap. Fuel temperatures are located at the boundaries of mesh cells, designated by the subscript k. Fuel pin properties are evaluated in the center of mesh cells denoted by the subscript $k+\frac{1}{2}$. The spatial differencing of Eq (A.1) is obtained by integrating the equation between the centers of two adjacent mesh cells:

$$\int_{r_{k-\frac{1}{2}}}^{r_{k+\frac{1}{2}}} \left[r\rho C_p \frac{\partial T}{\partial t} - \frac{\partial}{\partial r}\left(rk\frac{\partial T}{\partial r}\right)\right] dr = \int_{r_{k-\frac{1}{2}}}^{r_{k+\frac{1}{2}}} q''' \, r dr \qquad (A.2)$$

The terms in Eq (A.2) can be approximated as follows:

$$\int_{r_{k-\frac{1}{2}}}^{r_{k+\frac{1}{2}}} r\rho C_p \frac{\partial T}{\partial t} dr = \left[\frac{r_k^2 - r_{k-\frac{1}{2}}^2}{2}\langle\rho C_p\rangle_{k-\frac{1}{2}} + \frac{r_{k+\frac{1}{2}}^2 - r_k^2}{2}\langle\rho C_p\rangle_{k+\frac{1}{2}}\right]\frac{\partial T_k}{\partial t} \qquad (A.3)$$

$$\int_{r_{k-\frac{1}{2}}}^{r_{k+\frac{1}{2}}} \frac{\partial}{\partial r}\left(rk\frac{\partial T}{\partial r}\right) dr = (rk)_{k+\frac{1}{2}} \frac{T_{k+1} - T_k}{r_{k+1} - r_k} - (rk)_{k-\frac{1}{2}} \frac{T_k - T_{k-1}}{r_k - r_{k-1}} \qquad (A.4)$$

$$\int_{r_{k-\frac{1}{2}}}^{r_{k+\frac{1}{2}}} q_r''' \, dr = \frac{r_k^2 - r_{k-\frac{1}{2}}^2}{2}\langle q'''\rangle_{k-\frac{1}{2}} + \frac{r_{k+\frac{1}{2}}^2 - r_k^2}{2}\langle q'''\rangle_{k+\frac{1}{2}} \qquad (A.5)$$

There are four positions to require boundary conditions. For the center of the fuel pin, Eq (A.2) is integrated from $r=r_{\frac{1}{2}}=0$ to $r=r_{1\frac{1}{2}}$ and the resulting equation is:

$$\langle\rho C_p\rangle_{1\frac{1}{2}} \frac{r_{1\frac{1}{2}}^2}{8} \frac{T_1^{n+1}-T_1^n}{\Delta t} - \frac{k_{1\frac{1}{2}}}{2} (T_2^{n+1}-T_1^{n+1}) = q'''_{1\frac{1}{2}} \frac{r_{1\frac{1}{2}}^2}{8} \quad (A.6)$$

For the aroundner and outer surface around the gap, the term k is related to the gap heat transfer coefficient h_{gap} as follows:

$$k_{k-\frac{1}{2}} = h_{gap} \cdot d_{gap} \quad (A.7)$$

$$k_{k+\frac{1}{2}} = h_{gap} \cdot d_{gap} \quad (A.8)$$

where d_{gap} is the gap width.

For the clad outer surface node, Eq (A.2) is integrated from $r=r_{N-\frac{1}{2}}$ to $r=r_N$ =outside fuel pin radius, and introducing the clad surface heat flux q''_w we obtain the equation

$$\langle\rho C_p\rangle_{N-\frac{1}{2}} \frac{(r_N^2-r_{N-\frac{1}{2}}^2)}{2} \frac{(T_N^{n+1}-T_N^n)}{\Delta t} + \frac{r_N}{r_N-r_{N-\frac{1}{2}}} (T_N^{n+1}-T_{N-1}^{n+1})$$

$$+ q''_w r_N = q'''_{N-\frac{1}{2}} \frac{(r_N^2-r_{N-\frac{1}{2}}^2)}{2} \quad (A.9)$$

where

$$q''_w = h_\ell^n (T_N^{n+1}-T_\ell^{n+1}) + h_v^n (T_N^{n+1}-T_v^{n+1}) \quad (A.10)$$

T_ℓ and T_v: liquid and vapor temperature

h_ℓ and h_v: liquid and vapor heat transfer coefficient

The fully implicit difference scheme used for the fuel conduction model was proven to be unconditionally stable. In this way we ensure that a time step determined by the convective stability condition will not cause any stability problem for the fuel conduction solutions. As in the fuel conduction equations the temperature at a cell k is coupled with its neighbors k+1 and k-1, the fuel conduction equations must be solved simultaneously or iteratively. Both T_w and T_f in Eq (A.10) are treated implicitly in order to overcome the plausible large oscillation of fluid temperature. Since solving for T_f^{n+1} in the fluid equations requires information about wall heat flux, the fluid equations are coupled with the fuel conduction equations. The overall solution procedure for T_w and T_f is as follows:

1. Calculate h^n using wall and fluid properties at the previous time.
2. With the assumption $T_f^{n+1} = T_f^n$, find a first guess $T_w^{n+1,0}$ for T_w^{n+1} and the variation of $\partial T_w^{n+1}/\partial T_f^{n+1}$ by the forward elimination of the rod conduction problem.
3. Solve the fluid equations using

$$q_w'' = h^n(T_w^{n+1,0} - T_f^{n+1}) + h^n\left(\frac{\partial T_w^{n+1}}{\partial T_f^{n+1}}\right)(T_f^{n+1} - T_f^n) \qquad (A.11)$$

and find T_f^{n+1}

4. Set

$$T_w^{n+1} = T_w^{n+1,0} + \frac{\partial T_w^{n+1}}{\partial T_f^{n+1}} (T_f^{n+1} - T_f^n) \qquad (A.12)$$

and compute the backward substitution of the rod conduction problem to get the remaining new rod temperatures.

As we obtain Eq (A.10) by putting Eqs (A.11) and (A.12) together, this procedure does not contain any approximation. For a detailed description of this procedure refer to Ref. 17.

A.2 Structural Conduction Model

Unlike PWR systems the radial heat loss to the structure surrounding the system in the LMFBR may be significant. The primary reasons for this difference lie in the larger thermal conductivity of sodium, steeper radial temperature profile, and presence of a can in the LMFBR. The model employed for structural conduction is based on the fuel conduction model, but geometrical transformation is needed to keep the same volume. Figure A.1 shows the transformed structure from Fig. A.2. The hex can is transformed into an annulus, and sodium in the fluid channels contacting the hex can is formed to an imaginary annulus. The inner radius of the sodium annulus is determined by setting the cross-sectional area of the annulus equal to the sum of the cross-sectional area of

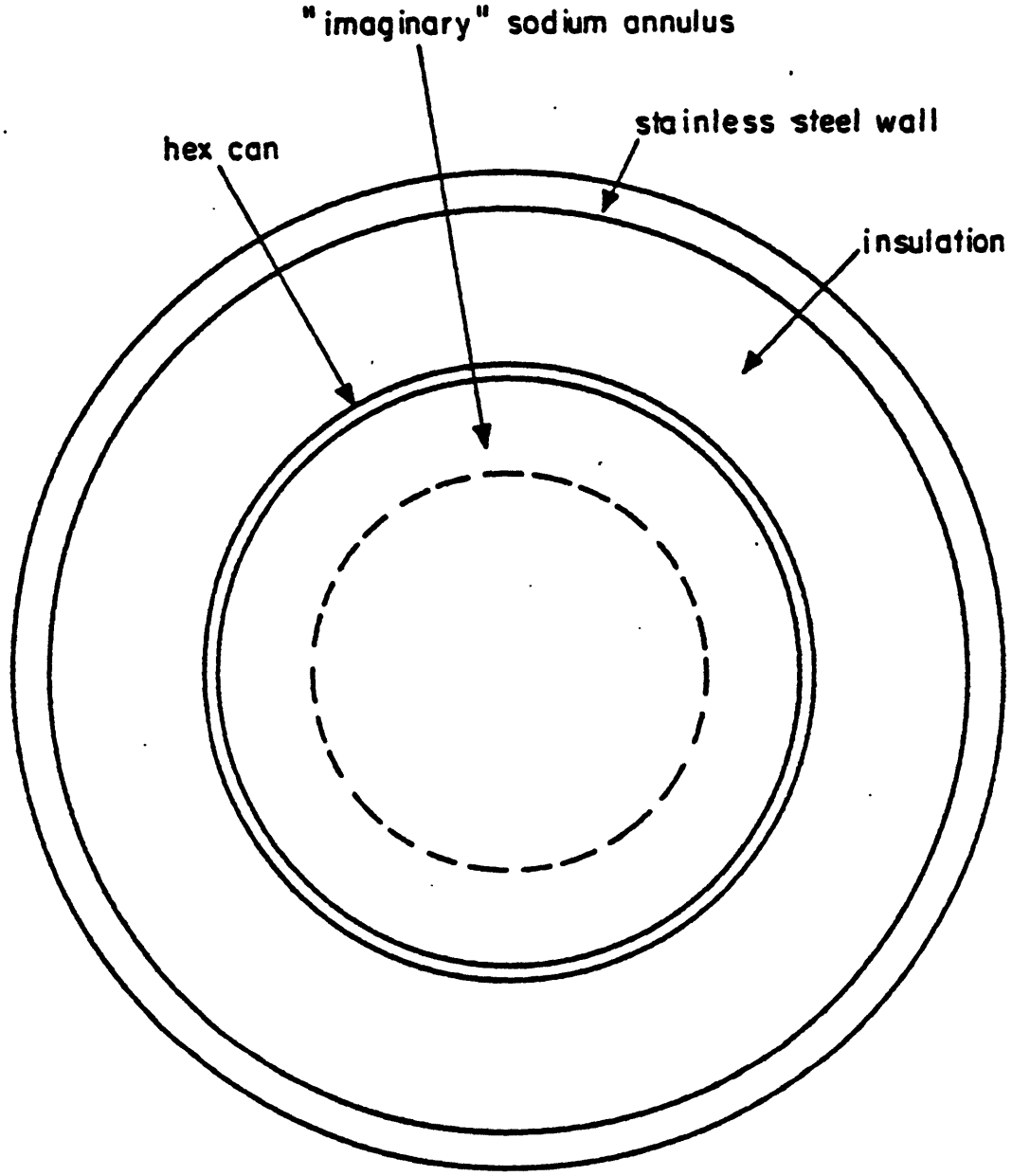

Fig. A.1: THERMIT Model of Hex Can with Associated Structure

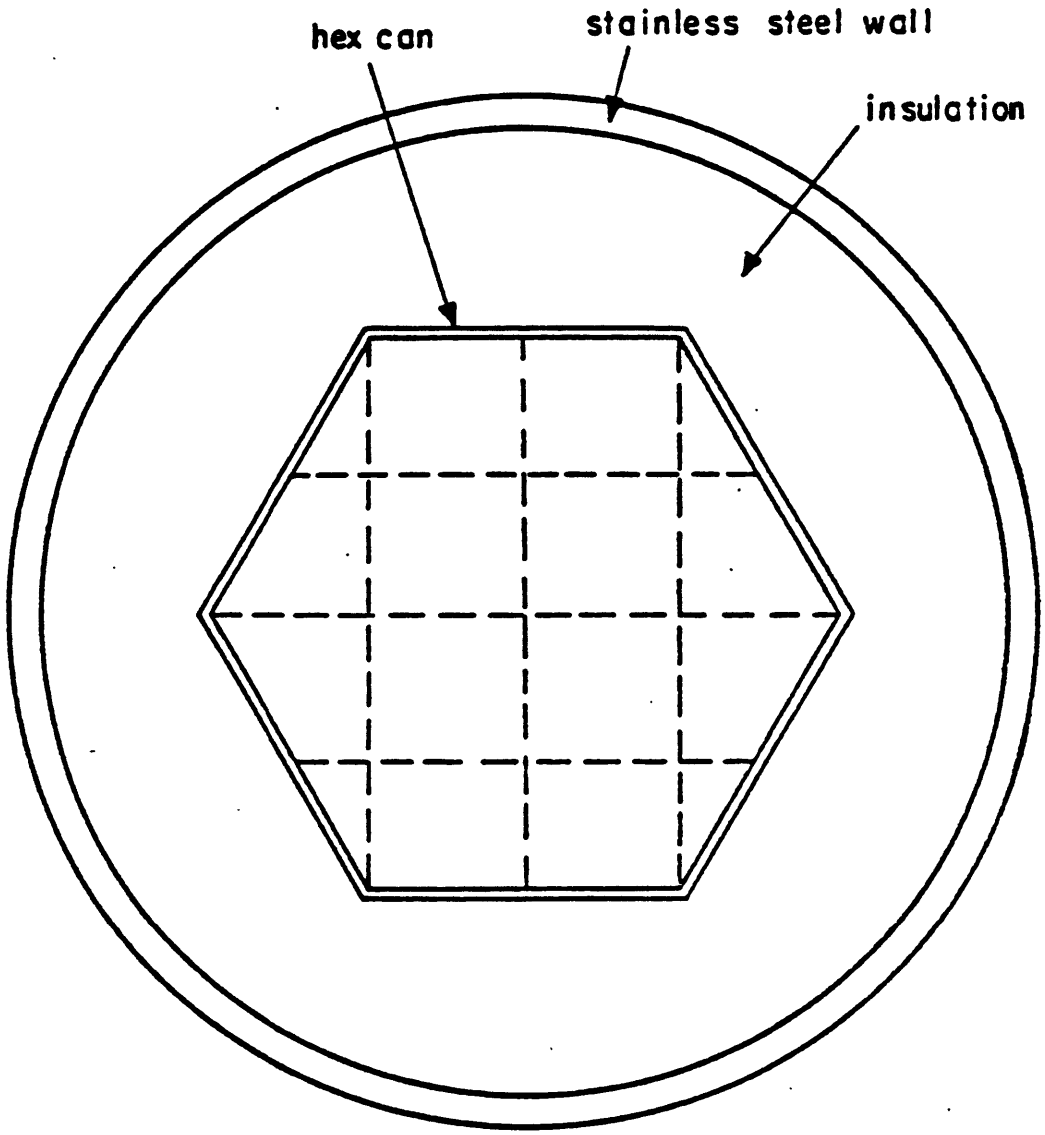

Fig. A.2: Hex Can with Associated Structure

sodium in each of the fluid cells adjacent to the structure.

The heat flux on the outer boundary, q''_{out} will be

$$q''_{out} = h_{out} (T_\infty - T_{w\,out}) \qquad (A.13)$$

where T_∞ : constant temperature outside the structure

$T_{w\,out}$: temperature at the outer boundary of the structure

If an adiabatic condition at the outer wall is desired, h_{out} is set as the zero value. For the inner boundary condition, the Dwyer correlation (103), which was developed for liquid sodium flowing in an annulus, is used.

$$Nu = A + C(\overline{\Psi}\ Pe)^{\beta}, \qquad (A.14)$$

where $A = 5.54 + 0.023\ r_{12}$

$C = 0.0189 + 0.00316\ r_{12} + 0.0000867\ r_{12}^2$

$\beta = 0.758\ r_{12}^{-0.0204}$

$r_{12} = r_2/r_1$

r_1 and r_2: inner and outer radius of sodium annulus

$\overline{\Psi}$ is assumed to be 1.0.

The heat flux on the inner boundary of the structure can be calculated as follows:

$$q''_{in} = Nu \frac{k}{D_e} (T_{sodium} - T_{w\,in}) \qquad (A.15)$$

where D_e: equivalent diameter of sodium annulus

T_{sodium} and $T_{w\,in}$: temperature in the sodium annulus and temperature at the inner boundary of the structure

This completes the list of boundary conditions necessary to solve the radial heat conduction equation which is described in the fuel conduction model.

The original model (45) assumes that there is no heat transfer between the structure and fluid, if vapor exists in cells contacting the structure. However, as it takes considerable time for the cells contacting the structure to reach dryout after vapor appears in the cells, the significant amount of energy can be transferred to the structure. After dryout little energy exchange between the structure and fluid may occur. Therefore, Eq (A.14) is used in the single phase region. As Eq (A.14) is valid only in the single phase region, the correlation for the wall heat transfer coefficient in two-phase flows, which is described in Section 5.2.3, is used to account for the effect of two-phase flow. In the post-dryout region (α >0.957), it is assumed that there is no heat transfer between the structure and fluid. The primary reason of this assumption comes from the experience that there is an instability of liquid temperature. This instability of liquid temperature induces the instabilities of structure heat flux and vapor temperature and at last significant pressure oscillation, which result in numerical problems. These instabilities are caused by the small heat capacity of fluid after dryout and

use of fluid temperature at the old time for the evaluation of the heat flux on the inner boundary of the structure. Moreover, for liquid metal, as the heat transfer coefficient is so large, these instabilities are understandable. Also as an attempt to include the T_{sodium} term implicitly would couple the fluid cells to each other through temperatures, the above assumption is adopted.

A.3 Fluid Conduction Model

In a bundle of LMFBR, a non-flat radial temperature profile exists in steady state conditions and the gradient of radial temperature profile sharply increases with time in flow transients. This steep radial temperature profile will affect the initiating time of boiling, two-dimensional voiding behavior, flow reversal, and dryout. This radial temperature profile is primarily controlled by energy exchange between channels. Expecially for liquid sodium, where its thermal conductivity is two orders of magnitude greater than that of water, conduction effects cannot be ignored. The conduction effects can be represented by the term $\nabla \cdot \alpha_k \langle\langle \bar{q}_k + \bar{q}_k^t \rangle\rangle$ in Eq (2.73). This term includes energy exchange by both molecular and turbulent conductions. Two options have been developed in THERMIT-6S for the inclusion of heat conduction between adjacent fluid channels: fully explicit formulation and partially implicit formulation. Three assumptions made for these two options are as follows:

1. The conduction effects between vapor and vapor, or liquid and vapor are negligible. This is justified, because the thermal conductivity of vapor sodium is three orders of magnitude lower than that of liquid sodium.
2. Only radial conduction is incorporated in the code now, though the model permits the inclusion of axial conduction if desired. Only in case of extremely low flow will axial conduction become significant. For the Clinch River Breeder Reactor the velocity in the core should be reduced by at least three orders of magnitude before axial conduction effects become as large as 2% of the amount of energy transferred by convection (104).
3. The effective Nusselt number for conduction is constant throughout transients. In order to obtain a practical value for the effective Nusselt number for radial heat conduction, the Westinghouse Blanket Heat Transfer Test Program (105) was numerically simulated with NATOF-2D by Zielinske (99). The heat transfer test section is a mockup of a LMFBR blanket assembly containing 61 rods in a hexagonal duct. From this experiment, the recommended value for the effective Nusselt number is 22.

A.3.1 Fully Explicit Formulation

The net rate of heat flow into a given fluid cell is expressed as the sum of the heat flows from each of the four

sides. For the configuration of Fig A.3.

$$q_T^{n+1} = q_{1-0}^{n+1} + q_{2-0}^{n+1} + q_{3-0}^{n+1} + q_{4-0}^{n+1} \tag{A.16}$$

where $$q_{1-0}^{n+1} = A_{1-0}^{n}\ h_{1-0}^{n}\ (T_{\ell 1}^{n} - T_{\ell 0}^{n}) \tag{A.17}$$

q_T: total heat flow into channel 0

q_{1-0}: heat flow from channel 1 to channel 0

A_{1-0} : heat flow area between channel 1 and 0

h_{1-0} : effective conduction heat transfer coefficient between channels 1 and 0

$T_{\ell 1}$ and $T_{\ell 0}$: liquid temperature in channels 1 and 0, respectively.

As heat flow entirely depends on quantities evaluated at the previous time n, this method is called the fully explicit formulation.

After boiling the liquid contact area between channels will be reduced. To account for it in a simple way, A_{1-0} is multiplied by the average void fraction of channels 0 and 1. This satisfies the energy conservation (i.e. $q_{1-0}^{n+1} = -q_{0-1}^{n+1}$). Wilson's model (45) assumes that there is no conduction after boiling. This assumption results in a sudden reduction of energy transfer between channels after boiling, even though large liquid contact areas due to large mesh sizes and low void fraction exist in the initial stage of boiling.

In Eq (A.17) h_{1-0} can be expressed in terms of heat transfer coefficients within each channel, h_1 and h_0 . By

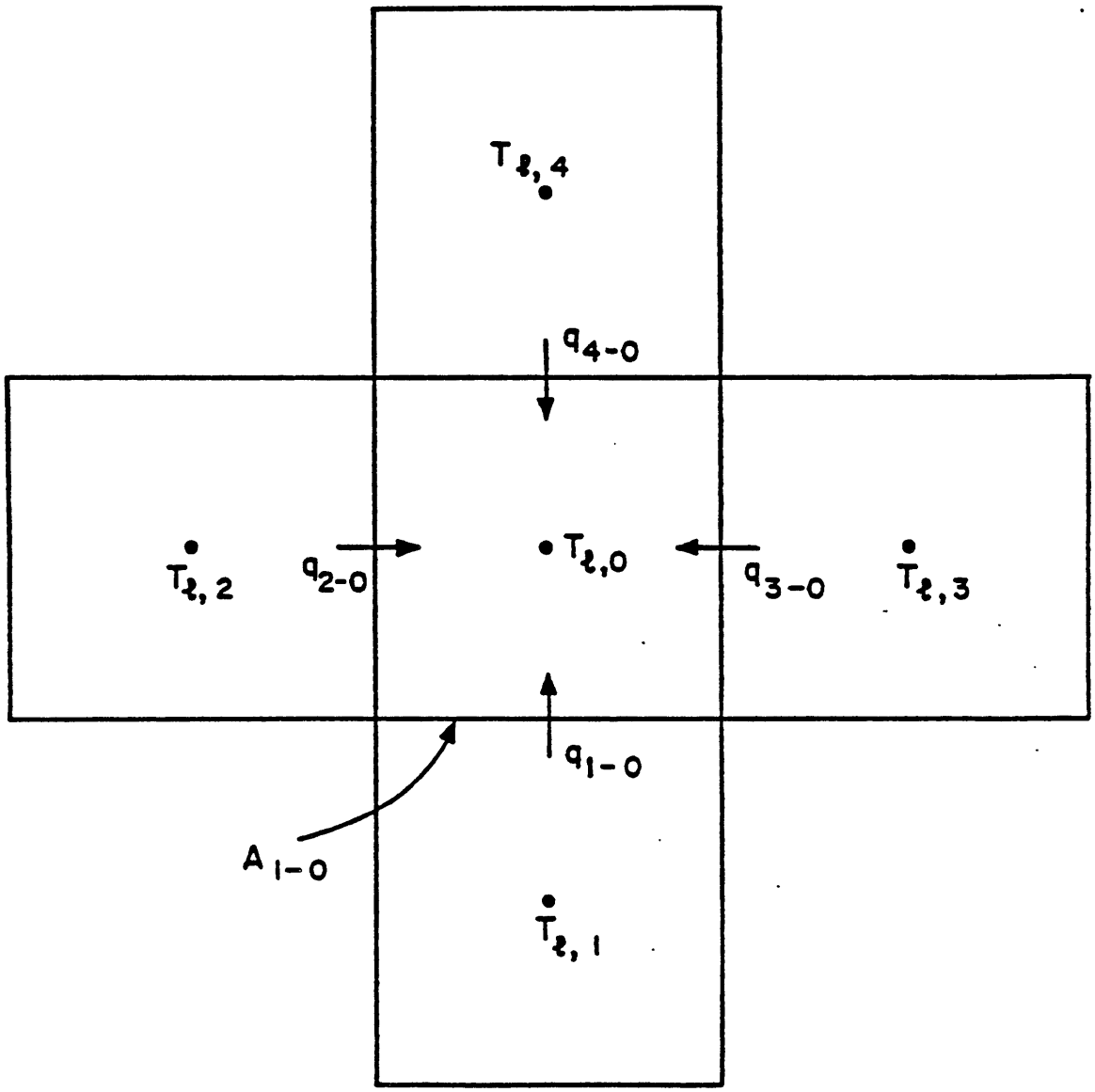

Fig. A.3: Top View of Fluid Channels

the boundary condition

$$q''_{1-0} = h_0(T_i - T_0)$$

$$= h_1(T_{\ell 1} - T_i) \qquad (A.18)$$

where T_i: interface temperature between two channels

To define h_0 and h_1, the constant Nusselt Number approximation is used

$$h_0 = Nu\ k_0/D_{e0}$$

$$h_1 = Nu\ k_1/D_{e1} \qquad (A.19)$$

where k: thermal conductiviy of sodium

D_e: equivalent diameter

Combining Eqs (A.16) and (A.18) and rearranging the resulting, we have

$$h_{1-0} = \frac{h_1 h_0}{h_1 + h_0} \qquad (A.20)$$

These steps are repeated for each face of the channel.

The major advantages of the explicit method are shorter computer time and strict conservation of energy. However, this method introduces a stability limit on the time step

size.

$$\Delta t < \frac{(\Delta x)^2}{4\alpha} , \qquad (A.21)$$

where $\alpha = k/\rho C_p$

Δx = radial mesh size

The minimal radial mesh size can be the radial channel size. With typical values for k, ρ, and C_p ($\Delta x=6.3x10^{-3}$ m, k=67w/m•K, C_p =1260J/kg•K, ρ=800kg/m), Δt must be less than 0.6 seconds. In the W-1 Experiment this corresponds to 2.8% of the steady-state velocity. Surely boiling will occur at 2.8% of the steady-state velocity and in turn the time step size will be reduced due to the high velocity of vapor. Therefore, in most of cases we can use the fully explicit formulation without more reduction of the time step size.

A.3.2 Partially Implicit Formulation

The partially implicit formulation was developed at MIT by Andrei Schor (15) in order to overcome the stability problem introduced by the explicit method. Eq (A.17) can be modified as follows:

$$q_{1-0}^{n+1} = A_{1-0}^{n+1} \, h_{1-0}^{n} \, (T_{\ell 1}^{n} - T_{\ell 0}^{n+1}) \qquad (A.22)$$

The primary reason to introduce this method instead of the fully implicit method is to avoid coupling of temperature of adjacent cells, which requres a new solution scheme and enormously increased computer time. When temperature in adjacent cells at the previous time is used like Eq (A.22), the decoupling of temperature can be achieved. It was proved that this method will not introduce the limitation of the time step size. The main drawback of this method is the lack of energy conservation, which can be serious in some conditions. Therefore, if a user assures that the time step size limited by convection is small enough than that by conduction throughout transients, use of the fully explicit formulation is recommended.

Appendix B PROPERTIES

B.1 Sodium Properties

The present version uses least squares polynomial fits derived from sodium properties correlations in ANL-RDP-72, ANL-RDP-74, and HEDL-TME-77-27, and the correlations presented in ANL-7323 (106) for liquid enthalpy, vapor conductivity and surface tension. All properties were converted in S.I. Units. These properties include the following approximation.

1. A perfect gas behavior for the vapor phase was assumed.
2. A constant sonic speed, 2100 m/sec was taken for the estimation of liquid compressibility.
3. The subcooled effect of liquid was neglected.

These approximations can be examined as follows. The equation of state for a real gas can be expressed in the following form:

$$\frac{Pv}{RT} = 1 + \frac{B}{v} + \frac{C}{v^2} + \frac{D}{v^3} + \ldots \qquad (B.1)$$

Stone et. al. fitted Eq (B.1) to their P-v-T data and obtained the following expressions for the coefficients with their average derivation of the equations from their

data, ± 0.26%.

$$B = -4.44734 \times 10^{-5} T \exp(15554.65/T) \ ft^3/mole$$

$$C = 0.243388 \exp(2495.8/T)$$

$$D = -0.811895 \exp(31175/T)$$

With typical values in the accident analysis of the LMFBR the deviation of an ideal gas behavior from Eq (B.1) is less than 10^{-3} . In the same condition the percentage error introduced by the second approximation is less than 10^{-4}. The first and second assumptions produce tolerable errors which are less than average deviations of the equations from data.

In order to analyze the effect of the third assumption on liquid enthalpy, we use Maxwellian reltionship.

$$dh(T,P) = \left(\frac{\partial h}{\partial T}\right)_p dT + \left(\frac{\partial h}{\partial P}\right)_T dP$$

$$= C_p(T,P)dT + [v - T\left(\frac{\partial v}{\partial T}\right)_p]dP \qquad (B.2)$$

Integrating Eq (B.2) from the system pressure P to the saturation pressure P_{sat} corresponding the system temperature T and assuming that $[v - T\left(\frac{\partial v}{\partial T}\right)_p]$ is constant, we obtain the expression of the enthalpy of subcooled

liquid.

$$h_\ell(T,P) = h_\ell(T,P_{sat}) + [v-T(\frac{\partial v}{\partial T})_p](P-P_{sat})$$

At T=661 K and P=1.5 bar

$$h_\ell(T,P) - h_\ell(T,P_{sat}) = 180\ J/m^3$$

The percentage error introduced by the third assumption is less than 10^{-3}%. which is much lower error than one standard deviation of data. It can be conclude that properties used in the present version represent well real properties.

Saturation Temperature

$$T_{sat} = \frac{683538}{-11484.6 + \sqrt{142665998.6 - 1.367076P}}$$

for $0.73 < P < 2.2x10^6$

Liquid Density

Among all correlations we have viewed for the liquid density, none shows a pressure dependence due to the negligible compressibility for the liquid phase. However, as described in Section 3.3, the diagonal dominance of the present numerical scheme in the single phase liquid region is provided by the compressibility of liquid. Therefore, a

term to represent the compressibiliy of liquid must be included in the correlation of the liquid density. In the presnt version a simple expression is used due to the inaccuracy of the estimation of liquid compressibility.

$$(\partial\rho/\partial P) = 1/a^2$$

where a is the speed of sound whiah is taken, equal to 2,100 m/sea at 900 C.

Then we have the liquid density

$$\rho_\ell = 1004.23 - 0.2139\ T_\ell - 1.1046\text{x}10^{-5}\ T_\ell^2 + 2.26\text{x}10^{-7}\ P$$

for $550 < T_\ell < 1644.4$

Vapor Density

For the vapor density the expression which gives the density in saturation conditions is used and a perfect gas behavior in the superheated zone is assumed.

$$\rho_v = P\ (4144.4/T_v - 7.4461 + 1.3738\text{x}10^{-2}\ T_v - 1.0834\text{x}10^{-5}\ T_v^{\ 2} + 3.8903\text{x}10^{-9}\ T_v^{\ 3} - 4.922\text{x}10^{-13}\ T_v^{\ 4})$$

for $T_v > 550$

Internal Energies

The source of sodium properties gives only the expressions for the enthalpies. The internal energies can be calculated by the following equation

$$e = h - P / \rho$$

For the liquid enthalpy

$$h_\ell = -67507.5 + 1630.4\ T_\ell - 0.41672\ T_\ell^2 + 0.15427\text{x}10^{-3}\ T_\ell^3$$

for $550 < T_\ell < 1644.4$

For vapor enthalpy

$$h_v = h_\ell + 5.3139\text{x}10^6 - 2.0296\text{x}10^3\ T_v + 1.0625\ T_v^2 + 3.3163\text{x}10^{-4}\ T_v^3$$

for $T_v > 550$

Liquid Thermal Conductivity

$$k_\ell = 110.45 - 6.5112\text{x}10^{-2}\ T_\ell + 1.543\text{x}10^{-5}\ T_\ell^2 - 2.4617\text{x}10^{-9}\ T_\ell^3$$

for $550 < T_\ell < 1250$

Vapor Thermal Conductivity

$$k_v = 2.83662\text{x}10^{-3} + T_a\ (6.88299\text{x}10^{-5} - 1.67826\text{x}10^{-8}\ T_a)$$

for $360 < T_v < 1644$,

where $T_a = 1.8\ T_v - 459.67$

Liquid Viscosity

$$\mu_\ell = 3.6522\text{x}10^{-5} + \frac{2.8733\text{x}10^4 - 45.6877T_\ell + 0.16626T_\ell^{\ 2}}{T_\ell^{\ 4}}$$

for $550 < T_\ell < 1250$

Vapor Viscosity

$$\mu_v = 1.261\text{x}10^{-5} + 6.085\text{x}10^{-9}\ T_v$$

for $360 < T_v < 1644$

Surface Tension

$$\sigma = 0.2067 - 10^{-4}\ T_\ell + 0.027314\ T_\ell^{\ 2}$$

for $550 < T_\ell < 1644$

Liquid Specific Heat

$$C_{p\ell} = 1.6301\text{x}10^{3} - 0.83344\ T_{\ell} + 4.6281\text{x}10^{-4}\ T_{\ell}^{2}$$

for $373 < T_{\ell} < 1773$

Vapor Specific Heat

$$C_{pv} = 0.5871\text{x}10^{3} - 0.83344\ T_{v} + 4.6281\text{x}10^{-4}\ T_{v}^{2}$$

for $873 < T_{v} < 1473$

B.2 Properties of Fuel and Structure

1) UO_2 Fuel

The properties of UO_2 fuel based on Ref (107). have been approximated by polynomial fits whose maximum errors are within one standard deviation in experimental data.

$$\rho C_p = F\ (1.78\text{x}10^{-6} + 3.62\text{x}10^{3}\ T - 2.61\ T^{2} + 6.59\text{x}10^{-4}\ T^{3})$$

$$k = P_f\ (10.8 - 8.84\text{x}10^{-3}\ T + 2.25\text{x}10^{-6}\ T^{2})$$

where $P_f = 1 - (2.74 - 5.8\text{x}10^{-4}\ T)\ (1-F)$

P : porosity

F: fraction of theoretical density

ρ, C_p, and k: fuel density, capacity and conductivity

2) Mixed Oxide Fuel (UO_2-PuO_2)

The following expressions come from Tang et. al.'s recommendation (108).

$$\rho = F\ (10.96\text{x}10^3\ F_{uo_2} + 11.45\text{x}10^3\ F_{puo_2})$$

$$C_p = 196.6 + 0.2666\ T - 1.834\text{x}10^{-4}\ T^2 + 4.814\text{x}10^{-8}\ T^3$$

$$k = 113.3\ (1/(0.78+0.02935T) + 6.6\text{x}10^{-13}T^3)\frac{(1-P_f)}{1+P_f+10P_f^2}$$

where F_{uo_2} and F_{puo_2} : mass fraction of UO_2 and PuO_2 in the fuel

3) Gap (Ref. 107)

The gap heat transfer coefficient is divided in three parts:

a) Open gap component, based on the conductivity of a mixture of four noble gases

b) Radiation component

c) Closed gap

d) Contribution from partial fuel-clad contact

The thermal conductivity equations of the individual gases are calculated as follows:

$$He : k_1 = 3.366\text{x}10^{-3}\ T^{0.668}$$

$$Ar : k_2 = 3.421\text{x}10^{-3}\ T^{0.701}$$

$$Zr : k_3 = 4.029\text{x}10^{-5}\ T^{0.872}$$

$$Kr : k_4 = 4.726\text{x}10^{-5}\ T^{0.923}$$

where T is the gas temperature.

The relationship for calculation the thermal conductivity of a monatomic gas mixture is based on the work of Brokaw (109).

$$k_{mix} = \sum_{i=1}^{n} \frac{k_i}{1 + \sum_{\substack{j=1 \\ j \neq i}}^{n} \Psi_{ij} \, x_j / x_i}$$

where

$$\Psi_{ij} = \Phi_{ij} \left[1 + 2.41 \frac{(x_i - x_j)(x_i - 0.142 x_j)}{(x_i + x_j)^2}\right]$$

$$\Phi_{ij} = \frac{[1 + (k_i/k_j)^{1/2} \, (x_i/x_j)^{1/4}]^2}{2^{3/2} \, (1 + x_i/x_j)^{1/2}}$$

n: number of components in mixture

M: Molecular weight

x: mole fraction

The thermal conductivity of the gas mixture plays an important role in determining so-called contact gap conductance as well as open gap conductance in a fuel rod when the ratio of the mean fuel path of the gas molecules to the characteristic dimension (gap) of the body exceeds about 0.01. Heat transfer from a solid to a gas in this knudsen domain is then dependent on an accommodation coefficient which is defined as the ratio of the actual energy

interchange to the maximum possible energy interchange between a surface and a gas. Generally, the accommodation coefficient of a heavey gas such as argon or xenon is near unity and this effect can be neglected. But the effect can not be neglected for the light gas such as helium. The following factor should be divided when temperature drops are calculated in the Knudsen domain.

$$f = 1 + C \frac{kT^{1/2}}{P\zeta}$$

where P: gas pressure

ζ: characteristic dimension

C: empirical constant

The characteristic dimension, ζ , is essentially equal to the gap dimension and during pellet-to-cladding contact should be equal to the root mean square of the surface roughness, approximately 4.389×10^{-6} meters in most commercial fuel rods. 0.2103 $N\sqrt{K}$ /W for C suggested in Ref. (107).

If a nominal open hot gap is calculated, a fraction of the fuel pellet is assumed to be in contact with the cladding at zero contact pressure and an effective fuel-to-cladding gap conductance is calculated as follows:

$$h_{gap} = (1-F)\ h_o + Fh_c$$

where h_{gap}: net gap conductance

h_o: nomical open gap conductance

h_c: contact gap conductance (zero contact pressure)

F: fraction of pellet circumference in contact with the cladding.

The nominal open gap conductance is determined from

$$h_o = k_{mix} / (dr + \delta)$$

where dr: nominal hot radial gap width

δ : root mean square of the fuel and the cladding surfaces roughness.

The fraction of pellet circumference in high contact with the cladding, F, is assumed to be an inverse power law function of the ratio of the nominal hot radial gap and the hot pellet radius as follows:

$$F = \frac{1}{a_1 + \left(\frac{100\ dr}{R_f}\right)^{a_2} + 1.429} + 0.3$$

where R : hot radius of the fuel pellet

a_1 and a_2 : empirical constants

The relationships for a_1 and a_2 as a function of burnup is greater than 600 Mwd/Mtu are described by the following equations, respectively:

$$a_1 = 100 - 98\ F'$$

$$a_2 = 4 - 0.5\ F'$$

where

$$F' = 1 - \frac{1}{\left(\frac{x-600}{1000}\right)^4 + 1}$$

x : burnup in Mwd/Mtu

When the burnup is less than or equal to 600 Mwd/Mtu, then $a_1 = 100$ and $a_2 = 4$

When the fuel and cladding are in contact, the contact gap conductance can be calculated

$$h_c = C_1 P^n + k_{mix} / \delta$$

where P is the pellet-cladding contact pressure in N/m^2 and is zero when F is less than one, the constant C_1 is estimated to be 4×10^{-4} for stainless steel-uranium dioxide pairs.

The value of the pressure exponent, n, is governed by the behavior of the fuel and cladding at the interface of the contact points. The following values are recommended in Ref. 107.

$n=1$ for $0 > P > 1000$ psi

$n=2$ for $P > 1000$ psi

The radiation heat transfer contribution on the gap heat transfer coefficient is accounted for as follows:

$$h_{gap} = h_{gap,o} + h_{gap,r}$$

where

$h_{gap,o}$: the gap heat transfer coefficient without the radiation heat transfer

$h_{gap,r}$: the gap heat transfer coefficient contributed

by the radiation heat transfer

$$h_{gap,r} = 5.279\text{x}10^{-8}\ (T_{fs} + T_{cs})\ (T_{fs}^2 + T_{cs}^2)\ /\ F_r$$

$$F_r = \max\ (1.1485,\ \min\ (2.451,\ -0.154 + 0.0013025\ T_{fs})$$

$$+\ 0.33\ R_{fs}\ /\ R_{cs}$$

T_{fs} and T_{cs} : fuel and clad surface temperature

R_{fs} and R_{cs} : fuel and clad surface radii.

Niobium (110)

$$\rho C_p = 1.808\text{x}10^6 + 826.7\ T$$

$$k = 41 + 0.01455\ T$$

Boron Nitride (108)

$$\rho C_p = 2.84\text{x}10^6 + 6.68\text{x}10^2\ T$$

$$k = 13.85$$

Copper (110)

$$\rho C_p = 3.151\text{x}10^6 + 1.0286\text{x}10^3\ T$$

$$k = 429.7 - 0.0962\ T$$

316 Stainless Steel (111)

$$\rho = 8084.2 - 0.42086\ T - 3.8942\text{x}10^{-5}\ T^2$$

$$C_p = 4.187\text{x}10^3\ (0.1097 + 3.17\text{x}10^{-5}\ T)$$

$$k = 9.248 + 1.571\text{x}10^{-2}\ T$$

Zircaloy (108)

$$1096 > T > 843 : \rho C_p = 1.892\text{x}10^6 + 570\ T$$

$$1230 > T > 1096 : \rho C_p = 2.3322\text{x}10^6$$

$$T > 1230 : \rho C_p = 4.4941\text{x}10^6$$

$$k = 9.724 + 0.00917\ T$$

304 Stainless Steel (111)

$$\rho = 7984.1 - 0.26506\ T - 1.158\text{x}10^{-4}\ T^2$$

$$C_p = 4.187\text{x}10^3\ (\ 0.1122 + 3.222\text{x}10^{-5}\ T\ )$$

$$k = 8.116 + 1.618\text{x}10^{-2}\ T$$

Marimet Insulation (40)

Degraded marimet insulation was used in the THORS experiments. Sodium leakage into the insulation occurred. Assuming that all void space was full of sodium, Ref. 40 estimated the effective conductivity and heat capacity.

$$\rho C_p = 1.32\text{x}10^6$$

$$k = 26.1$$

Appendix C DERIVATION OF Eq (5.2.1-13)

The derivation of Eq (5.2.1-13) is primarily based on analogy between shear stress in single-phase flow and that in two-phase flow.

In single-phase flow shear stress can be expressed as follows:

$$\tau_w = f \frac{\rho_\ell U_\ell^2}{2} , \qquad (C.1)$$

where $f = c / Re^n$

$Re = \rho_\ell U_\ell D_e / \mu_\ell$

$D_e = D$ for a tube

U_ℓ = average liquid velocity

According to analogy, shear stress in two-phase flow can be obtained as follows:

$$\tau_{w2\phi} = f_{2\phi} \frac{\rho_\ell U_{\ell f}^2}{2} \qquad (C.2)$$

where $f_{2\phi} = c / Re_{2\phi}^n$

$Re_{2\phi} = \rho_\ell U_{\ell f} D_e' / \mu_\ell$

$D_e' = 4 A_{\ell f} / P_{\ell f} = 4\delta$

$A_{\ell f}$ = flow area of liquid film

$P_{\ell f}$ = perimeter of liquid film

δ = liquid film thickness

$U_{\ell f}$ = liquid film velocity

The two-phase flow multiplier, ϕ_ℓ^2, is defined by the following equation:

$$\phi_\ell^2 = \tau_{w2\phi} / \tau_{w1\phi} \tag{C.3}$$

where $\tau_{w1\phi}$ is the single-phase shear stress at the same liquid mass flow rate as that in two-phase flow.

$$\tau_{w1\phi} = f_{1\phi} \frac{\rho_\ell j_\ell^2}{2} \tag{C.4}$$

where $f_{1\phi} = c / Re_{1\phi}^n$

$Re_{1\phi} = \rho_\ell j_\ell D_e / \mu_\ell$

$j_\ell = \alpha_\ell U_\ell$

$\alpha_\ell = \alpha_{\ell f} + \alpha_{\ell d}$

Substituting Eqs (C.2) and (C.4) and into Eq (C.3), then we have

$$\phi_\ell^2 = \left(\frac{f_{2\phi}}{f_{1\phi}}\right)\left(\frac{U_{\ell f}}{j_\ell}\right)^2 \tag{C.5}$$

$$= \left(\frac{D}{4\delta}\right)^n \left(\frac{U_{\ell f}}{j_\ell}\right)^{2-n} \tag{C.6}$$

Equation (C.6) can be expressed interms of liquid film volumetric fraction, $\alpha_{\ell f}$, and entrainment fraction, E.

$$\phi_\ell^2 = (1/\alpha_{\ell f})^2 \ (1-E)^{2-n} ,$$

where n=0.2 for turbulent flow

n=1 for laminar flow

Appendix D VALVE MODEL

A simplified valve model is needed to account for pressure drops between the inlet boundary and inlet of test section, and between the outlet of the test section and outlet boundary. (See Fig 6.1) From the definition of pressure drop, we have

$$\frac{\Delta p}{\Delta z} = f \frac{W^2}{2D_e \rho A^2} \qquad (D.1)$$

Considering the constant inlet temperature except in the case of flow reversal and assuming that the Blausius relationship, ($f=c/Re^{0.2}$), is applicable, we obtain a simplified equation:

$$\Delta p/\Delta z = C_1 \, W^{1.8} \qquad (D.2)$$

where $C_1 = 0.5 \, c \, \mu^{0.2} \, \rho^{-1} \, D_e^{-1.2} \, A^{-1.8}$

As C_1 is a function of geometry and properties, C_1 is set to be constant throughout transients. C_1 can be calculated for a given pressure drop by using Eq (D.2).

In the code Eq (D.2) is written as follows:

$$\Delta p/\Delta z = fwl * v^{n+1} \qquad (D.3)$$

where fwl = spd * (tarea * rol) **1.8 * v ** 0.8, and spd, tarea, and rol correspond to C_1, A, and ρ, respectively.

Note that v in Eq (D.3) is a numerically predicted velocity in a channel. When one-sixth of the fuel bundle is taken for 2-D analysis, then A and W are set to be one-sixth of the bundle area and of the bundle mass flow rate, respectively.

For example, let us calculate C_1 for the restricted area of the P3A test positioned between the inlet boundary and inlet of the test section by using Eq (D.2).
In Ref. 88 the test mass flow rate and pressure drop at that position, at steady state and boiling inception, are 9.46 lb/sec and 11.3 psi, and 3.87 lb/sec and 2 psi, respectively. Using the axial mesh length of the fictitious inlet mesh, $\Delta z=8''$, one-sixth of the test mass flow rate for W in 2-D analysis, and S.I. units, we obtain the values of C_1 at steady state and boiling inception: 7.1×10^5 and 6.4×10^5. The ratio of both cases is 1.11, which confirms the assumption of the consatant value, C_1.

Appendix E GENERALIZED NORMALIZATION OF HEAT SOURCE

The total power in the subassembly, Q_t, can be expressed as follows:

$$Q_t = \sum_i \sum_j \sum_k q'''(i,j,k)\ \Delta V\ (i,j,k) \qquad (E.1)$$

where q''' = volumetric heat generation rate in a cell

ΔV = volume of a cell

i,j,k = indicators of positions of a cell

Multipling Eq (E.1) by a normalization factor, N_f, we have

$$\sum_i \sum_j \sum_k Q_t\ q_z(j)\ q_t(i)\ q_r\ (k)\ \Delta V\ (i,j,k) = \sum_i \sum_j \sum_k \left\{ q'''\ (i,j,k) \right.$$

$$\left. [\sum_i \sum_j \sum_k q_z(j)\ q_t(i)\ q_r(k)\ \Delta V\ (i,j,k)]\ \Delta V\ (i,j,k) \right\}, \qquad (E.2)$$

where $N_f = \sum_i \sum_j \sum_k q_z(j)\ q_t(i)\ q_r(k)\ \Delta V\ (i,j,k)$,

and q_z, q_t, and q_r represent the axial power distribution, transverse power shape in the subassembly, and radial power distribution within a fuel rod.

From Eq (E.2) we can obtain the following relationship:

$$Q_t\ q_z(j)\ q_t(i)\ q_r(k) = q'''\ (i,j,k)\ N_f \qquad (E.3)$$

Therefore, the normarized volumetric heat generation rate can be expressed as follows:

$$q'''\ (i,j,k) = Q_t\ q_z(j)\ q_t(i)\ q_r(k)\ /\ N_f \qquad (E.4)$$

Appendix F INPUT INFORMATION

F.1 Added or Modified Input Description

The description of input, which is added to or modified from the previous version (45), is as follows:

nrzf (narf,nc)

= number of radial zones in each axial region of fuel

nrmzf (nrzfmx,narf,nc)

= number of radial meshes per zones in the fuel

mnrzf (nrzfmx,narf,nc)

= material in each radial zone of the fuel (1/2/3/4/5/6/7/8/9/10/11/12 : fuel/gap/316 stainless steel/304 stainless steel/liquid sodium/degraded Marimet insulation/air or void/zircaloy/niobium/tungsten/boron nitride/copper)

drzf (nrzfmx,narf,nc)

= thickness of each radial zone in the fuel (m)

cv = virtual mass coefficient

alpdry = void fraction when dryout occurs

pin = inlet pressure at steady state (Pa)

pout = outlet pressure at steady state (Pa)

vin = inlet velocity at steady state (m/sec)

vout = outlet velocity at steady state (m/sec)

spd1 = spatial pressure drop coefficient at inlet

spd2 = spatial pressure drop coefficient at outlet

tarea = total axial flow area

F.2 Input

Input for 2-D Analysis of the W-7b' Test at Steady State

```
                    2d17w
 $tidat
ntc=3
$end
SLSF Bundle (19 pin), W1 Test, Run 7b',
Steady state,  17 Channels
Heat Loss
$intdat
nc=3
nz=17
nr=1
nitmax=2
iitmax=30
narf=4
nx=1
itam=1
iht=33
ihtpr=1
ishpr=1100
itb=0
ibb=1
iwft=1
nrzs=1
$end
$readat
epsn=1.e-5
epsi=1.e-5
rnuss=22.
pin=8.6e5
pout=1.4952e5
vin=6.
vout=6.
hdt=3.258e-3
pdr=1.2435
velx=1.98
tdelay=80.
radf=2.921e-3
hdr=52.23
spd1=130.75e5
spd2=0.
tarea=64.162e-6
$end
$roddat
q0=1.103e5
ftd=0.9357
fpuo2=0.25
pgas=1.e5
gmix(1)=1.
$end
3              $ncr
```

```
0                    $indent
1 2 11 13                    $ifcar
3(4 4 4 4)                   $nrzf
3(4(1 6 1 3 )) $nrmzf
2(1 1 2 3 2(7 1 2 3) 7 7 7 3)
7 7 7 3 2(7 1 2 3) 7 7 7 3 $mnrzf
1 $inx
3 $mnrzs
4 $nrmzs
17(0.0) 1(1.139e-3) 9(0.5695e-3) 2(0.7119e-3) 5(1.139e-3)
1(0.575e-3) 9(0.2875e-3) 2(0.36e-3) 5(0.575e-3) $arx
51(0.0) $ary
18(28.653e-6) 18(26.955e-6) 18(8.654e-6) $arz
1(5.8223e-6) 9(2.911e-6) 2(3.639e-6) 5(5.8223e-6)
1(5.477e-6) 9(2.739e-6) 2(3.423e-6) 5(5.477e-6)
1(1.759e-6) 9(0.879e-6) 2(1.1e-6) 5(1.759e-6) $vol
5.353e-3 3.917e-3 3.772e-3 $hedz
2.675e-3 3.331e-3 3.034e-3 $wedz
3.6322e-3 2(6.335e-3) $dx
3(18.82e-3) $dy
2(0.2032) 9(0.1016) 2(0.127) 6(0.2032) $dz
3(4.6e5 17(4.e5) 1.4952e5) $p
57(0.0) $alp
3(2(662.) 17(800.)) $tv
54(6.) $vvz
3(1(662.) 16(800.)) $twf
0. .7475 1.05 1.26 1.39 1.415 1.35 1.2 0.94 0.6
7(0.) $qz
3(4(1.0)) $qt
2(11(0.0) 7(1.0) 26(0.0))
12(0.0) 6(1.0) 26(0.0) $qr
4(1.16667) 4(1.5) 4(0.5) $rn
2(4(1.0e-8 2.45745e-3 0.07974e-3 0.38e-3))
4(0.8763e-3 1.60528e-3 0.05588e-3 0.38e-3) $drzf
18.82e-3 $pcx
1.016e-3 $drzs
662. 16(780.) $tws
$timdat
tend=2.
dtmin=1.e-4
dtmax=1.e+1
dtlp=2.
dtsp=10.
$end
```

Input for 1-D Analysis for the W-7b' at steady state

1d17w

```
$tidat
ntc=3
$end
SLSF Bundle (19 pin) ,W1  Test, Run 7b',
Steady state,  17 Channels
Heat Loss
$intdat
nc=1
nz=17
nr=1
nitmax=2
iitmax=1
narf=4
nx=1
itam=0
iht=33
ihtpr=1
ishpr=1100
itb=0
ibb=1
iwft=0
nrzs=1
$end
$readat
epsn=1.e-5
epsi=1.e-5
rnuss=0
hdt=3.258e-3
pdr=1.2435
velx=1.98
vely=5.78
tdelay=80.
radf=2.921e-3
hdr=52.174
pin=8.6e5
pout=1.4952e5
vin=6.
vout=6.
spd1=130.75e5
spd2=1.734e4
tarea=64.162e-6
$end
$roddat
q0=1.103e5
ftd=0.937
fpuo2=0.25
pgas=1.7e5
hgap=0.285
gmix(1)=1.
$end
```

```
1                $ncr
0                  $indent
1 2 11 13                  $ifcar
4 4 4 4                  $nrzf
4(1 6 1 3) $nrmzf
7 7 7 3 2(1 1 2 3) 7 7 7 3 $mnrzf
1 $inx
3 $mnrzs
4 $nrmzs
17(0.0) $arx
17(0.0) $ary
18(64.162e-6)  $arz
13.058e-6 9(6.529e-6) 2(8.161e-6) 5(13.058e-6) $vol
4.39e-3 $hedz
3.37e-3 $wedz
16.e-3 $dx
18.82e-3 $dy
2(0.2032) 9(0.1016) 2(0.127) 6(0.2032) $dz
(4.6e5 17(4.e5) 1.4952e5) $p
19(0.0) $alp
(2(662.) 17(800.)) $tv
18(6.) $vvz
(1(662.) 16(800.)) $twf
0. .7475 1.05 1.26 1.39 1.415 1.35 1.2 0.94 0.6
7(0.) $qz
(4(1.0)) $qt
12(0.) 6(1.0) 26(0.) $qr
4(3.16667) $rn
4(0.889e-3 1.659e-3 0.0823e-3 0.38e-3) $drzf
18.82e-3 $pcx
1.016e-3 $drzs
662. 16(780.) $tws
$timdat
tend=2.
dtmin=1.e-4
dtmax=1.e+1
dtlp=2.
dtsp=10.
$end
```

Input for Analysis of the W-7b' Test in Transients (0-1.5 sec)

2dw

```
 $tidat
ntc=-2
 $end
$restart
nitmax=6
cv=1.e-2
iss=0
iitmax=40
t0=0.4
itb=0
ibb=1
ihtpr=1
ishpr=1100
epsn=1.e-4
epsi=1.e-5
 tdelay=2.
rnuss=-22.
ntabls=2
itbt=2
ibbt=1
natc=1
$end
   continue W-7b' transient, v-p bc
2
0. 1. 0.5 0.38 $vin
2
0. 1. 4. 1. $pout
 $timdat
 tend=3.5
 dtmin=1.e-4
 dtmax=5.e-1
dtlp=0.5
 dtsp= 30.
 $end
```

Input for Analysis of the W-7b' Test in Transients (1.5-3.5 sec)

2dw1

```
 $tidat
ntc=-2
 $end
$restart
nitmax=-10
iss=0
iitmax=40
t0=0.4
itb=0
ibb=0
ihtpr=0
ishpr=1100
epsn=1.e-4
epsi=1.e-5
alpdry=0.957
tdelay=2.
rnuss=-22.
spd2=1.743e4
tarea=6.46e-5
ntabls=2
itbt=2
ibbt=1
natc=1
$end
   continue W-7b' transient, p-p bc
2
0. 1. 1.5 0.64 $pin
2
0. 1. 1.5 1. $pout
 $timdat
 tend=4.7
 dtmin=1.e-4
 dtmax=5.e-1
dtlp=0.1
 dtsp= 0.02
 $end
```

Input for Analysis of the W-7b' Test in Transients (3.5-8 sec)

2dw2

```
 $tidat
ntc=-2
q0=0.05956e5
 $end
$restart
nitmax=-10
iss=0
iitmax=40
t0=0.4
itb=0
ibb=0
ihtpr=0
ishpr=1100
epsn=1.e-4
epsi=1.e-5
alpdry=0.957
tdelay=2.
rnuss=-22.
spd2=1.743e4
tarea=6.46e-5
ntabls=2
itbt=2
ibbt=1
natc=1
$end
   continue W-7b' transient, p-p bc
2
0. 1. 3.5 0.64 4.0 1. $pin
2
0. 1. 1.5 1. $pout
 $timdat
 tend=10.
 dtmin=1.e-4
 dtmax=5.e-1
dtlp=0.1
 dtsp= 0.02
 $end
```

Input for 2-D Analysis of the P3A Test at Steady State

p3a17

```
$tidat
ntc=3
$end
SLSF In-Reactor Experiment P3A  (37 pin)
Steady state,  2-D, 17 axial cells
Heat Loss & Gain
$intdat
nc=3
nz=17
nr=1
nitmax=1
iitmax=10
narf=3
nx=1
itam=1
iht=33
ihtpr=1
ishpr=1100
itb=0
ibb=1
iwft=1
nrzs=1
$end
$readat
epsn=1.e-5
epsi=1.e-5
rnuss=-22.
alpdry=0.957
pin=5.78e+5
pout=2.776e+5
vin=6.755
hdt=3.609e-3
pdr=1.2435
velx=2.014
vely=5.78
tdelay=80.
radf=2.92085e-3
hdr=52.23
spd1=7.1e5
spd2=0.
tarea=120.914e-6
$end
$roddat
q0=206.67e3
ftd=0.9357
fpuo2=0.25
pgas=1.e5
gmix(1)=1.
$end
3               $ncr
```

```
0                    $indent
1 2 11                    $ifcar
3(3 3 3)                    $nrzf
3(3(10 1 3)) $nrmzf
3(7 7 3 1(1 2 3) 7 7 3) $mnrzf
1 $inx
9 $mnrzs
4 $nrmzs
17(0.0) 1.7672e-3 9(0.8836e-3) 2(1.1045e-3) 5(1.7672e-3)
1.1438e-3 9(0.572e-3) 2(0.715e-3) 5(1.1438e-3) $arx
51(0.0) $ary
18(41.438e-6) 18(44.86e-6) 18(34.616e-6) $arz
8.42e-6 9(4.21e-6) 2(5.2625e-6) 5(8.42e-6)
9.12e-6 9(4.558e-6) 2(5.6975e-6) 5(9.12e-6)
7.034e-6 9(3.517e-6) 2(4.396e-6) 5(7.034e-6) $vol
5.419e-3 3.911e-3 3.772e-3 $hedz
2.749e-3 3.32e-3 3.034e-3 $wedz
3.6322e-3 6.2912e-3 12.5824e-3 $dx
3(25.99e-3) $dy
2(0.2032) 9(0.1016) 2(0.127)  6(0.2032) $dz
3(5.78e5 17(4.e5) 2.776e5) $p
57(0.0) $alp
3(2(695.) 17(800.)) $tv
54(6.755) $vvz
3(1(695.) 16(800.)) $twf
0. 0.7475 1.05 1.26 1.39 1.415 1.35 1.2 0.94 0.6 7(0.0) $qz
3(1.156) 3(1.07) 3(0.95) $qt
3(14(0.0) 10(1.0) 18(0.0)) $qr
3(1.6667) 3(2.5) 3(2.) $rn
3(3(2.47e-3 0.06985e-3 0.381e-3)) $drzf
25.99e-3 $pcx
3.048e-3 $drzs
695. 16(780.) $tws
$timdat
tend=2.
dtmin=1.e-4
dtmax=1.e+1
dtlp=2.
dtsp=2.
clm=0.95
$end
```

Input for Analysis of the P3A Test in Transients (0-8.8 sec)

2dp

```
 $tidat
ntc=-2
 $end
$restart
nitmax=2
iss=0
iitmax=20
itb=0
ibb=1
ihtpr=0
epsn=1.e-4
cpumax=10000.
epsi=1.e-4
 tdelay=2.
rnuss=-22.
ntabls=2
itbt=2
ibbt=1
natc=1
$end
   continue P3A transient, v-p bc
10
0. 1. 1. 0.883 2. 0.777 3. 0.69 4. 0.622 5. 0.553
6. 0.51 7. 0.468 8. 0.425 8.8 0.42 $vin
2
0. 1. 8.8 0.5126 $pout
 $timdat
 tend= 10.8
 dtmin=1.e-4
 dtmax=5.e-1
 clm=0.95
dtlp=2.
 dtsp= 10.
 $end
```

Input for Analysis of the P3A Test in Transients (8.8-30 sec)

2dp1

```
 $tidat
ntc=-2
 $end
$restart
nitmax=-5
cv=1.e-2
iss=0
alpdry=0.957
iitmax=40
ishpr=0100
itb=0
ibb=0
ihtpr=0
epsn=1.e-4
epsi=1.e-4
spd2=1.734e4
 tdelay=2.
rnuss=-22.
ntabls=2
itbt=2
ibbt=1
natc=1
$end
   continue P3A transient, p-p bc
2
0. 1. 8.8 0.455 $pin
4
0. 1. 8.8 0.5131 10.2 0.5131 11.6 0.5131 $pout
 $timdat
 tend= 30.
 dtmin=1.e-4
 dtmax=5.e-1
 clm=0.95
dtlp=0.2
 dtsp= 0.02
 $end
```

Input for 2-D Analysis of the OPERA 15-Pin at Steady State

opera

```
$tidat
ntc=3
$end
OPERA out of Pile 15-Pin
Steady state,  2-D, 30 axial cells
Heat Loss & Gain
$intdat
nc=5
nz=29
nr=1
nitmax=2
iss=1
iitmax=10
narf=4
nx=5
itam=1
iht=33
ihtpr=1
ishpr=1100
itb=0
ibb=1
iwft=1
nrzs=1
$end
$readat
epsn=1.e-5
epsi=1.e-5
rnuss=-22.
alpdry=0.957
pin=6.2885e+5
pout=1.013e+5
vin=4.3
hdt=3.98e-3
pdr=1.2435
velx=2.161
vely=5.78
tdelay=80.
radf=2.92085e-3
hdr=52.23
spd1=11.206e5
spd2=7.09e5
tarea=320.24e-6
$end
$roddat
q0=495.e3
$end
5                $ncr
0                  $indent
1 2 20 23                  $ifcar
5(4 4 4 4)                  $nrzf
```

```
5(4(3 2 1 4)) $nrmzf
5(12 12 2 3 11 10 11 3 4 4 2 3 7 4 2 3) $mnrzf
1 2 3 4 5 $inx
3 $mnrzs
4 $nrmzs
29(0.0) 1.98e-3 21(0.792e-3) 7(2.376e-3)
1.529e-3 21(0.6116e-3) 7(1.835e-3)
1.18e-3 21(0.472e-3) 7(1.416e-3)
0.882e-3 21(0.353e-3) 7(1.059e-3) $arx
145(0.0) $ary
30(81.365e-6) 30(84.395e-6) 30(67.085e-6) 30(49.775e-6)
30(37.62e-6) $arz
10.336e-6 21(4.133e-6) 7(12.4e-6) 10.718e-6 21(4.287e-6)
7(12.86e-6) 8.52e-6 21(3.408e-6) 7(10.224e-6)
6.321e-6 21(2.529e-6) 7(7.586e-6)
4.778e-6 21(1.911e-6) 7(5.733e-6) $vol
6.47e-3 4.09e-3 4.18e-3 4.34e-3 4.47e-3 $hedz
3.15e-3 2.74e-3 2.67e-3 2.57e-3 2.213e-3 $wedz
4.3434e-3 4(6.2912e-3) $dx
5(29.0576e-3) $dy
2(0.127) 21(0.0508) 8(0.1524) $dz
5(6.2885e5 29(4.e5) 1.013e5) $p
155(0.0) $alp
5(588.15 588.15 29(800.)) $tv
150(4.3) $vvz
5(588.15 588.15 27(800.)) $twf
0.0 18(1.0) 10(0.0) $qz
5(4(1.0)) $qt
5(13(0.0) 1.0 1.0 25(0.0)) $qr
4(2.66667) 4(4.5) 4(3.5) 4(2.5) 4(1.83333) $rn
5(2(1.525e-3 0.38e-3 0.635e-3 0.381e-3)
2.e-3 0.4765e-3 0.0635e-3 0.381e-3
2.0447e-3 0.1778e-3 0.3175e-3 0.381e-3) $drzf
4.48e-2 3(1.453e-2) 2.24e-2 $pcx
0.508e-3 $drzs
5(588.15 588.15 27(800.)) $tws
$timdat
tend=2.
dtmin=1.e-4
dtmax=1.e+1
dtlp=2.
dtsp=2.
clm=0.95
$end
```

Input for Analysis of the OPERA 15-Pin in Transients (0-9 sec)

2dop

```
 $tidat
ntc=-2
 $end
$restart
nitmax=4
cv=1.e-2
iss=0
iitmax=30
pout=1.013e5
itb=0
ibb=1
ihtpr=0
istrpr=0
epsn=1.e-4
epsi=1.e-4
 tdelay=2.
rnuss=-22.
ntabls=2
itbt=2
ibbt=1
natc=1
$end
   continue OPERA transient, v-p bc
7
0. 1. 0.86 0.93 2.86 0.78 3.86 0.719
5.86 0.59 10.86 0.48 15.86 0.349 $vin
2
0. 1. 20. 1. $pout
$timdat
 tend= 11.1
 dtmin=1.e-4
 dtmax=5.e-1
 clm=0.95
dtlp=2.
 dtsp= 10.
 $end
```

Input for Analysis of the OPERA 15-Pin in Transients (9-20 sec)

2dop1

```
 $tidat
ntc=-2
 $end
$restart
nitmax=-5
iss=0
alpdry=0.957
iitmax=30
cpumax=10000.
ishpr=0110
itb=0
ibb=0
ihtpr=0
epsn=1.e-4
epsi=1.e-4
tdelay=2.
rnuss=-22.
ntabls=2
itbt=2
ibbt=1
natc=1
$end
   continue OPERA transient, p-p bc
5
0. 1. 5.86 0.5083  9.51 0.44 10.86 0.424 15.86 0.35 $pin
2
0. 1. 20. 1. $pout
 $timdat
 tend= 20.
 dtmin=1.e-5
 dtmax=5.e-1
 clm=0.95
dtlp=0.2
 dtsp= 0.05
 $end
```

Input for 2-D Analysis of the test 71B, run 101 at Steady State

2din1

```
$tidat
ntc=3
$end
Thors Bundle 6A (19 pin), Test 72B, Run 101,
   Steady state, Heat losses to Sodium Soaked
   Insulation, Gas Plenum Represented, 17 Channels
$intdat
nc=3
nz=17
nr=1
nitmax=2
iitmax=30
iflash=1
narf=3
nx=1
itam=1
iht=33
itb=0
ibb=1
iwft=1
nrzs=5
$end
$readat
epsn=1.e-5
epsi=1.e-5
rnuss=22.
pin=2.137e5
pout=1.617e5
vin=1.572
vout=1.572
spd1=0.
spd2=0.
hdt=3.2e-3
pdr=1.2435
velx=2.76
vely=5.78
tdelay=80.
radf=2.921e-3
hdr=52.174
$end
$roddat
q0=0.316667e5
$end
3                $ncr
0                  $indent
1 11 12                 $ifcar
3(4 4 4)                   $nrzf
3(3(1 2 1 3)) $nrmzf
3(3(7 3 2 3 )) $mnrzf
1   $inx
```

```
3 6 4 5 4                                   $mnrzs
1 4 1 1 1                                   $nrmzs

17(0.0) 1.68e-3 9(0.56e-3) 1.05e-3 0.63e-3 5(1.12e-3)
0.84e-3 9(0.28e-3) 0.524e-3 0.314e-3 5(0.56e-3) $arx
51(0.0)  $ary
18(27.48e-6) 18(25.94e-6) 18(8.646e-6) $arz
8.38e-6 9(2.79e-6) 5.23e-6 2.81e-6 5(5.587e-6)
7.9e-6 9(2.64e-6) 4.94e-6 2.96e-6 5(5.267e-6)
2.635e-6 9(0.878e-6) 1.647e-6 0.988e-6 5(1.757e-6) $vol
4.6e-3 3.89e-3 3.42e-3 $hedz
2.21e-3 3.343e-3 2.304e-3 $wedz
3.63e-3 2(6.287e-3) $dx
3(1.87e-2) $dy
2(.3048) 9(.1016) .1905 .1143 6(.2032)        $dz
3(2.137e5 1.80e5 1.78e5 1.76e5 1.74e5 1.72e5 1.7e5 1.7e5
10(1.68e5) 1.617e5) $p
57(0.0)                     $alp
3(2(661.0) 17(800.0)) $tv
54(1.572)                    $vvz
3(661.0 16(800.0)) $twf
0.0 .466 .686 .856 .963 1.0 .963 .856 .686 .466 7(0.0)     $qz
3(3(1.0))                    $qt
3(0.0 2(1.0) 18(0.0)) $qr
3(1.16667) 3(1.5) 3(0.5) $rn
3(3(1.27e-3 3.2e-4 9.3e-4 3.8e-4)) $drzf
18.706e-3 $pcx
0.00051 0.02056 0.00549 0.00668 0.00602     $drzs
2(661.0) 15(780.0) $tws
$timdat
tend=8.
dtmin=1.e-3
dtmax=2.
dtlp=8.
dtsp=0.1
clm=0.95
$end
```

Input for Analysis of the test 72B, run 101 in Transients (0-9 sec)

2dpp1

```
 $tidat
ntc=-2
 $end
$restart
nitmax=5
iss=0
iitmax=40
iflash=0
itb=0
ibb=1
ihtpr=0
istrpr=1
epsn=1.e-4
epsi=1.e-4
 tdelay=8.
ntabls=2
itbt=2
ibbt=1
natc=1
$end
   continue 72B, 101 transient, v-p bc
2
0. 1. 5.3 0.4 $vin
2
0. 1. 5.4 0.9 $pout
 $timdat
 tend=17.
 dtmin=1.e-6
 dtmax=5.e+2
 clm=0.9
 dtlp=2.
 dtsp= 0.2
 $end
```

Input for Analysis of the test 72B, run 101 in Transients (9-40 sec)

2dpp2

```
 $tidat
ntc=-2
 $end
$restart
nitmax=-5
iss=0
iitmax=40
iflash=0
itb=0
ibb=0
ihtpr=0
epsn=1.e-4
epsi=1.e-4
alpdry=0.957
 tdelay=8.
ntabls=2
itbt=2
ibbt=1
natc=1
$end
   continue 72B, 101 transient, p-p bc
2
0. 1. 4.3 0.8243 $pin
2
0. 1. 4.3 0.9 $pout
 $timdat
 tend=40.
 dtmin=1.e-6
 dtmax=5.e+2
 clm=0.9
 dtlp=0.5
 dtsp= 0.025
 $end
```